VERTICAL PERTURBATIONS IN GALACTIC DISKS OF THE LOCAL UNIVERSE

Catalina Urrejola M.

Vertical Perturbations in Galactic Disks of the Local Universe

Catalina Urrejola M.

Doctoral Thesis

To fulfill the requirements for the degree of Doctorate in Astronomy
at Universidad de La Serena by

Catalina Urrejola M.

under the supervision of

Dr. Facundo Ariel Gómez, Universidad de La Serena
Dr. Sergio Torres Flores, Universidad de La Serena

Defended on April 6th, 2023 before the committee composed of

Dr. Philippe Amram, Laboratoire d'Astrophysique de Marseille
Dr. Laurent Chemin, Universidad Andrés Bello
Dr. Antonela Monachesi, Universidad de La Serena
Dr. Kathy Vivas, Cerro Tololo Inter-American Observatory (CTIO), NOIRLab

April 20, 2023

Contents

Acknowledgments

Throughout my doctoral period, I had the pleasure of meeting many people who became fundamental pieces to make this process one of the most meaningful experiences of my life.

I begin by thanking my two supervisors, Facundo and Sergio, who are responsible for my training as a researcher and for increasing my passion for galaxies. They were a great support in all areas and knew how to understand the good and not-so-good times that we went through during all these years.

I thank the thesis committee, Katy, Antonela, Philippe, and Laurent, who enriched the text with their comments. In addition, their valuable suggestions have opened up new ideas to continue on the research path.

Thank you very much to Jesús Gómez-López, my observing partner at OHP, who patiently taught me the entire observation and data reduction process. Without a doubt, Jesús, Mónica, Philippe, and Benoit, were fundamental in making my stay at Laboratoire d'Astrophysique de Marseille successful.

I am grateful to my colleagues and collaborators Ignacio Gargiulo, Franklin Aldas, Silvio Varela, and Diego Pallero, who have helped me a lot in the area of simulations, which was totally new to me.

Definitely one of the best parts of my Ph.D. was getting to know my great friends: Piera, Ciria, and Diego. Thank you for welcoming me as one of your own and integrating me into the group immediately. Piera, thank you for your company, our long conversations, and your support at all times. Ciria, you are one of the kindest and craziest people I have ever met. Thank you for the best moments throughout the whole process. And to my dear Diego, you are the best partner. You are an example for me, both professionally and personally. Thank you for those afternoons listening to Lucybell in the office and for the coffee at Pipi Cucú. To Catalina Labayru for the nice moments and good company and to Daniel for making me laugh and for helping me at all times despite the distance.

I would like to express my gratitude to all my friends and colleagues for sharing nice moments with me. I want to especially thank my roommates, Camila and Dania with whom we lived through the entire process of the social outbreak and pandemic. To Alex for always being so kind to me. I thank Ciria, Paulo, Mario, Sebas, Franklin, and Paty for playing board games and entertaining afternoons. Thank you all for making this a special experience.

I express my gratitude to the entire staff of the Physics Department, with special thanks to Don Jaime and Pacheco, who were always incredibly kind to me and provide the assistance I needed.

My greatest thanks to one of the most important people to me, Gustavo Morales. You definitely became my emotional and professional support during a large part of my doctoral process. Thank you for your infinite patience and your love at all times.

A ti mamá que sin lugar a dudas fuiste y eres el principal apoyo en mi vida. Eres la persona que creyó en mi desde el primer momento, regalándome mi primer telescopio y acompañándome en todas mis locuras astrónomicas. Hoy, luego de muchos años y en el término de esta etapa tan importante, sigues aquí conmigo.

Finalmente, dejo mi posición de científica y dedico esta tesis a mi padre y a mi hermana que en algún lugar del universo, seguramente en alguna galaxia disco de baja inclinación, siguen observándome y apoyándome incondicionalmente.

Abstract

This thesis focuses on the study of vertical perturbations in late-type galaxy disks through kinematic analysis using observational and cosmological simulations. These perturbations are movements above and below the midplane of galactic disks and are interpreted as coherent and extended global flows within these structures. One of the main objectives is to determine the frequency of perturbations in a sample of low-inclination galaxies in the local Universe.

The collaborative study of the nearby galaxy VV304a is presented as motivation for the main work. Additionally, a new set of observational data, WiNDS (Waves in Nearby galaxies Disk Sample), is introduced, which includes 40 late-type galaxies observed with a Fabry-Perot interferometer, with 12 new datasets and 28 archive data obtained from different studies. The aim is to identify possible vertical velocity flows associated with perturbations using 2D line-of-sight velocity (V_{los}) fields.

In complementing the observational study, TNG50 hydrodynamic simulations from IllustrisTNG are used to determine the frequency of vertical velocity patterns, which parameters can be used to quantify galaxies that reveal perturbations in their disks and, the environment in which they are generated. The total simulated sample comprises 251 galaxies with MW/M31 mass and disk-like morphology.

From the analyses described above, VV304a reveals vertical perturbations along the disk, likely associated with the recent interaction with its companion galaxy, VV304b. Furthermore, the analysis of the WiNDS sample revealed that 20% of galaxies potentially have velocity perturbations consistent with vertical perturbations, and these candidate galaxies reside in diverse environments, such as groups or recent interactions as well as isolated galaxies.

Finally, the simulated sample reveals that 70% of disks are deformed, which is consistent with previous studies. Deformed disks have a higher number of neighbors than flat or slightly deformed disks. The history of recent interaction reveals that only 16% of flat disks have not had interactions with massive satellites during the last 3 Gyr, compared to 70% of disks with complex deformations within the same period.

The results of this thesis provide a fresh perspective on the exploration of galaxy interactions and evolution. The characterization and modeling of the observed perturbations will enable us to establish constraints not only on the interaction history of nearby late-type galaxies but also on the structures of galactic discs and the effects associated with their density perturbations.

Chapter 1

Introduction

In this Chapter, we will focus on the galaxy formation paradigm, with a particular emphasis on disk galaxies and their kinematics. We will explore the dynamics of the galactic disk and the important role that vertical perturbations play in shaping its structure and evolution. We will examine the latest observational evidence for vertical perturbations in the Galactic disk, and discuss the various mechanisms that may induce them, from internal processes to external effects like tidal interactions and mergers.

1.1 Galaxy formation paradigm

Galaxies are one of the most interesting objects in the Universe, composed of baryons (stars, gas, and dust) and reside within extensive halos of dark matter. As established by the currently accepted ΛCDM paradigm (Peebles, 1980), the formation of galaxies is intrinsically linked to the environment in which they belong, wherein the hierarchical assembly of smaller structures merges over time to form larger and larger structures.

The formation process begins with small density fluctuations in the early universe. These fluctuations eventually collapse under their own gravity, forming the first generation of stars and galaxies. Over time, these small structures continue to merge and combine, forming larger and more complex structures such as groups and clusters of galaxies.

In Fig. 1.1.1, we present a schematic diagram of the hierarchical assembly for a late-type galaxy today.

Within this framework, one of the key factors in galaxy evolution is the gravitational interaction between galaxies. As galaxies move through the universe, they are influenced by the gravitational forces of other nearby galaxies. These kinds of gravitational interactions can cause galaxies to reshape. Therefore, these interactions play a fundamental role in the present-day structure and evolution of galaxies in the universe.

Although the universe continues to expand and the density of matter decreases, the hierarchical model predicts that galaxy formation will never truly end and that galaxies will continue to merge and evolve over time. Overall, the hierarchical model of structure formation provides a framework for understanding the origins and evolution of galaxies and has been supported by a wealth of observational evidence and cosmological simulations (White & Rees, 1978; Searle & Zinn, 1978; Davis et al., 1985; Frenk et al., 1988; White & Frenk, 1991; Warren et al., 1992; Cen et al., 1994; Gelb & Bertschinger, 1994; Hernquist et al., 1996; Navarro et al., 1996, 1997; Jenkins et al., 2001; Wambsganss et al., 2004; Springel et al., 2005, 2006, 2008).

As stated, throughout their evolution, galaxies are influenced by a variety of physical processes that have an important impact on their final morphological properties. As a result, a way to classify galaxies is based on their morphological features, which are the visual characteristics of a galaxy. The most commonly used system for classifying galaxies is the Hubble tuning fork diagram which was developed by Edwin Hubble in the 1920s. This diagram uses the shape of a galaxy and the presence or absence of a central bulge, and spiral arms, among others, to classify galaxies into three main types: elliptical, spiral, and irregular (see Fig. 1.1.2). Galaxies are classified from red giant elliptical galaxies to small blue irregular galaxies.

Clearly, it is of great interest to study the dependence of the shape of galaxies on the environment to fully understand the formation and dynamic processes of the stellar and gaseous content of galaxies.
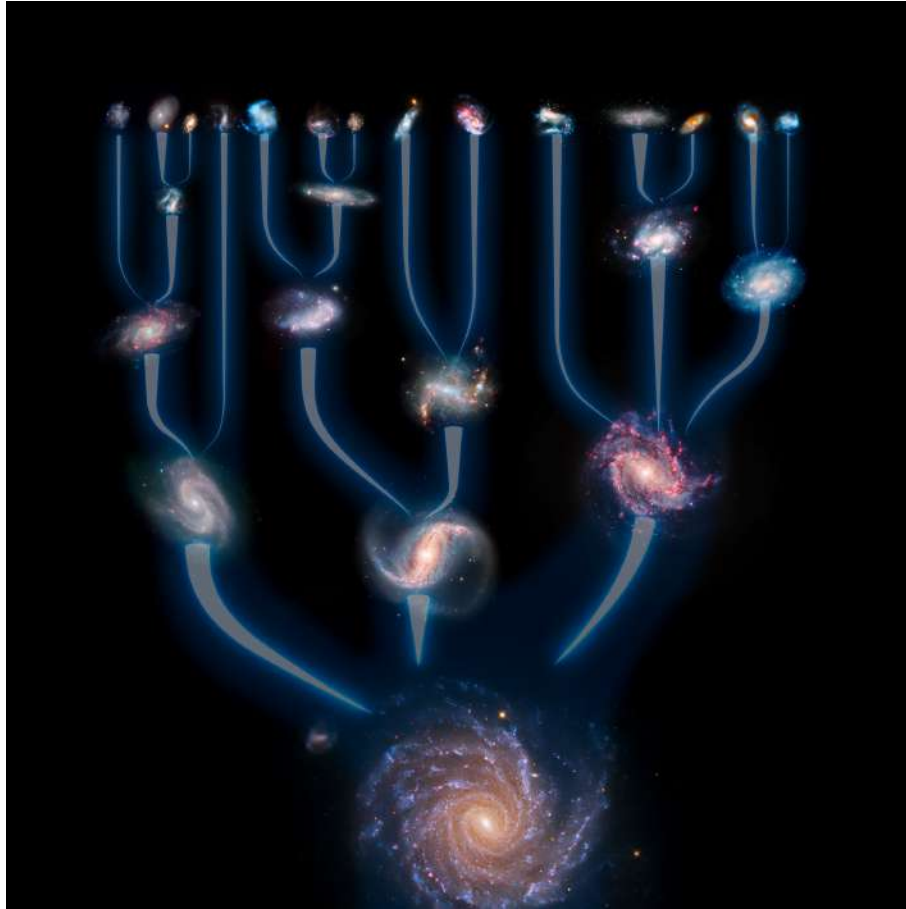
Figure 1.1.1: Scheme of galaxy formation through the hierarchical model of structure formation. Credit: ESO/L. Calçada

1.2 Spiral galaxies and disk kinematics

Within the different types of galaxies, spiral galaxies are the objects of study in this thesis and correspond to two-thirds of the massive galaxies in the present-day Universe (Lintott et al., 2011; Willett et al., 2013). This type of galaxy has, in addition to old stars, young stellar populations in their disk, which makes their appearance bluish due to the type of stars that compose them. In addition, these types of galaxies are rich in gas and with a high rate of star formation with respect to early-type galaxies. Among the main features of spiral galaxies, the disk components are supported by rotation, while the central regions typically contain a spheroidal-like component composed of an old stellar population dominated by velocity dispersion.
Within the spiral galaxies, we find the so-called "Grand Design", which has a regular pattern dominated by a pair of arms observed symmetrically. These types of spirals are often found in nearby galaxies. On the other hand, we observe "flocculent" spirals, which have many small spiral arms without any regular pattern. The arms are the most common sites of star formation and correlate with the galaxy's total luminosity. A brighter galaxy tends to have well-defined spiral patterns.
The kinematics of disk galaxies refers to the movement of the stars, gas, and dust. Disk galaxies are characterized by a flat, rotating disk of stars and gas and generally, a central bulge.
Using the observed Doppler shift of the spectral lines (e.g., H_α, HI, and CO) of a star/gas from their rest wavelengths, the velocity along the direction towards the star/gas can be measured. Several large surveys, such as PHANGS (Rosolowsky et al., 2019), THINGS (Walter et al., 2008), CALIFA (Sánchez et al., 2012) and SINGS (Kennicutt et al., 2003) have been dedicated, among other things, to measure the line-of-sight velocity of large numbers of relatively nearby galaxies. In particular, within the main studies of late-type galaxy kinematics, we find the GHASP survey (Garrido et al., 2002, 2003, 2004, 2005; Spano et al., 2008; Epinat et al., 2008a,b; Torres-Flores et al., 2011; Barbosa et al., 2015; Korsaga et al., 2018, 2019a,b). The whole

Figure 1.1.2: The Hubble tuning-fork diagram is used to classify galaxies based on their morphology taken from Cui et al. (2014)

sample of GHASP survey consists of more than two hundred H_α data cubes from which are computed H_α maps of late-type galaxies using the Fabr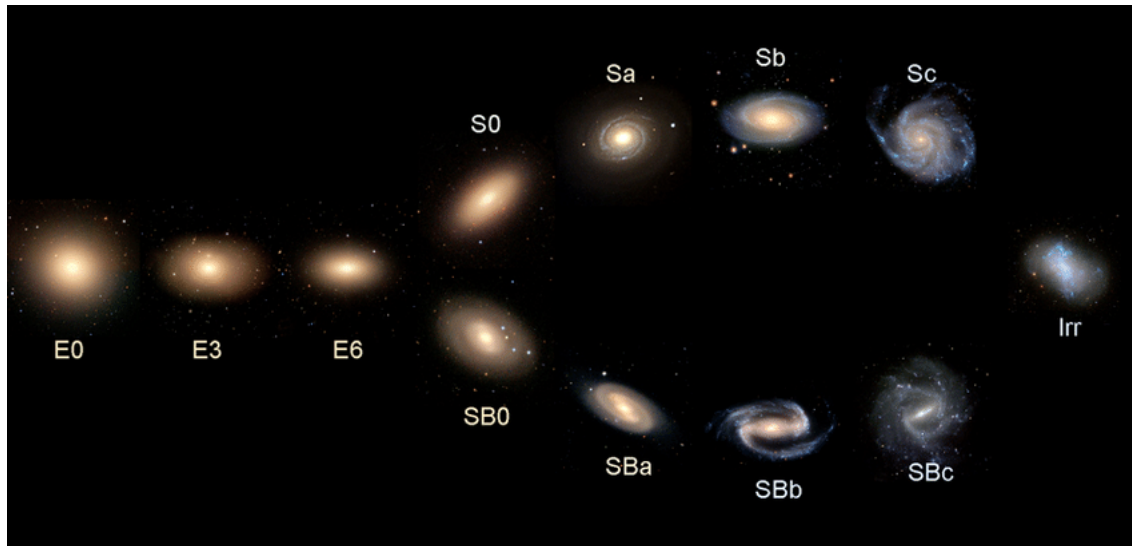y-Perot interferometer. It is one of the largest galaxy samples ever observed with this technique. This type of study gives us information on the internal structure and dynamics of this type of system. In addition to derived H_α maps, rotation curves can be constructed from a given velocity model, for example, the tilted-ring method (Rogstad et al., 1974). This rotation curve is one way to describe a spiral galaxy which is a function of the tangential velocity in the plane of the disk in terms of the distance to the center of the galaxy and is a tracer of the gravitational potential energy of the galaxy, i.e., of the total mass contained in the galaxy (baryonic and dark matter).

From the maximum rotation velocity derived from the rotation curves, the galaxy's luminosity can be estimated from the Tully-Fisher relation (Tully & Fisher, 1977). This empirical relationship between the maximum rotation velocity and luminosity allows us to infer a value for the galaxy's total mass through the mass-to-luminosity (M/L) ratio. Many works, such as Torres-Flores et al. (2011) and Gómez-López et al. (2019), infer the stellar, baryon, and total mass of late-type galaxies with Tully-Fisher relationship using H_α maximum rotation velocity for GHASP and HRS surveys, respectively. Furthermore, assuming that the axisymmetric rotation model to build the rotation curve only considers rotational velocity as dominant, the deviations that occur are associated with non-circular motions that could be of different origins, such as the effect of a bar, the structure spiral, fountain flows or warps. To detect non-circular movements, residual maps are used, which are derived by subtracting the axisymmetric velocity model from the observed velocity field. Various studies have shown galaxies present distortions in their disks (e.g., Sellwood & Sánchez, 2010). On a smaller scale, the V_{los} fields show asymmetries with amplitudes not exceeding 20 km s^{-1}, attributed to local gravitational instabilities or supernova explosions.

However, the GHASP survey has allowed us to represent the axisymmetric rotational component of galaxies with residual velocities that reveal real non-circular motions with amplitudes of > 20 km s^{-1} (Epinat et al., 2008a,b).

In Fig. 1.2.1, we show the different maps derived from the 3D H_α data cube of NGC 3893 from the GHASP survey (Epinat et al., 2008a). The top left panel corresponds to H_α monochromatic image, and the top right is H_α velocity field. The bottom left panel shows H_α dispersion map and the bottom right is the H_α residual velocity field from Epinat et al. (2008b). In the residual map, we can distinguish the non-circular movements of the galaxy NGC 3893 with color scale in km s^{-1}.

In the case of large-scale asymmetries such as warp or corrugation patterns, they can be produced by different mechanisms, for example, tidal forces due to interaction with a neighboring galaxy (Toomre & Toomre, 1972; Vesperini & Weinberg, 2000).

As described, the kinematics of a galaxy disk can provide valuable insights into the structure and dynamics of the galaxy. In particular, it is interesting to know the nature of the perturbations in the galactic disks, which can help us better understand the formation and evolution of galaxies and the role of gravitational interactions in shaping their structure.
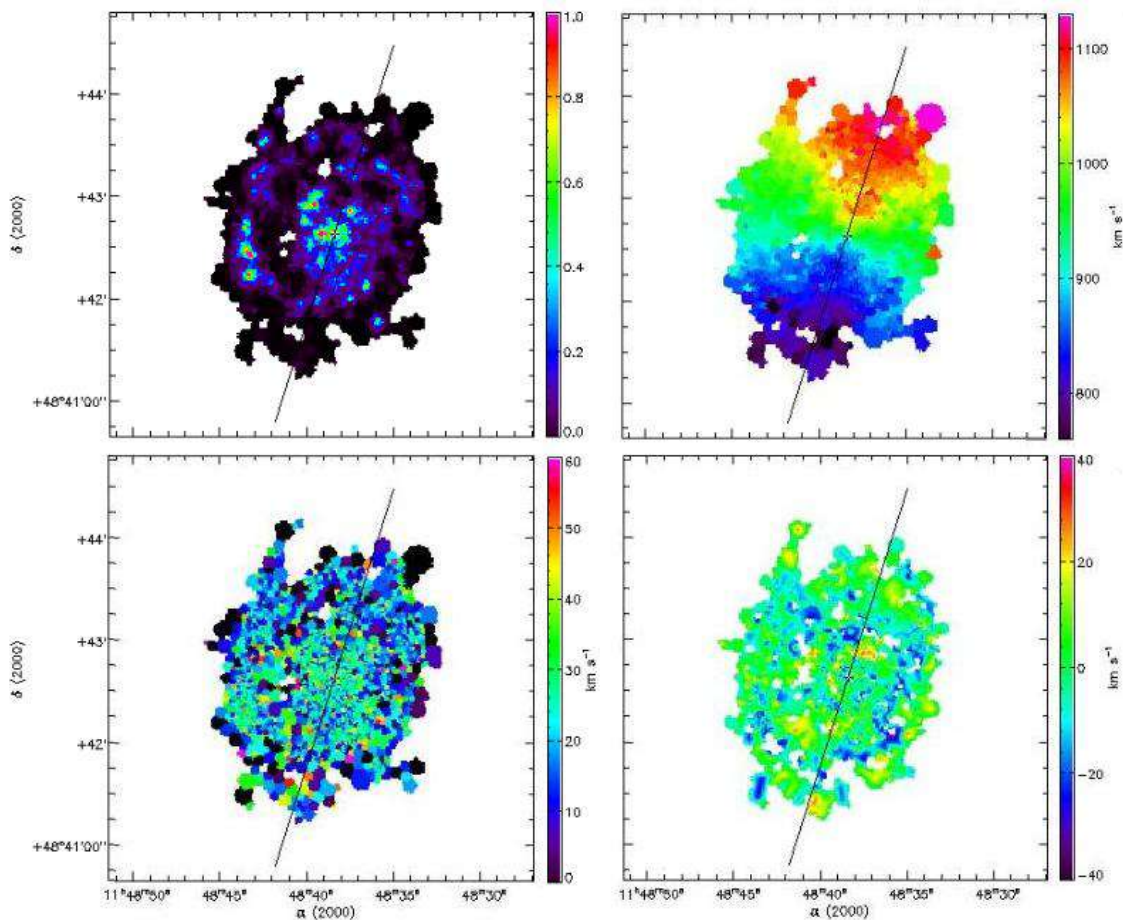
Figure 1.2.1: H$_\alpha$ maps of NGC 3893 from the GHASP survey. Top left-hand panel: H$_\alpha$ monochromatic image. Top right-hand panel: H$_\alpha$ velocity field. Middle left-hand panel: H$_\alpha$ dispersion map. Middle right-hand panel: H$_\alpha$ residual velocity field. The black line is the major axis. Image taken from Epinat et al. (2008b)

1.3 Vertical perturbation in disks

Galactic disks can show perturbations in the axisymmetric distribution of gas and stars. These perturbations correspond to the displacement of the gas or stellar component of the galactic orbit with respect to the mid-plane of the galaxy. For both components, the perturbations are generally observed in the outer regions of disk (Binney, 1992; Cox et al., 1996; Sellwood, 2013, and references therein). The widespread occurrence of warps in galaxy disks suggests that they are either constantly regenerated or are long-lasting phenomena, according to Sellwood (2013). The detection several decades ago of warps in the Milky Way (Burke, 1957; Kerr, 1957) and the spiral galaxies in the Local Group (Rogstad et al., 1976; Newton & Emerson, 1977) motivated the study of warps in external galaxies through different types of observations with the goal of exploring what could be the origins of such type of morphological perturbations in galactic disks. In the Milky Way, the cause of the warp remains debated. However, the similarity in shape between the warp of the stars and the warp of the gas suggests that the warp is caused by gravitational forces, as noted by researchers such as Miyamoto et al. (1988) and Drimmel et al. (2000). HI observations reveal an asymmetric warp in the Milky Way's disk, reaching a height ~ 4 kpc above the mid-plane in the North ($l \sim 90°$) and curving to the South ($l \sim 270°$) below 1 kpc at a distance of approximately 20 kpc (Levine et al., 2006). The HI disk is smaller in mass than the stellar disk but more extended, allowing for mapping beyond the Solar Neighborhood (SN, ~ 3 kpc) with extensive angular coverage.

In recent decades different studies of edge-on disk galaxies (Reshetnikov & Combes, 1998; Sánchez-Saavedra et al., 1990;

García-Ruiz et al., 2002; Ann & Park, 2006) have revealed deformed disks, and the S-shaped warp type in the outermost parts of galaxies are very common. Cosmological models support these results and exhibit a wide range of vertical structures (Gómez et al., 2017). About 30% of the simulated galaxies have an almost flat structure, while the remaining 70% show strong vertical perturbations. Half of these perturbations exhibit classic S-shaped warps, with amplitudes as large as 2 kpc in the outer regions. The other 35% of the disk sample displays more complex corrugation patterns, with amplitudes of mean height > 2 kpc. These patterns are often the result of the evolution of initial S-shaped warps, which distort into leading spirals due to the torque exerted by the inner, misaligned disk (Shen & Sellwood, 2006). Therefore, Gómez et al. (2017) suggests that warps should be common.

In Fig. 1.3.1, we show UGC 3697, an example of an integral-sign galaxy, which reveals a pronounced warp on both sides of its stellar and gaseous disk. Different mechanisms have been proposed to explain the origin and evolution of disk deformations, such as interactions with other galaxies, the gravitational influence of nearby structures, or the formation of new stars within the galaxy (Ostriker & Binney, 1989; Quinn et al., 1993; Velazquez & White, 1999; Bailin, 2003; Kazantzidis et al., 2009; Gómez et al., 2013; D'Onghia et al., 2016; Gómez et al., 2016, 2017; Laporte et al., 2018a, 2019b).

Figure 1.3.1: Integral-Sign galaxy. UGC 3697 is a spiral galaxy with pronounced deformation on both sides of its stellar and gaseous disk. Credits: NRAO/AUI/NSF.

Vertical perturbations in galactic disks are commonly detected by studying their morphology or the overall shape and structure of the galaxy. For example, a galaxy with a relatively thin and flat disk that is slightly warped or flared at the edges may be the product of gravitational influence or a secular process. In terms of galaxy mass, the study carried out in Struve et al. (2007) on the kinematics of massive spirals suggests that the frequency of warps is scarcer in galaxies of greater masses. On the other hand, if the environment in which the galaxies are found is analyzed, García-Ruiz et al. (2002) establishes that the galaxies with more asymmetric warps and larger amplitudes are found in denser environments. To understand the relationship between a galaxy's location and its warp type, it is crucial to study its surroundings.

As previously mentioned, there have been diverse studies on the frequency and environment of warp disks in edge-on galaxies. However, these observations are limited by projection effects and cannot provide insight into the distribution of vertical disturbances throughout the entire disk. In this case, observing face-on galaxies is the best way to know if the vertical disturbances are distributed locally or globally throughout the disk.

Currently, studies of vertical perturbations in face-on galaxies are scarce. Sánchez-Gil et al. (2015) analyze four low-inclination galaxies using the long-slit technique, where half of the galaxies reveals a potential corrugation pattern. Since a slit covers a limited region of the galactic disk, such patterns can be confused with the effects of local disturbances such as fountain flows. Fig. 1.3.2 presents an example of the galaxies that Sánchez-Gil et al. (2015). The left panel displays the long-slits used to study the gaseous disk of NGC 278. Along each slit, the vertical velocity relative to the radius is shown, revealing the wave-like behavior of the ionized gas in NGC 278.

Therefore, obtaining 2D maps of the entire galactic disk is of great interest to determine the distribution of vertical disturbances in the disks of low-inclination galaxies. This will make it possible to study the nature of vertical disturbances in the disks.
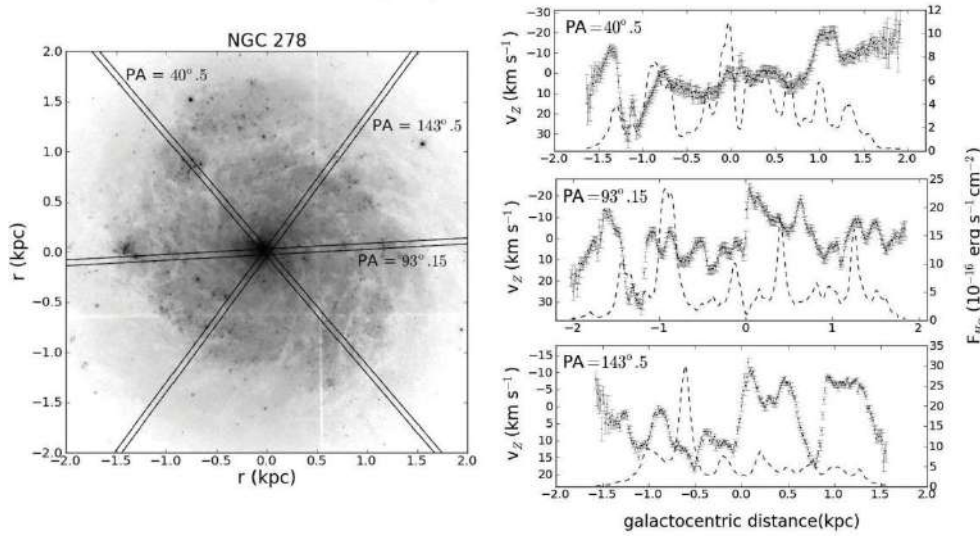
Figure 1.3.2: Corrugation pattern in NGC 278. Left panel: The different slit positions of the long-slit spectra for NGC 278. Right panel: vertical velocity V_Z, at each position angle. Image extracted from Sánchez-Gil et al. (2015)

1.4   Observations of vertical perturbations in the Galactic disk

Studies of the Galactic disk have provided evidence of wave-like vertical asymmetry in the SN (e.g. López-Corredoira et al., 2002; Momany et al., 2006; Widrow et al., 2012; Slater et al., 2014; Price-Whelan et al., 2015; Xu et al., 2015; Antoja et al., 2018; Gaia Collaboration et al., 2018).

In particular, Widrow et al. (2012) studied the kinematics of 11k main-sequence stars with Galactic latitudes $100° < l < 160°$ from the Sloan Extension for Galactic Understanding and Exploration (SEGUE) survey (York et al., 2000; Yanny et al., 2009) in the SN (within approximately 2 kpc of the Sun). They reported a detection of a north-south asymmetry in the number counts of stars as a function of height relative to the Galactic midplane. The asymmetry (north-south)/(north+south) shows a 10% deficit and excess in stars at $|z| \simeq 400$ pc and $|z| \simeq 800$ pc, respectively. This type of asymmetry strongly suggests, at least locally, the presence of a bending pattern, i.e., local displacements of the disk from its overall midplane. Additionally, Widrow et al. (2012) found that the bulk vertical motions of stars in the SN have characteristics of a breathing wave perturbation, i.e., rarefaction and compression of the Galactic disk.

The top panel of Fig. 1.4.1 presents the observed number density of stars, n_{obs}, where $z_{obs} \equiv z - z_{\odot}$ and $z_{\odot}$ is the vertical position of the Sun. The stars are within the color range of $0.6 \simeq (r-i) \simeq 1.1$ and 0.2 kpc $\simeq |z_{obs}| \simeq 1.6$ kpc. In the bottom panel, the residuals $\Delta \equiv (data - model)/model$ are presented, where the model is described in Press et al. (1992). The residuals show an odd function behavior in z. In the North, the stars are below the model for $z \simeq 400$ pc, and in the South, they are above the model for $z \simeq 800$ pc.

Later, different surveys with larger samples of stars have confirmed the behavior of the bulk vertical velocity observed in Widrow et al. (2012); among them, Williams et al. (2013) using 72k red-clump stars from the Radial Velocity Experiment (RAVE, Steinmetz et al., 2006) and Carlin et al. (2013) with 400k F-type stars using spectroscopic radial velocity measurements from the Large Sky Area Multi-Object Fiber Spectroscopic Telescope (LAMOST, Cui et al., 2012). As a result, it is clear that our galaxy shows a pattern of warping and flaring, which is a more complex pattern than an S-shaped warp detected on HI (Levine et al., 2006), stellar (Djorgovski & Sosin, 1989), and dust (Freudenreich et al., 1994) maps.

Xu et al. (2015) considering Galactic longitudes between $110° < l < 229°$, showed an oscillating asymmetry in star counts on both sides of the Galactic plane and found four Galactic disk anomalies: one north of the Galactic plane at 2 kpc from the Sun, one south of the plane at 4 - 6 kpc, a third north of the plane at 8 - 10 kpc, and evidence for a fourth south 12 - 16 kpc from the Sun, where the Monoceros Ring is associated with the third ripple. The Monoceros Ring is a structure observed both in the northern and southern Galactic hemispheres, showing a complex feature and sharp edge (Slater et al., 2014).

In Fig. 1.4.2, we show a representation of the asymmetries observed in the disk of the Milky Way, highlighting the asymmetries
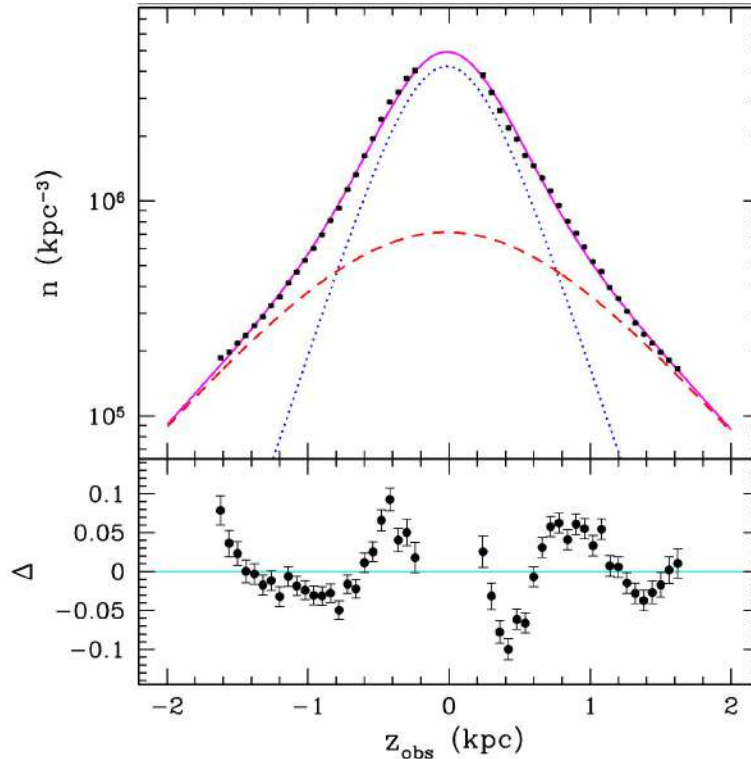
Figure 1.4.1: Numerical density as a function of the distance from the Sun. The data correspond to the black points, and the magenta curve represents the fit of the model. The dotted blue curve represents the contribution of the thin disk, while the dashed red curve represents the contribution of the thick disk. The bottom panel shows the residuals, calculated as Δ = (data - model)/model. Image taken from Widrow et al. (2012)

in the Monoceros Ring and Triangulum–Andromeda (TriAnd) cloud.

According to this discovery and other investigations, they infer that a dwarf galaxy passing through the Milky Way disk would produce a ripple effect similar to the anomalies found in Xu et al. (2015).

Detecting perturbations in the Galactic disk attempt to determine their origin using numerical simulations. One of the hypotheses to explain these perturbations is the interaction of the MW with a satellite galaxy (e.g., Gómez et al., 2013; Widrow et al., 2014; D'Onghia et al., 2016; Gómez et al., 2016, 2017; Laporte et al., 2018a,b; Antoja et al., 2022).

Within the numerical models that explore the origin of the Monoceros Ring asymmetry, Gómez et al. (2013) used high-resolution idealized numerical simulations of the interaction between the MW and Sagittarius (Purcell et al., 2011; Gómez et al., 2012). Exploring mean-height and mean vertical velocity maps, they observed patterns are indeed signatures of vertical density waves in the disk (see Fig. 1.4.3).

Additionally, it has been demonstrated by Gómez et al. (2013) that the vertical modes observed as a function of amplitude must be caused by an external agent acting on the disk. For the Milky Way, it is possible that the perturbations caused by the Sagittarius dwarf galaxy could account for several of the features observed in the disk.

Later, using fully cosmological magneto-hydrodynamical simulations from the Auriga project (Grand et al., 2017), Gómez et al. (2017) analyzes 16 Milky Way-like galaxies with a wide range of disk morphologies and extents. These simulations allowed for analysis of the environment and close encounters between galaxies through time. As previously mentioned in Section 1.3 the simulated disks displayed various vertical structures, with 30% showing a flat structure and 70% showing strongly disturbed disks. Half of these disturbed disks exhibited classic S-shaped warps, with amplitudes as large as 2 kpc in the outer regions. The remaining 35% of the sample showed more complex structures reminiscent of corrugation patterns observed in the Milky Way. These patterns were often the result of the time evolution of initial S-shaped warps and were caused by the torque exerted by the inner, misaligned disk (see Shen & Sellwood, 2006). The relatively high frequency of corrugation patterns in the simulated disks suggests that such behavior is common in galaxies.
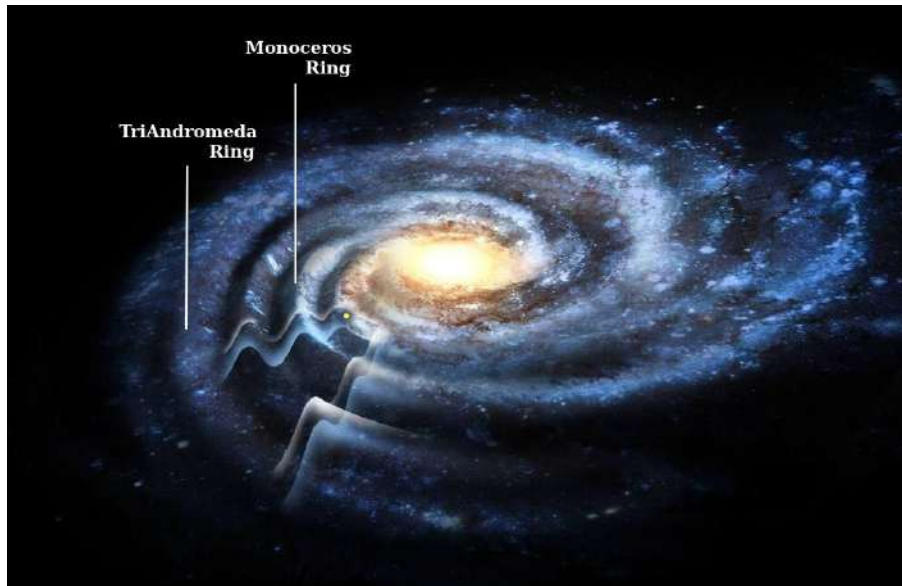
Figure 1.4.2: Representation of the Milky Way disk highlighting the asymmetries in the Monoceros Ring and TriAnd cloud. Credit: Rensselaer Polytechnic Institute.
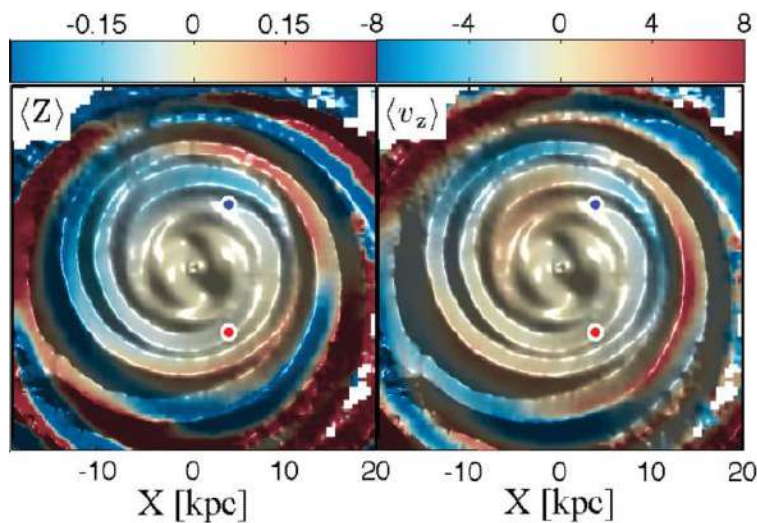
Figure 1.4.3: Mass weighted mean height and vertical velocity maps taken from Gómez et al. (2013).

The left and right panels in Fig. 1.4.4 display the mean height ($\langle Z \rangle$) and vertical velocity ($|V_z|$) maps of a galaxy with a corrugation pattern. The maps reveal an anti-correlation, where the maximum value of $\langle Z \rangle$ corresponds to a minimum value of $|V_z|$ ($|V_z| \sim 0$) and vice versa, respectively. This illustrates the wave-like nature of the bending waves in the galaxy (Gómez et al., 2016, 2017).

Recently, Gaia DR2 (Gaia Collaboration et al., 2018), through the largest and most accurate census of positions and velocities of a billion stars, makes it possible to investigate the origin, evolution, and structure of the Milky Way. Antoja et al. (2018) analyze the 6D phase-space (position and velocities) of more than six million stars within a few kiloparsecs of the Sun in the Galactic disk. The left panel of Fig. 1.4.5 shows a phase space projection of position and vertical velocity (Z-V_z) for stars, with the stars color-coded according to their azimuthal velocity. The pattern displayed is a snail-like shape, indicating a strong correlation between vertical and in-plane movements. The right panel presents a toy model replicating the same
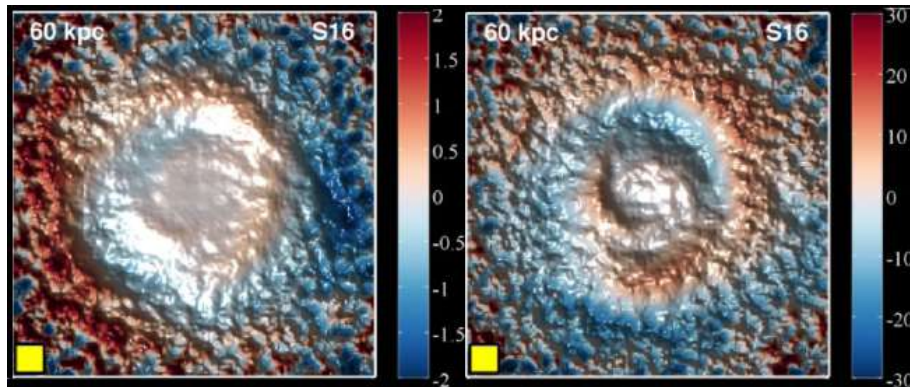
Figure 1.4.4: Maps of the simulated stellar disk's mass-weighted mean height (left panel) and vertical velocity (right panel) of a simulated galaxy from the Auriga project with a corrugation pattern (Gómez et al., 2017)

behavior as seen in the data. The model was created after 500 million years from a set of stars with an initial distribution that is non-equilibrium. The possible cause for this behavior could be the disturbance caused by a satellite galaxy. In particular, the last pericenter passage of the Sagittarius dwarf galaxy's orbit has been shown to have a strong impact on the stellar disk of the Milky Way. These studies represent a breakthrough in the understanding of the spiral structure and dynamics of the Milky Way.
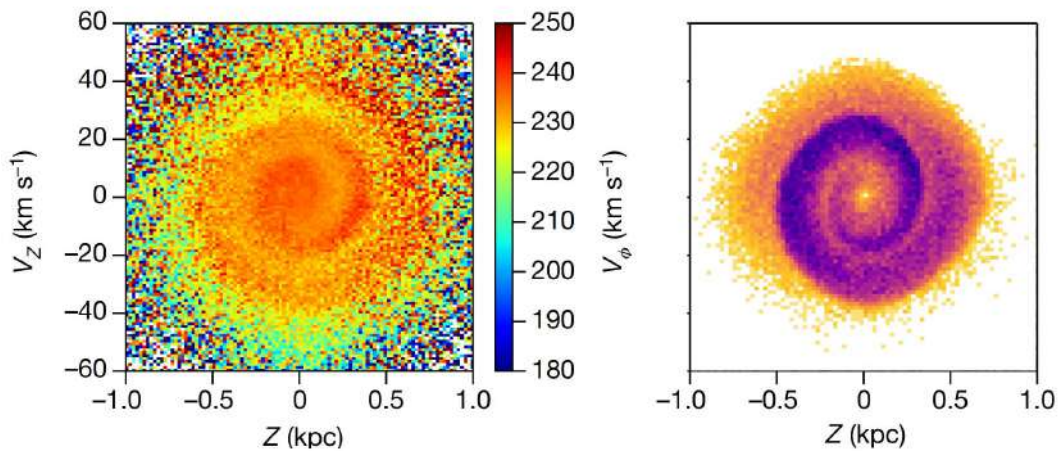
Figure 1.4.5: Left panel: Phase space projection on position and vertical velocity (Z-V_z) where stars are color-coded according to azimuthal velocity. Right panel: toy model. Image taken from Antoja et al. (2018).

1.5 Mechanisms that induce vertical perturbations

Galaxies that have shown vertically perturbed disks have been observed in different environments. Therefore, it is crucial to understand what mechanisms influence the formation of vertical patterns.
Among the main ones, we can mention

a) **Tidal distortion of a pre-existing disk by an external perturber**

As mentioned above, observational studies and simulations show that the perturbed galactic disk could be a response to tidal interaction, such as in the case of the MW and Sagittarius dwarf galaxy (Laporte et al., 2018a, 2019a). Using Auriga cosmological simulations, (Gómez et al., 2017) showed that disks with strong vertical perturbations had interacted at least once with a massive satellite more massive than $10^{10.5} M_{\odot}$ during the last 4 - 5 Gyr. The external perturber can be varied; for example, they can be low-mass satellites close flyby to the host galaxy (Ostriker & Binney, 1989; Quinn et al., 1993; Velazquez & White, 1999; Kazantzidis et al., 2009; Gómez et al., 2013; D'Onghia et al., 2016); the satellite can be massive with a distant fly-by (Vesperini & Weinberg, 2000; Gómez et al., 2016; Laporte et al., 2018a,b); or a misaligned dark matter halo (Debattista & Sellwood, 1999; Jiang & Binney, 1999; Shen & Sellwood, 2006; DeBuhr et al., 2012; Yurin & Springel, 2015; Gómez et al., 2016; Laporte et al., 2018a).

b) **Misaligned accretion of high angular momentum cold gas**

This mechanism is a phenomenon that occurs when cold gas with high angular momentum is accreted onto a galaxy. This type of accretion can occur through several mechanisms such as a close encounter with a gas-rich satellite (e.g. the Magellanic Stream), misaligned infall from the cosmic web, or cooling of a hot gas halo. The accretion of cold gas in the outer parts of the disk causes bursts of star formation, therefore the vertical perturbations will be dominated by a younger, newly formed population due to misaligned accretion with the pre-existing disk. In Fig. 1.5.1, we can see how the stellar component is distributed in one of the simulated galaxies in Gómez et al. (2017) that show a robust vertical pattern, depending on the age of the stellar population. The colored bar indicates the mean height in units of kpc. The older population is shown in the left panel, in the 4 - 6 Gyr range, which is more homogeneously distributed on the disk. On the other hand, the right panel shows the distribution of younger stars between 0 and 2 Gyr, which shows a distribution of mean height with more extreme values in the outermost parts of the disk, showing typical wave-like behavior. In particular, we can notice that when analyzing the older population, there does not seem to be a perturbation in the disk. However, the young population shows a clear pattern of corrugation.
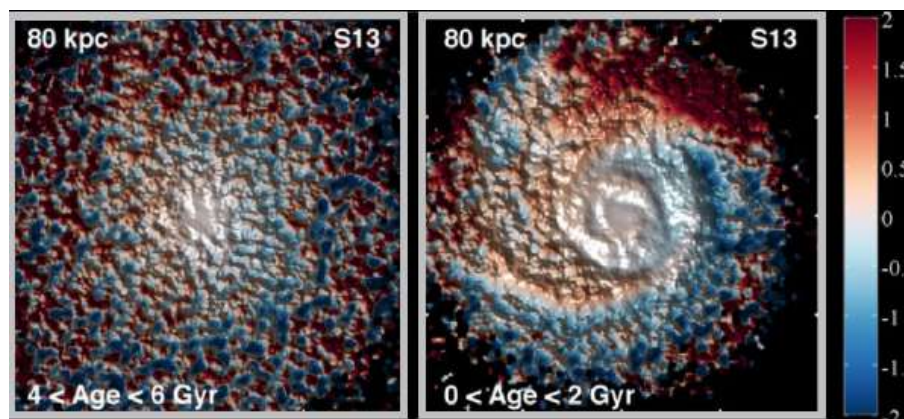
Figure 1.5.1: Mean height maps of the disk of a simulated galaxy at $z = 0$. In the left panel, the map shows stellar particles with ages between 4 to 6 Gyr, and in the right panel, stellar particles with ages between 0 to 2 Gyr. The color scale shows the disk's mean height in kpc units. Image from (Gómez et al., 2017)

Characterizing the types of perturbations that galaxies experience allows us to obtain more information about their environment and the history of galaxy interaction. For this reason, observational studies of the galactic disks in the local universe are essential. The maps presented in Fig. 1.4.4 are equivalent to mean V_{los} fields for perfectly face-on galaxies. Therefore,

the disturbances must be detectable in the vertical fields V_{los} both in stellar components obtained by field spectroscopy and the gaseous component obtained using interferometry. These perturbations should be easily detectable in galaxies observed almost face-on, V_{los} field analysis for the cold gas velocity component using interferometry. These observations provide a direct way to assess the frequency with which oscillating vertical patterns arise in late-type galaxies.

1.6   This thesis

In this thesis, within the main objectives, we aim to determine the frequency of vertically perturbed galactic disks in the local universe since these types of perturbations are indicators of a galaxy's recent interaction with its environment. We wish to understand to what degree vertical perturbations can be used to reconstruct the recent interaction activity of nearby galaxies, thus placing constraints on the current galaxy formation models.

Through a detailed study of the nearby low-inclination galaxy VV304a with similar kinematic characteristics to the Milky Way using high-resolution Fabry-Perot data, numerical models, and cosmological simulations, we were able to provide the first evidence of corrugation patterns in an external galaxy, similar to those seen in our own Galactic disk. This discovery prompted us to conduct a study of vertical perturbations in the local universe, the results of which are presented in this thesis.

Motivated by the results obtained for VV304a, we conducted a new survey, named WiNDS (Waves in Nearby Disk galaxies Survey), which currently includes 40 nearby low-inclination face-on spiral galaxies to determine the frequency of warps and corrugation patterns in nearby galaxies through V_{los} fields. The data sample presented corresponds to 3D data cubes obtained using a Fabry-Perot interferometer with a resolving power at the H_α rest wavelength of R $\approx$ 10000. Through the analysis of residual velocity fields, we seek to detect vertical patterns or warps in the galactic disks that would allow us to quantify and select galaxies that reveal bending modes in their disks. Additionally, by examining the vertical perturbations in the disks of galaxies from various environments, such as interacting with a satellite, belonging to a group, or being isolated, we can explore the role of the environment and the duration of perturbations in the disks of galaxies.

According to the observational results obtained, using cosmological simulations, we seek to answer questions related to the formation of vertical perturbations and how the environment in which each galaxy resides influences the formation of wave patterns in the disks. The sample of simulated galaxies corresponds to 251 galaxies with MW/M31-mass from TNG50 IllustrisTNG. This high-resolution galaxy simulation allows us to analyze the galaxy substructure and is an ideal tool for detecting vertical perturbations. Additionally, we explore how the environment influences the origin and evolution of warps in the galactic disks of the neighborhood and overdensity analysis.

Finally, as a matter of interest, it is essential to know if the perturbations due to the tidal effects exerted on the galaxy are long-lived warps. On the other hand, it is essential to know if the vertical perturbations could be the product of other mechanisms that the galaxy has suffered. For this, we detect satellites of the central galaxies within 6 Gyr lookback time, and considering a parameter related to the torque exerted by a satellite on the host galaxy, we can estimate if these tidal effects are the cause of the disturbances observed at the present day.

1.7   Key questions

There are still many unresolved questions in the field of vertical perturbations in the disks of late-type galaxies. In this thesis, we aim to provide insights that will help to address these questions.

(i) How often do vertical patterns appear in disks of nearby face-on spiral galaxies?

   The WiNDS survey presented in this thesis represents the first systematic search for vertical perturbations in low-inclination galaxies in the nearby Universe. Although the survey is not yet complete, it includes a diverse range of spiral morphological types and environments, such as clusters, groups, and fields. With a wide variety of spiral morphological types, this ongoing survey is expected to grow through future observations.

(ii) In what kind of environment is it most common to find galaxies with perturbed disks?

Using the WiNDS survey we can have a preliminary result of the vertical perturbations in different environments. Subsequently, this is complemented with the TNG50 sample where, through parameters of the number of neighbors within a certain radius and overdensity parameters, we can establish a statistic according to what type of environment is more common to find vertical perturbations.

(iii) What are the main physical mechanisms that cause the vertical patterns?

Vertical perturbations can be induced by various mechanisms previously mentioned, in this thesis we will focus on the formation of vertical patterns as a consequence of close encounters between galaxies.

(iv) Vertical perturbations are long-lived deformations?

In this study, we use the analysis of tidal forces over the past 6 Gyr to investigate the permanence of warps in galactic disks.

1.8   Outline of the thesis

This thesis is organized as follows: The description of both observational instrumentation techniques and simulations are presented in Chapter 2.

In Chapter 3, based on published paper Gómez et al. (2021), we present the results obtained by our collaboration in detecting vertical patterns in a galaxy with similar features to the Milky Way, VV304a, through a complete analysis using observational data, numerical models and cosmological simulations.

In Chapter 4, we present the new WiNDS survey, which consists of new observations and archival data of nearby nearly face-on spiral galaxies. The data reduction procedure, the data analysis, and the selection and quantification criteria of bending modes are described in addition to an individual description of galaxies that reveal vertical perturbations.

In Chapter 5, we present the galactic disk analysis of the sample of 251 disk-type galaxies from Illustris TNG50 cosmological simulations. We identify the fraction of disks that present vertical perturbations concerning flat or weakly perturbed disks and present the quantification of vertical perturbations using Fourier parameters. In addition, the environment of each galaxy is analyzed considering parameters of the neighborhood and overdensity in which each galaxy resides. Finally, we inspect the tidal effects the galaxy suffers over time to identify possible perturbs.

In Chapter 6, we provide a summary of the work carried out in this thesis, with a particular emphasis on the primary findings. Additionally, we propose potential avenues for future research to build upon the results obtained in this study.

Chapter 2

Instrumental Techniques and Numerical Models

This thesis analyzes the velocity fields of late-type galaxies to detect vertical perturbations using two data sets: H_α data cubes from a Fabry-Perot Interferometer, and simulated galaxies from the TNG50 Project. In this Chapter, we present an overview of the main instrumental aspects of the Fabry-Perot interferometer, and we describe the main characteristics of the TNG50 project.

2.1 Fabry Perot Interferometer

The Fabry-Perot interferometer (FPI) was developed by the French physicists Charles Fabry and Alfred Perot and is based on the interference of multiple light beams. FPI is an optical cavity made of two parallel reflecting plates separated by a certain distance. In Fig. 2.1.1, we present a diagram of an FPI, where the plates M_1 and M_2 are separated by a distance d. Light rays from an extended source are focused through a collimating lens L_1 and parallel to each other inside the cavities. The beams are reflected within the cavity towards a focusing lens L_2 and converge at a point P. If the condition at P is met for constructive interference, we will see a bright ring, while if the state corresponds to destructive interference, there will be a dark ring.
The interference pattern on the detector will alternate bright and dark rings, as shown in Fig. 2.1.1.
The nature of the superposition at the focal point depends on the path difference between successive parallel rays. The path difference can be expressed as:

$$\delta = 2nd\cos\theta_t \tag{2.1.1}$$

where, n corresponds to the refractive index; d is the distance between the plates and θ_t is reflected beam angle. θ_t is related the angle of incidence θ by $\sin\theta = n/n_0 \sin\theta_t$ with n_0 is refractive index of the environment.
A large number of interfering beams produces an interferometer with a high resolution.
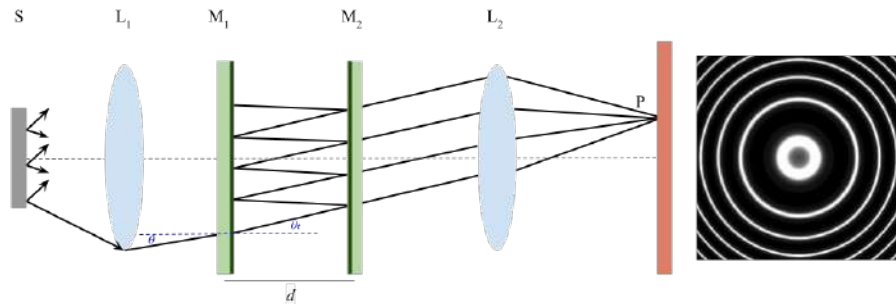
Figure 2.1.1: Schematic of a Fabry-Perot Interferometer

A transmission peak constructive interference of the multiple beams occurs when this optical path difference (Eq. 2.1.1) is an integer multiple of the wavelength, hence

$$\lambda p = 2nd \cos \theta_t \tag{2.1.2}$$

where p is called the interference order, p = 0, 1, 2, 3, ...
Equation 2.1.2 represents the fundamental Fabry-Perot equation.
The free spectral range (FSR) is measured for the distance in wavelength or frequency between successive transmission peaks.

$$FSR = \Delta\lambda_{FSR} = \lambda_i - \lambda_{i+1} = \frac{\lambda}{p} \tag{2.1.3}$$

For FPI, resolving power (R_P) relates to the minimum wavelength separation (λ_{min}) that can resolve, according to the Rayleigh criterion, i.e., if the maximum of the peak of one will be less than half the width of the other peak, then we cannot be sure that there are two peaks. R_P of any spectroscopic instrument is defined as:

$$R_P = \frac{\lambda}{\Delta\lambda_{min}} \tag{2.1.4}$$

Finally, the Finesse ($\mathscr{F}$) measures the interferometer's ability to resolve closely spaced spectral lines. The $\mathscr{F}$ is expressed as the ratio between power resolution and interferometer order.

$$\mathscr{F} = \frac{R_P}{p} \tag{2.1.5}$$

Fig. 2.1.2 shows a plot of transmittance versus wavelength for a fixed θ. The peaks correspond to different values of constructive interference order. The peaks are called resonant frequencies of the cavity. When $\Delta\lambda_{min}$ is smaller, the Finesse value is larger and has higher resolving power.

Figure 2.1.2: Transmission pattern showing the free spectral range (FSR) of a Fabry Perot interferometer with different Finesse, where $\mathscr{F}_2 > \mathscr{F}_1$.

2.1.1   FPI observations applications

The use of the Fabry-Perot Interferometer (FPI) for two-dimensional kinematic studies is a highly effective technique for gaining insights into the structure and evolution of extended sources. As such, it is an ideal tool to achieve the goals of this thesis.
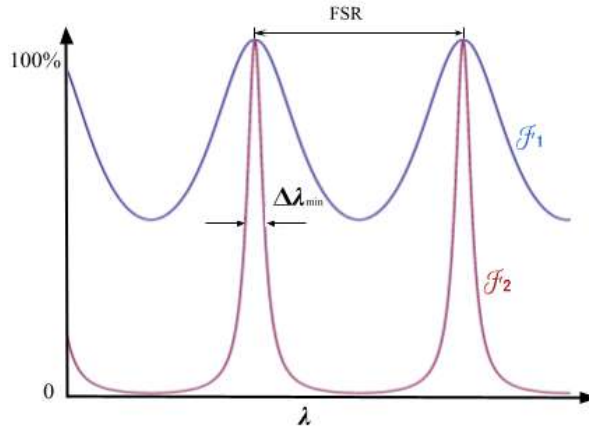
The study conducted by Torres-Flores et al. (2010) analyzed 46 galaxies located in Hickson compact groups, utilizing H_α data cubes from Fabry-Perot observations. These observations were conducted using a Fabry-Perot instrument on the Canada-France Hawaii Telescope (Amram et al., 2003) and the European Southern Observatory 3.6 m Telescope (CIGALE, Amram et al., 1991). The study aimed to examine the relationship between the kinematic and morphological parameters of these galaxies. To determine morphological parameters such as inclination, position angle, and galactic centers, broad-band imaging was used. Kinematic parameters were obtained by analyzing the velocity field, where a velocity model was fitted and the rotation curve was constructed. The authors find that one-third of the unbarred compact group galaxies have position angle misalignments between the stellar and gaseous components. Additionally, the asymmetric rotation curves are clear signatures of kinematic perturbations, probably because of interactions among compact group galaxies. To study the Tully-Fisher relation (TFR) for compact group galaxies, Torres-Flores et al. (2010) determined the maximum rotational velocity for each galaxy by analyzing its rotation curve. In Fig. 2.1.3, we show a comparison of the B-band TFR for compact group galaxies and for the H_α field-galaxy sample from GHASP survey (Epinat et al., 2008a) where that despite the high fraction of compact group galaxies with asymmetric rotation curves, these galaxies still fall within the relation defined by less dense environments, but with more scatter. This confirms previous findings and is supported by a larger sample of 41 galaxies. Additionally, it was found that compact group galaxies at the low-mass end of the TFR tend to have either a magnitude that is too bright for its mass or a low maximum rotational velocity for its luminosity, which suggests star formation or tidal stripping.
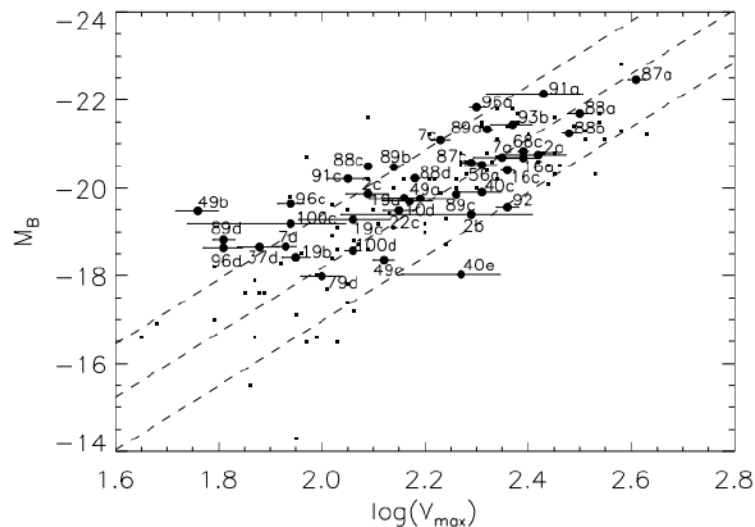
Figure 2.1.3: The B-band Tully-Fisher relation was studied for galaxies in compact groups (as reported in Mendes de Oliveira et al. 2003 represented by filled circles) and a sample of field galaxies (reported in Epinat et al. (2008a), represented by small squares). The position angle (*PA*) and inclination (*i*) were determined automatically for each rotation curve using IDL routines. The center was determined using the morphological center and the inclination was fixed using the morphological inclination. Image from Torres-Flores et al. (2010).

Among the studies carried out using FPI is the study of interacting systems. Font et al. (2011) analyzes the interacting pair Arp271 (NGC 5426 and NGC 5427) where, through the analysis of the velocity fields, the superposed of the H_α emission of the NGC 5426 disk on NGC 5427 was detected allowing estimate of the gas infall rate in NGC 5427.
The observations were conducted using the $GH_\alpha FaS$ FPI (Hernandez et al., 2008) at the 4.2m William Herschel Telescope located at the Observatorio del Roque de los Muchachos on La Palma. The Field-of-View (FoV) was 3.5 arcmin × 3.5 arcmin,
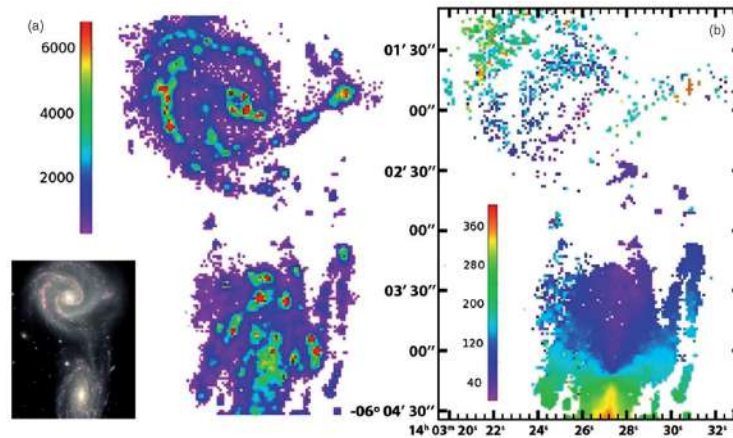
Figure 2.1.4: (a) Arp 271: NGC 5427 (top) and NGC 5426 (bottom) in H_α surface brightness taken with FPI. The color scale is in relative units of surface brightness. (b) Velocity map of NGC 5427 and NGC 5426, color-coded in kms^{-1}. Image from Font et al. (2011)

resulting in a complete map of NGC 5427 and a partial map of the bright disk of NGC 5426 (covering approximately 60%). Figure 2.1.4 displays an optical image from the Gemini Science Archive[1], with the intensity map highlighting the star-forming regions in the arms of the galaxies for both NGC 5426 and NGC 5427. The velocity map, derived from the observations, is presented in the right panel, where the velocity ranges of both galaxies overlap. The velocities associated with NGC 5426 along the line of sight were observed to originate from NGC 5427. Through modeling the distribution of ionized gas, it was inferred that gas is being stripped from NGC 5426 as it passes near NGC 5427. The estimated infalling mass rate was found on the order of 10 $M_\odot$ per year, which is consistent with the high star formation rate observed in the disk of NGC 5427 and with the presence of a detected circumnuclear galactic wind.

Another study (Fathi et al., 2008), detected mass transfer from the disk to the inner region of the galaxy M83 obtained with again the $GH_\alpha FaS$ FPI. The high-resolution data revealed a dominant disk rotation in the galaxy, as well as a rapidly rotating component in the inner 20" radius from the nucleus and a kinematic position angle twist at its edges (see Fig. 2.1.5). Derived H_α velocity field reveals signs of infall gas from outer to nuclear regions of the galaxy. The observations reveal star formation events at different times, which would be the result of the spiral entry of gas to feed the nuclear region of M83. The infalling gas, driven by the bar, is responsible for both forming the disk and fueling a circumnuclear starburst in M83.

Figure 2.1.5: Left panel: H_α velocity map of M83. The contours mark velocity steps of 40 kms^{-1}. Right panel: zoom-in into the center. Image from (Fathi et al., 2008).

---

[1] http://www.gemini.edu/twinspiral

2.2 Illustis TNG

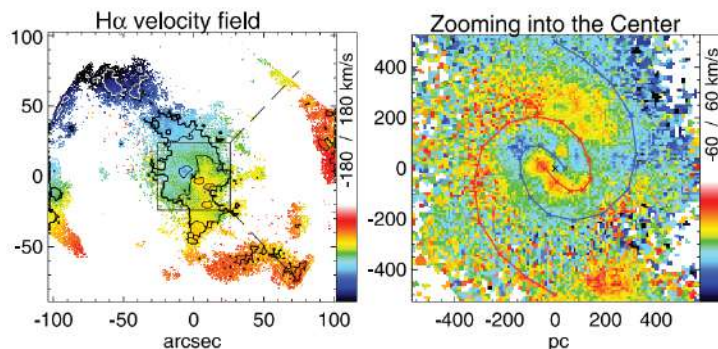The Illustris TNG (The Next Generation) cosmological simulations are a series of state-of-the-art computer simulations of the universe. They are designed to model the formation and evolution of galaxies and their surrounding environments, and provide a comprehensive view of the physical processes that shape the universe on large scales.

The TNG simulations (Pillepich et al., 2018; Naiman et al., 2018; Nelson et al., 2018; Marinacci et al., 2018; Springel et al., 2018) were carried out with the magneto-hydrodynamical moving-mesh code AREPO (Springel, 2010) and corresponded to an improved version of the Illustris simulations (Vogelsberger et al., 2014; Genel et al., 2014; Sijacki et al., 2015), which includes both numerical and physical improvements. Among the innovations, it contains an updated AGN kinetic feedback model for low-accretion, improved parameterization of galactic winds, and dynamic impact of magnetic fields(Weinberger et al., 2017; Pillepich et al., 2018). Illustris TNG consists of cosmological simulations run using the ΛCDM model from $z = 127$ to the present day ($z = 0$). There are 18 simulations with different physical sizes, resolutions, and physical complexity[2]. The cubic volumes of simulations correspond to 50, 100, and 300 Mpc in side length; each called TNG50, TNG100, and TNG300, respectively, as shown in Fig. 2.2.1. Each physical box considers a dark matter-only counterpart, with 100-time snapshots each.
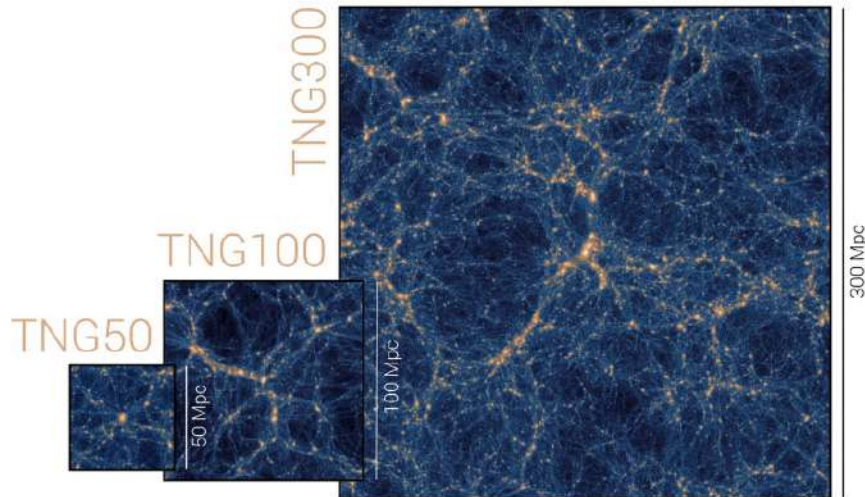
Figure 2.2.1: Comparison of sizes and resolution of the TNG50, TNG100 and TNG300 simulation boxes. For each projected dark matter density is shown. The image was taken from Illustris TNG website[2].

The cosmology used is based on the Planck constraints (Planck Collaboration et al., 2016), $\Omega_m = \Omega_{dm} + \Omega_b = 0.3089$ with $\Omega_b = 0.0486$, $\Omega_\Delta = 0.6911$, and Hubble constant $H_0 = 100$ h km s^{-1}Mpc^{-1} with h = 0.6774.

The TNG project aims to investigate various aspects of galaxy formation through simulations. TNG300 utilizes its large volume to study galaxy clustering and provides the largest statistical sample. TNG50 offers a higher mass resolution, enabling the examination of structural properties and gas phenomena of galaxies. TNG100 uses the same initial conditions as Illustris, allowing for the study of the large-scale structure of the universe, galaxy formation, and star formation within galaxies or in the intergalactic medium. The diversity of length scales represented in the TNG simulations allows for a comprehensive understanding of galaxy formation (Pillepich et al., 2018). The main parameters of each simulation are presented in Table 2.2.1 taken from Nelson et al. (2019).

In Fig.2.2.2 taken from Nelson et al. (2019), the differences between the current cosmological simulation volumes are presented. It is possible to distinguish that TNG50 presents an unprecedented combination of volume and resolution.

---

[2]https://tng-project.org.
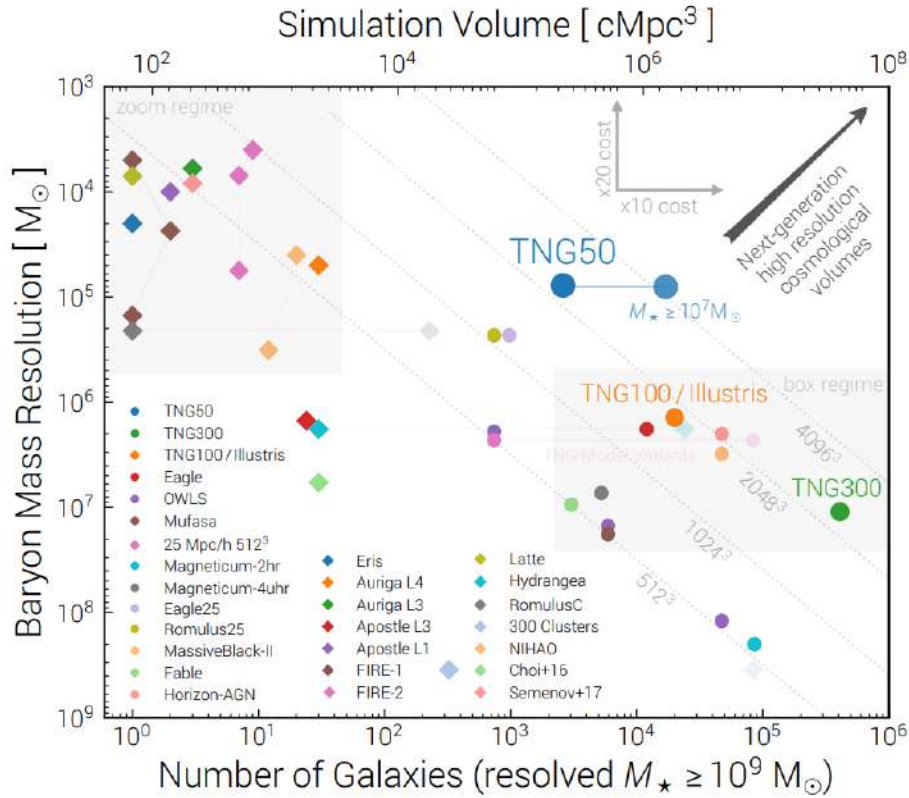
Figure 2.2.2: Comparison between current cosmological simulations. Image from Nelson et al. (2019)

2.2.1 TNG50

This thesis focuses on the kinematic and dynamic study of late-type galaxies to detect vertical perturbations in the galactic disks. The simulation that can provide this type of information corresponds to TNG50 (Nelson et al., 2019; Pillepich et al., 2019), and thus more suitable to use in this thesis work, due to its high mass and temporal resolution in both the stellar and gaseous components. In Fig.2.2.3, we show the gaseous structure (left panel) and the stellar structure (right panel) of one of the galaxies belonging to TNG50 at $z = 2$.

TNG50 offers a unique combination of high volume and high resolution, allowing for the study of large-scale structures and individual galaxies in great detail (Nelson et al., 2019). The mean spatial resolution of the star-forming gas in the interstellar medium is about 100 - 140 pc, similar to other modern *zoom-in* simulations of individual galaxies, such as Auriga (Grand et al., 2017). The simulation box of TNG50 contains about 20000 resolved galaxies, with a total mass over $10^7 M_\odot$. This enables the detailed examination of galaxy properties and their evolution from global and local perspectives, making TNG50 a powerful tool for understanding the formation and evolution of galaxies in the universe.

The large number of galaxies contained in TNG50 can provide fundamental information on how frequently perturbed disks are in the local Universe and the mechanisms that produce them. Within all the currently available simulations, TNG50 allows us to study the galactic structures, spiral arms, central bar, and protuberances that the disk present. The TNG50-1 simulations are also suitable for our study of vertical perturbations in disks of late-type galaxies, due to their spatial resolution power ($\varepsilon_{gas,min}$) ~ 70 pc in Table 2.2.1. This spatial resolution of TNG50 agrees with the order of the vertical perturbations detected in face-on galaxies using observational data, which correspond to ~ 500 pc (Gómez et al., 2021; Urrejola-Mora et al., 2022). As we mentioned before, for each simulation box, there are simulations with different resolutions; in the case of TNG50, four are available. In Table 2.2.2, are listed from highest to lowest resolution, TNG50-1, TNG50-2, TNG50-3, and TNG50-4, respectively.

	TNG50	TNG100	TNG300
Volume [Mpc^3]	51.7^3	110.7^3	302.6^3
L_{box} [Mpc/h]	35	75	205
N_{Gas}	2160^3	1820^3	2500^3
N_{DM}	2160^3	1820^3	2500^3
N_{TR}	2160^3	2×1820^3	2500^3
m_{baryon} [M$_\odot$]	8.5×10^4	1.4×10^6	1.1×10^7
m_{DM} [M$_\odot$]	4.5×10^5	7.5×10^6	5.9×10^7
$\varepsilon_{gas,min}$ [pc]	74	185	370
$\varepsilon_{DM,*}$ [pc]	288	740	1480

Table 2.2.1: Main parameters of the different TNG simulations. The parameters are volume and box side-length (L_{box}), the number of initial gas cells (N_{Gas}), dark matter particles (N_{DM}), and Monte Carlo tracers (N_{TR}). The mean baryon (m_{baryon}) and dark matter (m_{DM}) particle mass resolutions , in solar masses. The minimum allowed adaptive gravitational softening length for gas cells ($\varepsilon_{gas,min}$), the redshift zero softening of the collisionless components in physical parsecs ($\varepsilon_{DM,*}$)
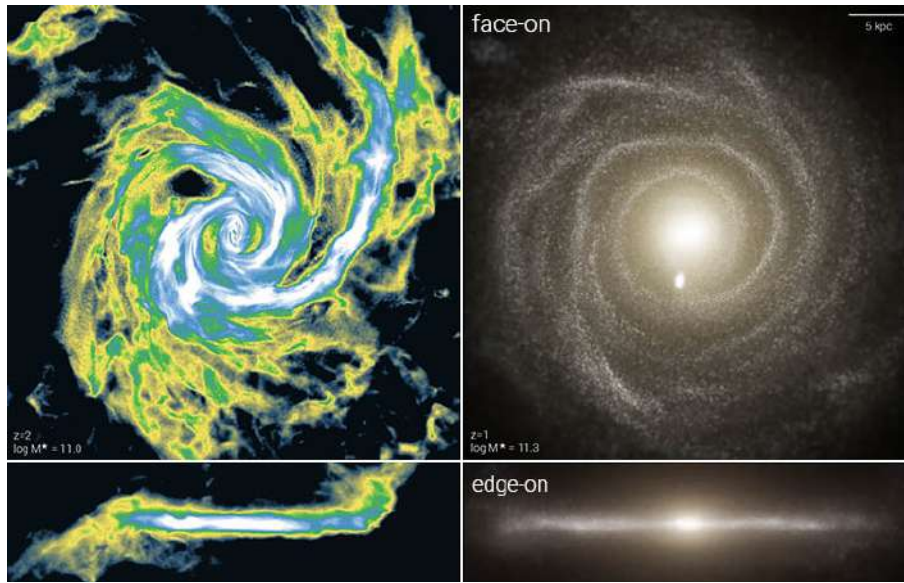
Figure 2.2.3: TNG50 simulations of gas density projections for a galaxy, viewed face-on and edge-on, are shown in the left panels. The right panels display the galaxy in JWST rest-frame bands (*F*200*W*, *F*115*W*, *F*070*W*) as it would appear in terms of stellar light. The image was taken from Illustris TNG website[2].

	L_{box} [Mpc/h]	N_{DM}	m_{DM} [M$_\odot$]	m_{gas} [M$_\odot$]	N_{snap}	$N_{subfind}$ (z=0)
TNG50-1	51.7	2160	4.5×10^5	8.5×10^4	100	5688113
TNG50-2	51.7	1080	3.6×10^6	6.8×10^5	100	859077
TNG50-3	51.7	540	2.9×10^7	5.4×10^6	100	134779
TNG50-4	51.7	270	2.3×10^8	4.3×10^7	100	22869

Table 2.2.2: TNG50 simulations

2.3 Galaxy selection from observational data and simulations

The research will investigate vertical perturbations in the disks of late-type galaxies using two distinct methods. The first approach will involve analyzing H_α data cubes with the use of FPI, enabling high-resolution observations as previously discussed in Section 2.1. The second sample will consist of a collection of simulated TNG5O galaxies in the mass range of the Milky Way and Andromeda-mass type galaxies. A more detailed description of both samples will be provided in Chapters 4 and 5 respectively. We present here a summary of the data used in this thesis.

- Observational data:

  The search for candidate galaxies to be observed using the Fabry-Perot interferometer was based on surveys of disk-type galaxies that showed Hα emission, including the Hα galaxy survey (James et al., 2004), CALIFA (Sánchez et al., 2012) and S^4G (Sheth et al., 2010) survey. Subsequently, we select the sample according to the following criteria since our objective is to analyze the vertical perturbations using V_{los} fields.

  - Distance: near galaxies with systemic velocities $v \leq 3000$ km s^{-1}.
  - Inclination: $i \leq 40$ degrees.
  - Size: galaxies have projected diameters, a_p, between 2 arcmin $\leq a_p \leq 4$ arcmin.

  The main parameters of the observed galaxies are listed in Table 2.3.1. Galaxies with an asterisk were not part of the analysis described in Section 4.4 in Chapter 4.

  The sample of galaxies used in this thesis, which we name WiNDS, corresponds to 40 nearby low-inclination disk-type galaxies. This sample includes new observations and archive data (Epinat et al., 2008a,b; Chemin et al., 2006; Daigle et al., 2006b; Dicaire et al., 2008; Gómez-López et al., 2019). The galaxies were observed using the Fabry-Perot interferometer, where the archive galaxies were reprocessed to homogenize the galaxy analysis.

  New observations were made after the study was carried out in sample WiNDS; eight data cubes of galaxies were obtained according to the aforementioned criteria, which are part of the follow-up WiNDS project.

  The WiNDS galaxy sample and the eight new observations are presented in Fig. 2.3.1 which shows the optical images of the whole sample taken from the SDSS DR9 using the g,r,z bands.

- Sample of simulated galaxies

  The sample selection of 251 analogous MW/M31-type simulated galaxies selected from TNG50-1 (Pillepich et al., 2019; Nelson et al., 2019) was made according to the criteria made in Gargiulo et al. (2022):

  - Range of stellar masses, M_*, in the range $[10^{10.5} - 10^{11.2}]M_\odot$, where M_* is the sum of all stellar particles within a 30 kpc sphere, centered on the most bound DM particle, at $z = 0$
  - Disk morphology
  - Size: isolation criteria where no other galaxy with stellar mass $M > 10^{10.5}M_\odot$ should lie within a distance of 500 kpc of the corresponding simulated galaxy

  We present the final sample of TNG50 galaxies in Appendix D.

  The kinematic and dynamic analysis of the sample of galaxies TNG50 is presented in Chapter 5.
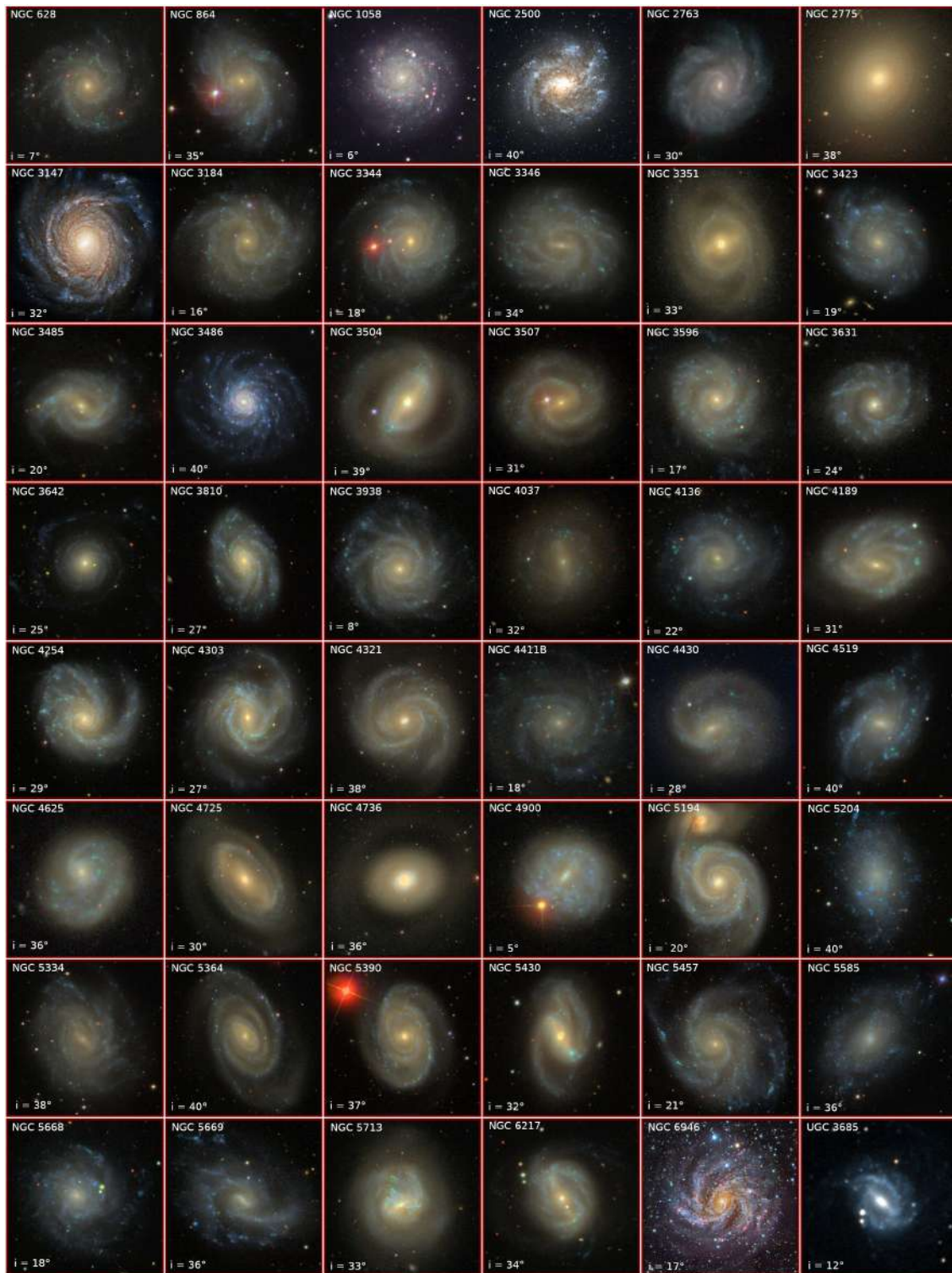
Figure 2.3.1: Optical images of the galaxies observed from SDSS

NGC	Morph (Type)	t_{morph}	R_{opt} (kpc)	v_{sys} (km s^{-1})	d (Mpc)	M_B (mag)	v_{rot}^{max} (km s^{-1})	$\log(M_{star})$ ($M_\odot$)	$\log(M_{HI})$ ($M_\odot$)	$\log(SFR)$	i (°)	PA (°)
(1)	(2)	(3)	(4)	(5)	(6)	(7)	(8)	(9)	(10)	(11)	(12)	(13)
New observations												
628	SAc	5.2	16.4	657.2	10.8	-20.7 ± 0.3	64	10.3[a]	9.7[b]		7[m]	252
1058	SAc	5.1	4.3	518.0	9.7	-18.9 ± 0.4	13		8.8[d]		6[m]	152
2500	SBd	7.0	4.5	503.9	10.5	-17.9 ± 1.7	131	9.4[a]	9.0[c]		40[k]	86
2763 (SAM-FP)	SBcd	9.9	10.0	1891.6	29.6	-19.8 ± 0.3	117				30[k]	50
3147	SAbc	3.9	26.1	2801.9	46.1	-21.9 ± 0.2	335	11.4[a]			32[m]	147
3184	SABcd	5.9	11.4	592.1	10.9	-19.1 ± 0.4	208	10.4[a]	9.3[c]		16[k]	1
3486*	Sc	5.2	10.2	678.1	9.7	-19.9 ± 0.4	126				40[m]	
3423	SAcd	6.0	8.5	1004.0	15.2	-20.0 ± 0.2	128	9.7[a]	9.1[b]		19[k]	45
3485	SBb	3.2	9.4	1436.0	28.2	-19.1 ± 0.8	188	9.9[a]	9.3[b]	0.6[e]	20[k]	116
3642	SAbc	4.0	23.3	1588.0	30.0	-20.6 ± 0.6	48	10.4[a]			25[k]	123
3507*	SBb	3.1	8.2	979.1	16.1	-19.1 ± 1.2	118				31[m]	
3810*	Sc	5.1	7.3	992.0	11.5	-20.1 ± 0.3	153				27[m]	
4136	SABc	5.2	4.2	608.9	7.2	-18.5 ± 1.5	102	9.5[a]	8.9[b]		22[k]	72
4303*	Sbc	4.0	14.1	1566.1	14.7	-20.4 ± 0.1	214				27[m]	
4900	SBc	5.1	3.2	959.6	9.8	-19.2 ± 1.1	112	10.4[a]	9.1[b]		5[k]	0
5194	SAbc	4.0	15.8	462.9	9.8	-21.3 ± 0.3	134	10.9[a]	9.3[c]		20[k]	13
5364*	Sbc	4.0	26.8	1267.5	25.5	-20.5 ± 0.3	136				40[m]	
5390*	Sbc	4.0	30.0	2558.1	45.8	-21.9 ± 0.3	223				37[m]	
5457*	SABc	5.9	38.4	241.0	6.7	-21.0 ± 0.2	274				21[m]	
Data Archive												
864 (G)	SABc	5.1	15.3	1561.9	22.6	-19.9 ± 0.4	134	10.2[a]	9.6[b]		35[k]	27
2775 (G)	SAab	1.6	14.3	1350.0	23.0	-20.6 ± 0.8	296	10.9[a]	8.6[b]		38[k]	157
3344 (G)	SABbc	4.0	7.7	580.1	7.4	-19.6 ± 0.3	217	9.7[a]	9.6[b]		18[k]	156
3346 (G)	SBcd	5.9	10.3	1274.1	24.5	-19.1 ± 0.9	126	10.2[a]	9.1[b]	0.6[e]	34[m]	113
3351 (S)	SBb	3.1	10.5	777.9	9.7	-19.8 ± 0.1	151	10.5[a]	9.0[b]		40[k]	11
3504 (G)	SABab	2.1	11.7	1525.0	29.8	-20.5 ± 0.7	194	10.4[a]	8.8[b]	3.6[e]	39[k]	164
3596 (G)	SABc	5.2	14.0	1192.9	24.2	-19.7 ± 0.9	157	10.0[a]	9.0[b]		17[k]	77
3631 (H)	SAc	5.1	17.3	1155.9	23.8	-21.0 ± 0.8	79	10.2[a]		2.7[e]	24[k]	171
3938 (S)	SAc	5.1	12.9	809.1	16.6	-20.1 ± 1.1	128	10.5[a]	9.3[d]		8[k]	17
4037 (H)	SBb	3.3	5.5	932.1	15.1	-18.0 ± 0.1	101	9.7[a]	8.5[b]	0.2[e]	32[k]	151
4189 (V)	SABcd	5.9	5.3	2115.0	15.1	-19.7 ± 0.5	196	10.5[a]	9.4[b]		31[k]	70
4254* (V)	Sc	5.2	37.3	2406.1	42.8	-20.6 ± 1.1	300				29[m]	
4321 (V)	SABbc	4.0	16.3	1570.9	15.1	-21.2 ± 0.1	279	10.9[a]	9.4[b]	6.2[e]	38[k]	149
4411B (H)	SABcd	6.2	5.5	1272.0	14.9	-19.4 ± 0.2	76	9.5[a]	9.0[b]		18[k]	52
4430 (H)	SBb	3.5	4.9	1451.0	14.7	-20.3 ± 0.5	87	9.8[a]	8.6[b]	0.7[e]	28[m]	60
4519 (V)	SBd	6.9	6.9	1218.1	14.8	-19.3 ± 0.2	117	10.2[a]	9.5[b]	0.9[e]	40[k]	180
4625 (S)	SABm	8.7	3.6	620.9	11.3	-17.9 ± 1.3	39	9.1[a]	8.5[c]		36[k]	126
4725 (S)	SABab	2.2	45.0	1206.1	28.8	-20.7 ± 0.2	257	10.9[a]	9.6[b]	1.6[e]	30[m]	28
4736 (S)	SAab	2.3	8.4	307.9	5.2	-19.7 ± 0.3	182	10.5[a]	8.3[c]		36[k]	118
5204 (G)	SAm	8.9	4.4	200.9	5.9	-17.0 ± 0.1	56	8.7[a]	8.6[c]		40[k]	17
5334 (H)	SBc	5.3	15.9	1385.9	26.1	-19.1 ± 1.1	133	10.4[a]	9.1[c]	0.5[e]	38[k]	6
5430 (G)	SBb	3.1	16.1	2961.1	50.5	-20.8 ± 0.4	188	10.7[a]			32[k]	8
5585 (G)	SABd	6.9	7.1	292.9	8.2	-18.7 ± 0.2	79	9.3[a]	8.8[c]		36[k]	50
5668 (G)	SAd	6.9	14.3	218.4	29.7	-20.1 ± 0.6	73	10.2[a]	9.9[b]	1.6[e]	18[k]	146
5669 (H)	SABcd	6.0	15.8	1367.9	27.3	-18.6 ± 0.7	102	10.2[a]	9.3[b]	1.0[e]	36[m]	71
5713 (S)	SABbc	4.0	13.5	1898.9	33.8	-21.2 ± 0.5	108	10.6[a]			33[k]	23
6217 (G)	SBbc	4.0	11.4	1362.0	26.1	-20.5 ± 0.7	113	10.5[a]	9.6[c]		34[k]	105
6946 (G)	SABcd	5.9	10.0	39.9	5.9	-20.9 ± 0.2	315		9.9[c]		17[m]	61
UGC 3685 (G)	SBb	3.0	14.6	1797.0	30.3	-19.9 ± 0.6	41		9.8[c]		12[k]	134

Table 2.3.1: WiNDS galaxy targets and Data Archive parameters. (1) Galaxy name in the NGC catalog except for UGC 3685 that do not have NGC name, the letter in parenthesis corresponds to the survey name: (G) for GHASP (Epinat et al. 2008a,b), (S) for SINGS (Daigle et al. 2006b; Dicaire et al. 2008), (V) for Virgo (Chemin et al. 2006) and (H) for HRS (Gómez-López et al. 2019); (2) and (3) Morphological Type found in the HyperLeda database; (4) Optical radius considering the isophotal radius at the limiting surface brightness of 25 B mag arcsec^{-2} from Third Reference Catalog of Bright Galaxies (RC3, de Vaucouleurs et al. 1991) corrected for the Virgo and Great Attractor (GA) infall, assuming $H_0 = 67.8$ kms^{-1}Mpc^{-1}; (5) Systemic velocity from NED; (6) Distance in Mpc from NED, corrected for the Virgo and GA infall, assuming $H_0 = 67.8$ kms^{-1}Mpc^{-1}; (7) Absolute B-band magnitude (HyperLeda); (8) Maximum rotation velocity corrected for inclination from HyperLeda; (9) Stellar mass a from Sheth et al. (2010); (10) HI mass b from Haynes et al. (2018), c from Karachentsev et al. (2013), d from radio survey Westerbork survey of HI in SPirals (WHISP) galaxies https://www.astro.rug.nl/~whisp/; (11) Star formation rate. e from Boselli et al. (2015); (12) Inclinations k correspond to kinematic values and m correspond to morphologycal values from literature; (13) Position angle

Chapter 3

First Evidence of Vertical Perturbations in a Milky Way-like Galaxy

Motivation for the Study of Vertical Perturbations in Low-Inclination Late-Type Galaxies Abstract[1]

In this chapter, we present the main results of the study of the kinematics of VV304a that strongly motivated this Thesis. We analyzed the 2D H$_\alpha$ line-of-sight velocity (V_{los}) field of the low-inclination late-type galaxy VV304a, revealing coherent, global, and extended perturbations. These perturbations are consistent with a corrugation pattern similar to that observed in the MW, the Monoceros ring structure. This result, obtained using Fabry-Perot observational data and compared against numerical models, shows that the perturbations present in the disk of VV304a could originate from the gravitational interaction with its companion galaxy VV304b. This study highlighted the possibility of addressing important questions regarding the nature and origin of vertical perturbations by measuring the line-of-sight velocities in low-inclination nearby galaxies.

keywords: Galaxy stellar disks; disk galaxies; Galaxy dynamics; Galaxy kinematics

---

3.1   Introduction

Studies of the Milky Way (MW) disk reveal regions with asymmetries, from the Solar Neighborhood towards the outermost part of the galaxy (Widrow et al., 2012; Xu et al., 2015). These observed asymmetries are known as Monoceros Ring (Newberg et al., 2002; Yanny et al., 2003), TriAnd (Price-Whelan et al., 2015) and A3 overdensity (Sheffield et al., 2018). The asymmetries have a wave-like behavior and are well described as a corrugation pattern (Laporte et al., 2018b). This type of disk characteristic was later confirmed with the Gaia DR2 data (Gaia Collaboration et al., 2018), which shows that the galactic disk is undergoing phase mixing of a non-equilibrium perturbation.

Various studies using models describe the possible origins of the perturbations in the Galactic disk (e.g., Gómez et al., 2013; Laporte et al., 2018b, 2019a; Bland-Hawthorn et al., 2019; Laporte et al., 2020; Bland-Hawthorn & Tepper-García, 2021), the most accepted being the past interaction between the MW and the Sagittarius dwarf galaxy.

Typically, disk vertical perturbations can show an Integral-sign (S-shaped) warp shape or a more complex structure as a corrugation pattern. This structure corresponds to an extended and oscillating vertical displacement of the disk with respect to the midplane. Studies of edge-on galaxies observed in HI (García-Ruiz et al., 2002) and optical (Ann & Park, 2006) reveal that about 70% have a warped disk, but observations of corrugation patterns have been very scarce (Alfaro et al., 2001; Sánchez-Gil et al., 2015; Jiménez-Vicente & Battaner, 2000). Using simulated galaxies from the Auriga project (Grand et al., 2017), Gómez et al. (2017) shows that current models of galaxy formation predict a similar percentage of vertically perturbed disks. Half of the vertically perturbed sample corresponds to disks with more complex vertical structures.

One of the best laboratories to study vertical perturbations of galactic disks corresponds to face-on galaxies. This is because the V_{los} field has less significant contributions from the in-plane components (radial and rotation velocity). However, studies of vertical perturbations in face-on galaxies are very scarce. In particular Sánchez-Gil et al. (2015) using long-slit spectroscopic observations detected velocity perturbations consistent with corrugation patterns in half of the sample analyzed. However, with this technique, typically, the kinematics of the overall disk are not mapped. Thus, these perturbations could be associated with local structures due to, e.g., the fountain flows. Due to the nature of the corrugation patterns, which are extended and global in the galactic disk, observation of the entire disk using 2D V_{los} fields is essential.

This chapter presents a full 2D kinematic map of a MW-type galaxy, VV304a, revealing an extended, global, coherent perturbation consistent with a corrugation pattern. This perturbation is probably associated with the recent interaction with its companion galaxy VV304b.

3.2   Overview of VV304

VV304a is a nearby late-type galaxy belonging to the VV304 pair located at 54 Mpc. It has a recent interaction with its companion, VV304b. VV304a has an optical radius of $R_{opt} \approx 18$ kpc and a rotational velocity peak at 245 km s^{-1} (Torres-Flores et al., 2014). The dynamic mass within the optical radius obtained based on Ha Fabry-Perot observations is M$_{<Ropt} \approx 2.5 \times 10^{11}$ M$_\odot$ obtained using H$_\alpha$ Fabry-Perot observations. These properties are similar to those of the MW (McMillan, 2017; Liu et al., 2017; Cautun et al., 2020). The companion galaxy VV304b has an optical radius of 18 kpc and a peak rotational velocity of 200 km s^{-1}.

Fig. 3.2.1 shows the optical image of pair VV304, where on the right is VV304a, and on the left is the companion galaxy VV304b. The image in the upper panel was obtained with the GMOS instrument at the Gemini South Observatory under the scientific program GS-2013B-Q-27. The lower panel corresponds to a multiband image from Wise 22 microns (red), FUV GALEX (1530 Å, Blue), and the r'-band optical image (Gemini/GMOS, green) with isophotal contours derived from the r'-band image. The lower panel reveals that VV304a does not have a bar, and the iso-contour curves in the outer regions are signs of a recent tidal interaction with its companion VV304b. In VV304b identify a strong bar structure and well-defined grand-design of the spiral arms.

3.3   H$_\alpha$ Fabry- Perot Observation

Observations from the H$_\alpha$ field of VV304a (Torres-Flores et al., 2014) were obtained with Fabry-Perot interferometry using the CInématique des GALaxiEs (CIGALE) instrument on the European Southern Observatory's 3.6 m telescope at La Silla (Chile). Due to its large Field of View (FoV, 3.5×3.5 arcmin^2) and high spectral resolution ($R_p \approx 13000$), it was possible to derive a 2D kinematic map of the entire galactic disk. The use of adaptive spatial binning, based on a 2D Voronoi tessellation
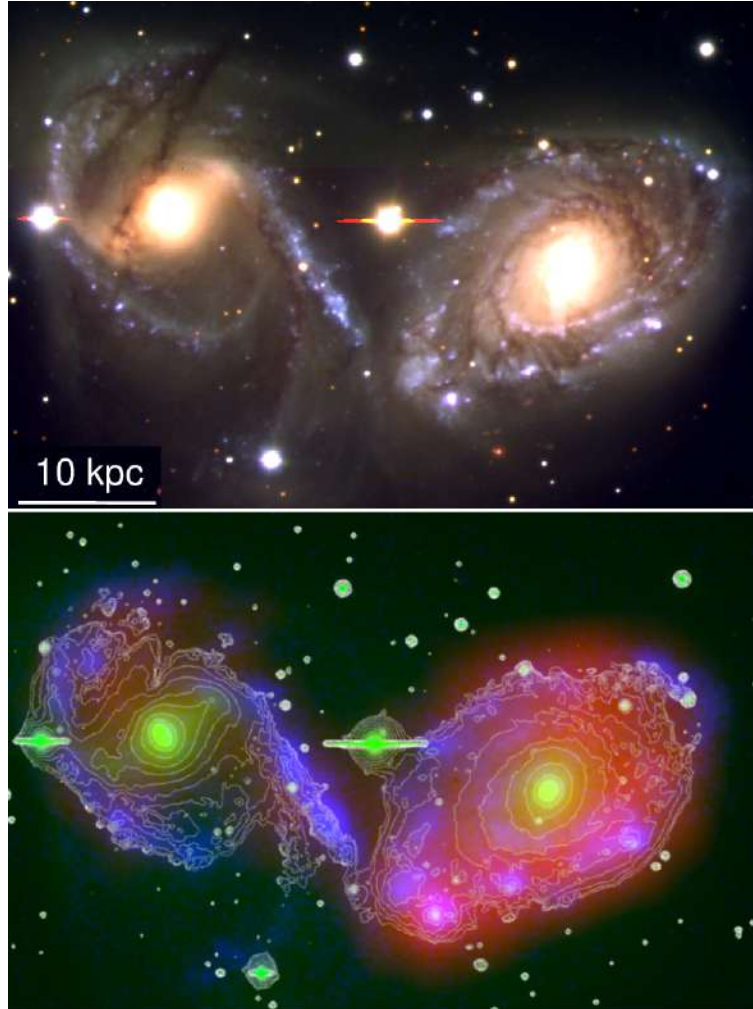
Figure 3.2.1: Upper panel: Optical image of the interacting pair VV304. VV304a, and VV304b corresponds to the right and left galaxy, respectively. The image shows u', g', and r'-band Gemini/GMOS false color. Blue, green, and red colors are associated with the three filters. Bottom panel: Multiband image of the VV304 galactic pair with isophotal contours. The isophotes were derived from the r-band image.

method, applied to the spatial dimensions of a 3D data cube, allows obtaining high spatial resolutions in high S/N regions and large spatial coverage in low S/N regions. The details of data reduction of VV304a are described in detail in Torres-Flores et al. (2014).

3.3.1   Residual Velocity Field

The V_{los} map derived from the H_α data cube is shown in the left panel of Fig. 3.3.1, the colored background shows the axisymmetric velocity model obtained by applying the method developed by Epinat et al. (2008a). The V_{los} has contributions from the three velocity components: distribution within the disk plane: radial V_R and rotational velocity V_ϕ and, vertical velocity V_Z. After fitting the model to the observational data, the obtained kinematic parameters of VV304a correspond to an inclination angle $i = 39° \pm 12°$, PA = $104° \pm 2°$ and $V_{sys} = 3811 \pm 3$ km s^{-1}.

For the detection associated with features of non-circular motions, potentially vertical perturbations, in the galaxy disks, we derive residual velocity (V_{res}) maps and search for global and coherent patterns. The V_{res} for VV304a is derived by subtracting the axisymmetric velocity model from the V_{los} map.
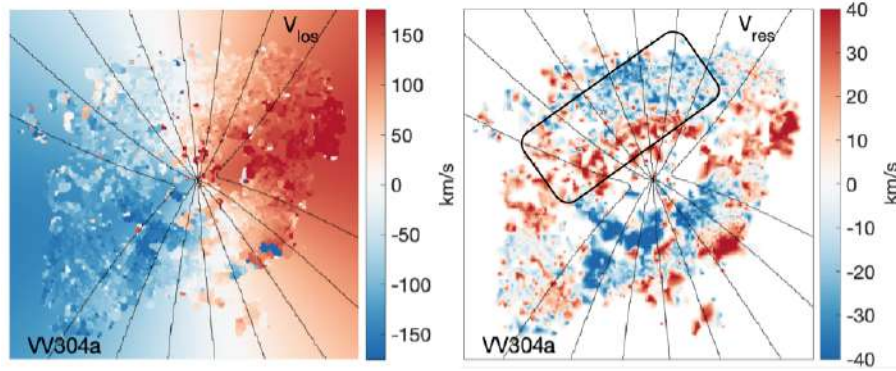
Figure 3.3.1: Left panel: Observed H_α V_{los} field of VV304a with the modeled axisymmetric velocity field in background. Right panel: V_{res} obtained from the difference between the observed and modeled V_{los} field. The transitions from positive to negative velocities are consistent with a corrugation pattern. The black lines show isovelocity contours of this axisymmetric field

The V_{res} map, shown in the right panel in Fig. 3.3.1, reveals a large, global, and coherent pattern across the overall disk, covering $\approx 180°$ of the galactic disk with velocity amplitudes of ≈ 40 km s^{-1}. This structure is consistent with what is expected for the vertical velocity field of a corrugated disk galaxy.

The V_Z flows in stellar and gaseous disks can reach large amplitudes and be induced by different mechanisms, including recent interaction with an external perturber, as shown by various studies (D'Onghia et al., 2016; Gómez et al., 2016, 2017; Laporte et al., 2018b). According to the study of simulated MW-type galaxies, (Gómez et al., 2017), stellar and gaseous perturbations in the galactic disk can remain coherent for more than 1 Gyr. In the case of VV304a, the V_{res} field amplitudes, reaching 50 km s^{-1}, are likely a sign of a recent interaction with its companion VV304b. In particular, larger transitions from positive to negative velocities are distinguished in the black box in Fig. 3.3.1. This behavior is correlated to the displacement above and below the disk concerning the midplane. A similar behavior is observed in the outer regions of the MW. As was mentioned, these observed asymmetries are known as Monoceros Ring (Newberg et al., 2002; Yanny et al., 2003), TriAnd (Price-Whelan et al., 2015) and A3 overdensity (Sheffield et al., 2018), which exhibits a north-south pattern of vertical perturbations that increases outward of the disk (Slater et al., 2014).

Since the inclination angle of VV304a is not negligible, the V_{los} can have a significant contribution from the velocity components of the disk plane, i.e., related to the influence of the spiral arms and a weak bar. According to Momany et al. (2006), the effects of the presence of a bar and spiral arms in the stellar component of the disk can cause perturbations associated with an $m = 2$ pattern with velocity amplitudes < 20 km s^{-1} (see also Canzian (1993)). As mentioned in Section 3.2, VV304a does not present a strong $m = 2$ bar.

The flocculent spiral structure of VV304a requires a 2D model of its light distribution to quantify the strength of the spiral structure. In particular, among the contributions to the study of VV304a, we used the ELLIPSE task in IRAF software to fit elliptical isophotes to the GEMINI/GMOS r'-band image, assuming an ellipticity of 0.2. The r'-band is a better tracer of the overall mass distribution than the blue bands. With this 2D model, I generated a residual overdensity map, assuming a constant mass-to-light rate throughout the disk.

The residual overdensity model was obtained by:

$$\Delta\rho = \frac{image - model}{model} \tag{3.3.1}$$

Figure 3.3.2 shows the overdensity distribution throughout the galactic disk. It is possible to notice that the bottom left region of the map shows a larger overdensity, which is a sign of the tidal interaction with its companion VV304b. As shown in Figure 3.2.1, the upper right region is dominated by dust extinction, resulting in lower overdensity. VV304a reveals a density contrast with respect to the background disk of the order $\Delta\rho \lesssim 30$ percent, similar to that observed in the MW. The overdensity contrast of the spiral structure with respect to the background allows us to estimate a threshold to create an analytical model to determine whether the force of the spiral structure can reproduce the observed residual velocity map of VV304a.
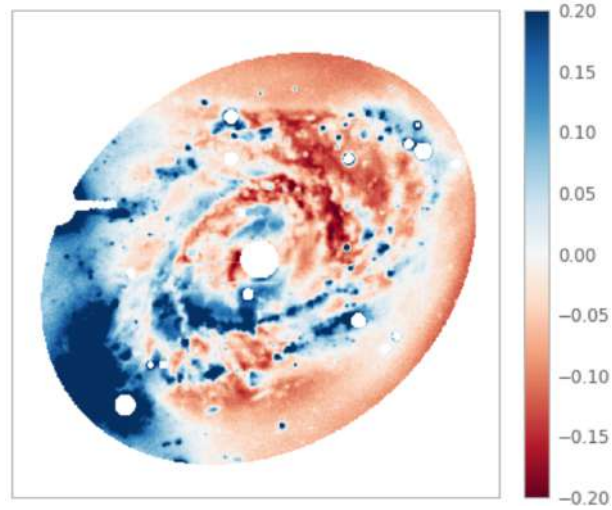
Figure 3.3.2: Estimated overdensity map of VV304a. The color bar indicates the value of $\Delta\rho = $ (image - model)/model. The light distribution model was obtained by fitting elliptical isophotes to the galaxy's Gemini/GMOS r'-band image. The spiral structure of VV304a shows a density contrast concerning the background disk of the order $\Delta\rho \lesssim 30$ percent.

3.4 Analytical Model

The radial and tangential flows in a disk can be the result of the presence of the spiral structure or a bar (Siebert et al., 2012; Monari et al., 2016; Grand et al., 2017). The amplitude of these flows vary with the strength of these $m = 2$ modes. According to the H_α velocity flows observed in VV304a, we will explore if such flows can be the product of the influence of the spiral arms. For this, we generate a 2D analytical model of VV304a to explore whether we can reproduce the observed V_{res} of VV304a. For this, we run and analyze a suite of test-particle simulations using an MW-like galactic potential. The parameters for our analytical model were chosen to reproduce the properties of VV304a mentioned in Section 3.2. The model is explained in detail in Gómez et al. (2021). The galactic analytical model includes a bulge component considering a Hernquist profile. For the disk component, a double exponential profile is used following the procedure described by Smith et al. (2015). For this, an exponential profile is approximated by a superposition of three different Miyamoto & Nagai profiles (Miyamoto & Nagai, 1975). Smith et al. (2015) allows to obtain the best-fitting parameters for an exponential disk obtaining total mass $M_{disk} \approx 5.9 \times 10^{10}$ $M_\odot$. For the dark matter halo, we use a Navarro-Frenk-White profile (Navarro et al., 1996). According to the chosen parameters, a total dynamic mass of $M_{<Ropt} \approx 2.55 \times 10^{11}$ $M_\odot$ is obtained within 18 kpc and a maximum circular velocity of 250 km s^{-1} in agreement with VV304a.

Although we mentioned that VV304a does not have strong signs of the presence of a bar, in our model we include a 3D potential bar to maximize the potential contribution from axisymmetric features in the V_{los} field (Monari et al., 2016). This bar potential is directly proportional to the ratio between the bar's and axisymmetric contribution to the radial force, along the bar's long axis at the line that connecting the Sun and the center of the Galaxy. Finally, a 3D spiral perturbation of a two-arm model is introduced as proposed by Cox & Gómez (2002). The potential of the spiral structure is proportional to the strength of the perturbation. Monari et al. (2016) considers two values for this parameter 341.8 km^2 s^{-1} and 638.7 km^2 s^{-1} which correspond to 30 and 60 percent density contrast of the spiral arms with respect to the background disk surface density at R = $R = R_0 = 8$ kpc, respectively, which represent a maximum radial force exerted by the spiral arms of 0.5 to 1% of the force due to the axisymmetric background at R_0. These arms introduced a velocity perturbation in V_R and $V_\phi < 15$ km s^{-1}. We want to quantify what kind of spiral arms are required to generate velocity perturbations with amplitudes that reach amplitudes those observed in the V_{los} field of VV304a. For this, we explore values of the amplitude of the spiral potential such that the density contrast for the background disk surface density at R_0 is of the order of 100%, 200%, 600% and 1000%. The later model correspond to a maximum radial force exerted by the spiral arms of $\sim 17\%$ of the force due to the axisymmetric background at R_0.

The resulting V_{los} map for each analytical model is presented in Fig.3.4.1 after rotating them into an inclination of 35° and a position angle of 105° to emulate VV304a orientation. Each panel shows the different density contrast values applied. In the
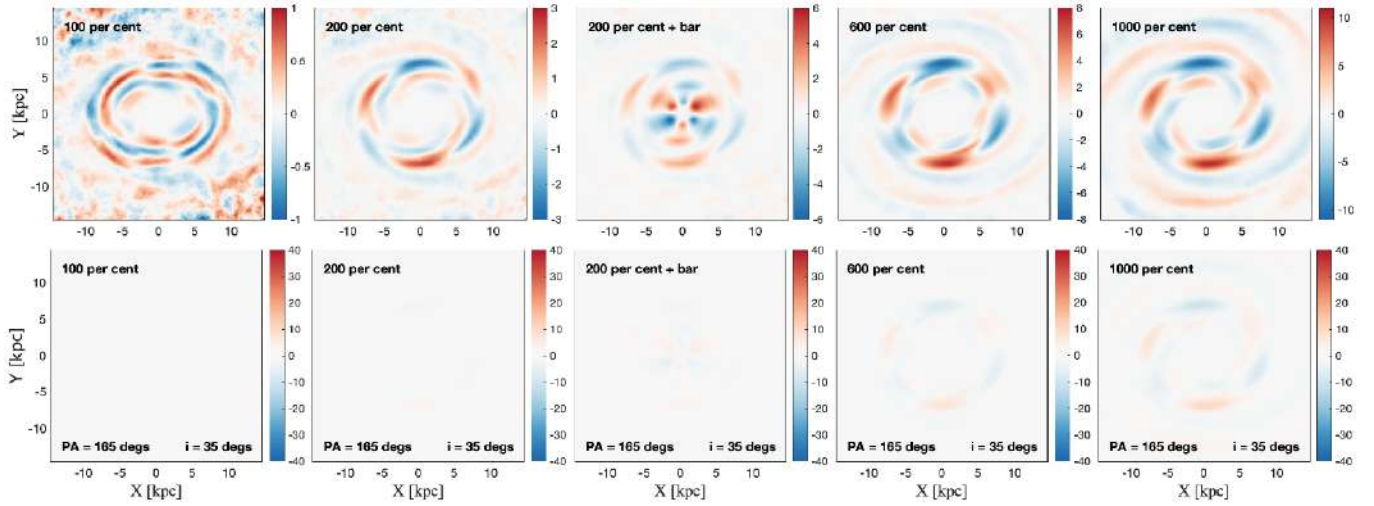
Figure 3.4.1: Results of V_{los} maps from the suite of test-particle simulations model after considering the orientation parameters of VV304a (i = 35° and PA = 105°). From left to right, the results are shown considering 100%, 200%, 200% plus the consideration of the bar, 600%, and 1000% contrast to the background.

upper row, we clearly show that the amplitude of V_{los} pertubation reaches ~ 10 km s^{-1}, even when the strongest arms and the influence of the bar are considered. In the lower rows, the color scale is adjusted to the values of the VV304a map in Figure 3.3.1. Thus, in the analysis of the secular response of the disk to the perturbation of the spiral arms and bar, it was shown that even when considering a value as large as 1000% density contrast, it is not possible to reproduce the velocity amplitude observed in the V_{res} map of VV304a.

3.5 Fully Cosmological Self-Consistent Hydrodynamical Simulations of VV304a-like Models

Considering very strong spirals and a bar, the models analyzed above show that the flows observed in VV304a and cannot generated secularly. We then study how the tidal interaction impacts the V_{res} field of in a low-inclination galaxy using a fully self-consistent cosmological simulation of VV304a-like models. The analysis is focused on recent interaction models and shows containing host disks with i) weak $m = 2$ modes and ii) strong $m = 2$ modes.

In fully cosmological simulations, galaxies with a relaxed disk are exposed yet to different mechanisms that can perturb it, such as previous close encounters with satellites, distant flybys of massive objects, and accretion of misaligned cold gas from halo infall or mergers. As a result, cosmological simulations provide a more realistic representation than tailored analytic models. Simulated galaxies belonging to the Auriga Project (Grand et al., 2017) are used for this study, corresponding to late-type galaxies within MW-size halos. Previous studies, using Auriga simulations have shown that vertical patterns in both the stellar component and the cold star-forming gas remain for more than 1 Gyr (Gómez et al., 2017). Due to this, in this work, we focus on the stellar component due to its better spatial resolution compared to the cold gas disk.

3.5.1 Weak $m = 2$ Model

For the weak $m = 2$ mode analysis, the galaxy Aq-C4 introduced in Marinacci et al. (2014) was chosen. Within the sample, Aq-C4 has properties most similar to the MW. The peak of the rotation curve at 250 km s^{-1} at ~ 4kpc. At present day, it reaches a total mass of $M_{tot} \approx 1.46 \times 10^{12}$ M$_\odot$ and baryonic disk + bulge mass $M_\star \approx 5.3 \times 10^{10}$ M$_\odot$ and a disk optical radius of 20 kpc, considering the radius at $\mu_B = 25$ mag arcsec^2. These parameters allow having a reasonable model of VV304a (See section 3.2). The galaxy Aq-C4 shows a quiet formation history since $z = 1$, where there is no close interaction with satellites more massive than a ratio $M_{sat}/M_{host} \approx 1/40$. The most significant pertuber is a low-velocity flyby with a pericenter passage of 80 kpc at a retrospective time of $t_{look} \approx 2.7 Gyr$. The satellite has a total mass of $\sim 4 \times 10^{10}$ M$_\odot$ ($M_{sat}/M_{host} \approx 1/50$).

In this model, the satellite is not massive enough to perturb the disk, but the density field of host dark matter halo responds to this interaction. This results in strong amplification of perturbation effects. In that model, the resulting dark matter wake is efficiently transmitted to the inner parts of the host galaxy perturbing the embedded disk. This perturbation causes the onset and development of a vertical pattern, similar to the Monoceros ring (Gómez et al., 2016).

In figure 3.5.1, the stellar distribution of C4-Ac is shown at $z = 0$. Similar to VV304a, a weak multiarm spiral structure with a weak bar is identified.
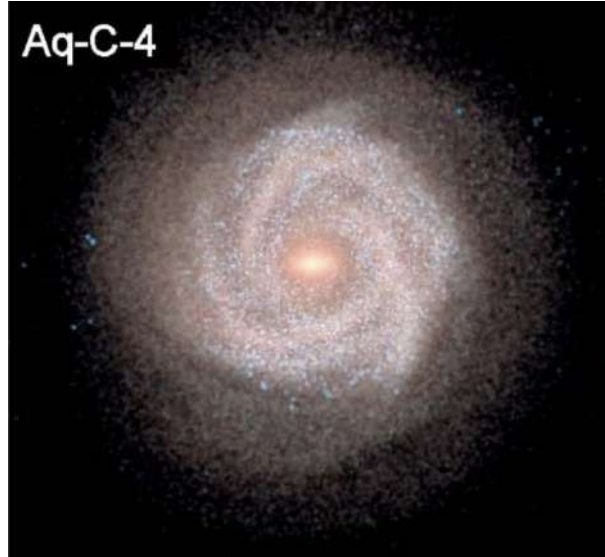

Figure 3.5.1: Stellar distribution of the Aq-C4 disk. Bluer and redder colors, respectively represent younger and older star particles. Note the simulated disk shows a weak bar and multiarm spiral structure, similar to what is observed in the VV304a disk. Figure from Marinacci et al. (2014)

3.5.2   Strong $m = 2$ Model

For this type of system, the Au25 model is chosen due to its similarity with the VV304 system considering its global properties. Galaxy Au25 is slightly less massive than VV304a and had a close encounter with a satellite 0.9 Gyr ago. The total mass of the satellite at infall was $M_{sat} \approx 3 \times 10^{11}$ $M_\odot$ with an orbit of 40 kpc from the host. This configuration is similar to the interaction between the galaxies of the VV304 system. In contrast to Aq-C4, the interaction between Au25 and its satellite causes strong tidal perturbations and a significant misalignment of the dark matter halo. As shown in Gómez et al. (2017), during Au25 interaction, the formation of two tidal arms and strong vertical patterns are induced. Their signs can be detected at $z = 0$, as shown in Fig. 3.5.2. Considering the M_{sat}/M_{host} = 1/4 mass ratio, this can be classified as a massive interaction.

3.5.3   Velocity Patterns in Simulated Residual V_{los} Fields

To compare the observed velocity patterns in VV304a with those obtained from the models Aq-C4 and Au25, the simulated host galaxies were rotated by $i = 35°$ and $PA = 105°$. To obtain the V_{res} maps, we subtract from every stellar particle the mean rotation velocity at the corresponding radial position. The results are presented in Fig. 3.5.3. The upper and bottom leftmost panels show the V_{los} from the Aq-C4 and Au25, respectively. In the case of Aq-C4, the velocity field is shown at $z = 0$, 2.4 Gyr after the flyby closest approach. For Au25, ~ 0.75 Gyr after the strong interaction, just one snapshot before $z = 0$. In the second column, we show the V_{res}, which present features with amplitudes as large as 50 km s^{-1}, similar to what was observed in VV304a. Despite the fact that the two models present $m = 2$ modes with different strengths, the resulting V_{res} is very similar for both galaxies. It should be noted that the V_{res} patterns of both galaxies have different origins. In the case of Aq-C4, the pattern observed in V_{res} is generated by an internal torque of the dark matter halo on the embedded disk induced by a dark matter overdensity wake (Shen & Sellwood, 2006; Gómez et al., 2016). In the case of Au25, the pattern was formed due to the recent interaction with its satellite galaxy. The morphology of the coherent flows in V_{res} of the simulated
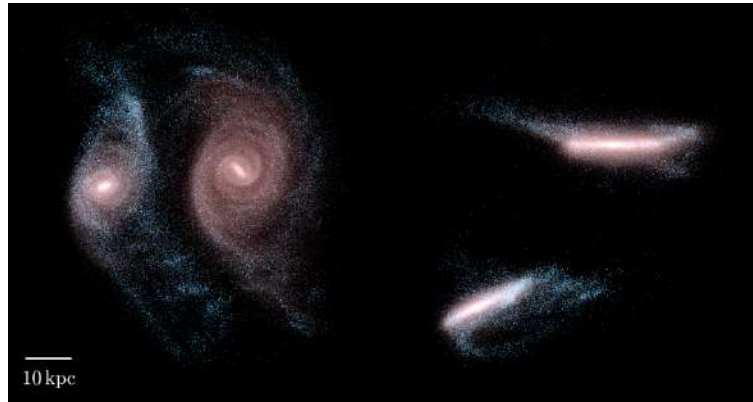
Figure 3.5.2: The moment of closest approach between the simulated Auriga galaxy, Au25, and its massive companion. The face-on (left) and edge-on (right) views are oriented for the Au25 disk. The disk shows a strong bar and a grand design spiral structure

galaxies are very similar to that observed in VV304a, showing abrupt transitions between positive and negative values. If the V_{res} are dominated by off-plane motions, V_z, this behavior is associated with extremes in the midplane displacement of the disks. To characterize the contribution of the different velocity components to the V_{res} field, on the third and fourth columns we show only of-plane and in-plane motions respectively. For Aq-C4 the contribution of the flows in-plane is negligible. This indicates, as shown in the third column, that the V_{res} field is strongly dominated by off-plane flows. In the case of Au25, we do observe some in-plane (fourth column) contributions to the V_{res} field. However, as thin in the third column, the V_{res} map is also strongly dominated by of-plane flows. The disk of VV304a does not show a strong bar or grand-spiral design (see Fig. 3.2.1), which is similar to the structure observed in Aq-C4. This result suggests that the coherent velocity patterns observed in V_{res} field of VV304a could be associated with vertical flows.
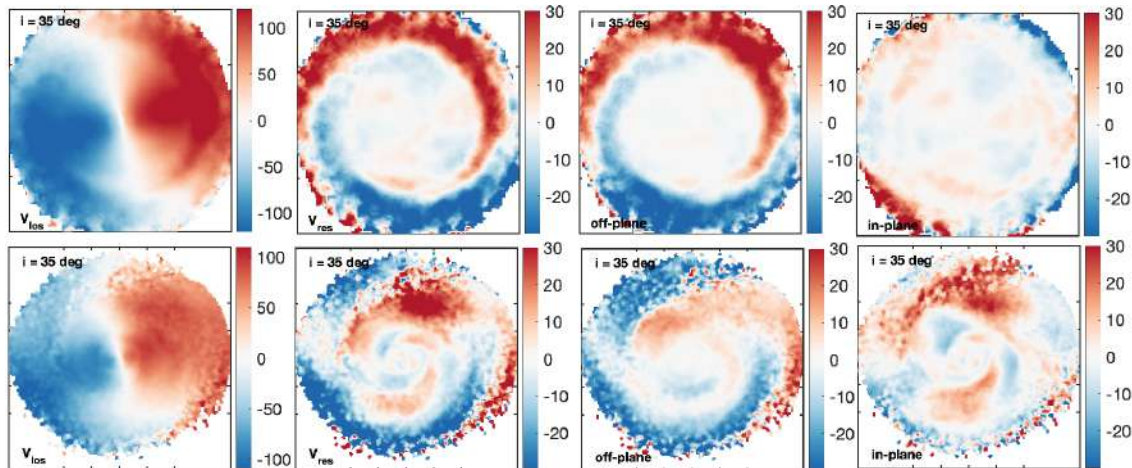
Figure 3.5.3: Upper panels show results of Aq-C4, and bottom panels show results of Au25. From left to right show line-of-sight velocity field, V_{los}, the second column shows residual, V_{res}, obtained after subtracting from every stellar particle the mean rotation velocity at the corresponding radial position. The third and fourth columns show the contributions from vertical and in-plane motions to the V_{res} fields, respectively.

3.6 Main results

The 2D velocity field of VV304a provides an ideal laboratory for studying vertical perturbations in galactic disks. Using H_α Fabry-Perot observations, we analyze V_{los} of VV304a, which interacted with a massive companion VV304b. After generating an axisymmetric model of the velocity field, we derived a residual velocity map which reveals strong, V_{res} strong, coherent, global patterns across the disk consistent with corrugation patterns. The amplitude of these patterns can reach velocities up to 50 km s^{-1}.

To analyze whether the patterns observed in the V_{res} field are indeed due to off-plane motions the analysis is complemented through a suite of test-particle simulations. The parameters similar to the MW are considered to investigate if the vertical perturbations observed in VV304a result from in-plane perturbations by the spiral structure or the influence of a bar. However, despite considering a density contrast of the spiral with respect to the disk background density of the background of 100%, 200%, 600% and 1000% in addition to the influence of a bar, the resulting velocity perturbations do not exceed 15 km s^{-1}. As a result, such in-plane flows can not explain the flows observer in the V_{res} map of VV304a which does not reproduce.

Finally, we use two simulated galaxies, Aq-C4 and Au25, with features similar to the VV304a and recent tidal interaction, the residual velocity fields were analyzed for two cases: weak and strong mode $m = 2$. The V_{res} map is obtained by subtracting the velocity field and the mean rotation velocity of each particle. This result shows that the V_{res} of Au25 reproduces the V_{res} patterns of VV304a with amplitudes of the order of 50 km s^{-1}. This result suggests that the corrugation pattern in the disk of VV304a is due to the interaction with its companion galaxy VV304b.

The deep study of VV304a presented in this Chapter and published in Gómez et al. (2021) gives clues about the nature and origin of vertical perturbations in galactic disks through the study of V_{res} fields in low-inclination galaxies.

According to the results obtained in this Chapter, we showed that the implemented technique allows us to study the velocity field of low-inclination galaxies in detail and to detect with high precision potential vertically perturbed galaxies. This leaf opens some interesting questions:

1. Are vertical perturbations in low-inclination galaxies frequencies in the Local Universe?

2. Vertical perturbations are long-lived deformations?

3. What physical mechanisms are responsible for forming perturbations in the galactic disks?

4. Do the vertical perturbations allow us to know the history of a recent interaction with its satellite galaxies?

This represents the main motivation for the study of low-inclination disk galaxies carried out in this thesis. The main results of the study of velocity fields of a large sample of low-inclination disk-type galaxies are presented in Chapter 4. On the other hand, vertical perturbations are quantified using cosmological simulations of type-MW/31 galaxies, analyzing mean height and velocity maps and their environment and the relationship with vertical perturbations in Chapter 5.

Chapter 4

WINDS: Waves in Nearby Disk Galaxies

Abstract[1]

We present the Waves in Nearby Disk galaxies Survey (WiNDS) consisting of 40 nearby low inclination disk galaxies observed through H_α high-resolution Fabry Perot interferometry. WiNDS consists of 12 new galaxy observations and 28 data archived observations obtained from different galaxy surveys. We derive two-dimensional line-of-sight velocity fields that are analyzed to identify the possible presence of vertical velocity flows in the galactic disks of these low-inclination late-type galaxies using velocity residual maps, derived from the subtraction of an axisymmetric rotation model to rotational velocity map. Large and globally coherent flows in the line-of-sight velocity of nearly face-on galaxies can be associated with large vertical displacement of the disk with respect to its mid-plane. Our goal is to characterize how frequent vertical perturbations, such as those observed in the Milky Way, arise in the Local Universe. Our currently available data have allowed us to identify 20% of WiNDS galaxies with strong velocity perturbations that are consistent with vertically perturbed galactic disks.

keywords: galaxies: kinematics – methods: dynamical – galaxies: spectrograph

---

4.1   Introduction

As already mentioned in Sections 1.3 and 1.4, over the last ten years, oscillatory perturbations towards the outskirts of the Solar Neighborhood in the Galactic disk have been reported several times (e.g. López-Corredoira et al., 2002; Momany et al., 2006; Widrow et al., 2012; Slater et al., 2014; Price-Whelan et al., 2015; Xu et al., 2015; Antoja et al., 2018; Gaia Collaboration et al., 2021). In particular, using 11k main-sequence stars from Sloan Digital Sky Survey (SDSS, York et al., 2000) Widrow et al. (2012) detected asymmetries in both, *i)* the bulk velocity of Solar Neighborhood stars associated to a breathing pattern, i.e. compression and rarefaction motions; and *ii)* in the vertical stellar number density distribution. The latter was related to a bending pattern, i.e. local displacements of the disk from the midplane (Widrow et al., 2014). This study was followed up by Xu et al. (2015) who analyzed measurements of stellar number counts of main-sequence stars located at Galactic latitudes $110° < l < 229°$, as a function of Galactocentric radius. They showed that the amplitude of the perturbations in the vertical stellar number counts, i.e. the displacement of the disk with respect to its midplane, increases towards the outskirts of the Galaxy. This type of oscillatory perturbation on the stellar and/or gaseous component of the disk is known as a corrugation pattern. Thanks to the analysis of the full 6D phase-space information for more than six million stars from Gaia Collaboration et al. (2018), Antoja et al. (2018) showed that, indeed, our own Galactic disk is undergoing phase mixing of a non-equilibrium configuration, a perturbation likely associated with the interaction of the Milky Way with Sagittarius dwarf galaxy in the past (e.g. Gómez et al., 2013; Laporte et al., 2018b, 2019a, 2020). More recently Gaia Collaboration et al. (2021) confirmed that the Milky Way disk has very complex dynamics, with vertical velocity perturbations that can be partially described as a bending wave.

Interestingly, evidence of such complex vertical oscillatory patterns on external galaxies, such as those observed in the Milky Way, are still extremely limited. Vertically perturbed disks have been extensively observed, especially in edge-on galaxies. Studies of 21 cm neutral hydrogen line observations show that most galaxies that have extended HI disks, with respect to the optical, are warped. Using a sample of 26 edge-on galaxies located in different environments with inclinations $i > 75°$ and blue diameters larger than $1.5'$, from Westerbork HI Survey of Spiral and Irregular Galaxies (WHISP, van der Hulst et al., 2001), García-Ruiz et al. (2002) showed that all galaxies in their sample with an extended HI disk ($\sim 76\%$) are warped with respect to the optical disk. They also found that warped disk galaxies are more often found in less dense environments, indicating that tidal interactions are not the only mechanism producing galactic warps. However, in denser environments, the disk vertical perturbations typically show larger amplitudes than those in less dense environments. This is likely due to the fact that, in denser environments, galaxies are more likely to undergo violent tidal interactions with companion galaxies.

For observations in optical bands, Ann & Park (2006) analyzed a sample of 325 galaxies from the SDSS, which consists of a majority of late-type spiral galaxies with inclinations $i > 84°$ and isophotal major axis length $D_{25} > 1'$ at $\mu_B = 25$ mag arcsec^{-2}. The study showed that 73% of the sample contained a warped disk: 51% corresponds to S-shaped and 22% to U-shaped perturbations. For the analysis of the environment-dependence on the frequency of warps, Ann & Park (2006) analyzed 75 galaxies with redshift data from the SDSS DR3, of which 56 have companion galaxies. For the subset of galaxies that have companions, 64% show warped disks. For galaxies without companions, 81% show warped disks. This result is consistent with those presented in García-Ruiz et al. (2002), i.e, in poor environments a higher frequency of warped disks is found than in rich environments. Vertical perturbations have also been studied in edge-on galaxies using dust lines. Narayan et al. (2020) analyzed a sample of five nearby objects with inclinations $i > 80°$ and also showed that such perturbations are common.

S-shaped warps are expected to be a very common feature of both interacting and isolated late-type galaxies. Gómez et al. (2016, 2017) studied in detail the origin and evolution of vertical perturbation in the disk of late-type galaxies using high-resolution cosmological magneto-hydrodynamical simulations of the Auriga Project (Grand et al., 2017). By means of the construction of mass-weighted mean height, $\langle Z \rangle$, and mean vertical velocities maps, $\langle V_Z \rangle$, for both the stellar and cold gas components, these studies found that 70% of the Milky Way-like models showed strongly vertically perturbed disks. Interestingly, while only half of the vertically perturbed disks showed integral-sign (S-shaped) warps, the remaining half showed a more complex vertical structure, i.e. corrugation patterns, indicating that such structures are expected to be common.

A possible reason behind the lack of detected vertical patterns relates to the complexity behind their observation. On edge-on galaxies, such pattern can be easily confused with S-shaped warps due to projection effects. However, as discussed in Gómez et al. (2017), such a corrugation pattern should be detectable along line-of-sight velocity (V_{los}) of nearly face-on galaxies. Due to the oscillating nature of a corrugation, global patterns on the (V_{los}) field can be directly linked to global patterns in a $\langle Z \rangle$ map. Until recently, previous efforts to detect corrugations in the cold gas disk component of nearby galaxies were based on H_α emission through long-slit spectroscopy. Alfaro et al. (2001) analyzed NGC 5427, a galaxy with an inclination angle of $30°$, and found wavy-like variations in the velocity profile of the ionized gas. Sánchez-Gil et al. (2015) analyzed

a sample of four spiral galaxies and showed that two presented corrugation patterns. However, due to the limited coverage associated with the long-lit spectroscopic observations, such patterns could be confused with the effects of local perturbations such as fountain flows. In Chapter 3 we presented a full 2D velocity map of the low inclination galaxy, VV304a based on Fabry-Perot interferometer H_α observations. This technique has the great advantage of providing high spectral resolution in a narrow frequency range, along with good spatial resolution (in this work $\sim 2''$). As such, it allows resolving local velocity perturbations with amplitudes of the order of 10 km s^{-1}. The study showed, for the first time, that VV304a presents global and coherent velocity perturbations that are consistent with a corrugation pattern published in Gómez et al. (2021). We also showed that these velocity perturbations cannot be described by the effects associated with the presence of axisymmetric features on its disk, such as the bar and spiral structure. Thus, we conclude that these perturbations are a direct consequence of the gravitational interaction with its similar mass companion galaxy, VV304b.

The characterization of vertical perturbations in nearby disk galaxies can provide very valuable information about their recent interaction with their environment. Several mechanisms can be behind the formation of warps and corrugation patterns (Sellwood, 2013; Gómez et al., 2016, 2017). One of them is the tidal distortion of a pre-existing disk by an external perturber, such as the cases of our own Milky Way (Antoja et al., 2018; Laporte et al., 2019a) and VV304a (Gómez et al., 2021). The strong tidal torques being exerted on a pre-existing disk as relatively massive satellites fly by or merge can induce strong vertical perturbations (Ostriker & Binney, 1989; Quinn et al., 1993; Velazquez & White, 1999; Bailin, 2003; Kazantzidis et al., 2009; Gómez et al., 2013; D'Onghia et al., 2016; Gómez et al., 2017; Laporte et al., 2018a,b). In addition, the torques associated with a non-spherical mass distribution of dark matter can also trigger the formation of vertical patterns (Debattista & Sellwood, 1999; Jiang & Binney, 1999; Shen & Sellwood, 2006; DeBuhr et al., 2012; Yurin & Springel, 2015; Gómez et al., 2016; Laporte et al., 2018a). Other possibilities may include misaligned accretion of cold gas due to the cooling of hot gas halo, infalling from the cosmic web, or being left by gas-rich host-satellite interactions (Sancisi et al., 2008; Jiang & Binney, 1999; Roškar et al., 2010; Aumer et al., 2013; Radburn-Smith et al., 2014; Gómez et al., 2017) and ram-pressure of the surrounding intergalactic material (Haan & Braun, 2014). The objective of this work is to search for velocity perturbations in the disks of nearby late-type galaxies. To achieve this goal we use high-resolution observations of near face-on galaxies obtained with a Fabry-Perot interferometer. For this purpose, we present the Waves in Nearby Disk galaxies Survey (WiNDS), which consists of a data set with high spectral resolving power ($R_P \sim 10000$) and large spatial coverage, making them ideal for investigating the kinematics of the ionized gas in galactic disks. This study is the first step in an effort that aims to characterize the history of interactions of nearby galaxies, and estimate the frequency with which vertical disturbances such as those observed in the Milky Way arise in the Local Universe.

This Chapter is organized as follows. In Section 4.2 we introduce the WiNDS data sample and we describe our new observations. In Section 4.3, we discuss the data reduction procedure. Section 4.4 and Section 4.5 describes the data analysis and selection and quantification criteria of bending modes. Finally, we present our results in Section 4.6, and in Section 4.7 we provide a discussion and our conclusions. In Appendix A, the comments for each individual galaxy and maps of the new observations made in this work are given. The residual velocity maps are shown in Appendix B. The rotation curves are displayed in Appendix C.

4.2   WiNDS Data Sample

In this Section, we present our survey WiNDS, an ongoing observational campaign currently comprising 40 nearby nearly-face-on spiral galaxies. WiNDS consists of 12 new observational data and we complement it with additional archival data of 28 late-type galaxies from different surveys. The entire data sample contains 3D data cubes obtained using a Fabry-Perot interferometer with a resolving power at the H_α rest wavelength of $R_P \approx 10000$. The galaxies in the WiNDS sample were selected according to three main criteria:

- Distance: nearby spiral galaxies were selected to have systemic velocities $v \leq 3000$ km s^{-1}, corresponding to less than 45 Mpc.

- Inclination: all galaxies have previously estimated low inclination angles $i \leq 40$ degrees. Both, morphologically and kinematically estimated inclinations were considered in this step.

- Size: all galaxies have projected diameters, a_p, between 2 arcmin $\leq a_p \leq 4$ arcmin.

The goal of this selection criteria is to allow us to resolve velocity perturbations in the observed disks with amplitudes as small as 10 km s^{-1}. In what follows we discuss WiNDS new observations in detail. We also briefly describe the additional surveys

utilized to complement WiNDS. In Table 2.3.1 in Chapter 2, we list some of the main properties of the WiNDS sample. The blue histograms in Figure 4.2.1 show the distribution of the most relevant parameters for the final WINDS sample. The solid curves depict the smooth continuous approximation of the underlying histograms. These smooth histograms were obtained using a Gaussian Kernel Density Estimator. The green histograms in the same figure show the parameter distribution of the vertically perturbed galaxy candidates within the WiNDS sample (see Section 4.5). Although the WiNDS sample is not complete in terms of, e.g., mass and magnitude, it allows performing a first systematic search of vertically perturbed disks in the nearby Universe. The 40 selected galaxies span different environments such as clusters, groups, and field galaxies, and a wide variety of morphologies (Sa to Sc). Note however that this is an evolving project, and more objects will be added in the future to complement the available sample. Fig. 2.3.1 of Chapter 2 shows the images optical images of the WiNDS sample, obtained from SDSS DR9 using the *g, r* and *z* bands.

4.2.1 WiNDS: New data cubes

The new observations for WiNDS were obtained using the Fabry-Perot interferometer at the Observatoire de Haute Provence (OHP, France). In addition to the selection criteria mentioned in Section 4.2, we focus on galaxies with previously reported H_α observations (James et al., 2004; Sheth et al., 2010). The new data cubes include galaxies with inclination angles ranging from $6°$ to $33°$, except for NGC 2500 which has a $i \approx 40°$. The sample contains galaxies with a range of morphological types (between Sa to Sc) and a wide absolute *B*-band magnitude range ($-17.9 \leq M_B \leq -21.9$ mag). It also contains both isolated and interacting galaxies belonging to different environments. The 12 new galaxies observed as part of WiNDS are mainly located in the Northern Hemisphere, the list of 12 galaxies is reported in Table 2.3.1. In particular, NGC 2763 is the only galaxy in our sample observed from the Southern Hemisphere using the SOAR Adaptive Module Fabry–Perot (SAM-FP, Mendes de Oliveira et al., 2017). This galaxy was added to the sample at a later time, based on the availability of the SAM-FP.

4.2.1.1 WiNDS: Observation of new data cubes

Most WiNDS observations for the new galaxies were performed in February 2019 using the 1.93-m telescope at the OHP. The observations were made with a mean integration time of 2 hours per galaxy. We note that due to poor weather conditions three galaxies in the sample were observed with a seeing slightly over 3 arcsec.

The new datacubes were obtained through the Gassendi HAlpha survey of Spirals (GHASP) instrument, a focal reducer containing a Fabry-Perot scanning interferometer which has a large field-of-view (FoV), of $\simeq 5.9 \times 5.9$ arcmin^2, an aperture ratio of $f/3.9$, and a pixel scale 0.68 arcsec pixel^{-1}. The Free Spectral Range (FSR) for the two used interferometers with interference orders of 798 and 2600 are 375.9 km s^{-1} and 115.4 km s^{-1}, respectively. The resolving power reached in our survey was $R_P = 10000 - 28600$, which translates into a velocity resolution of $11.6 - 3.6$ km s^{-1}, respectively. As discussed in Gómez-López et al. (2019) the detector, Image Photon Counting System (IPCS), has the advantage of a zero-readout noise, which allows a very fast scan of the interferometer through the entire FSR. The use of an IPCS makes it possible to carry out short exposures (10 seconds) and to make a large number of cycles (typically 20) to average the variations in observation conditions. Within new observation of WiNDS, the H_α line can be found within the range going from 6563 Å to 6627 Å. A total of seven filters, each with a Full Width at Half Maximum (FWHM) of 15 Å, are available to isolate the H_α emission line. For the wavelength calibration of the data, a cube is obtained before and after the observation of each galaxy to account for possible changes in observing conditions. Each calibration cube is obtained using the Neon emission line (6598.95 Å), which is isolated using a narrow-band interference filter (~ 15 Å) centered on this wavelength. This line is used because it is intrinsically narrow and close to the wavelength of the redshifted H_α line.

An additional galaxy, NGC 2763, was observed in February 2016 using the 4.1-meter telescope at the Southern Astrophysical Research (SOAR), Cerro Pachón, in Chile. The instrument used is called SOAR Adaptive Module Fabry-Perot (SAM-FP). It is a restricted-use instrument providing a new mode of operation of SAM for spectroscopy using a Fabry-Perot (FP) and SAM-Imager (SAMI). The SAM-FP provides a FoV of $\simeq 3 \times 3$ arcmin^2, a CCD pixel scale of 0.045 arcsec pixel^{-1} (after electronic binning on the detector) and 48 wavelength channels, in the third dimension of the datacube. For the SAM-FP observations, the interference order was 609 with a FSR of 492.6 km s^{-1} and resolving power of $R_P = 10000$ which translates into velocity sampling of 10.3 km s^{-1} per channel (for a resolution of ~ 20.6 km s^{-1}), see Mendes de Oliveira et al. (2017) for more details.

4.2.2 Additional Data Archive

The new data cubes described in Section 4.2.1 were complemented with 28 galaxies previously observed, available at the Fabry-Perot interferometer database[1] and Herschel database[2] at the Laboratoire d'Astrophisique de Marseille. The galaxies were selected from the GHASP (G), SINGS–H_α (S), VIRGO–H_α (V) and HRS–H_α (H) surveys, each of them briefly discussed below. Some basic parameters, describing the corresponding observations, are listed in Table 2.3.1.

We note that VV304a is part of the WiNDS sample, and therefore, this galaxy is considered in the statistical analysis of WiNDS. However, we have not included this object in this Chapter due to the in-depth analysis of VV304a conducted in Chapter 3.

Instrument	Telescope	Galaxies	Survey
(1)	(2)	(3)	(4)
GHASP	OHP	30	WiNDS, GHASP, HRS
Cigale	ESO	1	Virgo
FANTOMM	OMM/ESO/CFHT	8	SINGS, Virgo
SAM-FP	SOAR	1	WiNDS

Table 4.2.1: Setup. (1) Instrument; (2) Telescope; (3) Number of galaxies observed for each instrument; (4) Survey name.
OMM: Observatoire du mont Mégantic, Québec, Canada, 1.6-m telescope;
ESO: European Southern Observatory, La Silla, Chile, 3.6-m telescope;
CFHT: 3.6-m Canada–France–Hawaii Telescope, Hawaii, USA, 3.6-m telescope

The data cubes available from the previously mentioned surveys were reprocessed in order to homogenize the galaxy analysis. This was performed considering the same signal-to-noise and smoothing method for all data cubes. Data cubes from the GHASP, VIRGO–H_α, and SINGS–H_α surveys are available in the Fabry-Perot database website[1]. On the other hand, HRS–H_α data cubes are available in the Herschel Database[2].

4.2.2.1 GHASP

GHASP (Epinat et al., 2008a,b) survey consists of 3D H_α data cubes of 203 late-type galaxies (spiral and irregular). This sample contains a wide range of morphological types, from Sa to Irr, with absolute magnitudes in the range of $-16 \leq M_B \leq -22$ mag, stellar masses ranging from 10^9 $M_\odot$ to 5×10^{11} $M_\odot$ and are located in nearby low-density environments. From the total sample of 203 galaxies, 83 are strongly barred galaxies (SB or IB) and 53 moderately barred galaxies (SAB or IAB). According to our selection criteria described in Section 4.2, thirteen galaxies were selected and are reported in Table 2.3.1.

4.2.2.2 SINGS–H_α

The Legacy survey *Spitzer* Infrared Nearby Galaxies Survey (SINGS, Kennicutt et al., 2003) consists of 75 nearby galaxies selected with a wide coverage of morphological type (E to Im), luminosity types (IR quiescent to luminous IR galaxies) and CO/HI ratio covering over 3 orders of magnitudes. These galaxies are located in different environments such as galaxy groups, clusters, and low-density fields. The SINGS survey was created to characterize the infrared emission in a wide range of galaxy properties and star formation environments. The SINGS–H_α data is a H_α kinematic follow-up survey of SINGS (Daigle et al., 2006a; Dicaire et al., 2008) and consists of 65 late-type galaxies which present HII regions. According to the criteria described in Section 4.2, the selected galaxies are reported in Table 2.3.1.

4.2.2.3 VIRGO–H_α

The 3D H_α data cubes from the Virgo survey, VIRGO–H_α, (Chemin et al., 2006) consists of 30 spiral and irregular galaxies. This survey is a subsample of the Virgo Cluster Catalog (Binggeli et al., 1985, 1993), which is the nearest cluster to the Milky Way and counts ~ 1400 members, mainly dwarf-type galaxies. The galaxies considered in VIRGO–H_α have an apparent magnitude greater than $B_t^0 = 12$ mag, wide morphological types (S0/a to Im), and inclination angles between $25°$ and $89°$.

---

[1] https://cesam.lam.fr/fabryperot/
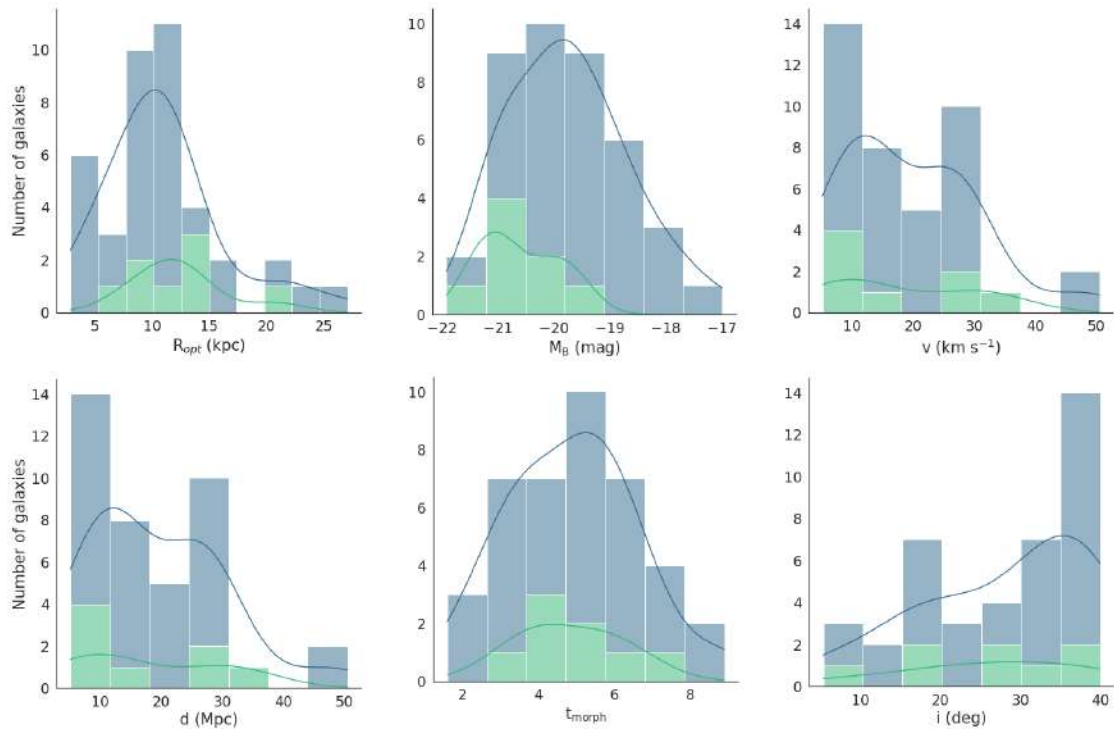[2] https://hedam.lam.fr/

Figure 4.2.1: Basic parameter distributions for our sample of 40 WiNDS galaxies. Top left: Optical radius distribution at the 25 mag arcsec^{-2} corrected for the effects of projection and extinction. Top middle: Absolute B-band magnitudes. Top right: Radial velocity distribution. Bottom left: Distribution of distances in Mpc (corrected for the Virgo, Great Attractor and Shapley supercluster infall). Bottom middle: Galaxy type distribution. Bottom right: Inclination angles distribution. The solid line corresponds to the smooth continuous approximation of the underlying distribution. The blue distributions correspond to the total sample of WiNDS galaxies, while the green distributions to the vertically perturbed galaxy candidates.

All galaxies are located in the cluster's core and its extension towards M49. According to our criteria selection described in Section 4.2, the three selected galaxies are reported in Table 2.3.1.

4.2.2.4 HRS–H$_\alpha$

The Herschel Reference Survey, HRS–H$_\alpha$, (Gómez-López et al., 2019) consists of 152 star-forming galaxies observed using the 1.93-m telescope at the OHP. This survey aimed to study the relationship between the baryonic and dynamical mass of galaxies. The HRS–H$_\alpha$ galaxies sample spans a wide range of morphologies (from Sa to Sm-types, including Blue Compact Dwarfs) and stellar masses (10^8 $M_\odot \leq M_{\text{star}} \leq 10^{11}$ $M_\odot$).

From the HRS–H$_\alpha$ sample, and excluding overlap with previous surveys (GHASP, SINGS–H$_\alpha$ and VIRGO–H$_\alpha$), we found seven galaxies that follow our selection criterion. The names of the six targets are listed in Table 2.3.1.

Note that not all of the galaxies come from the same source. Table 4.2.1 shows our observations broken-down by instrument, telescope, survey of origin, and number of galaxies observed. The most relevant observations parameters are listed in Table 4.3.1. For completeness, in the same table we also list the properties of the additional observations extracted from the data archive.

4.3 WiNDS: Data Reduction

The WiNDS data sample was reduced using the pipeline based program COMPUTEEVERYTHING[3] and the REDUCWIZARD [4] interface, following the steps described in Daigle et al. (2006b) and Epinat et al. (2008a).

The data reduction process includes *a)* the wavelength calibration, *b)* the night sky lines subtraction, *c)* the astrometry process, *d)* the adaptive spatial binning using the 2D Voronoi tessellation, whose implementation finally produces a smoothing specially adapted to a given SNR, *e)* the generation of the 2D momentum maps, *f)* a semi-automatic cleaning of the velocity fields and *g)* velocity dispersion correction. In the following we briefly describe these processes:

a) The calibration process consists of applying a phase map to provide the same wavelength/velocity origin to each profile, for each pixel of the observation datacube. The 2D phase map is computed from the two calibration datacubes. During the phase correction process, the individual exposures are re-centered with respect to each other, using field stars, to minimize telescope drifts and instrument bend.

b) The OH emission lines are the main foreground sky contamination. The sky subtraction is done by dividing the collapsed datacube into a galaxy-dominant and a sky-dominant region. The night-sky emission is interpolated from this galaxy-free region using a two-degree polynomial, and subsequently removed from the whole datacube.

c) The next step is astrometry which is done through the KOORDS task in the KARMA[5] package (Gooch, 1996), comparing star fields between XDSS[6] *R*-band images and our continuum images of each galaxy.

d) For the estimation of The Signal-to-Noise ratio (S/N), which is related to the flux in the line, to the spectral resolution and the r.m.s. in the continuum. We use adapted spatial binning through Voronoi tessellation, as described in Daigle et al. (2006b). This allows us to obtain the highest spatial resolution for a given S/N, which is the main advantage of this binning technique. The Voronoi bins are constructed iteratively from a given pixel, by accreting adjacent pixels until the resulting spectrum reaches the desired S/N. Pixels where the S/N is greater than the chosen threshold value will not be affected by the binning process, while regions of low S/N will emerge from noise without being contaminated by adjacent regions of higher S/N. For the WiNDS sample, the objective is to obtain a $S/N \geq 7$ per spatial bin, where S/N is considered as the square root of the flux in the line. We implemented a Hanning smoothing of a one-spectral-element of the spectrum which preserves the flux.

e) From this Voronoi binned datacube, the different momentum maps are computed as explained in Daigle et al. (2006b): after identifying the H$_\alpha$ line boundaries, the continuum emission around the line is estimated and subtracted from the spectrum. The moments of the line are then estimated. Namely, the line or monochromatic flux is the zeroth-order

---

[3] https://projets.lam.fr/projects/computeeverything
[4] https://projets.lam.fr/projects/fpreducwizard
[5] KARMA tools package is available on website https://www.atnf.csiro.au/computing/software/karma/
[6] ESO Online Digitized Sky Survey https://archive.eso.org/dss/dss

moment (intensity integrated within the line boundaries), the line-of-sight velocity (V_{los}) is the first-order moment (intensity-weighted velocity sum within line boundary), and the LoS velocity squared velocity dispersion (variance) as the second-order moment (difference between the intensity-weighted squared velocity and squared of the intensity-weighted velocity within the line boundaries).

f) In some cases, the lowest S/N regions are strongly affected by night sky line contamination. Thus a semi-automatic cleaning is performed. Indeed, to achieve the desired signal-to-noise ratio in the outer- most galactic regions very large Voronoi bins are produced. These are mainly associated with sky subtraction residuals and background emission. Those bins are first semi-automatically erased and then manually deleted when the semi-automatic process is not sufficient.

g) Finally, velocity dispersion maps were corrected by instrumental width. This correction was done by subtracting the mean dispersion of the instrument contribution to the observed velocity dispersion map, as follows:

$$\sigma_{corr} = \sqrt{\sigma_{obs}^2 - \sigma_{inst}^2}$$
(4.3.1)

where σ_{obs} corresponds to the observed velocity dispersion and σ_{inst} is the mean dispersion of the instrument contribution. Moreover, σ_{inst} is a function of the FSR, the interference order p, and the resolving power R_P:

$$\sigma_{inst} = \frac{\text{FSR } p}{R_P}$$
(4.3.2)

The results of the data reduction process are presented below for a WINDS subsample where panels a), b) and c) show the XDSS B-band image, the H_α line-of-sight velocity map, and the H_α velocity dispersion map, respectively. In addition, the results of the data reduction for the remaining new observations made in this work, where XDSS blue image (top left panel), the H_α monochromatic image (top right panel), H_α velocity field (bottom left panel), and the H_α residual velocity field (bottom right panel) are shown in Appendix A.

4.4   Residual Velocity Fields

Our goal is to analyze the previously derived line-of-sight velocity map, V_{los}, to search for evidence of large, global, and, coherent kinematic perturbations on our sample of late-type, low-inclination galaxies. In particular, we seek perturbations that are consistent with bending modes produced by warps and corrugation patterns. In this Section, we discuss the procedure followed to analyze our resolved velocity fields.

As discussed in Gómez et al. (2021), the observed V_{los} field of each galaxy is bound to contain contributions from three different velocity components: the distributions within the disk plane, radial V_R and rotational, V_{rot}; and the perpendicular velocity to the disk plane, V_Z. More precisely, each V_{los} can be described as:

$$\begin{aligned}
V_{los} = &V_{sys}(r) + V_{rot}(r)\cos\theta\sin i \\
&+ V_R(r)\sin\theta\sin i \\
&+ V_z(r)\cos i,
\end{aligned}$$
(4.4.1)

where V_{sys} is the systemic velocity of the galaxy and it is considered as a fixed value. The polar coordinates (r, θ) in the plane of the galaxy are measured from the position angle (PA), inclination (i) and sky position (α, δ) of the rotation center. The first step to identify global perturbations in the data is to subtract from the V_{los} map an axisymmetric model of V_{rot}. To obtain such an axy-symmetric velocity model we assume that, at first order, the contributions from the radial and the vertical velocities to V_{los} are negligible. Therefore, the observed velocity Equation 4.4.1 reduces to:

$$V_{los} = V_{sys}(r) + V_{rot}(r)\cos\theta\sin i$$
(4.4.2)

To obtain $V_{rot}(R)$ we use the tilted-ring method (Begeman, 1987), which assumes that the galaxy can be analyzed using concentric rings along the major axis, which are described by the parameters V_{rot}^r, i^r, PA^r. Here the supra index r indicates that we are referring to the rings. In this work, we use an improved tilted-ring method, described in detail in Epinat et al. (2008a), and derive $V_{rot}(R)$ for each galaxy bin is modeled using the modified Zhao function (Epinat et al., 2008a),

$$V_{\text{rot}}(r) = v_{\text{t}} \frac{(r/r_{\text{t}})^g}{1 + (r/r_{\text{t}})^a}.$$ (4.4.3)

This four-parameter model was especially chosen for its versatility to adjust to a very diverse set of different rotation curve shapes. The four parameters involved in the V_{rot} model are v_{t} and r_{t} which correspond to the velocity and radius when the rotation curve changes from an increasing velocity to a flat regime, respectively; a and g which are related with sharpness of the turnover. As discussed in Epinat et al. (2008a), for each galaxy the fitting procedure requires a set of initial values for the Zhao function parameters as well as for (α, δ), i and PA. In our work, the values of (α, δ) are set to the peak of the emission in the continuum image and set as fixed values. For the systemic velocity, PA, and i, initial values were extracted from the literature. The resulting values of i and PA, obtained as a result of the fitting procedure, are referred to as kinematically inferred values. Note that, in those cases where disks are projected nearly perfectly face-on ($i < 10°$), the value of i is not allowed to vary and, thus, is kept fixed to their estimated morphological value. Instead, v_{t}, r_{t}, a, g parameters are always allowed to vary. Finally, V_{rot} for each Voronoi binning is estimated through the minimization of χ^2 based on the Levernberg-Marquardt method (Press et al., 1992), computing an iterative 3.5σ clipping on the observed bin-centroid velocity field. All kinematical parameters (i_k, PA_k, V_{sys}) estimated for WiNDS galaxies are listed in Table 4.4.1. The estimation of errors in the determination of kinematic parameters for the WiNDS sample was calculated using the power spectrum of the residual velocity field and the application of a Monte Carlo method, as described in more detail in Epinat et al. (2008a). It is worth noting that the degeneracy between V_{max} and i when fitting our models (Begeman, 1989), especially for very low inclined disk, does not affect our results as we are focusing our analysis on residual velocity fields, V_{res}. The H$_\alpha$ V_{max} values derived in this work are listed in Table 4.4.1

Once an unperturbed axisymmetric model of V_{los} is obtained for each galaxy, we generate their corresponding V_{res} fields. This is done by subtracting the properly V_{los} model from the observed V_{los} maps. It is worth recalling that global and coherent features in a V_{res} field of a late-type galaxy could be the result of kinematic perturbations induced by features such as a bar or spiral structures, but also from improper model parameters (such as center, systemic velocity, position angle of the major axis, inclination or rotation curve model). The multi-polar signatures expected for ill-defined parameters (Warner et al., 1973) are not observed in our data.

It is also worth noticing that small variations in the magnitude of the V_{res} could be attributed to uncertainties in the determination of the kinematic parameters (i, PA, and center). In order to verify the sensitivity of the fitting process, the model is re-run considering $i \pm \delta i$, i.e., we used as input values the extreme values of the inclination that are within the error range shown in 4.4.1

The V_{res} maps for NGC 2763 are shown in the upper left and right panels of Fig. 4.4.1, each performed with a fixed value of inclination ($i \pm \delta i$). In the lower panels, we present the rotation curves derived from each value of inclination. Despite some variations in the estimated V_{rot}^{max} for each galaxy, we found that the residual velocity maps were not significantly altered by the different inclinations.

In particular, we are interested in whether this could introduce significant differences to the residual velocity maps. With this goal, we re-run our method for all galaxies using as initial i extreme values that fall within the error range, listed in Table 4. In Figures 5 and 6 of this report, we show two examples. The top panels of these figures show the residual velocity maps of NGC 2763 (Figure 5) and NGC 5668 (Figure 6). The bottom panels show their respective rotation curves (RC). As suggested by the referee on point c), even though we see changes in the estimated Vmax of each galaxy, the residual velocity maps are not significantly altered due to the different inclinations.

The contributions from in-plane flows are expected to be small in low-inclination galaxies such as those studied in this work. Using a suite of numerical simulations, we characterized the contribution from in-plane flows to the V_{los} driven by non-axisymmetric structures (see Chapter 3). The models consisted of a disk galaxy, projected into an inclination of 35°, considering a bar with similar characteristics to that of the Milky Way and spiral overdensities that ranged from 100% to 1000% density contrast ($\Delta\rho/\rho$) with respect to the disk background density. Even for $\Delta\rho/\rho = 1000$ the resulting velocity perturbations in the corresponding V_{res} field were $\lesssim 10 \text{ km s}^{-1}$.
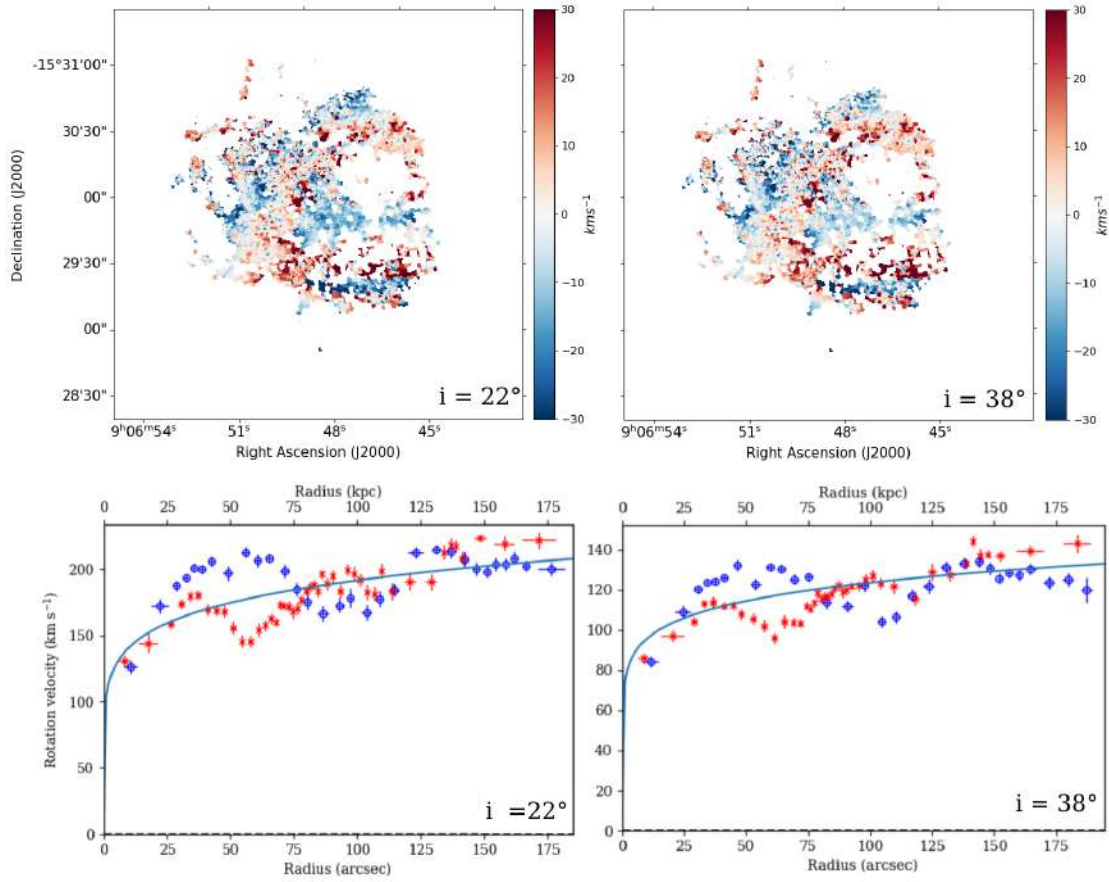
Figure 4.4.1: NGC 2763. Residual velocity map using fixed inclination of $22_\circ$ (upper left panel) and $38_\circ$ (upper right panel) and their respective rotation curves (bottom panels). The different symbols represent the receding (dots) and approaching (crosses) sides (with respect to the center). The green curve indicates the velocity model.

4.5 Quantification and Selection Criteria of Bending Modes

In this Section we describe the selection criteria applied to select those galaxies within the WiNDS sample that show velocity perturbations consistent with a bending mode, such as a warp or corrugation pattern. To avoid selecting discrete and local vertical perturbations, such as those associated, e.g., fountain flows we have established the main criteria to select strong candidates are the following:

- We focus on galaxies that present an extended H_α coverage, extending for at least $0.7\ R_{opt}$. This criterion allows us to globally explore the kinematics of the disks, especially on the outer regions where bending modes typically show their stronger amplitudes.

- We focus on galaxies where global perturbations show amplitudes that are > 10 km s^{-1}. This enhances the chances that the observed perturbations in this low inclination sample of disks are not mainly driven by the axisymmetric components of the galaxies.

- We applied a Gaussian low-pass filter to the V_{res} images in Fourier space with cutoff frequency equivalent to a spatial distance of ≈ 500 pc to highlight relevant and large perturbations

To highlight the larger velocity amplitudes in the V_{res} map, we use a filter on the residual field through the Fourier Transform and Gaussian low-pass filter. The image filtering process is performed according to the following steps and described in Fig. 4.5.1:

Let be a spatial image $f(x,y)$ with dimension $N \times N$, the Discrete Fourier Transform (DFT) of f called $F(u,v)$ is defined as

$$F(u,v) = \frac{1}{N} \sum_{x=0}^{N-1} \sum_{y=0}^{N-1} f(x,y) e^{-2\pi i(ux+vy)/N}$$ (4.5.1)

with $u = 0,1,2,...,N-1$ and $v = 0,1,2,...,N-1$, coordinates in Fourier space.
The Inverse Discrete Fourier Transform is defined as

$$f(x,y) = \frac{1}{N} \sum_{x=0}^{N-1} \sum_{y=0}^{N-1} F(u,v) e^{2\pi i(ux+vy)/N}$$ (4.5.2)

To remove or attenuate high frequencies in the Fourier domain, related to image noise, the Gaussian low-pass filter is used.

$$H(u,v) = e^{-D^2(u,v)/2D_0^2}$$ (4.5.3)

where $D(u,v)$ corresponds to the Euclidean distance from (u,v) to the origin of the frequency plane and D_0 is cutoff frequency in pixel in Fourier space.
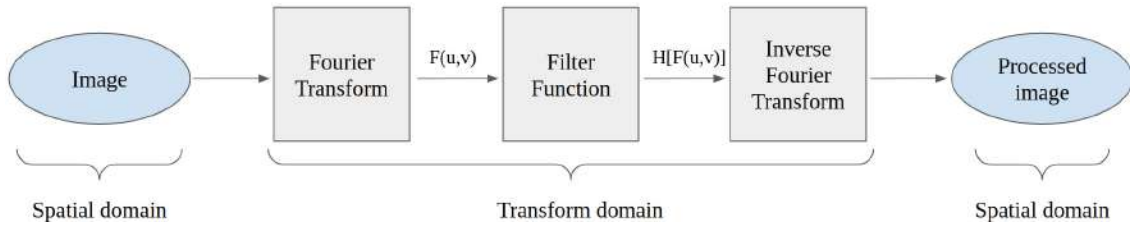
Figure 4.5.1: Sketch of the image processing pipeline adopted in this work.

This allows us to smooth out local and discrete perturbations, and focus on large-scale and coherent features. Based on these images, using a circular grid centred at the centre of the galaxy, evenly spaced by 0.3 R_{opt} as shown in Fig 4.5.2, we select as potential candidates all those galaxies where the perturbations cover at least an azimuthal extension of 60 degrees. We consider perturbations that at a given azimuthal angle cover a radial extension $\lesssim 0.3\ R_{opt}$ as corrugation patterns, whereas the remaining as typical warps.
Examples of the resulting filtered images are shown in Figure 4.5.2. The left panel shows an example of well-defined global and coherent velocity perturbations. The right panel shows the case where the map was consistent with an unperturbed velocity field. According to the these criteria eight galaxies show V_{res} maps consistent with a vertical perturbed disk.
We note that previous studies have analysed velocity dispersion maps, V_{disp}, to identify vertically perturbed disk galaxies. For example, Jiménez-Vicente & Battaner (2000) used V_{disp} to detect plausible shells or chimneys in the galactic disk of NGC 5668. This was done by comparing the geometry of the V_{res} and V_{disp} maps and associating local perturbations in both maps to vertical motions in the galaxy. In our work, V_{disp} maps are obtained as a sub product of the data reduction process (see Section 4.3) and, thus, we will present them together with the V_{res} maps. However, as opposed to Jiménez-Vicente & Battaner (2000), our goal here is to identify global rather than localised and discrete velocity perturbations. As a result, V_{disp} maps were not explored in detail. We will further analyse these maps in follow-up work.
We emphasise that our selection criteria cannot confirm or rule out the presence of vertical perturbations in our disks. Although the objective is to detect global and coherent perturbations, it should be noted that our method does not exclude the presence of fountain flows, which are shown as local and discrete perturbations but rather, both types of perturbations could coexist. Nonetheless, note that we have carefully checked the H_α intensity profiles in all galaxies that were selected as potential vertically-perturbed objects. We found that all candidates within the WiNDS sample show, in general, well-behaved Gaussian profiles. That is, there is no presence of strong and intense multiple components in the H_α profiles due to the presence of other velocity components (such as those observed in merging systems such as HCG31, for example, Amram et al., 2007).
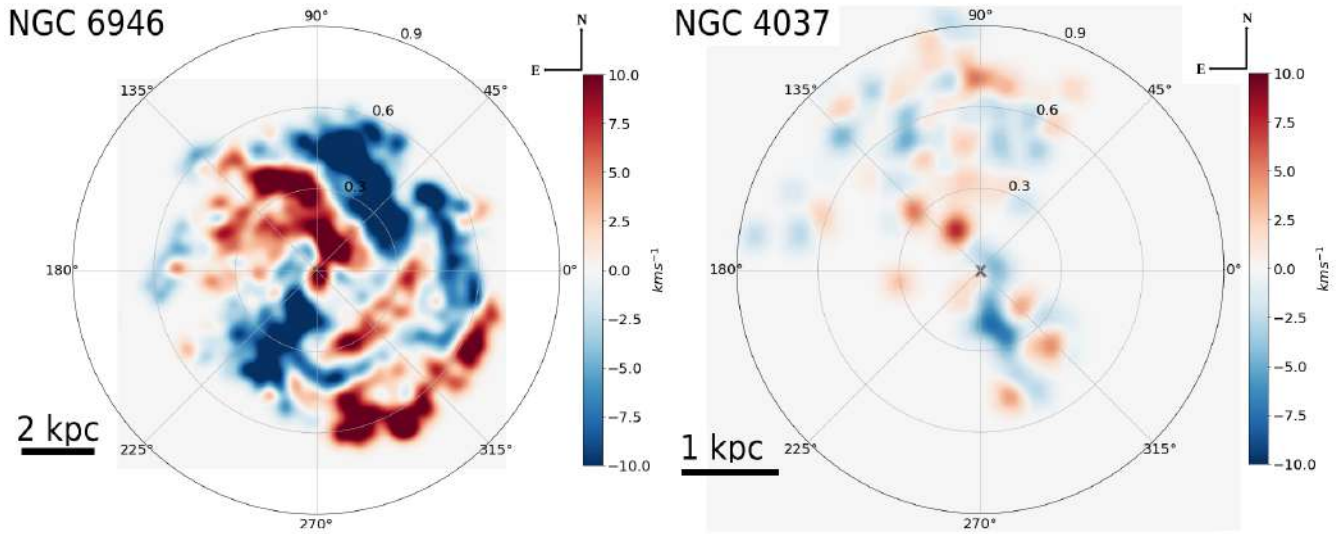
Figure 4.5.2: Filtered V_{res} images. Left panel: NGC 6946 galaxy with well-defined velocity perturbations covering azimuthal extensions $> 60°$ and radial extension $\leq 0.3 \, R_{opt}$ at a given azimuthal radius. Right panel: NGC 4037 galaxy without signs of global perturbation. The contours represent $0.3 \, R_{opt}$ for each galaxy.

4.6   Results

In this section, we analyze and discuss the resulting V_{res} fields of the eight WiNDS galaxies that fulfilled our quantification criteria described in Section 4.5. We discuss the remaining newly observed galaxies and we show the maps derived from the data reduction and their respective V_{res} in Appendix A. The V_{res} maps of archive galaxies that do not present vertical perturbations are presented in Appendix B.1. Finally, we present the rotation curves of the entire WiNDS sample in Appendix C.

4.6.1   NGC 3344

NGC 3344 has a very low morphological with $18°$ of inclination angle (Paturel et al., 1997) and, thus, represents an ideal candidate to search for vertical perturbations on its galactic disk. In Figure 4.6.1 we show the results obtained, in panel a) we show a *B*-band image of the galaxy, obtained from the XDSS[6]. The galaxy shows a well-defined flocculent spiral structure and a weak bar inside the inner ring (Verdes-Montenegro et al., 2000). It has an optical radius, R_{opt}, of 7.7 kpc (RC3, de Vaucouleurs et al., 1991), i.e. approximately half the size of the Milky Way. In panel b) we show the resulting V_{los} map, obtained following the procedure outlined in Section 4.3. The map shows a good H_α coverage of the overall disk (1 R_{opt}), despite being limited by the FoV of the GHASP instrument. The amplitude of V_{los} reaches ≈ 100 km s^{-1} . Panel c) shows the H_α velocity dispersion map, normalized to $\sigma_{95th} = 44.2$ km s^{-1} [7].

Panel d) shows the residual velocity field V_{res}, obtained after subtracting the axisymmetric rotational velocity model from V_{los}. Interestingly the V_{res} map reveals a global, strong, and coherent oscillating-like pattern throughout the entire disk of the galaxy, with an amplitude of the order of ± 30 km s^{-1}. To compare the disk morphology to the structure observed on its residual velocity field, on panel e) we show the galaxy *B*-band image with the contours obtained from the V_{res} field. Notice that no clear correlation between axisymmetric patterns and velocity perturbations can be observed. The extended black box or slit, placed across the disk on panel e), highlights the multiple transitions from positive to negative values experienced by V_{res} as a function of galactocentric distance. This is better shown on panel g) where we highlight the behavior of V_{res} across this particular slit (black crosses). Here the black line represents the corresponding smoothed data using a moving average function with a 7 data points window, while the dashed vertical line indicates the galaxy center. The direction of the slit was chosen to highlight transitions of the residual velocity values. NGC 3344 is a galaxy that is cataloged as isolated, with no

---

[7]A normalization of the velocity dispersion to the 95th percentile was used for all galaxies in order to avoid outlying dispersion measurements and better show possible correlations between residual velocity fields and velocity dispersion.
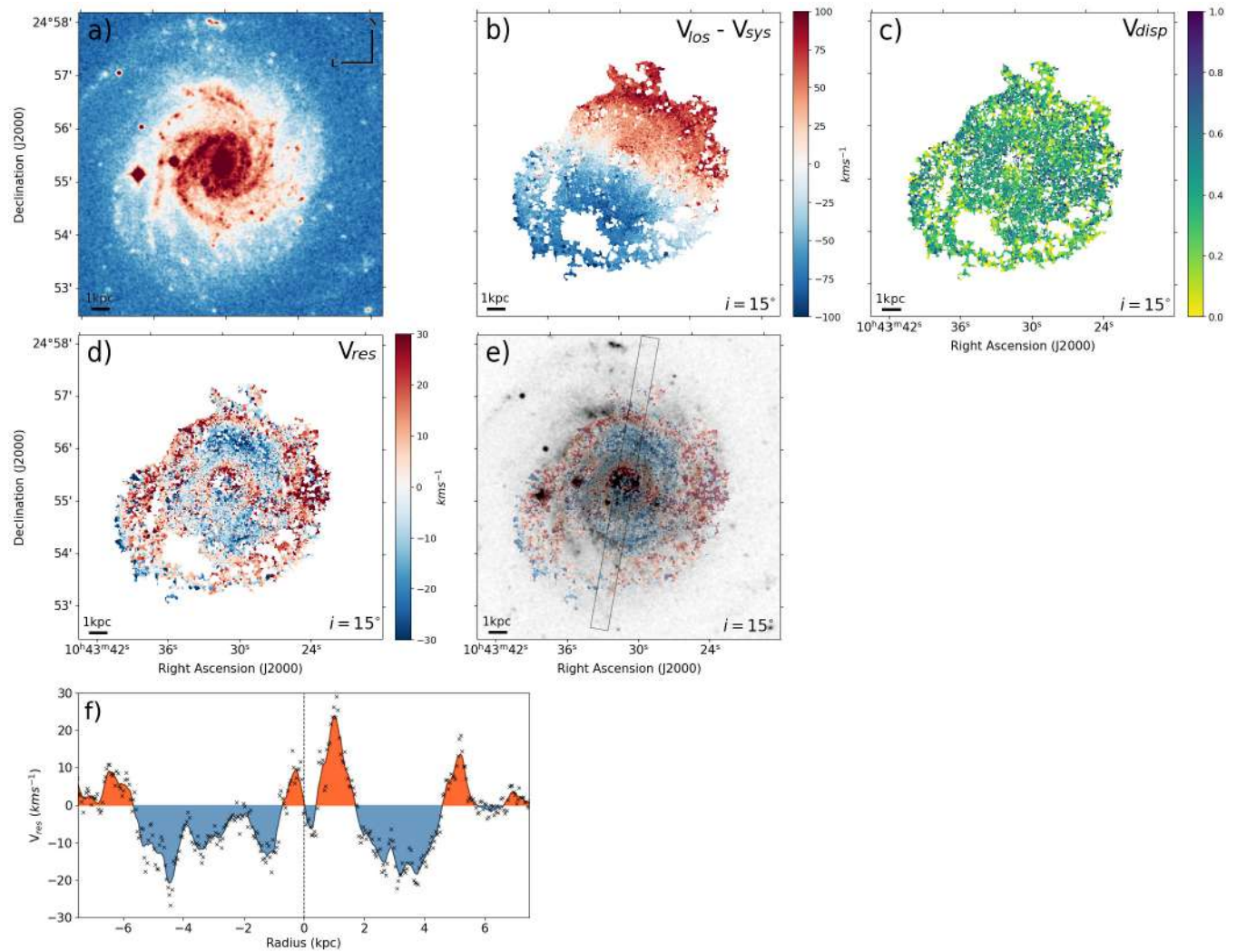
Figure 4.6.1: NGC 3344. Panel (a): XDSS blue-band image. Panel (b): H$_\alpha$velocity field. Panel (c): H$_\alpha$velocity dispersion map normalized to 44.2 km s^{-1} corresponding to the 95th percentile corrected for instrumental broadening. Panel (d): H$_\alpha$residual velocity field. Panel (e): Optical band image with H$_\alpha$residual velocity field. Panel (f): Residual velocity radial profile considering a slit indicated with black lines with position angle of 10° in Panel (e). The black line corresponds to smoothed curve and the dashed line fits center of galaxy indicated in the panel (e). The red (blue) area corresponds to velocities above (below) the midplane of the galaxy. The derived kinematic inclination is indicated in the lower right of each panel.

nearby galaxies within a projected radial distance of 150 kpc and radial velocity difference $\Delta \leq 500$ km s^{-1}. We recall that NGC 3344 has a very mildly inclined disk, $i \sim 18°$. Thus, the contribution from in-plane flows to the resulting V_{res}, associated with e.g. bars and/or spiral structure, is expected to be small. As previously discussed, a plausible interpretation of these V_{res} perturbations is associated with the contribution from a vertical corrugation pattern. Such corrugation pattern could be the result of several mechanisms, such as close interactions with satellites (Sancisi et al., 2008; Jiang & Binney, 1999; Roškar et al., 2010; Aumer et al., 2013; Radburn-Smith et al., 2014; Gómez et al., 2017), torques associated with either misaligned triaxial DM halos or even DM overdensity wakes (Ostriker & Binney, 1989; Quinn et al., 1993; Velazquez & White, 1999; Bailin, 2003; Kazantzidis et al., 2009; Gómez et al., 2013; D'Onghia et al., 2016). Vertical perturbations on this galaxy have been previously reported by other authors. Indeed Briggs (1990) reports the presence of a warp in the outer regions of NGC 3344 after analyzing observations of the HI 21 cm line. Verdes-Montenegro et al. (2000) presented a detailed study of this galaxy, also using HI 21 cm lines. The authors suggest a possible relationship between the inner and outer star-forming rings with a strong spiral structure and the warp in the HI layer. However, they were not able to clearly link the warp structure with the perturbation in the more internal regions. Our analysis of NGC 3344, with a spectral resolution ~ 10 km s^{-1}, reveals a very complex structure of NGC 3344. NGC 3344 is a very interesting candidate of the vertically perturbed galaxy that will be analyzed in greater detail on a follow-up study.

4.6.2 NGC 628

NGC 628 (M74) is a nearly face-on galaxy with an inclination angle of $6.5°$; thus, an ideal candidate to search for possible vertical perturbations. On panel a) we display a *B*-band image of the galaxy, obtained from the XDSS. NGC 628 is a non-barred galaxy with two main spiral arms emerging from its bulge. The H$_\alpha$ observation coverage of NGC 628 corresponds to a mean radius of 12.5 kpc, which represents $0.8\,R_{opt}$. The H$_\alpha$ velocity map (panel b), shows an amplitude of ~ 60km s^{-1}, as expected from a low inclination galaxy. For comparison we also show on panel f) the HI velocity map from The HI Nearby Galaxy Survey (THINGS) (Walter et al., 2008, THINGS), observed with Very Large Array (VLA), which is consistent with the H$_\alpha$ velocity map. Interestingly, studies based on neutral hydrogen (Kamphuis & Briggs, 1992) have detected the presence of an elongated warp structure at around $12'$ projected distance from the nucleus. On panel c) we show the derived H$_\alpha$ velocity dispersion map, normalized to $\sigma_{95th} = 14$ km s^{-1}. The V_{res} field of NGC 628 is shown on panel d). Interestingly, global and coherent velocity perturbations, of the order of 20 km s^{-1}, can be clearly observed. Panel e) allows us to correlate NGC 628-disk morphology with its residual velocity map. The velocity perturbations on this galaxy are more clearly highlighted on panel g) where we follow the mean V_{res} along the highlighted slit, suggesting a warp-like structure. As shown on its *B*-band image (panel a), an extended tail is observed in the southwest direction of the disk. This substructure has been previously reported in Kamphuis & Briggs (1992). Although NGC 628 has currently no close companions, a dwarf galaxy system (UGC 1176 and UGC 1171) is located at 140 kpc. The overall mass of the satellite system has been reported to lie on the order of magnitude of the total NGC 628 mass (Michałowski et al., 2020). This system may have played an important role in the evolution of NGC 628. As discussed by Briggs (1986), if the dwarf system is at rest at its current location concerning for to NGC 628, it would fall into its host in about 1 - 2 Gyr. However, a more recent study by Michałowski et al. (2020) suggests that a tidal origin for the asymmetric HI tail located on the south-western outskirt is an unlikely scenario. They argue that the tail does not resemble recent tidal features, whereas an older feature would wind almost symmetrically around the galaxy. In addition, recently induced tidal tails typically show $m = 2$ patterns, with two nearly symmetrical arms. Instead, NGC 628 shows a strong $m = 1$ like spiral structure. Nonetheless, they do not rule out a possible previous interaction with the neighboring dwarf pair. It is interesting to compare with the results presented in Gómez et al. (2017), based on fully cosmological simulations. In particular, their model S13 shows similar morphology to NGC 628, with a strong $m = 1$ arm extending from the inner galactic regions. This model displays a vertically perturbed stellar and cold gas disk, but no recent interaction with massive satellites ($M_{sat}/M_{host} > 0.03$). Instead, S13 experienced a massive gas-rich merger 5 Gyr in the past. As a result, its pre-existing disk is destroyed but a new thin disk quickly forms thereafter due to the re-accretion of misaligned gas. This gas accretion gives rises to both the vertical perturbations observed in this modeled galaxy and its strong $m = 1$ morphology. This suggests that the velocity perturbations observed in NGC 628, as well as its $m = 1$ spiral morphology, could be linked to the recent accretion of misaligned cold gas.

4.6.3 NGC 6946

NGC 6946 is a spiral galaxy classified as SABcd with a kinematical inclination of $i \sim 17°$, an optical radius of ≈ 10 kpc, and an estimated total mass of 1.2×10^{11} M$_\odot$ (Pisano & Wilcots, 2000). Optical and neutral hydrogen observations of NGC
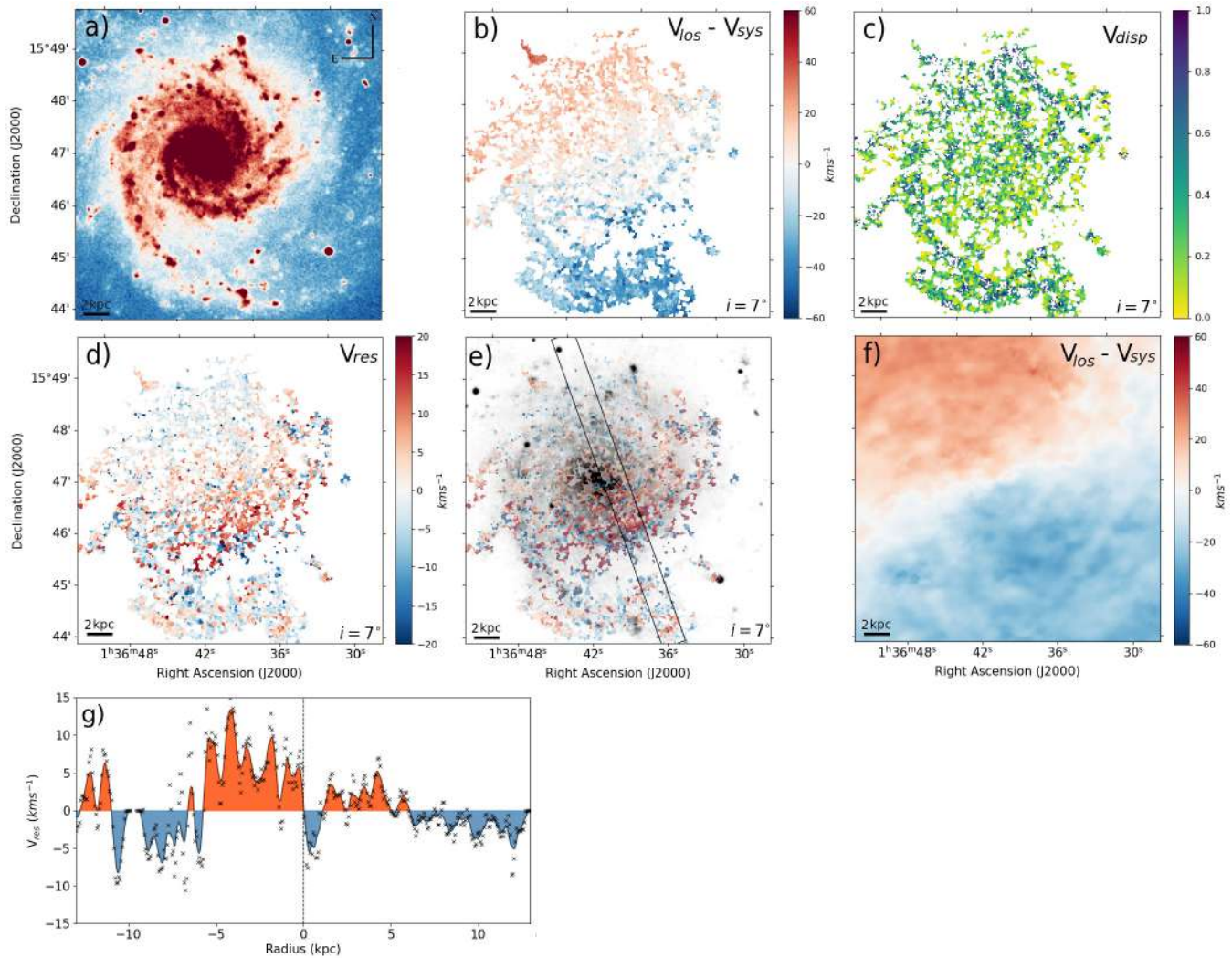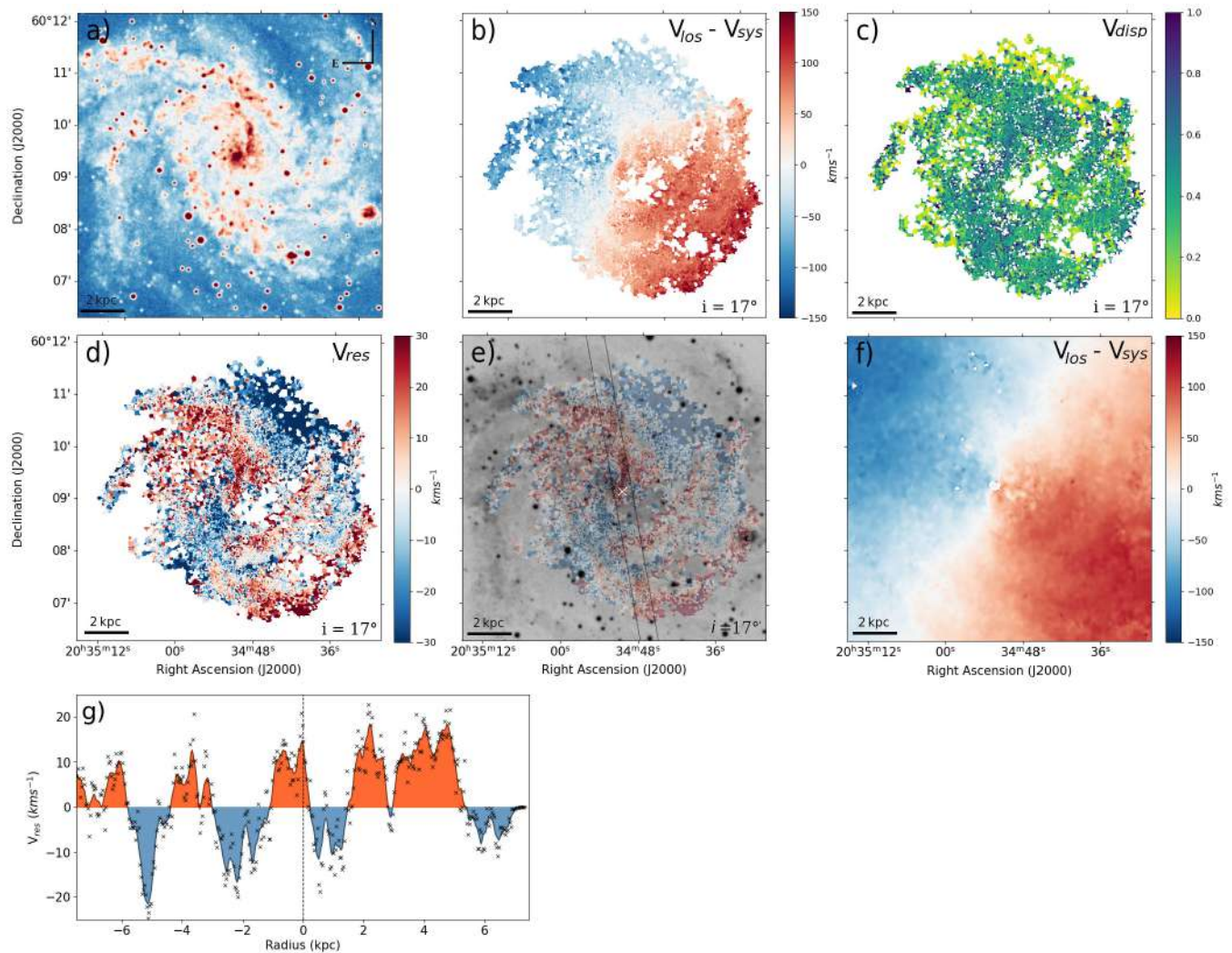
Figure 4.6.2: NGC 628. Panel (a): XDSS blue-band image. Panel (b): H$_\alpha$ velocity field. Panel (c): H$_\alpha$ velocity dispersion map normalized to 14 kms^{-1} corresponding to the 95th percentile. Panel (d): H$_\alpha$residual velocity field. Panel (e): Optical band image with H$_\alpha$ residual velocity field. Panel (f): HI velocity field from THINGS survey Walter et al. (2008). Panel (g): Residual velocity radial profile considering a slit indicated with black lines with position angle of 160° in Panel (e). The black line correspond to smoothed curve and the dashed line fits center of galaxy indicated in the panel (e). The red (blue) area corresponds to velocities above (below) the midplane of the galaxy. The derived kinematic inclination is indicated in the lower right of each panel.

Figure 4.6.3: NGC 6946. Panel (a): XDSS blue-band image. Panel (b): H$_\alpha$velocity field. Panel (c): H$_\alpha$velocity dispersion map normalized to 55.1 kms^{-1} corresponding to the 95th percentile. Panel (d): H$_\alpha$residual velocity field. Panel (e): Optical band image with H$_\alpha$residual velocity field. Panel (f): HI velocity field from THINGS survey Walter et al. (2008). Panel (g): Residual velocity radial profile considering a slit indicated with black lines with position angle of 170° in Panel (e). The black line corresponds to smoothed curve and the dashed line fits center of galaxy indicated in the panel (e). The red (blue) area corresponds to velocities above (below) the midplane of the galaxy. The derived kinematic inclination is indicated in the lower right of each panel.

6946 have revealed its strong spiral arms, a particularly high star formation rate, a nuclear starburst, and a weak bar (Pisano & Wilcots, 2000; Schinnerer et al., 2006). Panel a) shows its XDSS B-band image, where we can clearly see its spiral nature. NGC 6946 is considered to be isolated (Tully, 1988). Using HI observations, previous studies have detected a dozen of low mass irregular dwarf galaxies companions (Pisano & Wilcots, 2000; Karachentsev et al., 2000, 2005). However, at the present day NGC 6946 does not show any sign of undergoing strong direct gravitational interactions with its satellite population. Its two most massive companions, UGC 11583 and L149 have estimated total masses of 1.5×10^9 and 3.0×10^8 $M_\odot$ and projected distances of 83 and 75 kpc, respectively (Pisano & Wilcots, 2000). The H_α V_{los} maps of NGC 6946, shown in panel b), has an amplitude of ~ 150 km s^{-1}. Following our selection criteria, the map reveals a significant H_α coverage, reaching at least a radius of 7 kpc, corresponding to $0.7\,R_{\mathrm{opt}}$. As in the case of NGC 3344, the coverage for NGC 6946 is limited by the FoV of the GHASP instrument. For comparison, we show (on panel f) the HI velocity map, extracted from Walter et al. (2008). Both maps are consistent, even though they are considering different components of the ISM and come from different instruments and techniques. Note, however, that our observations have a better spatial resolution, of 3 arc sec against the 6 - 12 arc sec resolution in the HI observations. The H_α velocity dispersion map is shown on panel c), normalized to $\sigma_{95th} = 55.2$ km s^{-1}. On panels d) and e) we show the galaxy V_{res} map, which reveals global and coherent perturbations, reaching amplitudes $\lesssim 35$ km s^{-1}. The V_{res} velocity contours, overlaid on the B-band image (panel e), allow us to directly contrast this velocity structure with the morphology of NGC 6946. The oscillating nature of this velocity field is better highlighted on panel g), where we show the mean V_{res} along the highlighted slit on panel e). It is worth recalling NGC 6946 spiral nature, and its low but not negligible inclination. As a result, a contribution from in-plane flow to the V_{res} field can be expected. However, as shown by Gómez et al. (2021), for disks as inclined as NGC 6946 ($i \sim 40°$), even an spiral structure 1000 times denser than its mean background disk density cannot generate velocity perturbations with amplitudes $\gtrsim 10$ km s^{-1}. This indicates that the observed global velocity perturbation could be partially linked to vertical velocity flows.

It is interesting to consider what mechanisms could be driving the perturbations in this galaxy. As previously discussed, NGC 6946 does not have nearby massive satellites that could be directly tidally interacting with its disk. However, even low mass satellites at relatively large galactocentric distances could significantly perturb an embedded disk through the excitation of dark matter overdensity wakes (Weinberg, 1998; Vesperini & Weinberg, 2000). For example, using cosmological simulations of Milky Way-mass galaxies, Gómez et al. (2016) studied the onset and evolution of a strong vertical pattern in the disk. The vertical pattern in this model, with an amplitude of ~ 50 km s^{-1}, is the result of a satellite-host halo-disk interaction. Interestingly, the satellite had a total mass of ~ 5 per cent of the host and a pericentre distance of 80 kpc. The satellite was not massive enough to directly perturb the galactic disk but the density field of the host dark matter halo responded to the satellite passage and strongly amplified its perturbative effects. A similar scenario could be taking place in the case of NGC 6946, considering its low mass companions at a relatively large projected galactocentric distance. Other possible mechanisms, in addition to the previously discussed contribution from in-plane flows, could be related to smooth accretion of misaligned cold gas.

4.6.4 NGC 4321

NGC 4321 (M100) is a grand-design nearby spiral galaxy belonging to the Virgo Cluster, classified as SABbc (RC3). The galaxy has a small bulge and two well-defined, prominent and, symmetric spiral arms, as shown on its B-band image (panel a). The nucleus of the galaxy is compact and bright. NGC 4321 is a very low-inclination galaxy, with a kinematical inclination of $i \approx 25°$ and an optical radius of $R_{\mathrm{opt}} = 16.3$ kpc from RC3. Panel b) shows that the coverage of the V_{los} distribution, obtained from the H_α observations, is extensive and reaches nearly to its optical radius; i.e. 13 kpc $\sim 0.8 R_{\mathrm{opt}}$. The V_{los} map shows an amplitude of ≈ 150 km s^{-1}. For completeness, we show on panel c) the H_α velocity dispersion map, normalized to $\sigma_{95th} = 33.1$ km s^{-1}.

The derived residual velocity map, obtained after subtracting the axisymmetric velocity model is shown on panels d) and e). As in previous examples, this map reveals global and coherent velocity flows with amplitudes that can reach ~ 30 km s^{-1}. Panel f) more clearly shows the radial variations of the residual velocity along the highlighted slit in panel e). Note the oscillatory behaviour of V_{res} across the disk. These perturbations, observed in the ionized gas of NGC 4321, could be the result of a recent interaction with one of its satellite galaxies. Indeed, NGC 4321 has two dwarf companion galaxies, NGC 4328 and NGC 4323, located at projected distances of 24 kpc and 28 kpc from their host, respectively (Hernandez et al., 2005). Knapen et al. (1993) showed that the HI component of NGC 4321 is mostly contained within the optical disk. However, they also identify a large HI extension that could be the result of the tidal interaction with NGC 4323. Indeed, Knapen et al. (1993) find important differences in the behavior of its rotation between the approaching and the receding sides. They suggest these
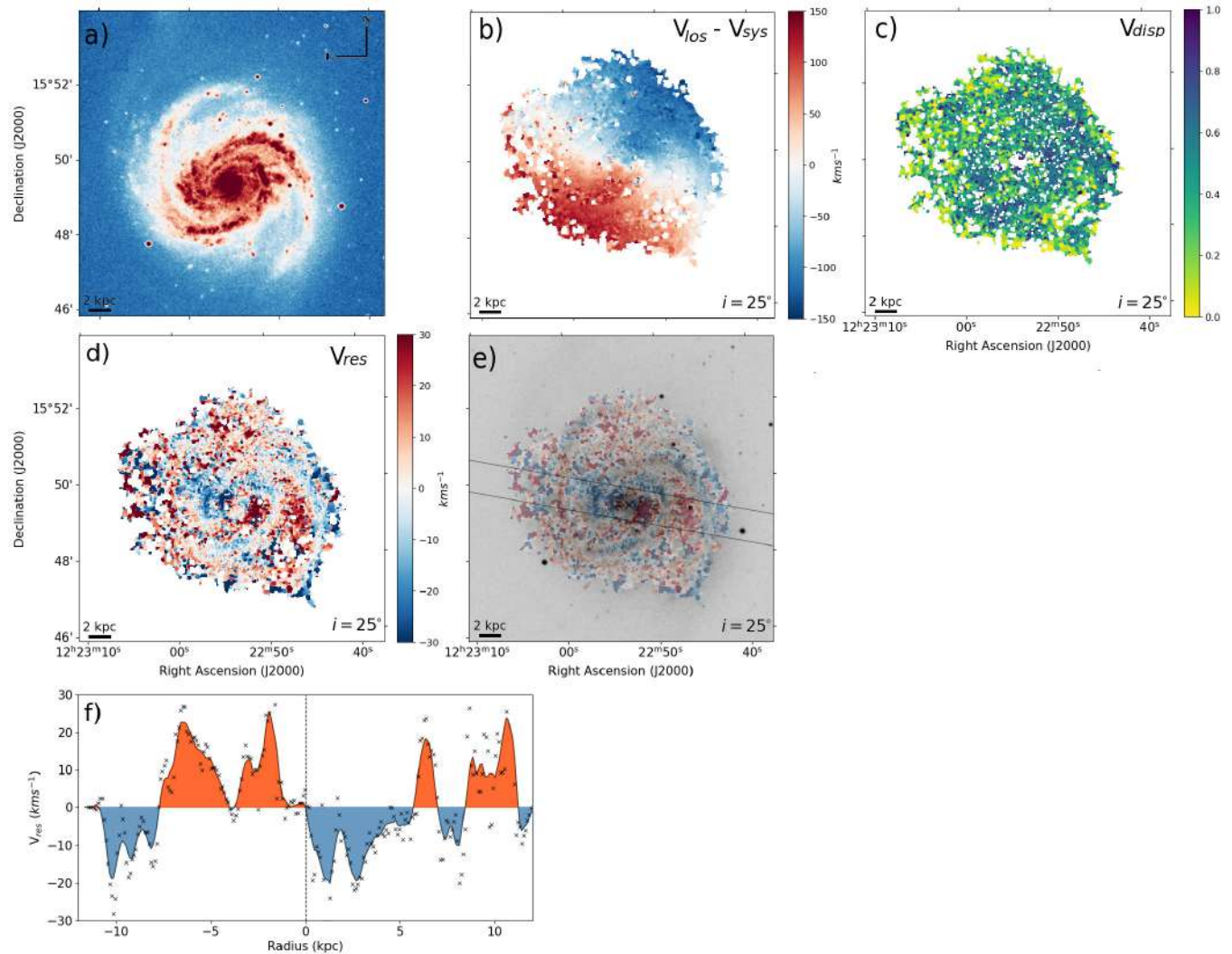
Figure 4.6.4: NGC 4321. Panel (a): XDSS blue-band image. Panel (b): H$_\alpha$ velocity field. Panel (c): H$_\alpha$ velocity dispersion map normalized to 33.1 kms^{-1} corresponding to the 95th percentile. Panel (d): H$_\alpha$ residual velocity field. Panel (e): Optical band image with H$_\alpha$ residual velocity field. Panel (f): Residual velocity radial profile considering a slit indicated with black lines with position angle of 100° in Panel (e). The black line corresponds to smoothed curve and the dashed line fits center of galaxy indicated in the panel (e). The red (blue) area corresponds to velocities above (below) the midplane of the galaxy. The derived kinematic inclination is indicated in the lower right of each panel.

differences could be caused by deviations from circular motions in the outer disk probably due to a close passage of its companion galaxy. They also suggest this interaction could be the cause of the observed asymmetry in the total HI distribution. NGC 4321 also shows diffuse stellar extension in two directions, one of them towards NGC 4323, likely the result of ongoing interaction with this satellite (Hernandez et al., 2005).

4.6.5   NGC 5194

NGC 5194 (M51a) is a well-known nearby grand design spiral galaxy classified as non-barred by RC3, with a very low inclination angle $i = 20°$. NGC 5194 is tidally interacting with its companion NGC 5195 (M51b), an early-type SB0 galaxy. NGC 5194 shows an intense star formation activity at its center and along its spiral arms. Panel a), on Figure 4.6.5, clearly shows its strong spiral structure with signs of being lopsided, likely due to the interaction with its companion. Panel b) shows that the H_α observations provide wide coverage of the disk, which allows us to obtain its velocity field up to distances of 12 kpc $\sim 0.8 \, R_{opt}$. The resulting V_{los} map shows a velocity range of ≈ 150 km s^{-1}. It is interesting to compare our H_α velocity map with the one derived from HI observations, obtained from THINGS using VLA (Walter et al., 2008), shown in panel f). As seen in NGC 628 and NGC 6946, the HI velocity map of NGC 5194, constrained to the same FoV as the H_α data, shows a very good agreement with the ionized gas velocity map, despite differences in both the spatial and spectral resolutions. In panel c), we show the velocity dispersion map normalized to $\sigma_{95th} = 15$ km s^{-1}.

The residual velocity map is shown in panels d) and e). It is interesting to note the large velocity perturbations throughout the disk, reaching amplitudes of 40 km s^{-1}. We recall the very low inclination angle of this galaxy, thus rendering it unlikely that these velocity perturbations are mainly due to in-plane velocity flow. Panel e) allows comparing the substructure of the V_{res} map with the galaxy morphology as seen in the B-band image. In panel g) we follow the smoothed residual velocity profile along the highlighted slit. As before, this allows appreciating the radial oscillatory behavior of V_{res}, consistent with what is expected for a corrugated disk. Shetty et al. (2007) presented a deep kinematic study of NGC 5194 using full 2D velocity distributions from interferometric CO and FP H_α observations. They report a complex velocity field, with variations of the disk's PA and inclination along the galactic radius that strongly suggest a vertically perturbed disk and very significant out-of-plane motions. An HI warp has also been previously reported in NGC 5194 (Rots et al., 1990; Oikawa & Sofue, 2014; Haan & Braun, 2014), which has been attributed to the tidal interaction with NGC 5195. The presence of vertical velocity flows in this very interesting galaxy will be further analyzed in a follow-up study, following the procedure described in Gómez et al. (2021).

4.6.6   NGC 5668

NGC 5668 is a nearly face-on late-type spiral galaxy with an estimated inclination angle 18° (Schulman et al., 1996) and R_{opt} of ~ 14.3 kpc, located at 27.6 Mpc. The galaxy is classified as a SA(s)d by RC3 and, on its optical image (panel a), it shows a weak bar or oval structure on its inner $12''$ region. Observations of NGC 5668 were extracted from the GHASP sample (Epinat et al., 2008a). The H_α coverage reaches out to 20 kpc corresponding to $\sim 1.4 \, R_{opt}$. On panel b) we show the resulting V_{los} field, with a velocity amplitude reaching ≈ 70 km s^{-1}. The velocity dispersion map, normalized to $\sigma_{95th} = 57.5$ km s^{-1}, is shown on panel c).

The V_{res} map, shown on panel d), reveals global perturbations with amplitudes > 20 km s^{-1} which are also consistent with a warped H_α disk. In panel e) we present the optical image with the overlay of the residual velocity map. The warp is better shown in panel f), where we can see the mean velocity profile along the highlighted slit on panel e). Note the large amplitude of this kinematical perturbation reaching velocities > 20 km s^{-1} at the disk outskirts. High-resolution observations in the 21-cm line of the neutral hydrogen velocity field, from the Very Large Array (VLA), have detected a kinematic warp that begins, at least, at the end of the optical radius (Schulman et al., 1996). Note that the H_α warp is very well aligned with the previously reported HI warp, indicating that the perturbation extends even within the optical radius of the galaxy. In addition to the HI kinematic warp, Schulman et al. (1996) detected high-velocity wings beyond the double-horned 21 cm profile, related to High-Velocity Clouds (HVCs) in the disk and halo of the galaxy. As discussed by Schulman et al. (1996), the high-velocity wings located outside the optical disk may be the result of infalling material, comparable to the Magellanic Stream observed in the Milky Way.

The origin of the kinematic warp, and the infalling material, could be related to a past interaction with its neighbor galaxy UGC 9380, currently located at a projected distance of ~ 200 kpc of NGC 5668. It is worth mentioning that Jiménez-Vicente
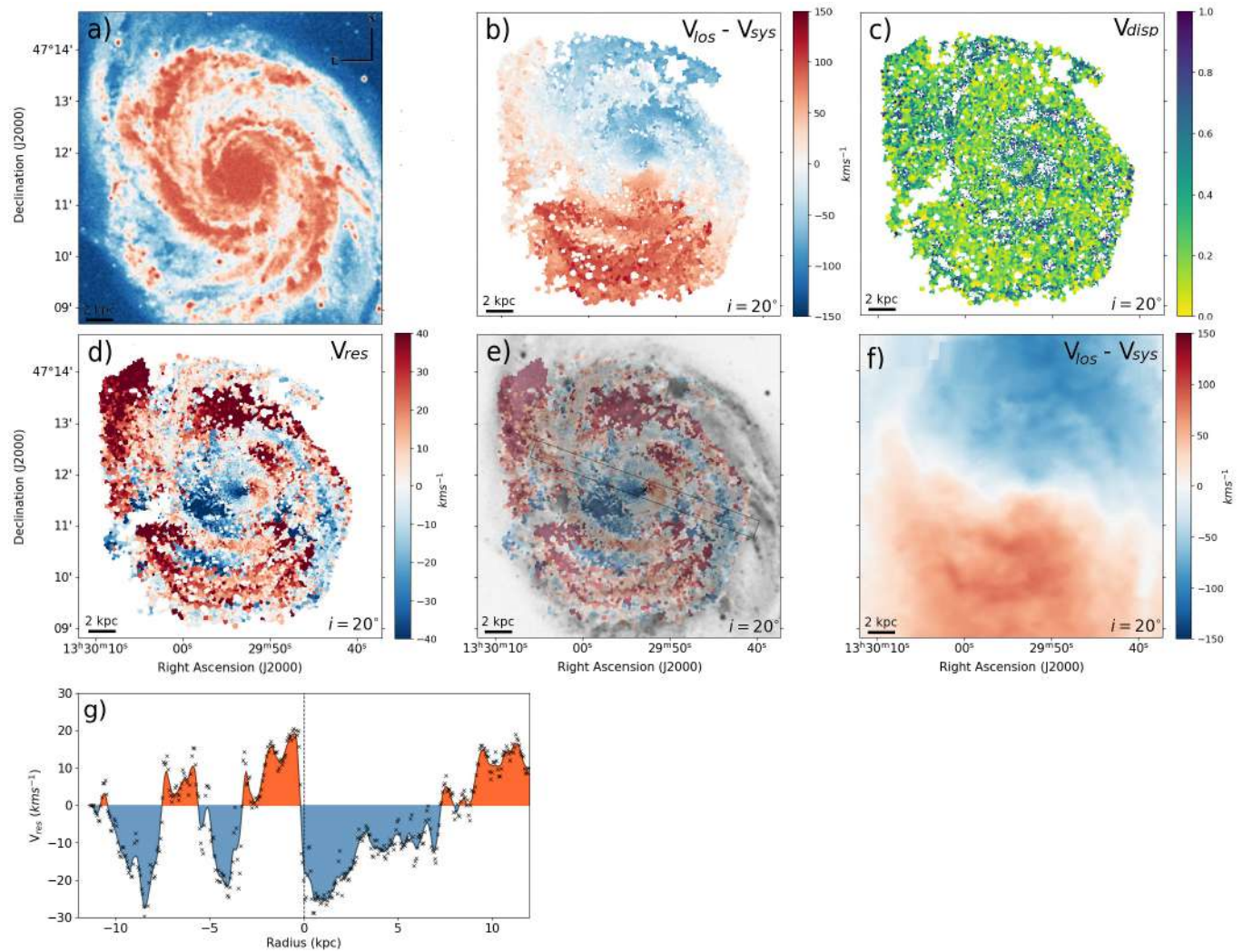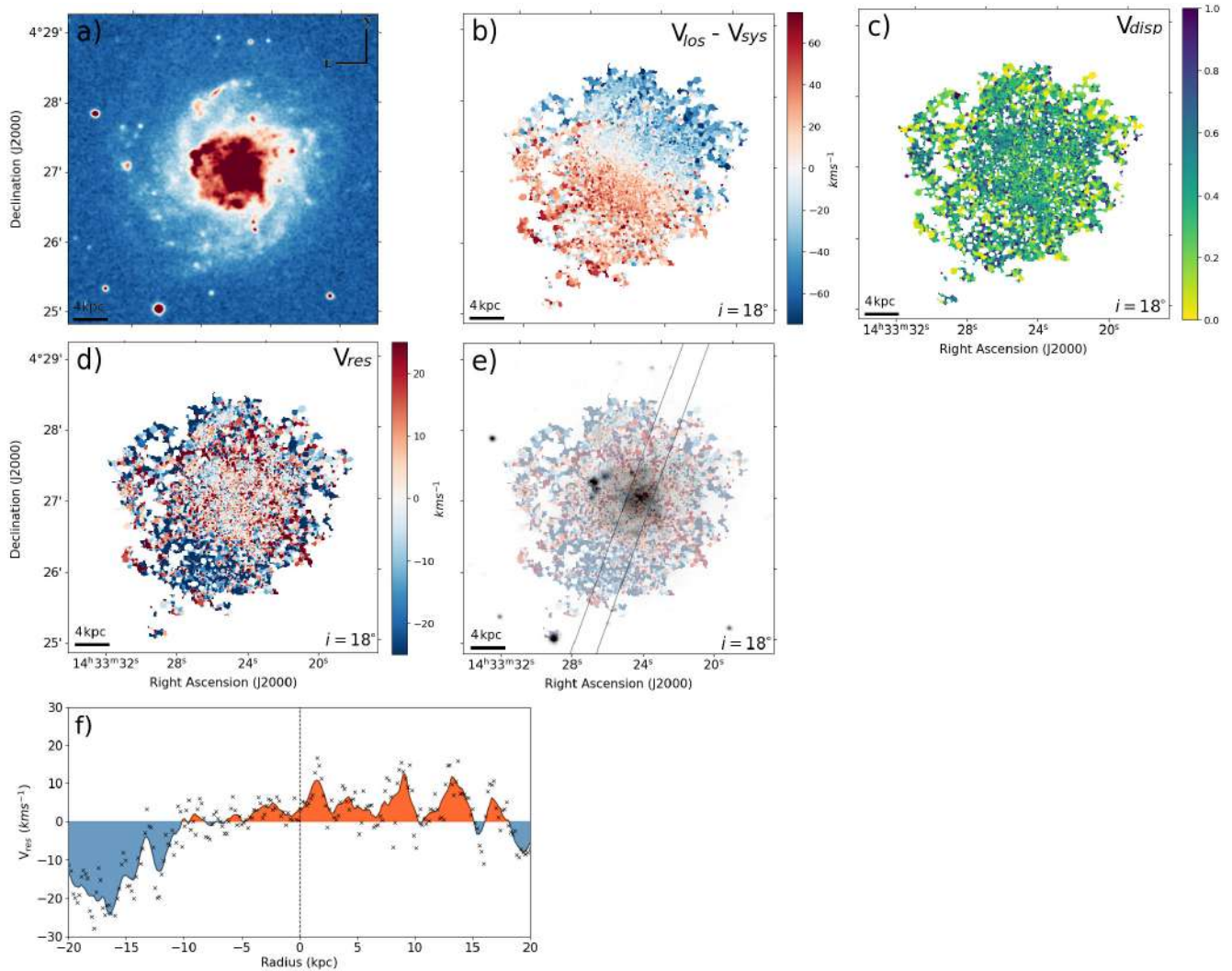
Figure 4.6.5: NGC 5194. Panel (a): XDSS blue-band image. Panel (b): H$_\alpha$velocity field. Panel (c): H$_\alpha$velocity dispersion map normalized to 15 kms^{-1} corresponding to the 95th percentile. Panel (d): H$_\alpha$residual velocity field. Panel (e): Optical band image with H$_\alpha$residual velocity field. Panel (f): HI velocity field from THINGS survey Walter et al. (2008). Panel (g): Residual velocity radial profile considering a slit indicated with black lines with position angle of 110° in Panel (e). The black line corresponds to smoothed curve and the dashed line fits center of galaxy indicated in the panel (e). The red (blue) area corresponds to velocities above (below) the midplane of the galaxy. The derived kinematic inclination is indicated in the lower right of each panel.

Figure 4.6.6: NGC 5668. Panel (a): XDSS blue-band image. Panel (b): H$_\alpha$velocity field. Panel (c): H$_\alpha$velocity dispersion map normalized to 57.5 kms^{-1} corresponding to the 95th percentile, corrected for instrumental broadening. Panel (d): H$_\alpha$residual velocity field. Panel (e): Optical band image with H$_\alpha$residual velocity field. Panel (f): Residual velocity radial profile considering a slit indicated with black lines with position angle of 20° in Panel (e). The black line corresponds to smoothed curve and the dashed line fits center of galaxy indicated in the panel (e). The red (blue) area corresponds to velocities above (below) the midplane of the galaxy. The derived kinematic inclination is indicated in the lower right of each panel.

& Battaner (2000) also analyzed the 2D velocity field of this galaxy through its H$_\alpha$ emission using FP interferometer. However, they did not cover the region where we detect the kinematic warp. Instead, they reported the detection of HVCs and localized high residual velocity dispersion regions, associating them to shell/chimney regions. Even though we present a velocity dispersion map in panel c), in this work we have not attempted to recover these regions, typically associated to vertical motions of ionized gas due to star-forming processes.

4.6.7   NGC 2763

NGC 2763 is low inclination disk galaxy ($i \approx 29.5°$) is the only object in WiNDS observed in the Southern Hemisphere, and one of the first galaxies observed with the SAM-FP instrument (Mendes de Oliveira et al., 2017). The *B*-band image on panel a) reveals two main spiral arms, each with multiple sub-arms, and a small bar. In addition, it shows a significant lopsided structure. The galaxy shows an extended H$_\alpha$ emission across the disk, reaching up to 0.9 R_{opt}, with $R_{opt} \approx 9.9$ kpc. Panel b) shows its V_{los} maps, with an amplitude of ≈ 100 km s^{-1}. The velocity dispersion map, normalized to $\sigma_{95th} = 37.2$ km s^{-1} is shown on panel c).

The resulting V_{res} maps, shown on panel d), reveals a very complex structure with global residual velocity flows reaching amplitudes $\gtrsim 20$ km s^{-1}. In panel e) we can observe the *B*-band image of NGC 2763 with the residual velocity map overlapped, highlighting the region where complex residual velocity perturbations are observed. Interestingly, no detailed kinematical studies of NGC 2763 velocity field, nor companion galaxies within 150 kpc, have been reported. We have confirmed the lack of massive nearby companions by performing a systematic search within a radial projected distance of 250 kpc and radial velocity difference $\Delta \leq 1000$ km s^{-1} using NASA/IPAC Extragalactic Data base. Thus, NGC 2763 is considered as an isolated galaxy. As such, it is not clear whether its significantly perturbed morphology and kinematics are the results of a previous minor merger event or due to significant misaligned smooth gas accretion.

4.6.8   NGC 5713

NGC 5713 is oriented nearly face-on, with inclination $i \approx 10°$, and shows a significant lopsided morphology. This can be seen in panel a) of Figure 4.6.8, where we show its XDSS *B*-band image. NGC 5713 has an $R_{opt} \sim 13.5$ kpc, it is a barred and multiple arm spiral galaxy (SABb-type de Vaucouleurs et al., 1991), and is located at 33.4 Mpc. The H$_\alpha$ V_{los} map, shown on panel b) covers approximately a region of 0.9 R_{opt}, and shows an amplitude of ~ 100 km s^{-1}. The velocity dispersion map, normalized to $\sigma_{95th} = 54.2$ km s^{-1}, is shown on panel c).

The V_{res} (panel d) reveals a very peculiar structure, with several global and coherent perturbations reaching peak velocities ≥ 30 km s^{-1}. The galaxy is currently undergoing a very strong tidal interaction with its similar mass Sab-type companion, NGC 5719 (Vergani et al., 2007), and shows two HI tidal tails. Both galaxies (NGC 5713 and NGC 5719) show an optical radius at a similar galactocentric distance and are connected by two HI tidal bridges. The projected distance between these two galaxies is ~ 77 kpc. NGC 5719 shows an ionized gas disk that counter rotates with respect to its neutral gas counterpart. According to Vergani et al. (2007), this counter-rotating disk is the result of the accretion of NGC 5713 material onto NGC 5719 during their closest approach. Interestingly NGC 5719 shows a nearly edge-on configuration with a clearly visible warped disk. In addition, NGC 5713 is interacting with the Sm-type dwarf galaxy, PGC 135857, which is located at a projected distance of ~ 64 kpc (Vergani et al., 2007). These interactions are likely behind the observed NGC 5713 strongly perturbed velocity field. The interacting system will be compared against numerical models in a follow-up study.
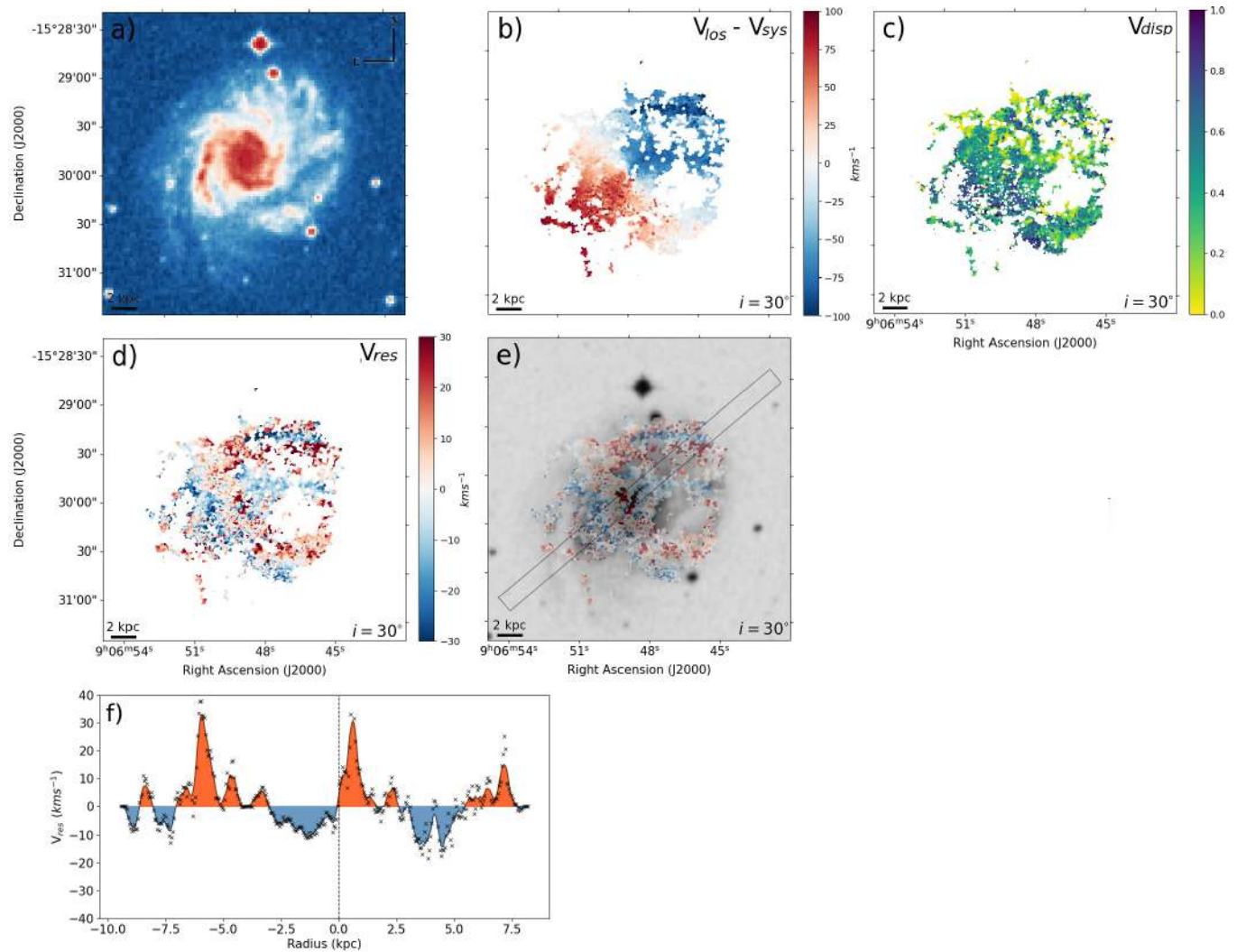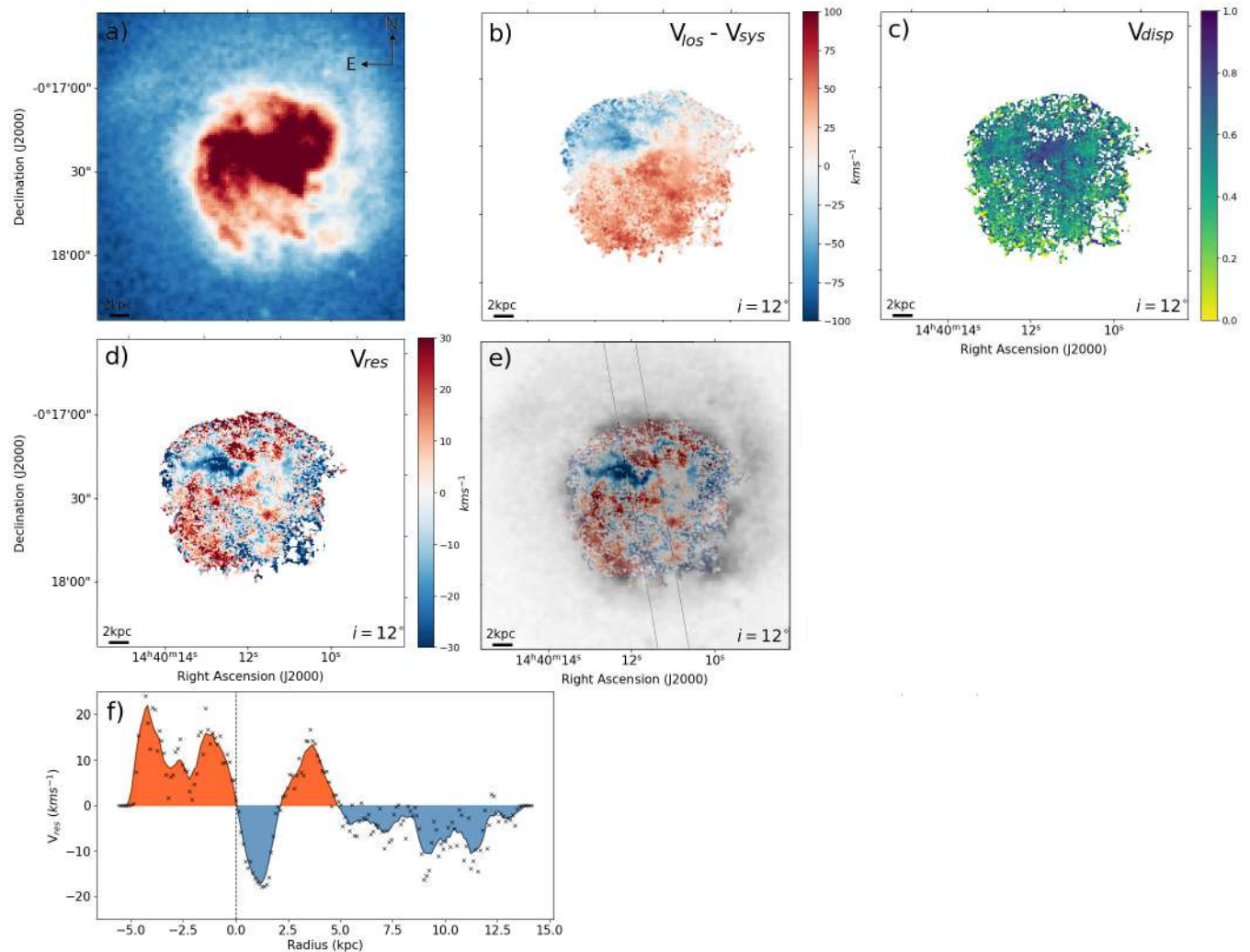
Figure 4.6.7: NGC 2763. Panel (a): XDSS blue-band image. Panel (b): H$_\alpha$velocity field. Panel (c): H$_\alpha$velocity dispersion map normalized to 37.2 kms^{-1} corresponding to the 95th percentile. Panel (d): H$_\alpha$residual velocity field. Panel (e): Optical band image with H$_\alpha$residual velocity field. Panel (f): Residual velocity radial profile considering a slit indicated with black lines with position angle of 40° in Panel (e). The black line corresponds to smoothed curve and the dashed line fits center of galaxy indicated in the panel (e). The red (blue) area corresponds to velocities above (below) the midplane of the galaxy. The derived kinematic inclination is indicated in the lower right of each panel.

Figure 4.6.8: NGC 5713 Panel (a): XDSS blue-band image. Panel (b): H$_\alpha$velocity field. Panel (c): H$_\alpha$velocity dispersion map normalized to 54.2 kms^{-1} corresponding to the 95th percentile. Panel (d): Optical band image with H$_\alpha$residual velocity field. Panel (e): H$_\alpha$residual velocity field. Panel (f): Residual velocity radial profile considering a slit indicated with black lines with position angle of 170° in Panel (e). The black line corresponds to smoothed curve and the dashed line fits center of galaxy indicated in the panel (e). The red (blue) area corresponds to velocities above (below) the midplane of the galaxy. The derived kinematic inclination is indicated in the lower right of each panel.

4.7   Discussion and Conclusions

In this Chapter, we have presented the Waves in Nearby Disk galaxies Survey (WiNDS), which currently consists of 40 nearby low-inclination spiral galaxies, including objects with diverse morphological features. The WiNDS sample contains galaxies within a distance limit of 45 Mpc and absolute B magnitude between -17.0 and -21.9 mag, all observed in H$_\alpha$ with Fabry-Perot interferometer. These observations allow us to obtain very detailed velocity maps of the ionized gas distribution, with velocity sampling precision as low as 3 km s^{-1}, which translates into a resolution of 6 km s^{-1}. Our sample was selected such that galaxies have an inclination angle $i \lesssim 40°$. WiNDS consists of 12 new data observed, and includes archival data for 28 low-inclination late-type galaxies, extracted from the GHASP, SINGS–H$_\alpha$, VIRGO–H$_\alpha$, HRS–H$_\alpha$ surveys. For each galaxy in the final sample, we derived their line-of-sight velocity field, an unperturbed axy-symmetric velocity model, kinematical parameters, the corresponding residual velocity fields, $V_{\rm res}$ and rotation curves (see Appendix C).

Our main goal in this work was to examine the resulting V$_{\rm res}$ fields to search for evidence of large, global, and coherent kinematic perturbations in our sample of low-inclined late-type galaxies. In particular, we seek perturbations that are consistent with those produced by warps and corrugation patterns. Through three criteria we identify clear signatures of perturbations. First, we are interested in objects that present a wide H$_\alpha$ coverage ($\geq 0.7R_{\rm opt}$) so that the kinematics of the disks could be globally explored. Second, we focused on galaxies with V$_{\rm res}$ amplitude that are > 10 km s^{-1}, which allows us to be more confident in observing perturbations in the low-inclination disks that are not the result of the axisymmetric components of the galaxies.

Finally, we also searched for perturbations in the $V_{\rm res}$ fields that show global and coherent velocity flows, avoiding local and discrete perturbations that could be linked to, e.g., fountain flows.

We emphasize that our selection criteria cannot confirm nor rule out the presence of vertical perturbations in our disks. Instead, our goal is to select potentially strong candidates for follow-up studies. Note however that, as shown by Monari et al. (2016) as we showed in Chapter 3 and Gómez et al. (2021), the amplitude of the observed velocity flows in these low-inclined disks are, typically, much too large to be driven either by spiral structure or by a bar. Within the subset of galaxies with vertical perturbations considered as candidates, those displaying discrete and local perturbations that could be associated to fountain flows are not excluded since such signatures can coexist with the global and coherent perturbations that we aim at detecting in this study.

A vertical perturbation such as a warp or a corrugation pattern is manifested by an extended and oscillatory vertical displacement of the disk with respect to the overall mid-plane. Its characterization can allow us to constrain the recent interaction history of a galaxy. Previous studies based on cosmological simulations (e.g. Gómez et al., 2017) have identified four main mechanisms behind such perturbations: distant fly-by massive companions, close satellite encounters, re-accretion of cold gas from progenitors of a gas-rich major merger and accretion of misaligned cold gas. Out of 40 observed low-inclination galaxies, we find that approximately 20 percent of the sample shows clear signatures of global and coherent perturbations. Adding to this statistic the results of our pilot study based on VV304a (see Chapter 3) bring this number to 22 percent. We note however that, as further discussed below, some of our observations were either not sufficient or not adequate to identify velocity perturbation on the disk outskirts and, thus, this percentage could be higher. In fact, out of the 40 galaxies in the WiNDS sample, only 70% show good H$_\alpha$ coverage. If we only consider this subset, the fraction of vertically perturbed galaxy candidates rises to 32%.

From the galaxies that show signs of potential vertical perturbation, six of them are interacting with a satellite galaxy and/or belong to a group. Thus, the observed kinematic perturbations are likely directly linked with recent environmental interactions. The rest of the perturbed subsample of galaxies are considered to be isolated. Therefore, their perturbations could be the result of previous minor mergers or misaligned cold gas accretion. A deeper and more detailed study must be performed for each galaxy to constrain the origin of their perturbed velocity field. As shown in Fig. 4.2.1, the vertically perturbed candidates within WiNDS sample (green distribution) shows no preferential distribution of the main parameters with respect to the overall WiNDS sample.

Previous studies, either in HI (García-Ruiz et al., 2002) or in the optical (Reshetnikov & Combes, 1998; Ann & Park, 2006, for the edge-on galaxies), that have characterized the frequency at which vertically perturbed disks arise in the local Universe, have found that approximately 70% of them present a warped disk, typically displaying S-shaped configuration. However, evidence for more complex corrugation patterns in external galaxies, such as those hinted at in this work, has been extremely scarce. Indeed, only a handful of previous studies have previously reported corrugations on external galaxies (e.g. Sánchez-Gil et al., 2015; Narayan et al., 2020; Gómez et al., 2021). In agreement with observations, using cosmological simulations of high-resolution late-type galaxies within Milky Way-sized halos, Gómez et al. (2016, 2017) estimated that 70% should show

strongly vertically perturbed disks, and 35% should present a corrugated structure. The scarcity in the detection of corrugation patterns on external galaxies so far was not that surprising since most studies attempting to characterize stellar disk vertical structures have been focused on edge-on systems in which corrugation is difficult to detect due to projection effects. Our study shows that high resolution velocity maps, obtained with techniques such as Fabry-Perot interferometer, allows us to reveal much more complex velocity structures on external galactic disks. Furthermore, due to the low inclination angles of the disks in our sample, these are likely linked with vertical flows and consistent with corrugations patterns. Eight galaxies from WiNDS show potential vertical patterns, of which 25% are in a close interaction with a massive companion, 50% show nearby dwarf satellite galaxies, and 25% can be regarded as isolated.

However, the fraction of low inclination galaxies with detected velocity flow, i.e. $\approx 20\%$, is currently significantly lower than the expected fraction of vertically perturbed disks. Several factors can be playing a role here. The first and most obvious reason is that a fraction of $\approx 30\%$ of the galaxies in our sample did not show a wide H_α coverage. Such cases either presented a patchy and poor H_α emission distribution, or it was concentrated within the inner $\sim 0.5\ R_{opt}$. As a result, we were not able to globally explore the kinematics of their disks, especially on the outer disk regions where warps and vertical perturbations are expected to be stronger. Second, the weather conditions in $\approx 12.5\%$ of our observations were not ideal. As a result, the observations were not sufficient to generate kinematic maps accurate enough to properly resolve their velocity fields. Considering these caveats, it is not surprising that we have been able to detect kinematic perturbation, consistent with a vertical perturbed disk, in a smaller fraction of galaxies than previously reported.

In a follow-up study deeper and better observation will be presented. Following Gómez et al. (2021) we will compare our observations against detailed analytic kinematic models that account for the axisymmetric perturbations measured on each galaxy and thus constrain the origin of their velocity perturbations.

NGC	UGC	RA (hh mm ss)	DEC (° ′ ″)	Cube xyz	Pixel scale (arc sec)	Int Order	Date (yyyy-mm-dd)	λ_{scan} (Å)	R	seeing (arc sec)
(1)	(2)	(3)	(4)	(5)	(6)	(7)	(8)	(9)	(10)	(11)
New observations										
628	1149	01 36 41.8	15 47 00	512 512 32	0.68	2600	2019-02-05	6577.2	28600	⋆
1058	2193	02 43 30.1	37 20 28	512 512 32	0.68	798	2019-02-03	6574.2	10000	⋆⋆
2500	4165	08 01 53.2	50 44 14	512 512 32	0.68	798	2019-02-04	6573.8	10000	⋆⋆
2763 (SAM-FP)		09 06 49.1	-15 29 59	1024 1028 48	0.045	609	2016-02-18	6604.2	10000	⋆
3147	5332	10 16 53.7	73 24 03	512 512 32	0.68	798	2019-02-08	6624.1	10000	⋆⋆
3184	5557	10 18 16.9	41 25 28	512 512 32	0.68	2600	2019-02-05	6575.8	28600	⋆⋆
3423	5962	10 51 14.3	05 50 24	512 512 32	0.68	2600	2019-02-07	6584.8	28600	⋆⋆
3485	6077	11 00 02.4	14 50 29	512 512 32	0.68	798	2019-02-03	6574.2	10000	⋆⋆
3642	6385	11 22 17.9	59 04 28	512 512 32	0.68	2600	2019-02-06	6597.6	28600	⋆⋆
4136	7134	12 09 17.7	29 55 39	512 512 32	0.68	2600	2019-02-06	6576.1	28600	⋆⋆
4900	8116	13 00 39.2	02 30 03	512 512 32	0.68	798	2019-02-04	6583.8	10000	⋆⋆
5194	8493	13 29 52.7	47 11 42	512 512 32	0.68	2600	2019-02-06	6572.9	28600	⋆
Data Archive										
864 (G)	1736	02 15 27.6	06 00 09	512 512 24	0.68	793	2000-10-23	6597.0	≃ 10000	⋆⋆
2775 (G)	4820	09 10 20.1	07 02 17	512 512 24	0.68	793	2003-03-06	6592.4	≃ 10000	⋆⋆
3344 (G)	5840	10 43 31.2	24 55 20	512 512 24	0.68	793	2002-03-20	6575.5	≃ 10000	⋆⋆
3346 (G)	5842	10 43 38.9	14 52 19	512 512 24	0.68	793	2004-03-20	6590.7	≃ 10000	⋆⋆
3351 (S)	5850	10 43 57.7	11 42 13	512 512 48	1.61	765	2005-02-03	6579.8	13750	⋆⋆⋆
3504 (G)	6118	11 03 11.2	27 58 21	512 512 24	0.68	793	2002-03-18	6596.2	≃ 10000	⋆⋆
3596 (G)	6277	11 15 06.2	14 47 13	512 512 24	0.68	793	2004-03-19	6588.9	≃ 10000	⋆⋆
3631 (H)	6360	11 21 02.9	53 10 10	512 512 32	0.68	798	2016-02-03	6587.3	≃ 10000	⋆⋆⋆
3938 (S)	6856	11 52 49.5	44 07 15	512 512 48	1.61	765	2004-03-11	6579.7	12852	⋆⋆⋆
4037 (H)	7002	12 01 23.7	13 24 04	512 512 32	0.68	798	2016-02-15	6582.4	≃ 10000	⋆⋆⋆
4189 (V)	7235	12 13 47.3	13 25 29	512 512 24	0.68	793	2003-03-07	6609.1	7950	⋆⋆
4321 (V)	7450	12 22 54.8	15 49 19	512 512 52	1.61	899	2003-02-25	6597.2	21000	⋆⋆
4411B (H)	7546	12 26 47.2	08 53 05	512 512 32	0.68	798	2016-02-04	6589.0	≃ 10000	⋆⋆⋆
4430 (H)	7566	12 27 26.4	06 15 46	512 512 32	0.68	798	2016-02-15	6593.7	≃ 10000	⋆⋆⋆
4519 (V)	7709	12 33 30.3	08 39 17	512 512 48	1.61	899	2003-04-04	6589.5	21000	⋆
4625 (S)	7861	12 41 52.7	41 16 26	512 512 48	0.48	899	2003-04-06	6576.4	14294	⋆⋆⋆
4725 (S)	7989	12 50 26.6	25 30 03	512 512 48	1.61	765	2004-02-19	6589.2	14305	⋆⋆⋆
4736 (S)	7996	12 50 53.1	41 07 14	512 512 48	1.61	765	2005-05-11	6569.6	12745	⋆⋆⋆
5204 (G)	8490	13 29 36.5	58 25 07	256 256 24	0.68	793		6567.2	≃ 10000	⋆⋆
5334 (H)	8790	13 52 54.5	-01 06 53	512 512 32	0.68	798	2018-12-07	6592.1	≃ 10000	⋆⋆⋆
5430 (G)	8937	14 00 45.7	59 19 42	512 512 24	0.96	897	2003-03-03	6627.6	≃ 10000	⋆⋆
5585 (G)	9179	14 19 48.2	56 43 45	512 512 24	0.68	793	2004-03-20	6569.2	≃ 10000	⋆⋆
5668 (G)	9363	14 33 24.3	04 27 02	512 512 24	0.68	793	2003-04-26	6597.3	≃ 10000	⋆⋆
5669 (H)	9353	14 32 43.5	09 53 26	512 512 32	0.68	798	2016-02-16	6591.9	≃ 10000	⋆⋆⋆
5713 (S)	9451	14 40 11.5	-00 17 20	512 512 24	0.42	609	2004-04-13	6604.4	5785	⋆⋆⋆
6217 (G)	10470	16 32 39.2	78 11 53	512 512 24	0.68	793		6592.6	≃ 10000	⋆⋆
6946 (G)	11597	20 34 52.3	60 09 14	512 512 24	0.68	793	2002-06-14	6563.7	≃ 10000	⋆⋆
	3685	07 09 05.9	61 35 44	512 512 24	0.68	793	2002-03-17	6602.1	≃ 10000	⋆⋆

Table 4.3.1: Log of the WiNDS. (1) Galaxy name in the NGC catalog except for UGC 3685 that do not have NGC name, the letter corresponds to the survey name; (2) Name of the galaxy in the UGC catalog when available (3-4) Right Ascension and Declination (J2000); (5) Cube dimension: x (Right ascension α), y (Declination δ) and z (number of channels); (6) Pixel scale; (7)Interference order (at the H$_\alpha$ rest wavelength); (8) Date of observation; (9) Scanning wavelength; (10) Spectral resolution ($\Delta\lambda/\lambda$) according to the computed Finesse; (11) ⋆ is for a seeing < 2 arc sec, ⋆⋆ is for a seeing between 2 and 4 arc sec, ⋆⋆⋆ see papers (H) (Gómez-López et al., 2019) and (S) (Daigle et al., 2006b; Dicaire et al., 2008).
.

ID	i_k	PA_k	V_{sys}	v_{rot}^{max}
	(°)	(°)	(kms^{-1})	(kms^{-1})
(1)	(2)	(3)	(4)	(5)
New observations				
NGC 628	7^*	155 ± 2	658 ± 1	147
NGC 1058	6^*	34 ± 2	521 ± 0	140
NGC 2500	41 ± 11	85 ± 2	512 ± 1	49
NGC 2763	30 ± 8	47 ± 1	1884 ± 1	123
NGC 3147	32 ± 20	37 ± 8	2894 ± 3	164
NGC 3184	16 ± 9	5 ± 1	592 ± 0	155
NGC 3423	40 ± 8	134 ± 1	1007 ± 1	76
NGC 3485	30 ± 7	156 ± 2	1428 ± 1	146
NGC 3642	36 ± 8	70 ± 8	1581 ± 1	72
NGC 4136	20 ± 6	108 ± 1	606 ± 1	82
NGC 4900	5^*	80 ± 2	959 ± 1	297
NGC 5194	20 ± 11	13 ± 2	464 ± 2	189
Data Archive				
NGC 864 (G)	35 ± 18	30 ± 3	1525 ± 3	52
NGC 2775 (G)	38 ± 3	157 ± 0	1350 ± 1	262
NGC 3344 (G)	15 ± 11	153 ± 2	580 ± 1	262
NGC 3346 (G)	29 ± 8	113 ± 2	1245 ± 1	95
NGC 3351 (S)	21 ± 5	169 ± 1	781 ± 1	289
NGC 3504 (G)	39 ± 13	160 ± 3	1523 ± 2	100
NGC 3596 (G)	17 ± 12	78 ± 2	1190 ± 2	87
NGC 3631 (H)	24 ± 14	151 ± 2	1150 ± 2	59
NGC 3938 (S)	14 ± 8	164 ± 1	809 ± 0	143
NGC 4037 (H)	32 ± 20	151 ± 3	924 ± 1	50
NGC 4189 (V)	31 ± 11	169 ± 1	2102 ± 1	128
NGC 4321 (V)	25 ± 9	29 ± 1	172 ± 1	190
NGC 4411B (H)	18 ± 15	49 ± 3	1267 ± 1	37
NGC 4430 (H)	28 ± 13	75 ± 2	1424 ± 1	180
NGC 4519 (V)	40 ± 16	180 ± 4	1216 ± 2	124
NGC 4625 (S)	8 ± 12	124 ± 3	626 ± 1	105
NGC 4725 (S)	43 ± 4	156 ± 1	1198 ± 2	227
NGC 4736 (S)	25 ± 7	122 ± 1	318 ± 1	245
NGC 5204 (G)	40 ± 11	166 ± 1	186 ± 1	87
NGC 5334 (H)	38 ± 4	6 ± 1	1402 ± 7	105
NGC 5430 (G)	32 ± 8	2 ± 1	2963 ± 3	255
NGC 5585 (G)	36 ± 20	53 ± 3	298 ± 2	59
NGC 5668 (G)	18 ± 14	146 ± 2	1575 ± 1	94
NGC 5669 (H)	36 ± 9	65 ± 1	1377 ± 1	116
NGC 5713 (S)	12 ± 12	154 ± 3	1896 ± 1	84
NGC 6217 (G)	18 ± 10	104 ± 1	1356 ± 1	207
NGC 6946 (G)	17 ± 14	61 ± 2	38 ± 2	185
UGC 3685 (G)	12 ± 19	118 ± 10	1815 ± 3	25

Table 4.4.1: Model Parameters. (1) Galaxy name, the letter corresponds to the survey name; (2) Kinematic inclination, those marked with an asterisk (*) have been fixed equal to morphological value; (3) Kinematic Position Angle; (4) Systemic Velocity; (5) Maximum rotation H_α velocity corrected for inclination derived in this work

Chapter 5

Vertical Perturbations using TNG50 simulations

Abstract

This Chapter presents our analysis of 251 MW/M31-type galaxies using TNG50 magnetohydrodynamic cosmological simulations. Based on a Fourier decomposition of the mean height and vertical velocity maps to quantify vertical disk perturbations, we show that about 70% of disks are strongly vertically perturbed, while the rest have a weakly perturbed or flat disk. To understand the nature of the vertical perturbations, we analyze the environment of each galaxy. In particular, we focus on the number of nearby neighbors and the local overdensity considering different volumes. The first results indicate vertically perturbed galaxies at $z = 0$ have more neighbors than unperturbed galaxies within 250 kpc. We determine the density of the surroundings of each galaxy by measuring the local overdensity in relation to a specific number of neighboring galaxies and a given minimum mass limit. Our results indicate that galaxies with warped disks have a higher concentration of nearby galaxies compared to those with flat or slightly perturbed disks. Finally, for central galaxies, we analyze the time evolution of the interactions with their satellite population. We show that unperturbed galaxies tend to show fewer satellites at present-day. In addition, recent strong interactions with satellites are more common on vertically perturbed disks than on unperturbed objects.

keywords: Galaxy stellar disks; disk galaxies; Galaxy dynamics; Galaxy kinematics

5.1   Introduction

Many studies have been carried out to get more details about the structure of the Galactic disk. Among several different results, they have shown that its structure is more complex than a classical S-shape (e.g. López-Corredoira et al., 2002; Momany et al., 2006; Slater et al., 2014; Price-Whelan et al., 2015; Xu et al., 2015; Antoja et al., 2018; Gaia Collaboration et al., 2021). In particular, the Milky Way (MW) disk reveals a displacement of the stellar component above and below the mid-plane of the disk (Widrow et al., 2012; Widrow et al., 2014) with an amplitude that increases with radius (Xu et al., 2015). The Sagittarius dwarf galaxy ranks among the most plausible pertubers (e.g. Gómez et al., 2013; Antoja et al., 2018; Laporte et al., 2018b,a, 2020; Gaia Collaboration et al., 2021; McMillan et al., 2022; Antoja et al., 2022; Ramos et al., 2022).

Observational studies indicate that vertical perturbations in stellar disks are not uncommon. Indeed, as shown by surveys of edge-on late-type galaxies García-Ruiz et al. (2002); Ann & Park (2006), more than 70% reveal significant warps. García-Ruiz et al. (2002) finds a dependence on the environment with the perturbations in the extended HI disks. In less dense environments, there is a higher frequency of warped disks. On the other hand, the amplitude of the disturbances in the galactic disks is larger in denser environments. This can be explained by the fact that in denser environments, galaxies are exposed to more violent tidal interactions with their companion galaxies.

Due to this, Gómez et al. (2016, 2017) studied the origin of the vertical perturbations in the galactic disks using the Auriga cosmological simulations (Grand et al., 2017). This suite of MW-type models allowed them to characterize vertical disk perturbations in velocity space. It allowed us to precisely characterize the phase-space distribution of stellar and gaseous disks and quantify their perturbations. This study revealed that 70% of the simulated galaxies are perturbed, where half correspond to corrugation patterns. This fraction of warped galaxies is in full agreement with the results obtained with observations. Because warps and corrugations are very common morphological perturbations in late-type galaxies, it is of great interest to characterize the main driving mechanisms and the relationship between their properties and the environment in which the galaxies reside and, as well as how the environment in which galaxies live is related to their evolution over time. As discussed in Gómez et al. (2017), several mechanisms can be behind the formation of warps and corrugation patterns. One is the tidal force produced by an external disturber, such as the case of the MW and Sagittarius dwarf galaxy (Laporte et al., 2018a, 2019a). The strong tidal torques being exerted on a pre-existing disk as relatively massive satellites fly-by or merge can also induce strong vertical disturbances (Ostriker & Binney, 1989; Quinn et al., 1993; Velazquez & White, 1999; Bailin, 2003; Kazantzidis et al., 2009; Gómez et al., 2013; D'Onghia et al., 2016; Gómez et al., 2016, 2017; Laporte et al., 2018a,b). In the early research on bending modes, Hunter & Toomre (1969) utilized numerical models to investigate vertical patterns. They found that an isolated disk allows for a wide range of modes, and as a result, any bending disturbance will dissipate. However, when the disk is embedded in a spherical halo, only a discrete mode with zero frequency is produced. Conversely, when the disk is embedded in a flattened halo, the tilt mode is distorted but remains discrete, which could account for the prolonged existence of warps. However, other studies behind vertical perturbation formation are associated with a non-spherical mass distribution of Dark Matter (DM) because the disk embedded within the DM halo experiences a dynamic frictional force causing deformation when the angular momentum axes of the disk and the halo are misaligned (Debattista & Sellwood, 1999; Jiang & Binney, 1999; Shen & Sellwood, 2006; DeBuhr et al., 2012; Yurin & Springel, 2015; Gómez et al., 2016; Laporte et al., 2018a). Another possible mechanism for the formation of vertical perturbations is the ram pressure of the surrounding intergalactic material (Haan & Braun, 2014) and the misaligned accretion of cold gas due to the cooling of gas falling from the halo, falling from the cosmic web or being left by the interaction between a host galaxy and a gas-rich satellite (Jiang & Binney, 1999; Sancisi et al., 2008; Roškar et al., 2010; Aumer et al., 2013; Radburn-Smith et al., 2014; Gómez et al., 2017).

The long-lived warps can be explained by considering a disk embedded within a flattened halo, as mentioned above. This was analyzed in detail by Toomre & Toomre (1972), Sparke (1984) and Sparke & Casertano (1988), where they considered the disk a system of concentric rings within a static potential of a flattened halo. Using this model, Binney et al. (1998) interpreted that the internal halo responds to the disk quickly, and therefore the vertical structures last a few gigayears due to external perturbations.

This Chapter aims to quantify the predominance of the vertical perturbations through simulated MW/M31-mass disk galaxies using the Illustris TNG50 cosmological magnetohydrodynamic simulations (Nelson et al., 2019; Pillepich et al., 2019). The volume of the TNG50 cosmological box ($\sim$ 50 Mpc co-moving box) is representative of the Local Universe where we find hundreds of MW-type galaxies, thus allowing us to study the frequency of perturbations in a Local Universe-type environment. The mass and spatial resolution of TNG50 are similar to modern zoom-in simulations allowing us to reproduce with unprecedented detail the galaxy's structure and chemo-dynamical evolution. In addition to providing small-scale galaxy properties such as spiral arms and bulge together with the extremely thin scale-heights of galactic disks.

This Chapter is organized as follows. In Section 5.2, we describe the sample of galaxies TNG50. In Section 5.3, the statistics of vertical patterns are discussed. Section 5.4 analyzes how the environment depends on the vertical perturbations at $z = 0$. Section 5.5 we analyze the relationship between galaxies with vertical perturbation at the present day with their recent interaction history. Finally, we present the main conclusions of this work in Chapter 5.6.

5.2 TNG50 Sample

As described in more detail in Chapter 2, the Illustris TNG50 cosmological simulation allows studying the structure of spiral arms and bulges due to the high mass (8.5×10^4 M$_\odot$) and spatial (~ 300 pc) resolution within a relatively large cosmological volume. As a result, they represent an ideal laboratory to study the formation of galactic warps and their environmental dependence. In general, TNG50 bridges the gap between large-scale volumes and the regime of zoom-in simulations.

The selection of galaxies was carried out according to Gargiulo et al. (2022), which consists of 251 MW/M31-like galaxies with a stellar mass within the range $10^{10.5} < M_\star < 10^{11.2}M_\odot$ within a sphere of radius 30 kpc centered at the most bound DM particle at $z = 0$. We focus on objects with flattened stellar mass distribution to select galaxies with disk morphologies. More precisely, we select objects which ratio between the semi-minor and semi-major axis of the stellar mass inertial tensor s < 0.45

To analyze the vertical structure of the simulated stellar disks, for convenience, we have aligned each disk with the X-Y plane through an iterative calculation of the total angular momentum. As a result, the final angular moment vector of each disk is aligned with Z-axis. To perform this rotation, we select all the stellar particles inside a 7 kpc cylinder with decreasing height from 10 kpc. The youngest stars are associated with regions of star formation regions and the cold gas disk; therefore, they are the best tracers of the galactic disk. For a correct rotation of the disks, we consider the 20% younger stars. This is essential for analyzing vertical structures because an incorrect galaxy rotation can be confused with disturbances in the disk.

The TNG50 MW/M31-type mass selected in this work consists of 65 central galaxies within their subhalo, while 186 galaxies are satellites in their respective subhalos.

In Fig. 5.2.1, we show 12 representative examples of the final selection processes. The panels show the present-day surface brightness maps of the galaxies computed in the B-band Note the different morphologies and sizes of each model.

5.3 Methods for classifying warped disks

5.3.1 Mean height and vertical velocity maps

To study the vertical structure of the galactic disks at $z = 0$, we compute mass-weighted mean height, $\langle Z \rangle$, and mean vertical velocity $\langle V_z \rangle$ maps, following Gómez et al. (2013). The stellar disk is binned to construct these maps by considering a Cartesian mesh of 1 kpc bin size and selecting only particles within $\pm$ 10 kpc from the mid-plane. Within each bin, we compute the mean values of $\langle Z \rangle$ and $\langle V_z \rangle$.

In Fig. 5.3.1 and 5.3.2, we show the $\langle Z \rangle$ and $\langle V_z \rangle$ maps, respectively, at the present day of the same set of galaxies shown in Fig. 5.2.1. The color scale in both figures indicates different height and vertical velocity values, respectively. The red (blue) color indicates values above (below) the disk for $\langle Z \rangle$ in kpc and $\langle V_z \rangle$ and in km s^{-1}.

We classify galactic disks into three categories using the $\langle Z \rangle$ and $\langle V_z \rangle$ maps: flat or weakly perturbed, simple warp, and more complex vertical patterns. First, flat or weakly perturbed disks do not exhibit large amplitudes in the $\langle Z \rangle$ and $\langle V_z \rangle$ maps. These galaxies show almost flat disks along their entire extension and, thus, appear vertically unperturbed. Second, we classified the galactic disks as warped when the amplitudes in the $\langle Z \rangle$ map reached over 2 kpc in the outer regions and presented the classical S-shape-like pattern or 'integral-sign' warp. Lastly, disks that exhibit more intricate oscillatory structures and that also have large amplitudes are categorized as corrugation patterns. These perturbations resemble spiral-like morphology, winding in the inner region of the disk, similar to the structure observed in the Milky Way (Slater et al., 2014; Price-Whelan et al., 2015; Xu et al., 2015; Antoja et al., 2018; Gaia Collaboration et al., 2021). The amplitude of the mean height of the disk increases as it moves further outwards. We show a diversity of vertical structures in Fig. 5.3.1 and Fig. 5.3.2.

In warped disks, the vertical patterns in the $\langle Z \rangle$ distribution and $\langle V_z \rangle$ map manifest similarly with a 90 degrees azimuthal phase offset. This anti-correlation, i.e., when $\langle Z \rangle$ is the maximum value and $|V_z| \sim 0$ and vice versa, represents the wave-behavior nature of the bending waves (Gómez et al., 2016, 2017).

Figure 5.2.1: Surface brightness profile in the B-band of 12 galaxies seen in face-on and edge-on orientation. The colored bar indicates μ_B between 19 and 25 mag arcsec^{-2}. The side length of each panel is indicated in its top left corner.

5.3.2 Fourier parameter

In addition to the classification made according to the $\langle Z \rangle$ and $\langle V_z \rangle$ maps, another method that can be used to classify the disks as vertically perturbed or not is the Fourier modes (Quillen et al., 2011). As previously discussed, different modes of vertical oscillation can be excited in the disk due to interactions with other galaxies or the passage of a satellite galaxy. The main modes are bending and breathing modes (Toomre & Toomre, 1972; Araki, 1985; Weinberg, 1991; Widrow & Bonner, 2015). Bending modes in disk galaxies refer to disk oscillations, i.e., a bulk displacement and vertical motion of stars and gas either above or below the disk mid-plane. This mode is associated with the lowest Fourier mode, $m = 1$, and is seen largely in the outer galactic disk.
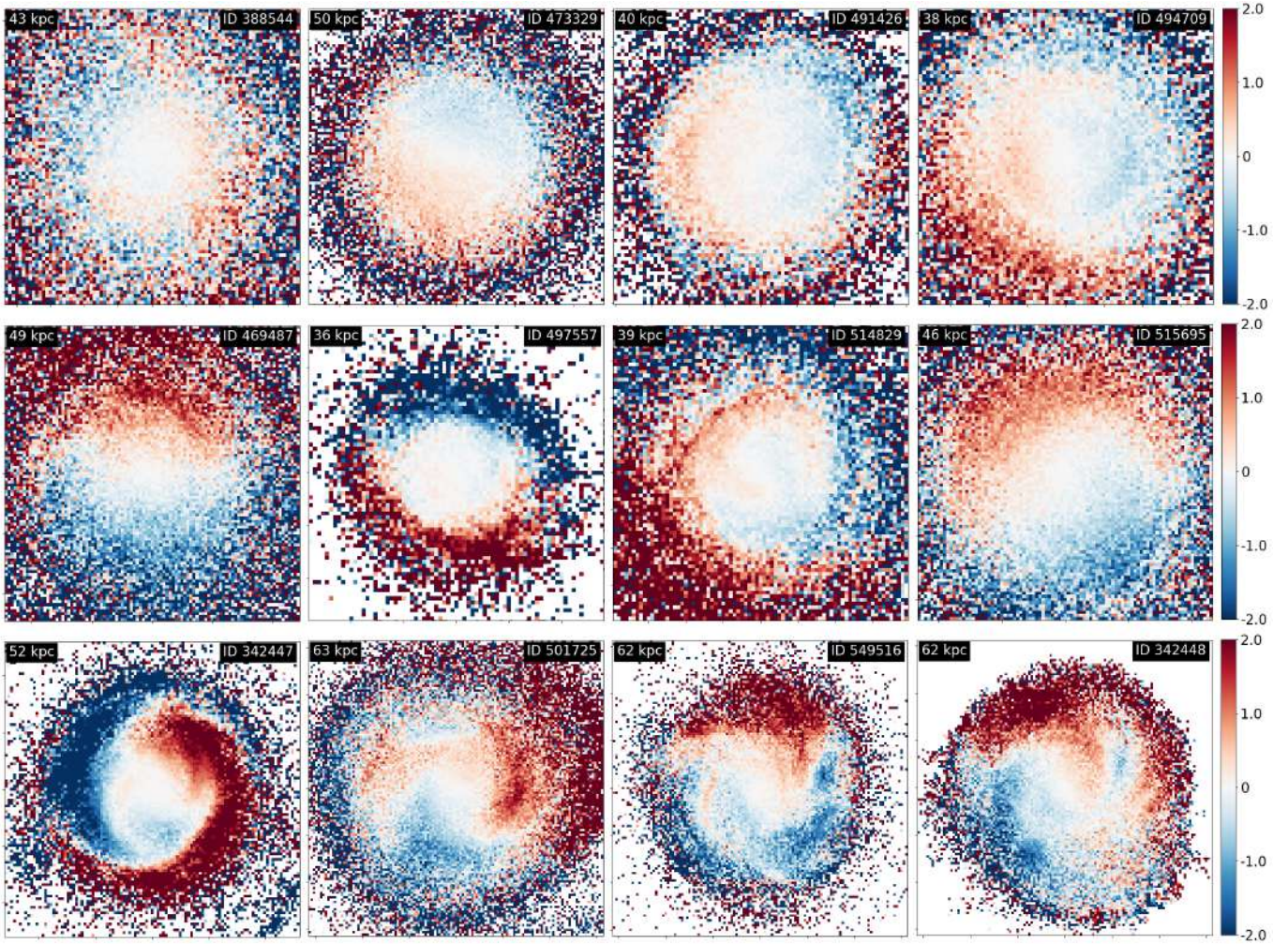
Figure 5.3.1: Mass-weighted mean height, $\langle Z \rangle$, maps at $z = 0$ of 12 simulated stellar disks taken from the whole sample. The color scale shows $\langle Z \rangle$ above (red) and below (blue) the disk of each galaxy, and the map color indicates different values of $\langle Z \rangle$ in kpc. The upper panels correspond to weakly perturbed disks, the middle panels to simple warps, and the bottom panels to more complex vertical patterns.

On the order hand, breathing modes correspond to compression and expansion of the disk with respect to the disk midplane. In addition to high-velocity interaction, this mode can be generated by the influence of spiral arms and bars.

In this thesis, we analyze the vertical perturbations in the galactic disks by applying the Fourier transform to the mass-weighted mean height at $z = 0$. The $m = 1$ allows us to distinguish and quantify the strength of the displacement with respect to the mid-plane.

The complex Fourier coefficients for an azimuthal pattern in the galactic disk mean height distribution with n-fold axisymmetry are calculated as

$$C_n(R_j, t) = \sum_i^N \langle Z_i \rangle m_i e^{-in\theta_i} \tag{5.3.1}$$

where $\langle Z_i \rangle$ and m_i correspond to the mass-weighted mean height and mass, respectively; θ_i is the azimuthal coordinate of the ith star particle found within the jth equally radial annuli. The amplitude of the nth Fourier mode in a given radial bin is given by
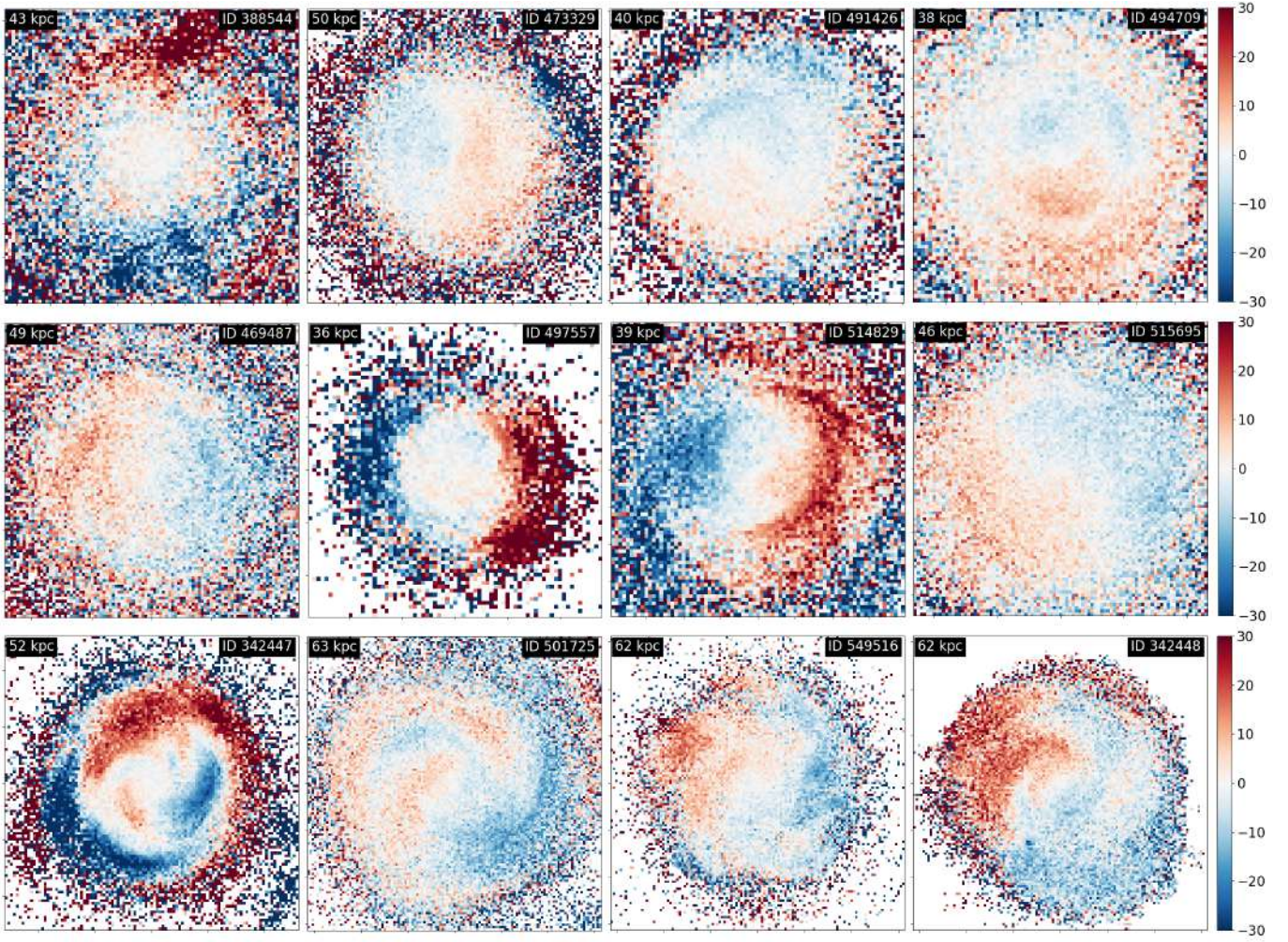
Figure 5.3.2: Mass-weighted vertical velocity ,$\langle V_z \rangle$ for the same set of galaxies of Fig.5.3.1. The map color indicate different values of $\langle V_z \rangle$ in kms^{-1}.

$$Bn(R_j,t) = \sqrt{a_n(R_j,t)^2 + b_n(R_j,t)^2} \tag{5.3.2}$$

where a_n and b_n are real and imaginary parts of the complex Fourier coefficient, $C_n(R_j,t)$ defined as

$$a_n(R_j,t) = \sum_i^N \langle Z_i \rangle m_i cos(n\theta_i') \tag{5.3.3}$$

$$b_n(R_j,t) = \sum_i^N \langle Z_i \rangle m_i sin(n\theta_i') \tag{5.3.4}$$

the phase angle θ_i' is related to the ratio between b_n and a_n, returning a phase angle within the range $\pi/2$ to $-\pi/2$ and is expressed as follows

$$\theta_n' = \frac{1}{2} atan2(b_n, a_n) \tag{5.3.5}$$

Finally, the amplitude A_n nth Fourier modes of the mass-weighted mean height distribution within a radial range is given by

$$A_n = \frac{\sum_j B_n(R_j, t)}{\sum_j B_0(R_j, t)} \tag{5.3.6}$$

As discussed, bending patterns are a signature of a global vertical perturbation that extends to the disk's outer regions, with an amplitude that increases with galactocentric distance (Gómez et al., 2016, 2017). Thus since warps are usually more easily detected in the outermost parts of the galaxy disks, we calculate Fourier mode amplitudes in the range 0.3 to 1.2 R_{opt}, where R_{opt} is defined as the radius at which the surface brightness in the B-band is $\mu_B = 25$ mag arsec^{-2}.

5.3.3 Warps and corrugation patterns statistic

According to the above-mentioned methods, we can distinguish the different types of perturbed disks in our sample of simulated galaxies.

In the performed visual inspection of the $\langle Z \rangle$ in kpc and $\langle V_z \rangle$ maps, we can detect examples of galaxies with small variations in height and vertical velocity, respectively, across both disk maps. Examples of flat (F) disks can be seen in the upper panels of Fig. 5.3.1 and Fig. 5.3.2. Concerning the entire sample, this type of disk corresponds to 36%, which is in agreement with observational data (García-Ruiz et al., 2002; Ann & Park, 2006) and Auriga simulations (Gómez et al., 2017). The rest of the galaxies, corresponding to 64%, exhibit warped (W) disks, i.e., strong 'integral sign' (S) warps and corrugation patterns (C). In particular, on the middle panels of Fig. 5.3.1 and Fig. 5.3.2, we show the perturbed disks with a classic S-shape which reaches 51% of our sample. In the case of corrugated disks, 32 galaxies reveal more complex structure patterns corresponding to 13% of our sample and are shown in the lower panels. Interestingly, we find a smaller fraction of galaxies with corrugation-like patterns compared to the results of Gómez et al. (2017). This could indicate that either corrugation patterns are less common than previously suggested or that the numerical resolution of TNG50 is not large enough to resolve for enough time this more complex vertical mode. This will be explored later on.

In the lower panels of Fig. 5.3.2 it is possible to observe in the perturbed disks the velocity variation can reach values greater than 60 km s^{-1}; this is in agreement with what is observed in galaxies like that NGC 5194 from WiNDS in Urrejola-Mora et al. (2022) (see Chapter 4).

The $\langle Z \rangle$ and $\langle V_z \rangle$ maps of the total sample are presented in Appendix D.2 and D.3, respectively.

Although this method, based on $\langle Z \rangle$ and $\langle V_z \rangle$ inspection, is useful for having a statistic of the number of perturbed disks in a sample, it is subjective to classify galactic disks due to human bias in classification. Therefore, we applied a more quantitative method to discriminate between perturbed and unperturbed disks.

The second method described is based on quantifying the strength of the $m = 1$ Fourier mode. In Fig. 5.3.3 we show the A_1 radial profile of the 12 galaxies shown in Figs. 5.2.1, 5.3.1 and 5.3.2. A Savitzky-Golay filter (red points) is applied for each radial profile to smooth the data curve (dashed curve). To select disks with different vertical perturbations, we focus the following analysis on max(A_1), the maximum value in the smoothed distribution of A_1. The value is indicated at the top right corner of each profile in Fig. 5.3.3. Flat or weakly perturbed disks (upper panels) show a A_1 distribution with lower values. These disks have max(A_1) less than or equal to 0.3. The warped disks, including S-shaped (middle panels) and corrugation patterns (bottom panels), have max(A_1) values greater than 0.3. However, based on the radial profiles of A_1, we cannot clearly distinguish between these two types purely based on max(A_1).

In Fig. 5.3.4, we show the max(A_1) distribution of the total sample of galaxies considered in this work. In Fig. 5.3.4, we highlight F and W disks in the left panel, and F, S, C in the right panel from $\langle Z \rangle$ and $\langle V_z \rangle$ maps classification. In the left panel, we indicate the mean value of max(A_1) for each disk type: $\bar{x}_F$ for F and, $\bar{x}_W$ for the S disk. In the right panel, for F, S, and C disks, we highlight their mean values $\bar{x}_F$, $\bar{x}_S$ and $\bar{x}_C$ respectively.

Considering max(A_1) distribution, we can separate our sample into two types: flat (F_{A_1}) and warped (W_{A_1}) disks, considering a threshold of max(A_1) = 0.3. However, in the right panel of Fig. 5.3.4 it is not possible to establish a limit to separate between flat, simple, or corrugated pattern disks.

In both panels, the solid curves depict the smooth continuous approximation of the underlying histograms. These smooth histograms were obtained using a Gaussian Kernel Density Estimator (KDE). Considering max(A_1) > 0.3, we cover $\sim$ 70% galaxies showing a warped disk in their $\langle Z \rangle$ and $\langle V_z \rangle$ maps.

As a method to quantitatively compare the visual subsamples, we use a two-sample Kolmogorov-Smirnov ($K - S$) test. We establish that both subsamples belong to the same distribution in our null hypothesis. The hypothesis test can be carried out at a specific statistical significance level of 5%, equivalent to a 95% confidence interval ($\alpha = 0.05$). When we apply the
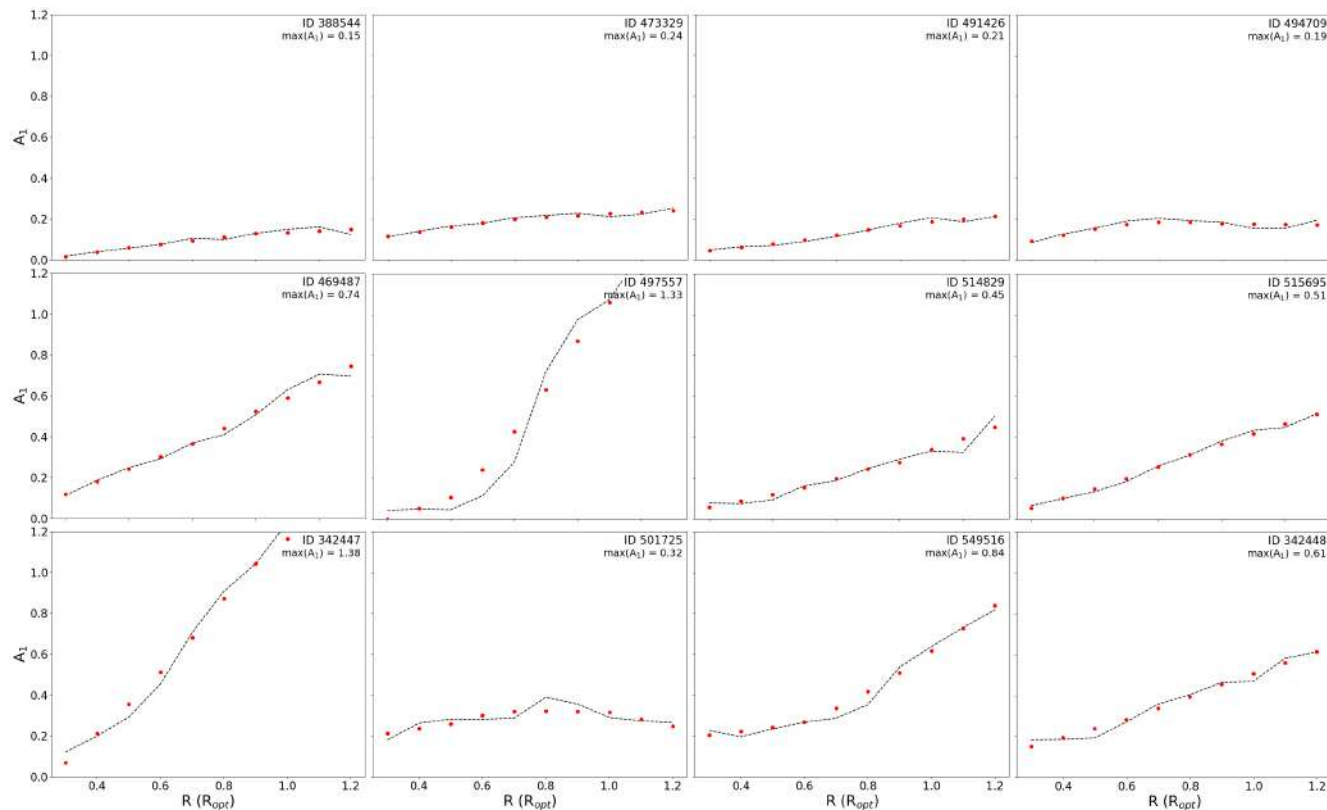
Figure 5.3.3: Radial profile of the mode amplitude $m = 1$, A_1, within 0.3 to 1.3 R_{opt} of 12 galaxies taken from the whole sample. The dotted line corresponds to the values of A_1 in the iteration of 0.1 R_{opt}. The points correspond to the Savitzky-Golay smoothing.
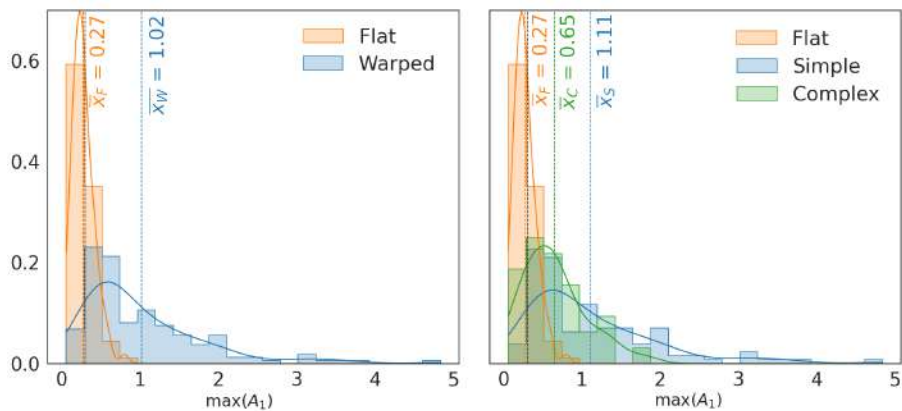

Figure 5.3.4: Distribution of max(A_1). The left panel shows the distribution highlighting the warped (blue color), and flat or weakly perturbed disk galaxies (salmon color). In the right panel, the distribution of A_1 highlights the classification of flat (salmon color), simple warp (blue color), and complex warp (green color) disk galaxies and their respective mean value of each distribution. The mean values of disk type are indicated in each panel. The solid line corresponds to the smooth continuous approximation of the underlying distribution.

$K - S$ test, if the p-value (p) $< \alpha$, the null hypothesis is rejected. In Fig. 5.3.5, we show the cumulative distribution function between F and W (left) and F, S, and C (right) subsamples. In the left panel, we can see a clear difference between flat and warped cumulative distributions. When applying the $K - S$ test, $p_{W-F} = 6.7 \times 10^{-16}$, where it is less than the α and the null hypothesis is rejected, i.e., the subsamples do not come from the same distribution. This test shows good agreement between our visually inspected galaxies and the results obtained from the Fourier decomposition of disk vertical structures.
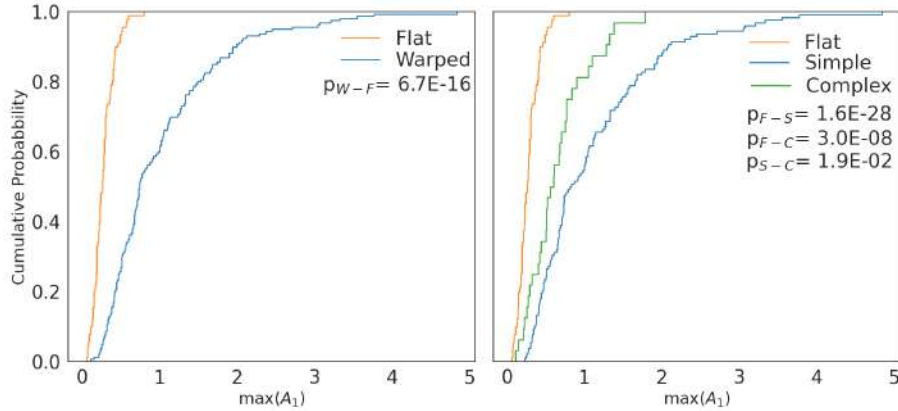
Figure 5.3.5: Empirical cumulative distribution function of subsamples.

In the right panel, we show the three cumulative function curves of the subsamples F, S, and C. We apply the $K - S$ test for three pairs of subsamples: F - S, F - C, and S - C. For the subsamples of flat and simple disks, $p_{F-S} = 1.6 \times 10^{-28} < \alpha$, which do not correspond to subsamples of the same distribution. The same scenario occurs for the flat and corrugation pattern subsamples, where $p_{F-C} = 3.0 \times 10^{-8}$. Finally, for the subsamples of simple warps and corrugation patterns, the estimated p-value is $p_{S-C} = 1.9 \times 10^{-2} < \alpha$, which allows us to distinguish the two subsamples.

In general, the value $\max(A_1) = 0.3$ allows for the separation of the disks type between flat and warped. When we make this cut in the sample, 70 galaxies show flat disks corresponding to 28% of the total sample and 181 galaxies of warped disks equivalent to 72%, including simple warp and corrugation patterns. This method is in agreement with that obtained in other studies of warped disks observed and using cosmological simulations (García-Ruiz et al., 2002; Ann & Park, 2006; Gómez et al., 2017)

From the analysis of $\max(A_1)$, we can see that the simple disks can reach higher values of $\max(A_1)$ than in the disks with corrugation patterns. This means that the simple warps have a stronger warp and the corrugation patterns have a wave-like behavior but with a smaller amplitude than a classic S-shape warp.

5.4 Environmental dependence

Various studies have revealed that the environment where galaxies reside causes changes in their global properties, such as morphology, color, star formation, gas content, etc. (Dressler, 1980). As previously stated in Chapter 1, various mechanisms can cause perturbations in galactic disks, with interactions with the surrounding environment being a significant contributor to disk deformations. In observational terms, García-Ruiz et al. (2002) show that two-thirds of galaxies reveal vertically perturbed disks. In particular, the authors show that there is a higher frequency of perturbed disks in less massive environments. On the other hand, the amplitude warped asymmetries in dense environments are larger than in less dense environments due to more violent tidal interactions. Recently, using TNG100 from IllustrisTNG, Semczuk et al. (2020) focused on galaxies with S-shape warp and showed that one-third of the warps were formed by tidal interaction, another 15% by minor mergers, and around 15% by flyby encounters.

Therefore, the environmental study of a galaxy is key to understanding the formation of perturbations and the recent interaction history of the galaxy.

The first parameter of interest for environmental analysis is the local density of galaxies, defined as the number of satellites within a sphere of a fixed radius with a certain range of masses at $z = 0$ (Blanton & Moustakas, 2009; Gargiulo et al., 2022). For this analysis, we considered the total selected sample of 251 galaxies and then, we considered only central galaxies of

their subhalos. The second analysis of the environment is done considering the overdensity parameter $(1+\delta)$ that relates the distance at which a satellite galaxy is from its host galaxy in different ranges of mass and number of neighbors.

5.4.1 Relationship between numbers of neighbors and perturbed disks

In this first analysis of the environment of MW/M31-type galaxies, we consider the number of neighbors within a fixed radius and mass cut. This analysis is performed on the total sample of 251 galaxies defined in Section 5.2.
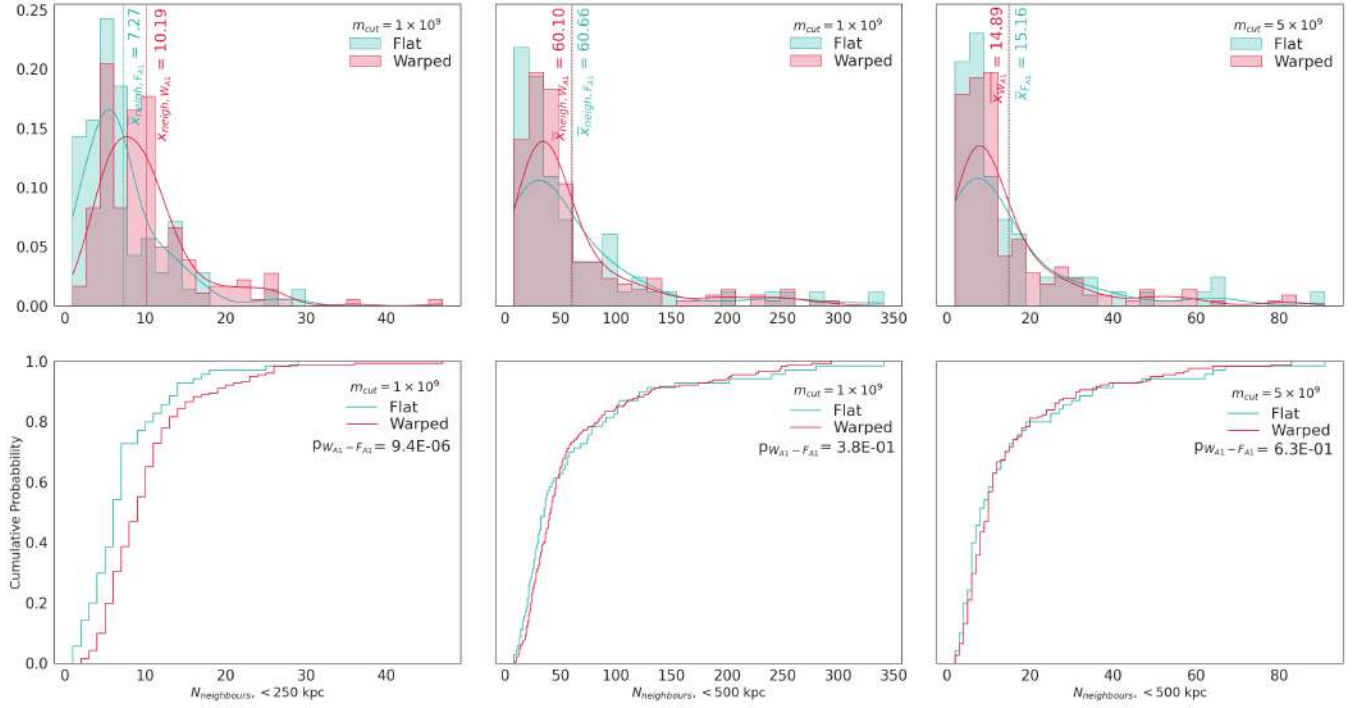
Figure 5.4.1: Distribution of the neighbors in our sample of TNG50 MW/M31-like galaxies, considering the cutoff value of $A_1 = 0.3$ to distinguish between flat (F_{A_1}) and warped (W_{A_1}) disk galaxies. Upper panels, from left to right, correspond to the distribution of neighbors with different mass cuts. Left panels: Number of neighbors within radii of 250 kpc and a stellar mass cut 1×10^9. Middle panels: Number of neighbors within radii of 500 kpc and mass cut 1×10^9. Right panels: Number of neighbors within radii of 500 kpc and mass cut 5×10^9. The $K-S$ test is applied for samples of F and W disks. The dashed lines correspond to the mean values of each sample, and the solid line corresponds to the smooth continuous approximation of the underlying distribution.

In the upper panels of Fig. 5.4.1 we show the distribution of the number of neighbors of each galaxy within a sphere of fixed radius. In each panel, we highlight the selection obtained when using $\max(A_1) = 0.3$ from the analysis made in Section 5.3.3. We rename the flat disks as F_{A_1} (cyan) and the warped disks as W_{A_1} (red). In addition, we include the mean value of each subsample as $\bar{x}_{neigh,F_{A_1}}$ and $\bar{x}_{neigh,W_{A_1}}$, for F_{A_1} and W_{A_1} disks, respectively. The stellar mass cut (m_{cut}) indicates that we only consider neighbors with stellar masses larger than the mass cut value, where the total mass corresponds to the sum of all subhalo particles. In the bottom panels, we present the cumulative distribution functions of each of the neighbor distributions. In the upper right in each panel, we indicate the value of the p-value when the $K-S$ test is applied to the subsamples of disks F_{A_1} and W_{A_1}.

The left upper panel shows the results obtained when the number of neighbors within 250 kpc with a mass cut $m_{cut} = 1 \times 10^9$ are considered. In this case, we can see F_{A_1} disks show fewer neighbors ($\bar{x}_{neigh,F_{A_1}} = 7.27$) than W_{A_1} disks ($\bar{x}_{neigh,W_{A_1}} = 10.19$). It is possible to distinguish both subsamples.

To confirm that the samples do not come from the same distribution, we apply the $K-S$ test to the cumulative functions of each subsample. In this case, the value of the $p-$value is $p_{F_{A_1}-W_{A_1}} = 9.4 \times 10^{-6}$, which allows us to reject the null hypothesis,

i.e., both distributions do not come from the same distribution. As a preliminary result, we can say that warped disks live in a denser environment than flat disks, increasing the probability of close encounters with neighbors.

In the middle and right panels, we show the results obtained when considering the number of neighbors within 500 kpc and $m_{cut} = 1 \times 10^9$ and $m_{cut} = 5 \times 10^9$, respectively. Unlike what was found in the left panel, in these cases, it is not possible to distinguish a clear difference between the distribution of F_{A_1} and W_{A_1} disks. The mean values are very close and when observing the cumulative function for both cases, we notice that the curves are very close. By applying the $K - S$ test for both mass cuts, where $p_{F_{A_1} - W_{A_1}} = 0.38$, and $p_{F_{A_1} - W_{A_1}} = 0.63$ respectively, indicating that we can not rule out that the samples come from the same distribution.

The study of neighbors allows us to infer that, as expected, the number of neighbors that influence the formation of galaxy vertical perturbations is directly related to the volume considered. Within a smaller volume, (in this case, with a radius of 250 kpc), the perturbed galaxies present a greater number of neighbors. Therefore, the chances of close encounters between the satellite galaxies and the host galaxy increase.

We now focus on the subsample of only central galaxies. This sample contains 65 objects.
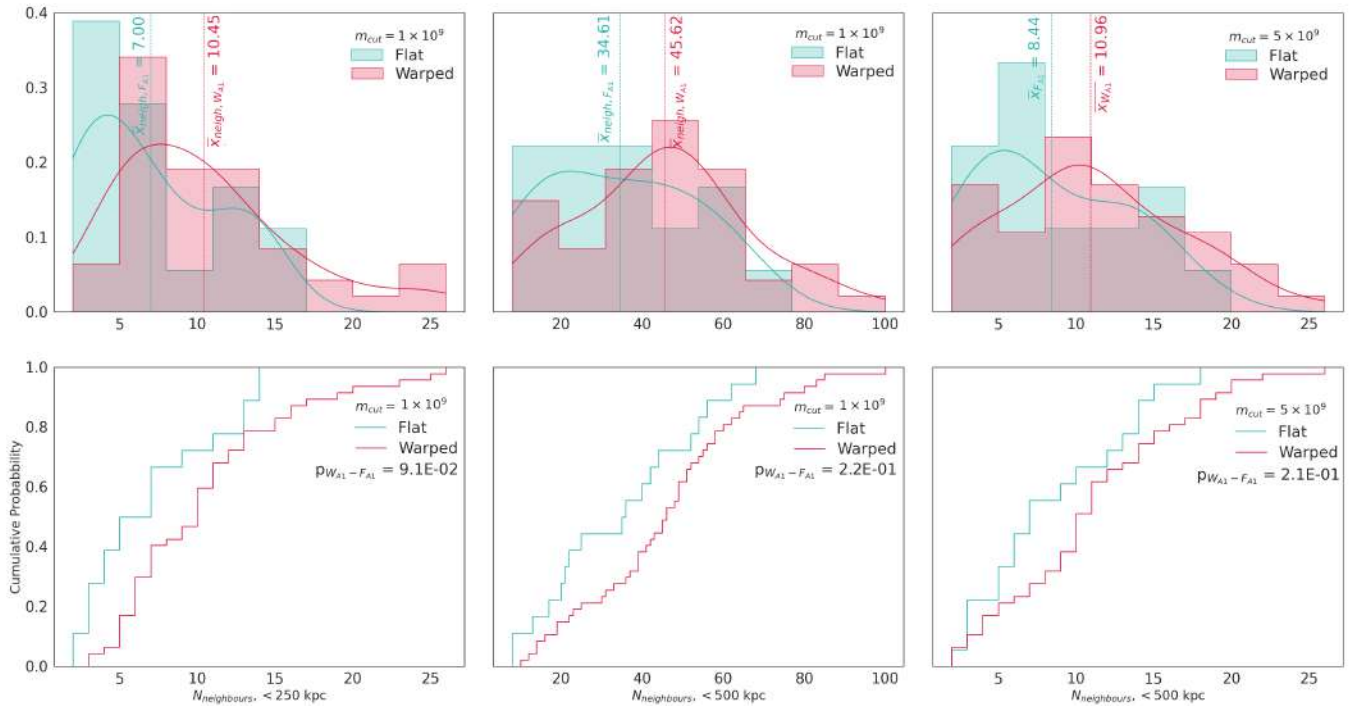
Figure 5.4.2: As in Fig. 5.4.1 but only considering central galaxies

After performing a comprehensive analysis, we have observed in the upper left panel of Fig. 5.4.2 that it is possible to distinguish between F_{A_1} and W_{A_1} disks for a volume of 250 kpc with a mass cut $m_{cut} = 1 \times 10^9$. However, this discrepancy is not significant enough to reject the null hypothesis through the $K - S$ test. This shows a difference from the total sample shown in Fig. 5.4.1, where W_{A_1} disks have a larger number of neighbors than F_{A_1} disks in the same volume.

On the other hand, when considering a larger volume of 500 kpc and two mass cuts ($m_{cut} = 1 \times 10^9$ and $m_{cut} = 5 \times 10^9$) in the upper center and right panels of Fig. 5.4.2, we observe a different trend from what was observed considering the total sample in Fig. 5.4.1. Although the $K - S$ test cannot distinguish between the two different samples, the F_{A_1} disk galaxies were found to have fewer neighbors than the W_{A_1} disk galaxies. This finding is in stark contrast to what was observed in the total sample for the same volume and mass cut.

As general results of the study of neighbors of the sample of type-MW/M31 mass galaxies, we see that within a volume of 250 kpc (approximately a virial radius for this object mass range) the galaxies that reveal vertical perturbations are directly proportional to the number of neighbors. When considering neighbors at further distances the signal disappears, indicating that those further objects do not play a significant role in setting the present-day structure of galaxies. When considering only

central galaxies within their subhalos, we note that the trend changes when we consider the volume of 250 kpc where the number of neighbors does not seem to play a determining role in the appearance of vertical perturbations. However, when considering larger volumes, the perturbed central galaxies would be in denser environments, increasing the probability of interaction with neighbors.

5.4.2 Overdensity parameter

Another parameter to explore the environment of our sample is the galaxy overdensity (Gargiulo et al., 2022) which is defined as follows

$$1 + \delta = \frac{P}{P_{median}} \tag{5.4.1}$$

where P corresponds to the volumetric density of galaxies at the position of ith galaxy MW/M31-like galaxy defined as:

$$P(\mathbf{r}_i) = \frac{3k}{4\pi \sum_{j=1}^{k} d_{ij}^3} \tag{5.4.2}$$

In this case, $\mathbf{r}_i$ is the position of the ith MW/M31-like galaxy, d_{ij} corresponds to the distance between ith MW/M31-like galaxy and its jth neighbor with mass above given mass cut (m_{cut}), and k is the number of neighbors considerate. P_{median} corresponds to the median volumetric density of galaxies with the adopted m_{cut} in the cosmological volume of the simulation. For this analysis, the $(1 + \delta)$ is calculated for different values of k and m_{cut}.
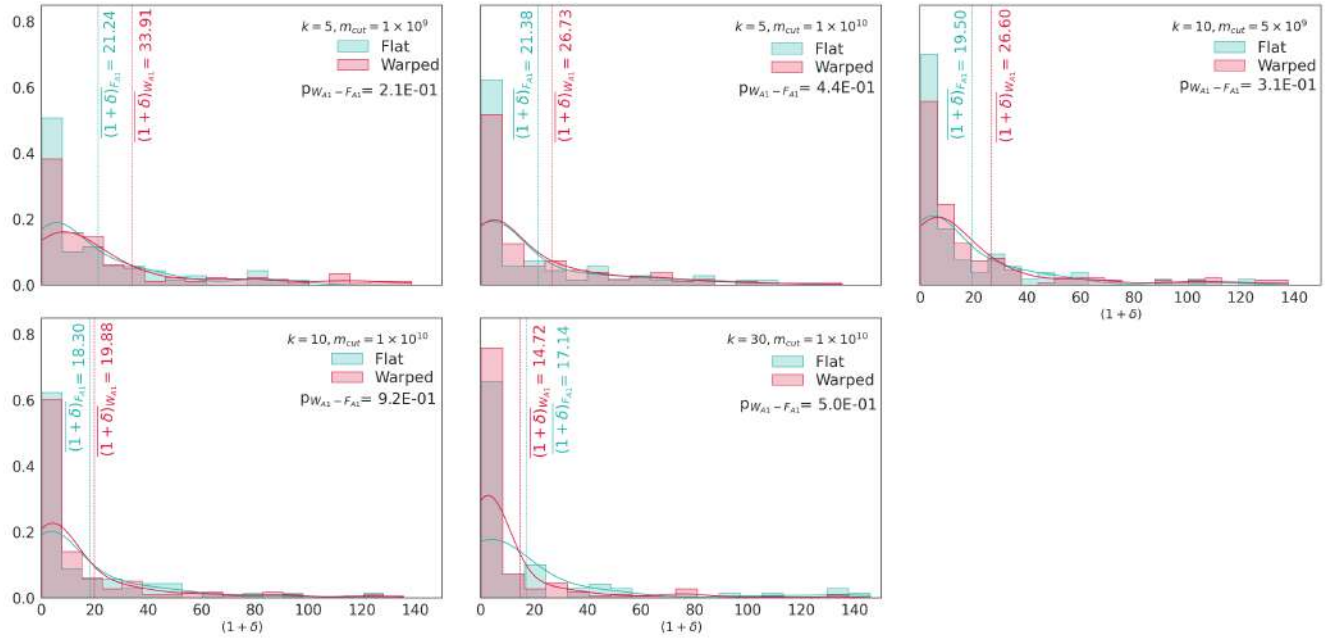
Figure 5.4.3: Distribution of the overdensity parameter $(1 + \delta)$ considering different numbers of neighbors (k) and mass cuts (m_{cut}) at $z = 0$. The disks are distinguished between flat (F_{A_1}) and warped (W_{A_1}) disks according to the parameter $\max(A_1) = 0.3$. The dotted lines correspond to the mean values of each sample, and the solid line corresponds to the smooth continuous approximation of the underlying distribution.

In Fig. 5.4.3, we show the distribution of our sample of the overdensity parameter $(1 + \delta)$, distinguishing between flat and warped disks according to $\max(A_1) = 0.3$.

In the upper left panel, $(1 + \delta)$ is calculated considering five neighbors with a cutoff mass $m_{cut} = 1 \times 10^9$ and $k = 5$. For the sample of flat disks, the mean value reaches $\overline{1 + \delta_{F_{A_1}}} = 21.24$, which is lower than that found for vertically perturbed disks,

$\overline{1+\delta}_{W_{A_1}} = 33.91$. This indicates that the neighbors of warped disks are at a shorter distance from the galaxy, so they are more likely to interact and influence the disk's structure.

By increasing the mass cut $m_{cut} = 1\times10^{10}$ and $k = 5$, that even though perturbed disks continue to show smaller means, the difference between the means of both distributions decreases.

When analyzing the overdensity considering ten neighbors with a $m_{cut} = 1\times10^9$ in the upper right panel, the flat and warped disk samples belong to the same distribution according to the $K-S$ test applied. As in the previous cases, the mean value for flat disks is lower than for warped disks, which means that the neighbors are further away from the galaxy for warped disks.

By increasing the cut mass ($m_{cut} = 1\times10^{10}$) and $k = 10$ in the bottom left panel, we notice that the difference between the mean values of both samples is narrower, that is, the more massive neighbors are further away from the galaxy.

An inflection point is found when calculating an overdensity with a larger number of neighbors, $k = 30$, and a cut mass m_{cut} = 1×10^{10} in the bottom middle panel. The mean values are inverted, i.e., the mean value of the flat disks ($\overline{1+\delta}_{F_{A_1}} = 17.14$) is greater than that of the warped disks ($\overline{1+\delta}_{W_{A_1}} = 14.72$), so when considering more galaxies, the neighbors are closer to the flat disks than the warped disks. In Fig. 5.4.3, according to the $K-S$ test in all the cases mentioned above, we cannot reject the null hypothesis. This result is expected. The volumes required to enclose this number of satellites are much larger than before and, as previously discussed, satellites at such large distances are not expected to have an impact on the morphology of a host.

In the analysis of the overdensity of the galaxy environment, we found that warped galaxies typically have closer neighbors than those with flat or slightly perturbed disks. This together with the results shown in the previous Section, show that vertically perturbed galaxies typically have a larger number of intermediate-mass satellites spatially distributed at shorter distances.

5.5 Relationship between galaxies with vertical perturbations at $z = 0$ with recent interaction history of the galaxy

According to the classification of galaxies in Section 5.3.1 as a flat disk (F), the simple warp (S), and corrugation pattern (C), we found 36% for F disks, 51% for S disks, and 13% as C disks. In Section 5.3.2, according to the $\max(A_1) > 0.3$ criteria, we found 73 as F_{A_1} disk corresponding to 28% and 181 W_{A_1} disk equivalent to 72%.

Here we study how the present-day vertical structure is related to recent galaxy interaction history. For this, we focus our analysis only on the central galaxies from our sample of MW/M31-type galaxy models and their respective satellites in the last 6 Gyr. As previously discussed, one of the possible disturbing agents of galactic disks is the torque exerted by interacting satellites. In this Section, we analyze this perturbation mechanism for the subsample of central galaxies, considering the tidal field effect as a function of lookback time.

The effect of the tidal field exerted by the satellites on the host galaxy is estimated through $|\alpha_{sat}| = G\,M_{sat}\,R^{-3}$, where M_{sat} is the mass of the satellite and R is the distance to the host. This indicates that the strength of the tidal field grows with satellite mass and decreases with satellite galactocentric distance.

In Fig. 5.5.1, we show, for each simulated galaxy, the tidal field exerted on the host by its ten most massive satellites at each time on the stellar disk for a representative sample of 65 central galaxies. The color coding indicates the mass of each satellite at the corresponding time. Triangles represent higher tidal field values than the Y-axis limit.

Following the same scheme as the analysis in the previous Section 5.3.1, the upper panels correspond to flat or unperturbed disks, the middle panel shows simple warps, and the bottom panels correspond to the disks with corrugation patterns. In central galaxies, the number of flat galaxies is 25, equivalent to 38% of the sample; disks with simple warp are 33, equivalent to 51%; and corrugation patterns are seven galaxies corresponding to 11%.

We see that we have different scenarios in the case of flat disks. We find that $\sim 30\%$ of these flat disks have not experienced any significant close interaction during the last 6 Gyr of evolution. On the other hand, most reminder disks only experienced interactions with satellites less massive than $M_{min} = 10^{10} M_{\odot}$. Those few flat disks that did experience massive interactions did so more than 4 Gyr ago. This result agrees with that obtained with another set of Auriga cosmological simulations galaxies in Gómez et al. (2017). In the case of the vertically perturbed disks (middle and bottom panels), we find diversity in recent interactions. Only three galaxies ($\sim 10\%$) do not have tidal interactions with satellites within the time period. Those perturbed disks observed at the present day could result from another mechanism, such as misaligned cold gas accretion, as mentioned in Section 1.5. In general, the majority of warped disks have tidally interacted with a massive companion. For simple warp disks, in the middle panels, 58% of the sample had violent interaction with massive satellites ($> M_{min}$) in the last 3 Gyr. These
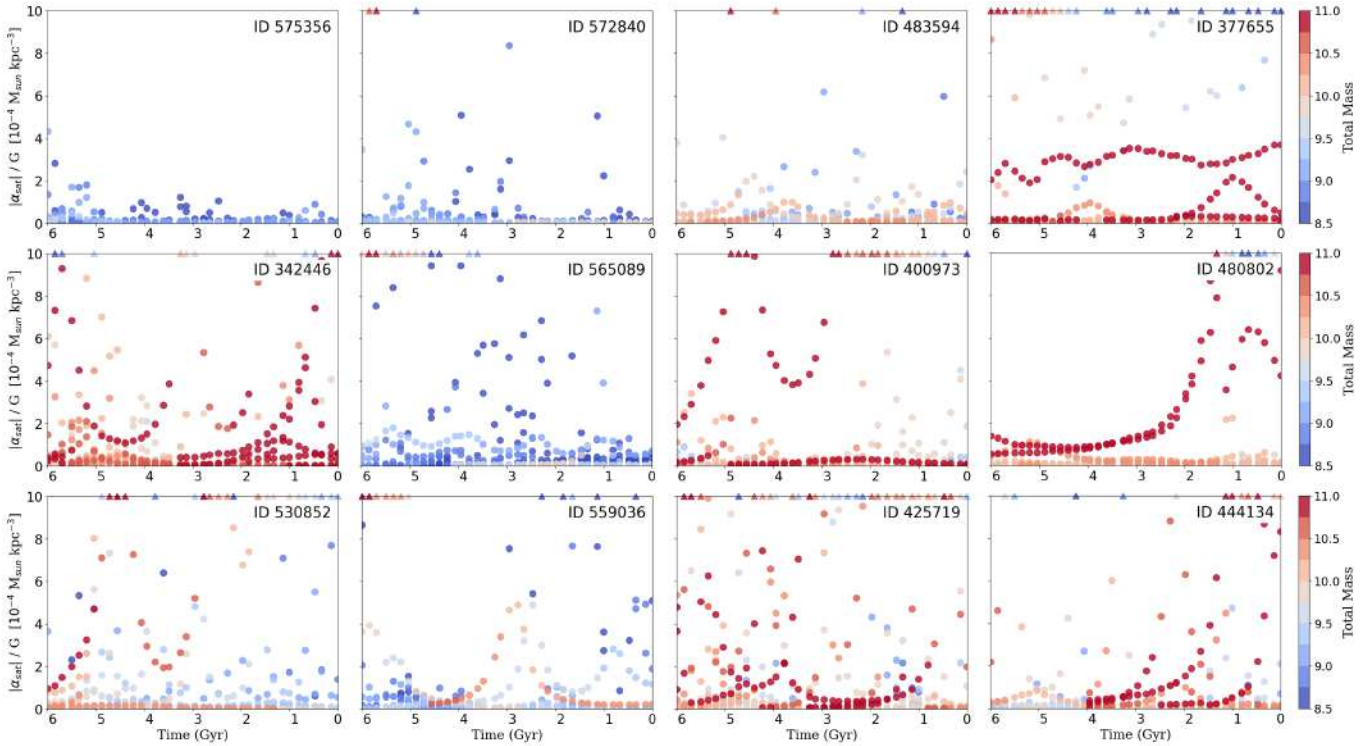
Figure 5.5.1: The tidal field exerted on each host by its ten most massive satellites as a function of time. Points are color-coded according to the mass of each satellite at the corresponding time. Triangles indicate tidal field values that are above the Y-axis limit.

can be seen in the examples shown in the middle panels in Fig. 5.5.1 in the first column, we can see that the present-day host galaxy is interacting with two massive satellites of the order of $\sim 10^{11} M_\odot$. In the second column in the middle panels, another galaxy with a warped disk shows a last strong tidal interaction 3 Gyr ago with various satellites in a wide mass range and, in particular, a violent interaction with two massive companions ($10^{11} M_\odot$). Other examples of warped disks (third and fourth column in the middle panels) show that the host galaxy undergoes violent interactions in short periods of time (< 1 Gyr) with satellites of masses greater than M_{min}.

Finally, in the disks with corrugation patterns, shown in the lower panels, we find a similar trend to simple warp disks. In particular, all host corrugated galaxy disks shown in the bottom panels in Fig. 5.5.1 experience violent interactions with satellites within the mass range $[10^{10} - 10^{10.5}]$ $M_\odot$ for almost the entire time period of 6 Gyr. In the first column of corrugated disks, we can see that the galaxy host has a close tidal encounter within small periods of time with massive satellites ($>$ $10^{10.5} M_\odot$). In the case of the second column, the galaxy shows tidal interaction with massive satellites 5 Gyr ago. On the other hand, for the third and fourth columns, the host galaxies have violently interacted with satellites of the order of $10^{11} M_\odot$ in the last Gyr.

In summary, within the flat disks, 28% have no interaction within 6 Gyr and, while 84% of the flat models has not interacted closely with any satellite more massive than $10^{11} M_\odot$ within the last 3 Gyr. Compared with flat disks, the warped disk, only 10% have no interaction within the analyzed period of time.

For disks with a simple warp, the close tidal encounter rate with massive satellites within the last 1 Gyr reaches 33%, while for corrugated disks, 43%. In the case of the last 3 Gyr period, the violent interaction fraction reaches 58% and 71% for simple and corrugated warp disks, respectively.

To complement the preliminary results of the study on the influence of satellites on central galaxies, we will work on analyzing the galaxies that are not central in their subhalo, which correspond to 186 galaxies. This will allow a complete quantification of how the tidal interaction of the satellites influences the host and the long-lived warp. This fully agrees with the results found in Gómez et al. (2017) using the Auriga simulated galaxies.

5.6 Conclusions

In this Chapter, we study vertical perturbations in MW/M31-type galaxies using a sample of late-type galaxies extracted from the TNG50 cosmological simulations. The sample was selected according to the mass and morphology of Milky Way and M31 galaxies, following Gargiulo et al. (2022) and Pillepich et al. (2021).

Our study involved a sample of 251 MW/M31-type galaxies. We rotated the galaxy disks to align them with the X-Y plane through an iterative calculation of the total angular momentum of the 20% youngest stars on each disk. This alignment process avoids detecting false vertical perturbations or warps. Following the methods outlined in Gómez et al. (2016) and Gómez et al. (2017), we constructed maps of mean height ($\langle Z \rangle$) and mass-weighted maps of vertical velocity ($\langle V_z \rangle$) for the entire sample. As described in Gómez et al. (2017), we classified the disks into three categories: flat, simple warp, and corrugation patterns, using the $\langle Z \rangle$ and $\langle V_z \rangle$ maps. For flat disks, the values of $\langle Z \rangle$ and $\langle V_z \rangle$ are close to zero. On the other hand, in the simply warped disks, we observed an anti-correlation between the distribution of $\langle Z \rangle$ and $\langle V_z \rangle$. For galaxies displaying corrugation patterns, studies such as those presented in Chapters 4 and 4 have found that the distribution of $\langle Z \rangle$ and $\langle V_z \rangle$ exhibit wave-like behavior, with values reaching above 60 km s^{-1}. The classification using the $\langle Z \rangle$ and $\langle Vz \rangle$ maps revealed that 36% of the simulated disks were classified as flat, while 64% were classified as warped, including both simple and corrugated disks. This proportion of each class of disks is in agreement with previous studies using HI samples and optical bands (García-Ruiz et al., 2002; Ann & Park, 2006) and with the results obtained in Gómez et al. (2017) using Auriga cosmological simulations (Grand et al., 2017).

To quantify the vertical structures of galactic disks, we use Fourier modes to analyze asymmetries (Quillen et al., 2011). To identify structures with various vertical perturbations, we focus on the $m = 1$ parameter (Bournaud et al., 2005; Saha et al., 2007; Ghosh et al., 2022). To quantify the disk's structures, we consider $m = 1$ between 0.3 and 1.2 R$_{opt}$. We observe that flat disks have a flatter $m = 1$ trend than the increasing profile seen in warped disks. However, it is difficult to separate radial profiles between disks with S-shaped warp and corrugation patterns. We set the max(A_1) parameter to 0.3 to distinguish between flat and warped disks and confirm this using the $K - S$ test. Later, we examine how the environment affects the formation and detection of vertical perturbations. We use the density of galaxies within a fixed radius and at $z = 0$ as the first parameter for our environmental analysis. We find that flat disks have fewer neighboring galaxies than S-shaped warped disks when considering a radius of 250 kpc and a stellar mass cut of $1 \times 10^9 M_\odot$. However, when we increase the radius to 500 kpc and vary the mass cut, we do not observe a significant difference in the number of neighboring galaxies for flat and simple warped disks. This could be due to the negligible effect of satellites at greater distances on the host galaxy's disk.

Another way to analyze the environment is by studying the overdensity of galaxies, as proposed by (Gargiulo et al., 2022). This is done by counting the number of neighboring galaxies within a fixed mass cut. We find that flat and warped disks have a similar distribution of overdensity. To further examine this, we consider the mean values of the overdensity for each disk type, where we observe that flat disks have satellites at a greater distance than disks with warped disks. However, when we consider a sample of 30 neighbors, we notice that the mean values are inverted; flat disks have their neighbors closer than warped disks.

We investigate the relationship between the structure of a disk at $z = 0$ and its recent interaction history by focusing on the central galaxies of subhalos. We select the ten most massive satellites that have interacted with these central galaxies within the last 6 Gyr and calculate the tidal field exerted on each central galaxy by these satellites. Our preliminary results show that different interaction scenarios with satellites affect the structure of disks. For example, we found that 30% of galaxies with unperturbed disks have not had close interactions with their satellites in the last 6 Gyr. Additionally, 84% of flat disks had no significant interactions with massive companions $\sim 10^{11} M_\odot$ in the last 3 Gyr. In contrast, warped disks have had significant interactions with satellites of wide mass ranges, particularly violent tidal encounters with massive satellites $> 10^{10} M_\odot$ in short periods of time. For example, a third of the disks with an S-Shaped warp had a tidal interaction with a massive satellite in the last 1 Gyr compared to the 43% observed in the disks with a corrugation pattern. In the last 3 Gyr, the fraction of S-Shaped warped disks and with corrugation patterns that interact with mass satellites increased to 58% and 70%, respectively.

While a small fraction of warped disks ($\sim 10\%$) have no tidal interaction at 6 Gyr, it is important to consider other potential mechanisms that may contribute to the formation of these disks. These mechanisms may include misaligned cold gas accretion, as previously discussed in Section 1.5. This is supported by the findings of Urrejola-Mora et al. (2022) (see Chapter 4), we observed that even isolated galaxies (such as NGC 3344) can exhibit corrugation patterns, which aligns with the results obtained through simulations in this Chapter. This serves as a crucial example for understanding the formation of vertical disturbances and the recent interaction history of galaxies.

As work to complement this result, it will be to analyze the interaction of the 186 galaxies that are satellites within the subhalo.

This may give us more information if the trend is reflected in the central galaxies. This fully agrees with the results found in Gómez et al. (2017) using the Auriga simulated galaxies.

The use of a large sample of simulated galaxies with masses similar to that of the MW/M31-mass galaxy can provide valuable insights into understanding the dynamics of host galaxies and their interactions with satellites. Specifically, analyzing these simulations can help uncover the mechanisms responsible for inducing the vertical perturbations commonly observed in present-day galactic disks. By quantifying these perturbations, we can gain a better understanding of the interaction history of galaxies with their environment.

Chapter 6

Concluding Remarks and Future Perspectives

Several studies have been conducted to understand the complex structure of the Galactic disk, which is more intricate than a traditional S-shape structure (López-Corredoira et al., 2002; Momany et al., 2006; Slater et al., 2014; Price-Whelan et al., 2015; Xu et al., 2015; Antoja et al., 2018; Gaia Collaboration et al., 2021). In particular, the Milky Way disk is observed to have a displacement of the stellar component above and below the mid-plane (as studied by Widrow et al., 2012; Widrow et al., 2014) with an amplitude that grows with radius (Xu et al., 2015). The recent survey of the Milky Way using GAIA DR2 (Gaia Collaboration et al., 2018) also reveals that Sagittarius dwarf galaxy is one of the most likely perturbers (e.g. Gómez et al., 2013; Antoja et al., 2018; Laporte et al., 2018b,a, 2020; Gaia Collaboration et al., 2021; McMillan et al., 2022; Antoja et al., 2022; Ramos et al., 2022).

Previous studies, including those by García-Ruiz et al. (2002); Ann & Park (2006); Narayan et al. (2020), have found that approximately 70% of nearby edge-on late-type galaxies have warped disks. This finding is consistent with the results of the Auriga project (Gómez et al., 2017), which found that around three-quarters of simulated galaxies had warp structures. Among these, half had an S-shaped warp, while the rest had more complex structures as corrugation patterns. This suggests that warped disks are relatively common in late-type galaxies. While it is possible to detect corrugation patterns (characteristic of warped disks) in nearly face-on galaxies using line-of-sight velocity measurements, such studies were limited in scope. In a sample of four galaxies, Sánchez-Gil et al. (2015) detected corrugation patterns in two out of four galaxies using long-slit spectroscopic observations. However, these results can be misleading as they can be confused with local disturbances, such as fountain flows, and would not correspond to global, coherent, and extended patterns.

The current understanding of the frequency, causes, environmental influences, and longevity of vertical perturbations in low-inclination galaxies in the local universe raises several questions. These include: How prevalent are these perturbations in low-inclination galaxies compared to those observed in edge-on galaxy samples? What processes are responsible for the formation of these perturbations? How do the galaxy's surroundings influence the presence and characteristics of these perturbations? Are these perturbations transient or long-lasting structures in the galaxy? These questions highlight the need for further research to fully understand the nature and dynamics of vertical perturbations in low-inclination galaxies.

This thesis represents a first step towards addressing these questions. It comprises two main sections: the first section conducts a kinematic analysis of the H_α velocity fields of galaxies using Fabry-Perot interferometry, while the second section examines simulated galaxies from Illustris TNG50 to investigate the properties and origins of vertical perturbations and the effect of the environment on their formation.

The kinematic analysis of galactic disks is performed using H_α data cubes and the Fabry-Perot interferometer, which allows for a large field-of-view (FoV) and the detection of global patterns in the disks of galaxies. As the main motivation of this thesis is the in-depth examination of the late-type galaxy VV304a. As a member of the VV304 pair, VV304a interacts with its companion galaxy VV304b and has similar characteristics to the Milky Way, making it an ideal candidate for studying vertical perturbations.

The analysis of VV304a is approached from three perspectives: observational data, numerical modeling, and cosmological simulations. In the case of observational data, we derived a H_α residual velocity (V_{res}) map, after generating an axisymmetric model of the velocity field, which reveals strong, coherent, global patterns across the disk consistent with corrugation patterns. The amplitude of these patterns can reach velocities up to 50 km s^{-1}. In order to determine if the patterns observed in the H_α

V_{res} field are caused by off-plane motions, the analysis is supplemented by a series of test-particle simulations. Parameters similar to those of the Milky Way are considered to investigate whether the vertical perturbations observed in VV304a are a result of in-plane perturbations caused by the spiral structure or the influence of a bar. However, even when considering a density contrast of the spiral relative to the disk background density of 100%, 200%, 600% and 1000%, in addition to the influence of a bar, the resulting velocity perturbations do not exceed 15 km s^{-1}. Therefore, these in-plane flows can not explain the flows observed in the V_{res} map of VV304a, and the simulation results based on in-plane perturbations generated by axisymmetric disk features do not match the observations.

Finally, two simulated galaxies, Aq-C4 and Au25, were analyzed. These have similar features to VV304a and have undergone recent tidal interaction, are used to analyze the V_{res} fields in two cases: weak and strong mode $m = 2$. The results show that the V_{res} of Au25 reproduces the V_{res} patterns of VV304a, with amplitudes of around 50 km s^{-1}. This suggests that the corrugation pattern in the disk of VV304a is likely caused by its interaction with its companion galaxy VV304b.

In Chapter 4, we present the WiNDS sample, a new collection of nearby late-type galaxies with low inclinations. The total sample includes a total of 40 observed galaxies comprising new observations and archival data extracted from the GHASP, SINGS-H$_\alpha$, VIRGO-H$_\alpha$, and HRS-H$_\alpha$ surveys. The WiNDS sample has a high spectral resolution at the H-alpha rest wavelength, with a resolving power of $R_P \sim 10000$, and large spatial coverage, with a velocity sampling precision as low as 3 km s^{-1}. This translates to a resolution of 6 km s^{-1}, making these galaxies ideal for studying the kinematics of ionized gas in galactic disks. The galaxies in the WiNDS survey and the new observations correspond to 48 galaxies and are listed in Table 2.3.1.

To identify bending modes, such as warps or corrugation patterns, in galactic disks, we derived V_{res} maps for each galaxy in the sample. The complete WiNDS sample, comprising of 40 galaxies, was analyzed. After deriving the residual maps, we selected galaxies that met specific criteria to identify clear signatures of perturbations. First, we focused on objects that have a wide H$_\alpha$ coverage $\geq 0.7R_{opt}$ to globally explore the kinematics of the disks. Second, we targeted galaxies with V_{res} amplitudes greater than 10 km s^{-1}, which increases the confidence of observing perturbations in low-inclination disks that are not the result of the axisymmetric components of the galaxies. Finally, we searched for perturbations in the V_{res} fields that have global and coherent velocity flows, avoiding local and discrete perturbations that could be linked to, e.g., fountain flows. We emphasize that our selection criteria cannot confirm nor rule out the presence of vertical perturbations in our disks.

From WiNDS sample, approximately 20% show clear signatures of global and coherent perturbations. Including results from VV304a, previously described, brings this number to 22%. However, some of our observations may not have been sufficient or adequate to identify velocity perturbations on the disk outskirts, and this percentage could be higher. In fact, only 70% of the galaxies in the WiNDS sample have good H$_\alpha$ coverage. When considering this subset, the fraction of vertically perturbed galaxy candidates increases to 32%. Candidate galaxies displaying evidence of vertical perturbations are found in a variety of environments. Six of these candidates are currently interacting with a satellite galaxy or belong to a group, suggesting that their perturbations may be a direct result of environmental interactions. The remaining candidates are considered isolated, and their perturbations may be caused by previous minor mergers or misaligned cold gas accretion. Further study is necessary to determine the specific origins of these perturbed velocity fields.

The percentage of low inclination galaxies with detected velocity flows (approximately 20%) is lower than expected for the presence of vertical perturbations in disk galaxies. This discrepancy may be due to several factors. One reason is that a significant portion ($\sim 30\%$.) of the galaxies in the sample did not have adequate HH$_\alpha$ coverage, either due to patchy or concentrated emission within the inner regions of the galaxy. This limits the ability to globally study the kinematics of the disk, particularly in the outer regions where warps and vertical perturbations are more likely to occur. Additionally, the weather conditions during approximately 12.5% of the observations were not optimal, resulting in insufficient data to accurately resolve the velocity fields. Given these limitations, it is not surprising that fewer galaxies were found to have kinematic perturbations consistent with a vertically perturbed disk compared to previous studies.

The second goal of this thesis was to study vertical perturbations in simulated galaxies. We analyzed MW/M31-type galaxies using a sample of late-type galaxies extracted from the TNG50 cosmological simulations. The sample comprises 251 disk-type galaxies with an MW/M31-type mass range. Following the method of Gómez et al. (2017), mass-weighted mean height, $\langle Z \rangle$, and mean vertical velocity $\langle V_z \rangle$ maps were created and visually classified into three categories: flat, S-shaped, and corrugation patterns disks. The results show that 36% of the disks were classified as flat, while 64% were classified as warped, including both S-shaped and corrugated disks. For galaxies displaying corrugation patterns, studies have found that the distribution of $\langle Z \rangle$ and $\langle V_z \rangle$ exhibit wave-like behavior. These proportions are in agreement with previous studies using HI samples (García-Ruiz et al., 2002) and optical bands (Ann & Park, 2006) and with the results obtained in Gómez et al. (2017) using Auriga cosmological simulations (Grand et al., 2017).

To measure the vertical disturbances in the simulated disk sample, we use the $m = 1$ Fourier mode to analyze disk asymmetries within the range of 0.5 to 1.2 $R_{opt} = 0.3$ (Bournaud et al., 2005; Saha et al., 2007; Quillen et al., 2011; Ghosh et al., 2022). The $m = 1$ profile along the radius demonstrates that flat disks exhibit a flatter profile compared to warped disks. However, it is not easy to distinguish between profiles of disks with an S-shaped warp and corrugation patterns. Therefore, we establish a threshold of $\max(A_1) = 0.3$ to differentiate between flat and warped disks, which is supported by a $K - S$ test.

We analyzed the environments of galaxies at $z = 0$ based on their number of neighbors within a fixed radius. Our findings indicate that flat disks have fewer neighboring galaxies than S-shaped, warped disks when considering a radius of 250 kpc and a stellar mass cut of $1 \times 10^9 M_\odot$. However, when we increased the radius to 500 kpc and varied the mass cutoff, we did not observe a significant difference in the number of neighboring galaxies for flat and S-shaped warped disks. This may be due to the minimal impact satellites at these large distances have on the disk of the host galaxy. Additionally, we also analyzed the environment using the overdensity of galaxies approach proposed by Gargiulo et al. (2022), which considered a fixed number of neighbors and a mass cutoff. We find that flat disks have neighbors at a greater distance than warped disks. However, when we consider a sample of 30 neighbors, we notice that the mean values are inverted; flat disks have their neighbors closer than warped disks. Finally, we examined the relationship between the structure of the disk at $z = 0$ and the recent interaction history of central galaxies in subhalos. We focused on the ten most massive satellites that have interacted with these galaxies within the last 6 Gyr. We estimated the tidal field exerted by each galaxy on its satellites. Our main findings indicate that 30% of galaxies with flat or unperturbed disks have not had close encounters with their satellites in the last 6 Gyr. Additionally, 84% of this type disk had no significant interaction with massive partners ($\sim 10^{11} M_\odot$) in the last 3 Gyr. Those few flat disks that did experience massive interactions did so more than 4 Gyr ago. For warped disks, we found a significant interaction with satellites of a wide mass range, particularly with satellites of masses $\geq 10^{10} M_\odot$ in short periods of time. We also found that one-third of the S-shaped warp disks interacted with a massive satellite in the last 1 Gyr, with this percentage increasing to 43% for disks with corrugation patterns. When considering a broader time range, in the last 3 Gyr, the fraction of S-shaped disks and corrugation patterns that have interacted with massive satellites increases to 58% and 70%, respectively. Compared with unperturbed disks, we observed that about 10% of the warped disks did not have a tidal interaction during 6 Gyr. Therefore, it is important to consider other mechanisms, such as misaligned cold gas accretion, that may contribute to the formation of the vertical structure of these disks. This is crucial, as we found in a WiNDS survey where an isolated galaxy, NGC 3344, has a clear corrugation pattern at present-day (Urrejola-Mora et al., 2022) (see Chapter 4). Our results with TNG50 and H_α data cubes are consistent with this finding.

The analysis presented in this Thesis represents the foundations of our efforts to characterize the onset of vertical disk perturbation and their connection with the galaxy's recent interaction history. Several different avenues for follow-ups arise as a result of this analysis.

In this thesis, 20% of the galaxies in the WiNDS sample show vertical perturbations in the galactic disks, called candidate galaxies in this work. We aim to determine the cause of perturbations in galactic disks. We plan to examine the surroundings of our candidate galaxies for evidence of interaction or perturbation, even those that are currently considered isolated. This can be done through a more extensive analysis beyond the 500 kpc already studied using SDSS. Moreover, analysis of the kinematics and neutral hydrogen distribution can help determine interaction by revealing the decoupling of the accumulated material with respect to the material of the pre-existing galaxy.

One of our main goals is to determine the frequency with which late-type galaxies display vertical patterns (warp-shaped or corrugation). We have eight H_α data cubes not analyzed yet, which will be added to our sample following the procedure described in Section 4.3. Our purpose is to search for a larger number of galaxies to complement what has been done with WiNDS and to analyze the frequency of vertical patterns in the local universe. We will also re-observe targets with poor data quality due to weather conditions. To further improve our study, we will also increase observation time for some galaxies and search for new targets to observe using the Fabry-Perot interferometer, expanding both the mass and magnitude range of our sample.

So far, we have only analyzed the gaseous component of the galaxies observed in the WiNDS sample. It is thus of great interest to study the behavior of the stellar component in galaxies that show vertical perturbations using H_α velocity fields. Does the stellar component show vertical disturbances? If so, how much does the amplitude of the stellar component vary with respect to the gaseous component? Our interest lies in determining if the younger stellar population has stronger vertical patterns than the older population, as suggested by Gómez et al. (2017), a clear indication of a tidal origin for the pattern. Do observed galaxies show the same trend? Is there a phase shift in the gaseous component concerning the stellar component? Among the alternatives to observe the vertical component of the candidate galaxies is to use the long-slit spectroscopy tech-

nique in the regions of the disk where vertical perturbations have been previously detected. As mentioned in this work, vertical perturbations are global, coherent, and extended in galactic disks. This is fundamental to cover a significant part of the disk with long-slits so that they cannot be considered local patterns, such as fountain flows. Finally, we seek to complement our study carried out on the gaseous and stellar components with available databases such as MUSE and ALMA. This is through the study of regions where corrugation patterns were identified in H_α in this Thesis.

For our sample of galaxies from TNG50, we will investigate the recent interaction history of non-central galaxies (as outlined in Section 5.5). Additionally, we will closely examine other mechanisms beyond satellite interaction that can cause vertical perturbations, such as warped disks, if they have not had any tidal interaction in the past 6 Gyr.

Bibliography

Alfaro E. J., Pérez E., González Delgado R. M., Martos M. A., Franco J., 2001, ApJ, 550, 253

Amram P., Boulesteix J., Georgelin Y. M., Georgelin Y. P., Laval A., Le Coarer E., Marcelin M., Rosado M., 1991, The Messenger, 64, 44

Amram P., Plana H., Mendes de Oliveira C., Balkowski C., Boulesteix J., 2003, A&A, 402, 865

Amram P., Mendes de Oliveira C., Plana H., Balkowski C., Hernandez O., 2007, A&A, 471, 753

Ann H. B., Park J. C., 2006, NewA, 11, 293

Antoja T., et al., 2018, Nature, 561, 360

Antoja T., Ramos P., López-Guitart F., Anders F., Bernet M., Laporte C. F. P., 2022, A&A, 668, A61

Araki S., 1985, PhD thesis, Massachusetts Institute of Technology

Aumer M., White S. D. M., Naab T., Scannapieco C., 2013, MNRAS, 434, 3142

Bailin J., 2003, ApJL, 583, L79

Barbosa C. E., et al., 2015, MNRAS, 453, 2965

Begeman K. G., 1987, PhD thesis, -

Begeman K. G., 1989, A&A, 223, 47

Bianchi S., et al., 2012, MNRAS, 426, 3225

Binggeli B., Sandage A., Tammann G. A., 1985, AJ, 90, 1681

Binggeli B., Popescu C. C., Tammann G. A., 1993, A&AS, 98, 275

Binney J., 1992, ARA&A, 30, 51

Binney J., Jiang I.-G., Dutta S., 1998, MNRAS, 297, 1237

Bland-Hawthorn J., Tepper-García T., 2021, MNRAS, 504, 3168

Bland-Hawthorn J., et al., 2019, MNRAS, 486, 1167

Blanton M. R., Moustakas J., 2009, ARA&A, 47, 159

Boselli A., Fossati M., Gavazzi G., Ciesla L., Buat V., Boissier S., Hughes T. M., 2015, A&A, 579, A102

Bournaud F., Combes F., Jog C. J., Puerari I., 2005, A&A, 438, 507

Briggs F. H., 1986, ApJ, 300, 613

Briggs F. H., 1990, ApJ, 352, 15

Burke B. F., 1957, AJ, 62, 90

Canzian B., 1993, ApJ, 414, 487

Carlin J. L., et al., 2013, ApJL, 777, L5

Cautun M., et al., 2020, MNRAS, 494, 4291

Cen R., Miralda-Escudé J., Ostriker J. P., Rauch M., 1994, ApJL, 437, L9

Chemin L., et al., 2006, MNRAS, 366, 812

Cox D. P., Gómez G. C., 2002, ApJS, 142, 261

Cox A. L., Sparke L. S., van Moorsel G., Shaw M., 1996, AJ, 111, 1505

Cui X.-Q., et al., 2012, Research in Astronomy and Astrophysics, 12, 1197

Cui Y., Xiang Y., Rong K., Feris R., Cao L., 2014, in IEEE Winter Conference on Applications of Computer Vision. pp 213–219, doi:10.1109/WACV.2014.6836098

D'Onghia E., Madau P., Vera-Ciro C., Quillen A., Hernquist L., 2016, ApJ, 823, 4

Daigle O., Carignan C., Amram P., Hernandez O., Chemin L., Balkowski C., Kennicutt R., 2006a, MNRAS, 367, 469

Daigle O., Carignan C., Hernandez O., Chemin L., Amram P., 2006b, MNRAS, 368, 1016

Davis M., Efstathiou G., Frenk C. S., White S. D. M., 1985, ApJ, 292, 371

DeBuhr J., Ma C.-P., White S. D. M., 2012, MNRAS, 426, 983

Debattista V. P., Sellwood J. A., 1999, ApJL, 513, L107

Dicaire I., et al., 2008, MNRAS, 385, 553

Djorgovski S., Sosin C., 1989, ApJL, 341, L13

Dressler A., 1980, ApJ, 236, 351

Drimmel R., Smart R. L., Lattanzi M. G., 2000, A&A, 354, 67

Epinat B., et al., 2008a, MNRAS, 388, 500

Epinat B., Amram P., Marcelin M., 2008b, MNRAS, 390, 466

Fathi K., et al., 2008, ApJL, 675, L17

Font J., et al., 2011, ApJL, 740, L1

Frenk C. S., White S. D. M., Davis M., Efstathiou G., 1988, ApJ, 327, 507

Freudenreich H. T., et al., 1994, ApJL, 429, L69

Gaia Collaboration et al., 2018, Astronomy & Astrophysics, 616, A11

Gaia Collaboration et al., 2021, Gaia Early Data Release 3: The Galactic anticentre (arXiv:2101.05811)

García-Ruiz I., Sancisi R., Kuijken K., 2002, A&A, 394, 769

Gargiulo I. D., et al., 2022, MNRAS, 512, 2537

Garrido O., Marcelin M., Amram P., Boulesteix J., 2002, A&A, 387, 821

Garrido O., Marcelin M., Amram P., Boissin O., 2003, A&A, 399, 51

Garrido O., Marcelin M., Amram P., 2004, MNRAS, 349, 225

Garrido O., Marcelin M., Amram P., Balkowski C., Gach J. L., Boulesteix J., 2005, MNRAS, 362, 127

Gelb J. M., Bertschinger E., 1994, ApJ, 436, 467

Genel S., et al., 2014, MNRAS, 445, 175

Ghosh S., Saha K., Jog C. J., Combes F., Di Matteo P., 2022, MNRAS, 511, 5878

Gómez-López J. A., et al., 2019, A&A, 631, A71

Gómez F. A., et al., 2012, MNRAS, 423, 3727

Gómez F. A., Minchev I., O'Shea B. W., Beers T. C., Bullock J. S., Purcell C. W., 2013, MNRAS, 429, 159

Gómez F. A., White S. D. M., Marinacci F., Slater C. T., Grand R. J. J., Springel V., Pakmor R., 2016, MNRAS, 456, 2779

Gómez F. A., White S. D. M., Grand R. J. J., Marinacci F., Springel V., Pakmor R., 2017, MNRAS, 465, 3446

Gómez F. A., et al., 2021, ApJ, 908, 27

Gooch R., 1996, Astronomical Data Analysis Software and Systems V, A.S.P. Conference Series, 101, 80

Grand R. J. J., et al., 2017, MNRAS, 467, 179

Gusev A. S., Zasov A. V., Kaisin S. S., 2003, Astronomy Letters, 29, 363

Haan S., Braun R., 2014, MNRAS, 443, 186

Haynes M. P., et al., 2018, ApJ, 861, 49

Hernandez O., Wozniak H., Carignan C., Amram P., Chemin L., Daigle O., 2005, ApJ, 632, 253

Hernandez O., et al., 2008, PASP, 120, 665

Hernquist L., Katz N., Weinberg D. H., Miralda-Escudé J., 1996, ApJL, 457, L51

Hunter C., Toomre A., 1969, ApJ, 155, 747

James P. A., et al., 2004, A&A, 414, 23

Jenkins A., Frenk C. S., White S. D. M., Colberg J. M., Cole S., Evrard A. E., Couchman H. M. P., Yoshida N., 2001, MNRAS, 321, 372

Jiang I.-G., Binney J., 1999, MNRAS, 303, L7

Jiménez-Vicente J., Battaner E., 2000, A&A, 358, 812

Kamphuis J., Briggs F., 1992, A&A, 253, 335

Karachentsev I. D., Sharina M. E., Huchtmeier W. K., 2000, A&A, 362, 544

Karachentsev I. D., Kajsin S. S., Tsvetanov Z., Ford H., 2005, A&A, 434, 935

Karachentsev I. D., Makarov D. I., Kaisina E. I., 2013, AJ, 145, 101

Kazantzidis S., Zentner A. R., Kravtsov A. V., Bullock J. S., Debattista V. P., 2009, ApJ, 700, 1896

Kennicutt Robert C. J., et al., 2003, PASP, 115, 928

Kerr F. J., 1957, AJ, 62, 93

Knapen J. H., Cepa J., Beckman J. E., Soledad del Rio M., Pedlar A., 1993, ApJ, 416, 563

Korsaga M., Carignan C., Amram P., Epinat B., Jarrett T. H., 2018, MNRAS, 478, 50

Korsaga M., Amram P., Carignan C., Epinat B., 2019a, MNRAS, 482, 154

Korsaga M., Epinat B., Amram P., Carignan C., Adamczyk P., Sorgho A., 2019b, MNRAS, 490, 2977

Laporte C. F. P., Gómez F. A., Besla G., Johnston K. V., Garavito-Camargo N., 2018a, MNRAS, 473, 1218

Laporte C. F. P., Johnston K. V., Gómez F. A., Garavito-Camargo N., Besla G., 2018b, MNRAS, 481, 286

Laporte C. F. P., Agnello A., Navarro J. F., 2019a, MNRAS, 484, 245

Laporte C. F. P., Minchev I., Johnston K. V., Gómez F. A., 2019b, MNRAS, 485, 3134

Laporte C. F. P., Belokurov V., Koposov S. E., Smith M. C., Hill V., 2020, MNRAS, 492, L61

Lee H. M., Kim H., Ann H., 1998, Journal of Korean Astronomical Society, 31, 95

Levine E. S., Blitz L., Heiles C., 2006, ApJ, 643, 881

Lintott C., et al., 2011, MNRAS, 410, 166

Liu C., et al., 2017, Research in Astronomy and Astrophysics, 17, 096

López-Corredoira M., Cabrera-Lavers A., Garzón F., Hammersley P. L., 2002, A&A, 394, 883

Marinacci F., Pakmor R., Springel V., 2014, MNRAS, 437, 1750

Marinacci F., et al., 2018, MNRAS, 480, 5113

McMillan P. J., 2017, MNRAS, 465, 76

McMillan P. J., et al., 2022, MNRAS, 516, 4988

Mendes de Oliveira C., Amram P., Plana H., Balkowski C., 2003, AJ, 126, 2635

Mendes de Oliveira C., Amram P., Quint B. C., Torres-Flores S., Barbá R., Andrade D., 2017, MNRAS, 469, 3424

Michałowski M. J., Gotkiewicz N., Hjorth J., Kamphuis P., 2020, A&A, 638, A47

Miyamoto M., Nagai R., 1975, PASJ, 27, 533

Miyamoto M., Yoshizawa M., Suzuki S., 1988, A&A, 194, 107

Momany Y., Zaggia S., Gilmore G., Piotto G., Carraro G., Bedin L. R., de Angeli F., 2006, A&A, 451, 515

Monari G., Famaey B., Siebert A., Grand R. J. J., Kawata D., Boily C., 2016, MNRAS, 461, 3835

Naiman J. P., et al., 2018, MNRAS, 477, 1206

Narayan C. A., Dettmar R.-J., Saha K., 2020, MNRAS, 495, 3705

Navarro J. F., Frenk C. S., White S. D. M., 1996, ApJ, 462, 563

Navarro J. F., Frenk C. S., White S. D. M., 1997, ApJ, 490, 493

Nelson D., et al., 2018, MNRAS, 475, 624

Nelson D., et al., 2019, MNRAS, 490, 3234

Newberg H. J., et al., 2002, ApJ, 569, 245

Newton K., Emerson D. T., 1977, MNRAS, 181, 573

Oikawa S., Sofue Y., 2014, PASJ, 66, 77

Ostriker E. C., Binney J. J., 1989, MNRAS, 237, 785

Paturel G., et al., 1997, A&AS, 124, 109

Peebles P. J. E., 1980, The large-scale structure of the universe

Pillepich A., et al., 2018, MNRAS, 475, 648

Pillepich A., et al., 2019, MNRAS, 490, 3196

Pillepich A., Nelson D., Truong N., Weinberger R., Martin-Navarro I., Springel V., Faber S. M., Hernquist L., 2021, Monthly Notices of the Royal Astronomical Society, 508, 4667

Pisano D. J., Wilcots E. M., 2000, MNRAS, 319, 821

Planck Collaboration et al., 2016, A&A, 594, A13

Press W. H., Teukolsky S. A., Vetterling W. T., Flannery B. P., 1992, Numerical recipes in C. The art of scientific computing

Price-Whelan A. M., Johnston K. V., Sheffield A. A., Laporte C. F. P., Sesar B., 2015, MNRAS, 452, 676

Purcell C. W., Bullock J. S., Tollerud E. J., Rocha M., Chakrabarti S., 2011, Nature, 477, 301

Quillen A. C., Dougherty J., Bagley M. B., Minchev I., Comparetta J., 2011, MNRAS, 417, 762

Quinn P. J., Hernquist L., Fullagar D. P., 1993, ApJ, 403, 74

Radburn-Smith D. J., et al., 2014, ApJ, 780, 105

Ramos P., et al., 2022, A&A, 666, A64

Reshetnikov V., Combes F., 1998, A&A, 337, 9

Rogstad D. H., Lockhart I. A., Wright M. C. H., 1974, ApJ, 193, 309

Rogstad D. H., Wright M. C. H., Lockhart I. A., 1976, ApJ, 204, 703

Rosolowsky E., et al., 2019, in American Astronomical Society Meeting Abstracts #233. p. 450.01

Rots A. H., Bosma A., van der Hulst J. M., Athanassoula E., Crane P. C., 1990, AJ, 100, 387

Roškar R., Debattista V. P., Brooks A. M., Quinn T. R., Brook C. B., Governato F., Dalcanton J. J., Wadsley J., 2010, MNRAS, 408, 783

Saha K., Combes F., Jog C. J., 2007, MNRAS, 382, 419

Sánchez-Gil M. C., Alfaro E. J., Pérez E., 2015, MNRAS, 454, 3376

Sánchez-Saavedra M. L., Battaner E., Florido E., 1990, MNRAS, 246, 458

Sánchez S. F., et al., 2012, A&A, 538, A8

Sancisi R., Fraternali F., Oosterloo T., van der Hulst T., 2008, A&A Rv, 15, 189

Schinnerer E., Böker T., Emsellem E., Lisenfeld U., 2006, ApJ, 649, 181

Schulman E., Bregman J. N., Brinks E., Roberts M. S., 1996, AJ, 112, 960

Searle L., Zinn R., 1978, ApJ, 225, 357

Sellwood J. A., 2013, Dynamics of Disks and Warps. p. 923, doi:10.1007/978-94-007-5612-0˙18

Sellwood J. A., Sánchez R. Z., 2010, MNRAS, 404, 1733

Semczuk M., Łokas E. L., D'Onghia E., Athanassoula E., Debattista V. P., Hernquist L., 2020, MNRAS, 498, 3535

Sheffield A. A., Price-Whelan A. M., Tzanidakis A., Johnston K. V., Laporte C. F. P., Sesar B., 2018, ApJ, 854, 47

Shen J., Sellwood J. A., 2006, MNRAS, 370, 2

Sheth K., et al., 2010, PASP, 122, 1397

Shetty R., Vogel S. N., Ostriker E. C., Teuben P. J., 2007, ApJ, 665, 1138

Siebert A., et al., 2012, MNRAS, 425, 2335

Sijacki D., Vogelsberger M., Genel S., Springel V., Torrey P., Snyder G. F., Nelson D., Hernquist L., 2015, MNRAS, 452, 575

Slater C. T., et al., 2014, ApJ, 791, 9

Smith R., Flynn C., Candlish G. N., Fellhauer M., Gibson B. K., 2015, MNRAS, 448, 2934

Spano M., Marcelin M., Amram P., Carignan C., Epinat B., Hernandez O., 2008, MNRAS, 383, 297

Sparke L. S., 1984, ApJ, 280, 117

Sparke L. S., Casertano S., 1988, MNRAS, 234, 873

Springel V., 2010, MNRAS, 401, 791

Springel V., et al., 2005, Nature, 435, 629

Springel V., Frenk C. S., White S. D. M., 2006, Nature, 440, 1137

Springel V., et al., 2008, MNRAS, 391, 1685

Springel V., et al., 2018, MNRAS, 475, 676

Steinmetz M., et al., 2006, AJ, 132, 1645

Struve C., Józsa G., Kenn F., Klein U., Pizzella A., Salcuci P., 2007, Nature, 51, 120

Toomre A., Toomre J., 1972, ApJ, 178, 623

Torres-Flores S., Mendes de Oliveira C., Amram P., Plana H., Epinat B., Carignan C., Balkowski C., 2010, A&A, 521, A59

Torres-Flores S., Epinat B., Amram P., Plana H., Mendes de Oliveira C., 2011, MNRAS, 416, 1936

Torres-Flores S., Amram P., Mendes de Oliveira C., Plana H., Balkowski C., Marcelin M., Olave-Rojas D., 2014, MNRAS, 442, 2188

Tully R. B., 1988, Nearby galaxies catalog

Tully R. B., Fisher J. R., 1977, A&A, 54, 661

Urrejola-Mora C., Gómez F. A., Torres-Flores S., Amram P., Epinat B., Monachesi A., Marinacci F., de Oliveira C. M., 2022, ApJ, 935, 20

Velazquez H., White S. D. M., 1999, MNRAS, 304, 254

Verdes-Montenegro L., Bosma A., Athanassoula E., 2000, A&A, 356, 827

Verdes-Montenegro L., Bosma A., Athanassoula E., 2002, A&A, 389, 825

Vergani D., Pizzella A., Corsini E. M., van Driel W., Buson L. M., Dettmar R. J., Bertola F., 2007, A&A, 463, 883

Vesperini E., Weinberg M. D., 2000, ApJ, 534, 598

Vogelsberger M., et al., 2014, Nature, 509, 177

Walter F., Brinks E., de Blok W. J. G., Bigiel F., Kennicutt Robert C. J., Thornley M. D., Leroy A., 2008, AJ, 136, 2563

Wambsganss J., Bode P., Ostriker J. P., 2004, ApJL, 606, L93

Warner P. J., Wright M. C. H., Baldwin J. E., 1973, MNRAS, 163, 163

Warren M. S., Quinn P. J., Salmon J. K., Zurek W. H., 1992, ApJ, 399, 405

Weinberg M. D., 1991, ApJ, 373, 391

Weinberg M. D., 1998, MNRAS, 299, 499

Weinberger R., et al., 2017, MNRAS, 465, 3291

White S. D. M., Frenk C. S., 1991, ApJ, 379, 52

White S. D. M., Rees M. J., 1978, MNRAS, 183, 341

Widrow L. M., Bonner G., 2015, MNRAS, 450, 266

Widrow L. M., Gardner S., Yanny B., Dodelson S., Chen H.-Y., 2012, ApJL, 750, L41

Widrow L. M., Barber J., Chequers M. H., Cheng E., 2014, Monthly Notices of the Royal Astronomical Society, 440, 1971

Willett K. W., et al., 2013, MNRAS, 435, 2835

Williams M. E. K., et al., 2013, MNRAS, 436, 101

Xu Y., Newberg H. J., Carlin J. L., Liu C., Deng L., Li J., Schönrich R., Yanny B., 2015, ApJ, 801, 105

Yanny B., et al., 2003, ApJ, 588, 824

Yanny B., et al., 2009, AJ, 137, 4377

York D. G., et al., 2000, AJ, 120, 1579

Yurin D., Springel V., 2015, MNRAS, 452, 2367

de Vaucouleurs G., de Vaucouleurs A., Corwin Herold G. J., Buta R. J., Paturel G., Fouque P., 1991, Third Reference Catalogue of Bright Galaxies

van der Hulst J. M., van Albada T. S., Sancisi R., 2001, in Hibbard J. E., Rupen M., van Gorkom J. H., eds, Astronomical Society of the Pacific Conference Series Vol. 240, Gas and Galaxy Evolution. p. 451

Appendix A

New Observation Data

A.1   Comments for individual galaxies

NGC 1058 is a nearly normal Sc face-on spiral galaxy with an inclination angle of 6°. NGC 1058 does not present well-defined arms in H_α emission and reveals a weaker emission in the innermost than in outer regions. The galaxy is located at a distance of 9.93 Mpc, the most recent work distance value is considered. It has an angular diameter of 3 arcmin with apparent magnitude in B band about 12 mag. NGC 1058 belongs to the group NGC 1023 being the least bright member. This galaxy was observed in H_α line (Sánchez-Gil et al., 2015) to analyze if it presents vertical flows using the long-slit technique using different P.A. and finding that velocity peaks are associated with star-forming regions. Two supernovae 1961V and 1969L have been reported in the outer disk.

NGC 2500 is a nearby spiral galaxy with a short bar aligned with its minor kinematical axis, classified as SB(rs)d, located at 9.79 kpc and inclination angle 40°. This galaxy was observed using H_α filter by Epinat et al. (2008b) who find diffuse emission in their observed H_α maps. NGC 2500's corrugated velocity patterns were studied using long-slits with H_α observations in Sánchez-Gil et al. (2015), where the vertical displacements do not seem to be related with an H_α emission peak. Like NGC 1058, this galaxy is part of the sample by Sánchez-Gil et al. (2015) but unlike in NGC 1058 where they find speed peaks, in NGC 2500 it was not conclusive.

NGC 3147 is a non-barred galaxy and it is classified as SA(rs)bc. It is considered as the best type 2 Seyfert candidates using optical and X-ray observations, simultaneously (Bianchi et al., 2012).

NGC 3184 nearby grand design spiral SABc type. Located at a distance of 10.05 Mpc, it has a nearly face-on orientation with inclination angle 16.7° and 184.5° deviated in this article using the methodology described previously. This galaxy belongs to the group NGC 3184 being the brightest with 9.7 mag. Other members are NGC 3198, NGC 3432, and NGC 3319.

NGC 3423 nearby spiral galaxy Sc type, absolute B-band magnitude of 12 mag and angular size 3.56 arcmin and is located at 15 Mp. No previous analysis studies in particular of this galaxy.

NGC 3485 nearby spiral galaxy located at 28.17 Mpc with absolute B-band magnitude 12.7 mag . The kinematical inclination derived in this work is 26°. There are no individual works for this galaxy previously. In this work, the H_α emission is faint and is it located in the galaxy arm.

NGC 3642 Non-barred galaxy with three rings and dusty spiral arms classified SABc-type. The galaxy shows a warped outer disk in HI line (Verdes-Montenegro et al., 2002). NGC 3642 belongs to a group composed of 5 galaxies. NGC 3642 is the brightest member with elliptical galaxies NGC 3610 and NGC 3613 with similar magnitude. Another member is NGC 674 and NGC 3683 are fainter by more than 2 magnitudes. It is an extended galaxy and shows around internal disk from which a spinal arm appears that forms an external disk

NGC 4136 nearby face-on galaxy with a bar and a ring as well as a well-developed spiral structure in its outer disk with low-luminosity, classified SBc type (Gusev et al., 2003).

NGC 4900 is a spiral barred galaxy, classified as SB(rs)c located in the Virgo cluster at a distance of 13.3 Mpc and at about 12° south-east of M87. NGC 4900 presents HII nucleus using CO observations (Lee et al., 1998).

A.2 Presentation of the H_α maps of the new observation data
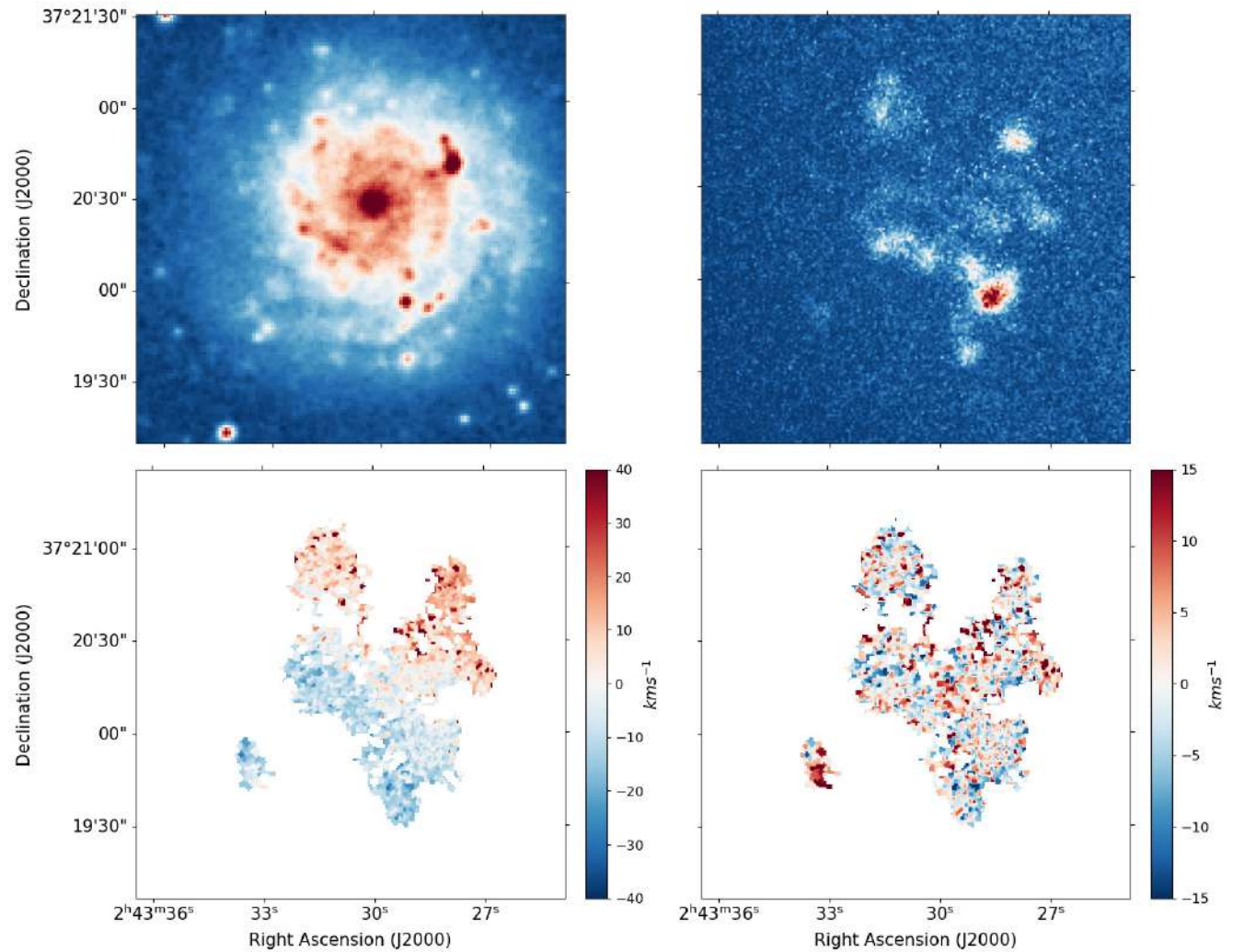
Figure A.2.1: NGC 1058. Top left: XDSS Blue Band image. Top right: H_α monochromatic image. Bottom left: H_α velocity field. Bottom right: Residual map H_α field
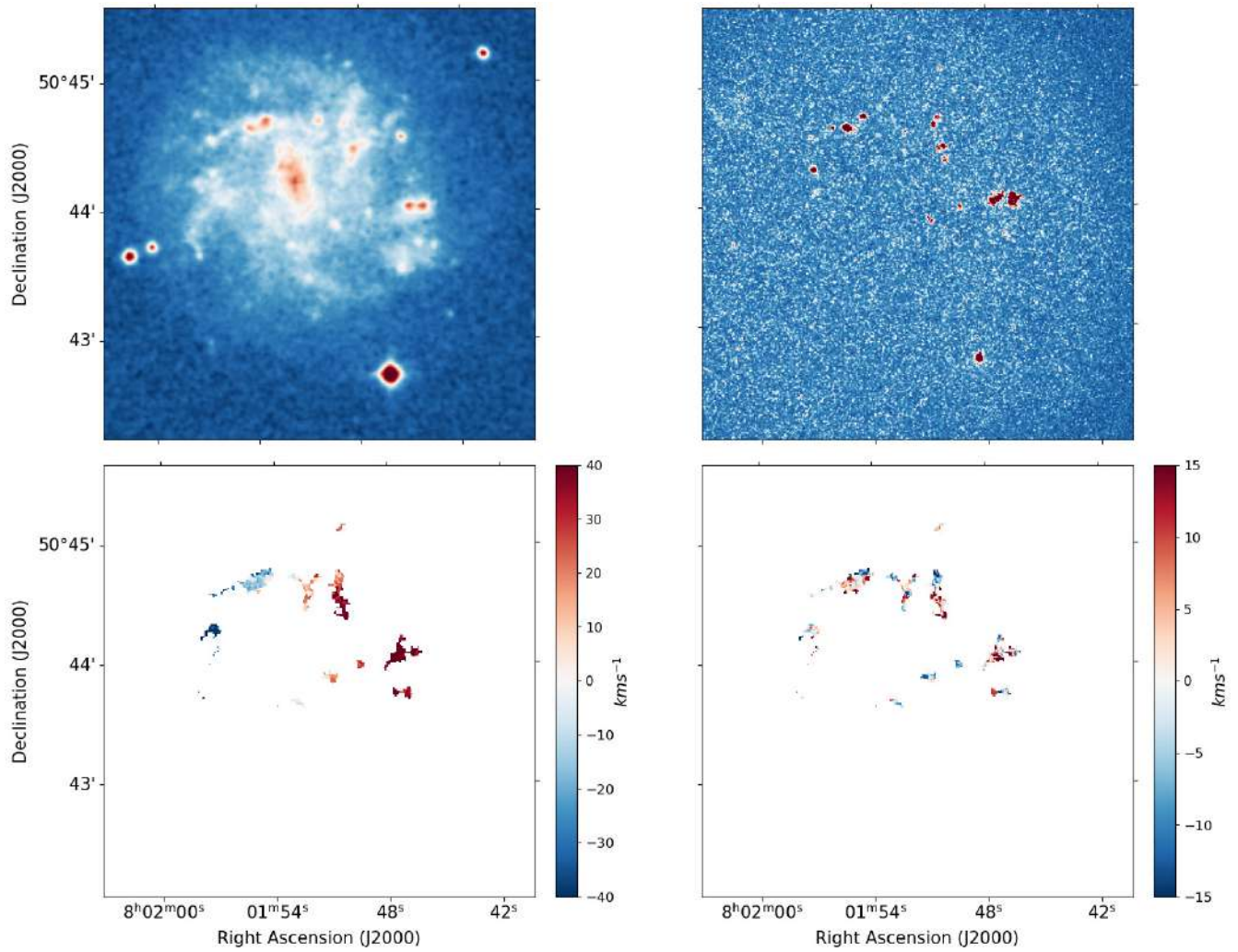
Figure A.2.2: NGC 2500. Top left: XDSS Blue Band image. Top right: H$_\alpha$ monochromatic image. Bottom left: H$_\alpha$ velocity field. Bottom right: Residual map H$_\alpha$ field
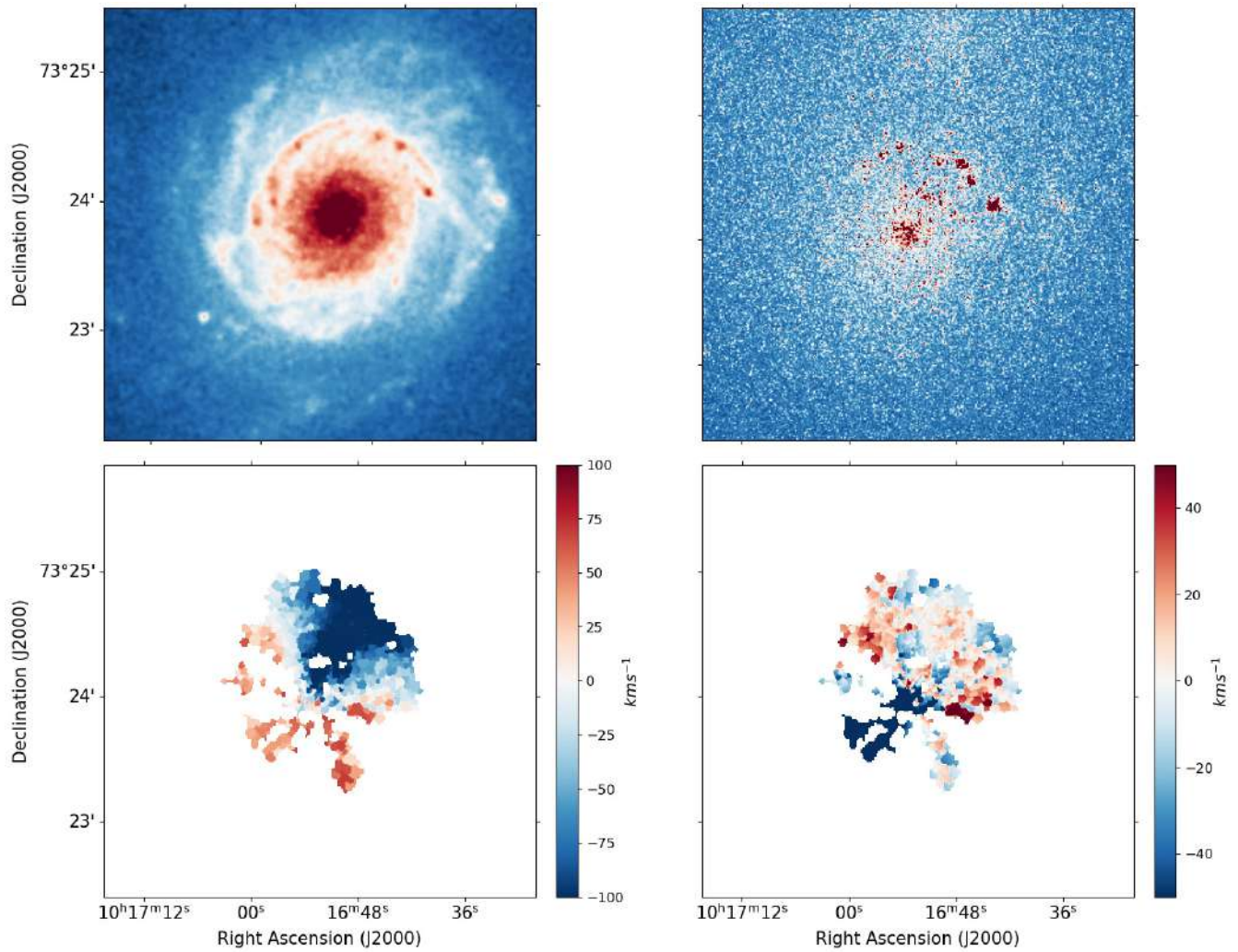
Figure A.2.3: NGC 3147. Top left: XDSS Blue Band image. Top right: H$_\alpha$ monochromatic image. Bottom left: H$_\alpha$ velocity field. Bottom right: Residual map H$_\alpha$ field
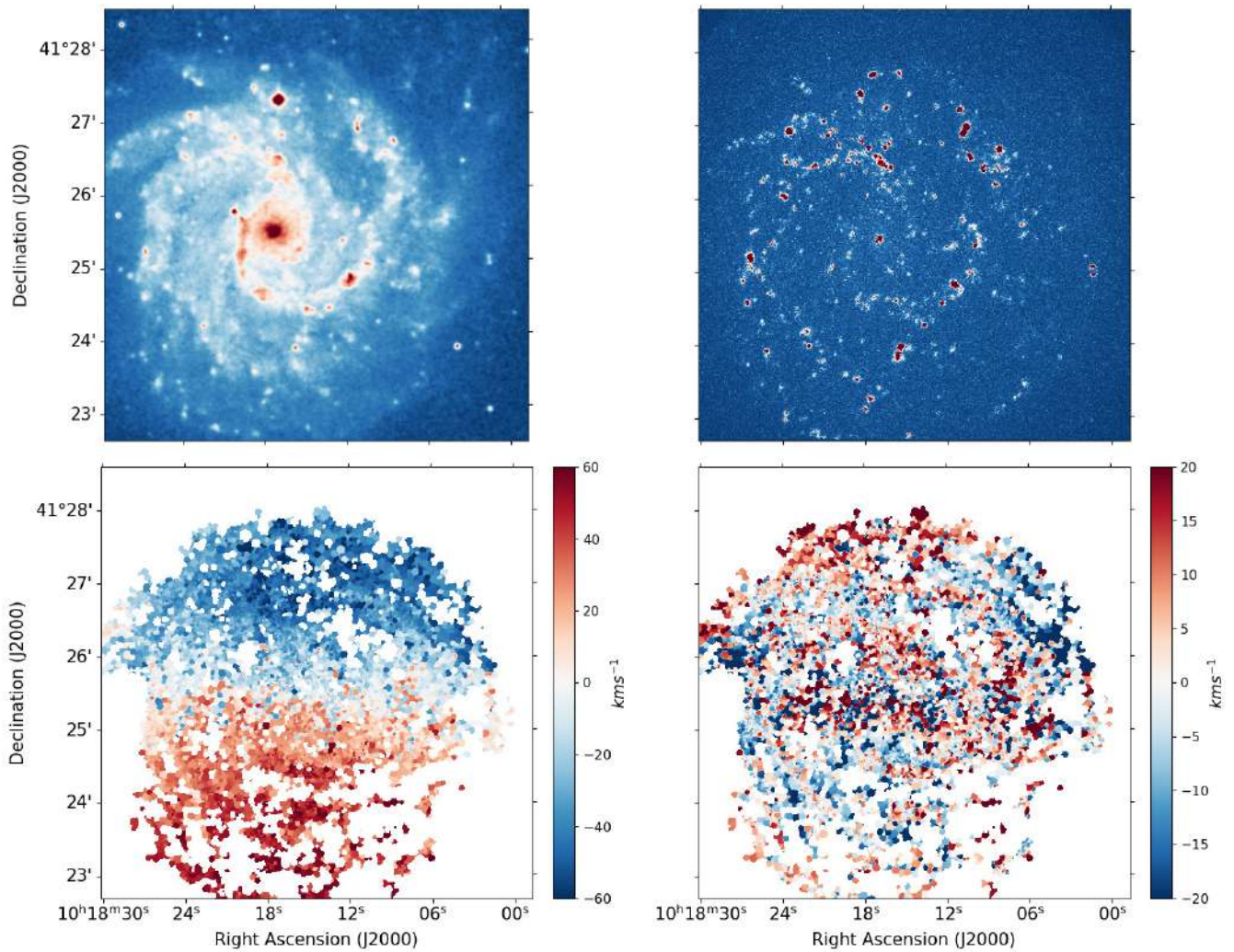
Figure A.2.4: NGC 3184. Top left: XDSS Blue Band image. Top right: H_α monochromatic image. Bottom left: H_α velocity field. Bottom right: Residual map H_α field
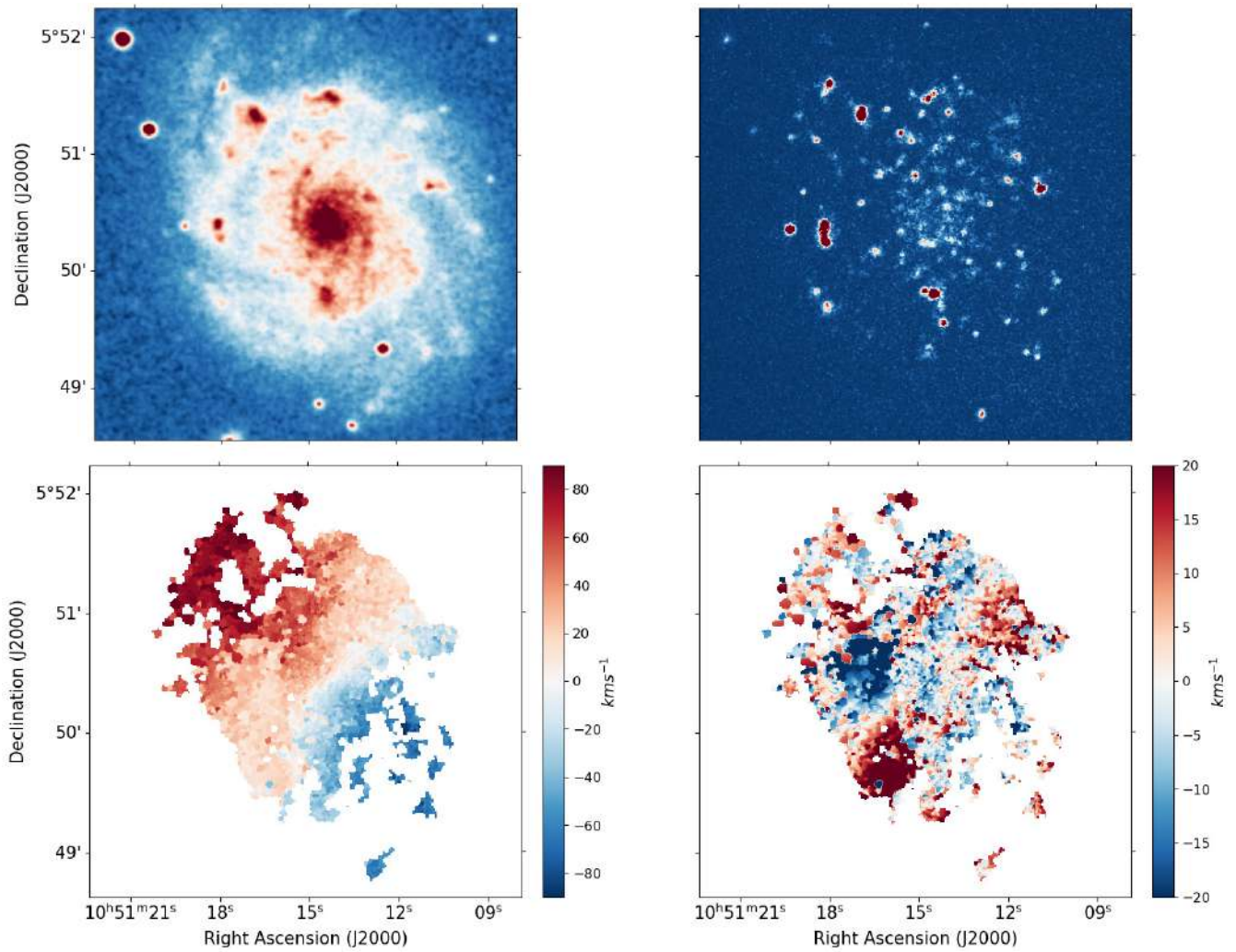
Figure A.2.5: NGC 3423. Top left: XDSS Blue Band image. Top right: H$_\alpha$ monochromatic image. Bottom left: H$_\alpha$ velocity field. Bottom right: Residual map H$_\alpha$ field
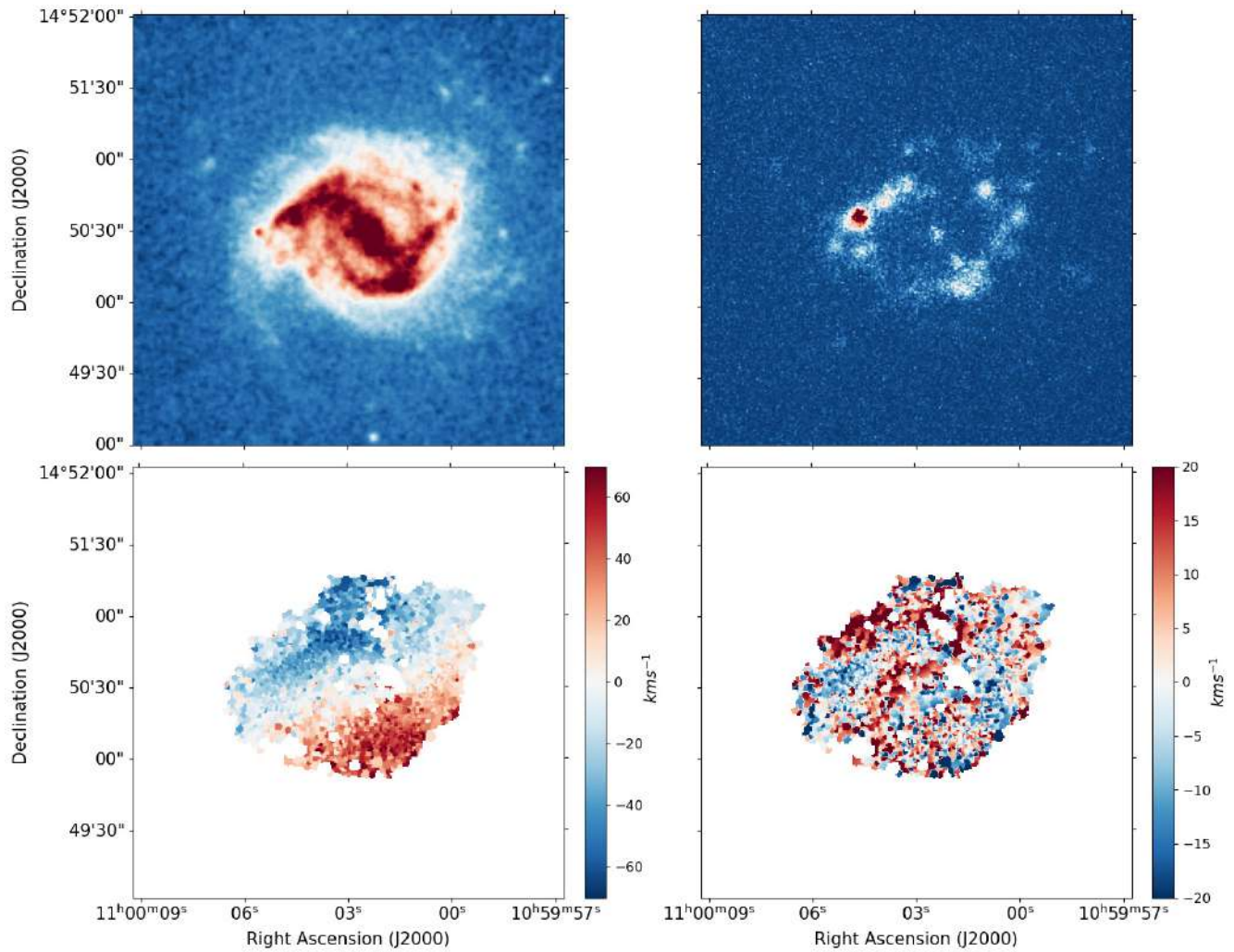
Figure A.2.6: NGC 3485. Top left: XDSS Blue Band image. Top right: H$_\alpha$ monochromatic image. Bottom left: H$_\alpha$ velocity field. Bottom right: Residual map H$_\alpha$ field
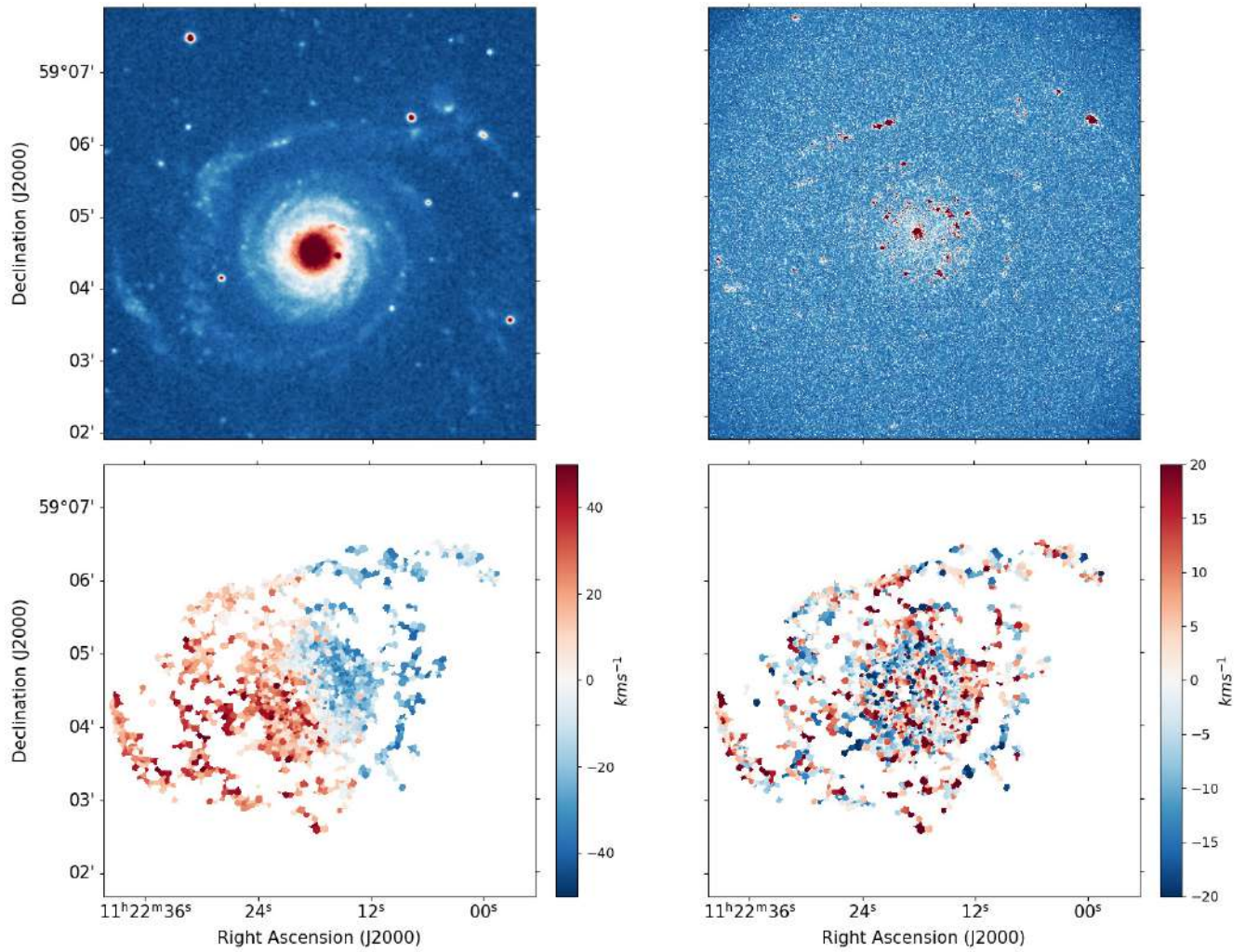
Figure A.2.7: NGC 3642. Top left: XDSS Blue Band image. Top right: H$_\alpha$ monochromatic image. Bottom left: H$_\alpha$ velocity field. Bottom right: Residual map H$_\alpha$ field
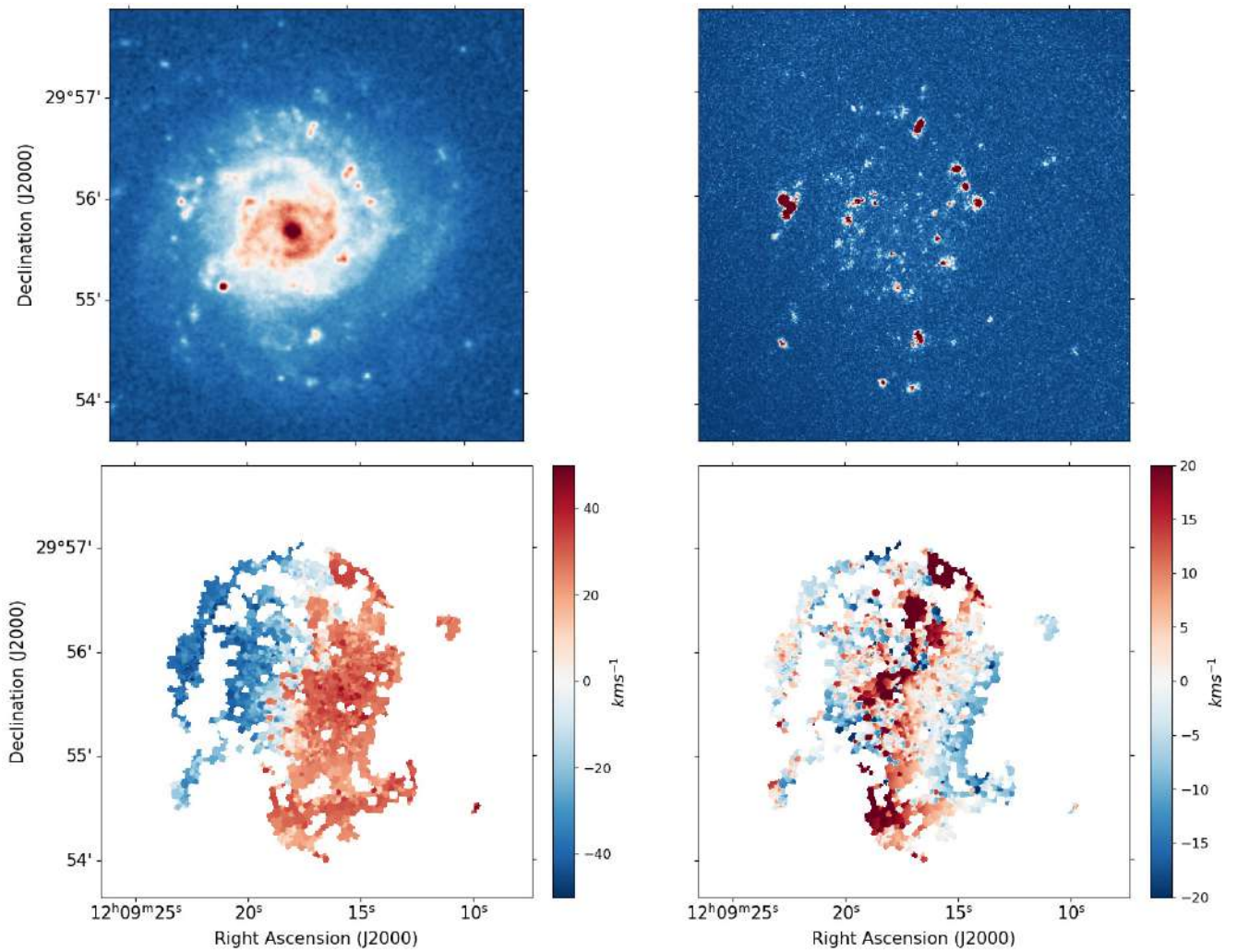
Figure A.2.8: NGC 4136. Top left: XDSS Blue Band image. Top right: H$_\alpha$ monochromatic image. Bottom left: H$_\alpha$ velocity field. Bottom right: Residual map H$_\alpha$ field
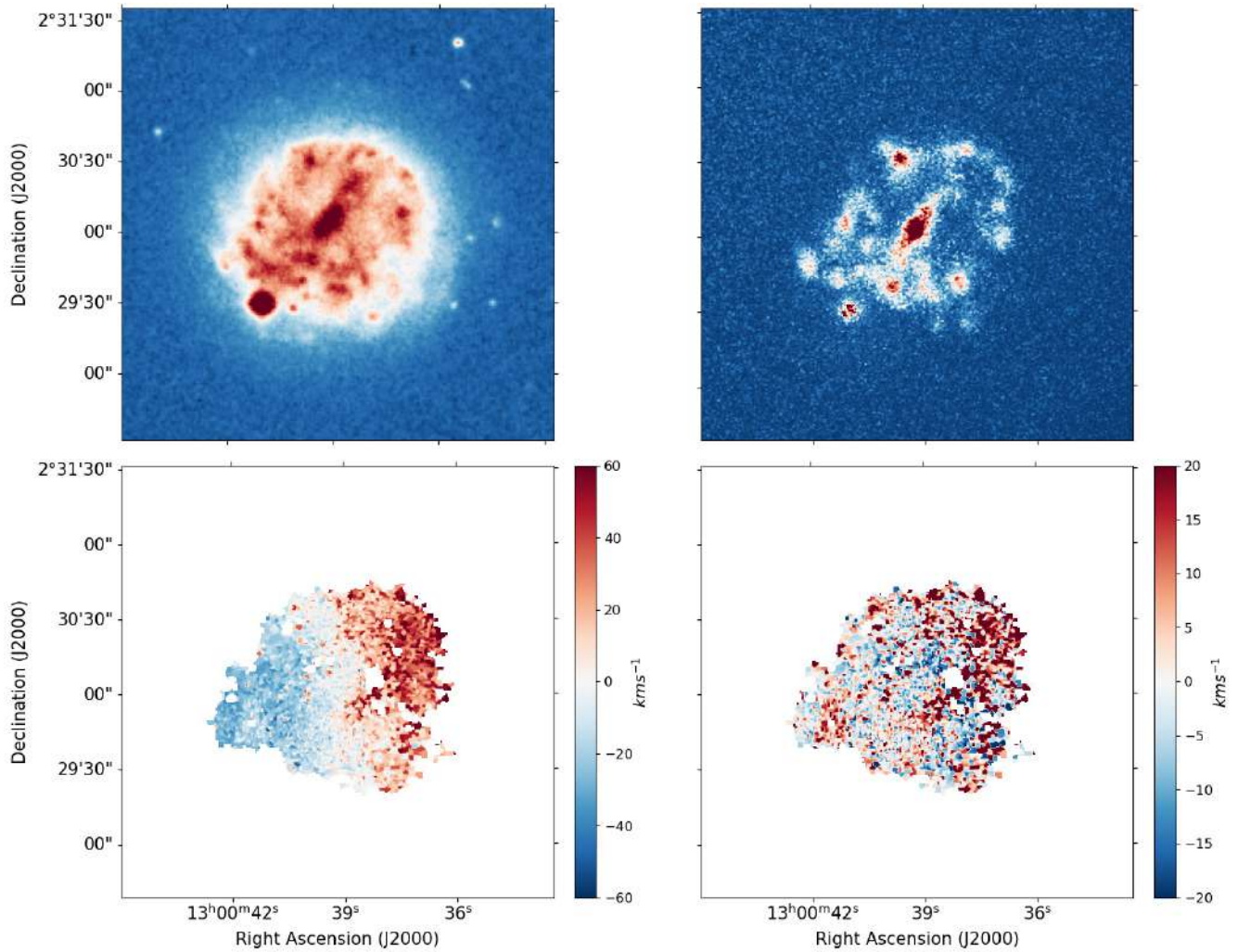
Figure A.2.9: NGC 4900. Top left: XDSS Blue Band image. Top right: H$_\alpha$ monochromatic image. Bottom left: H$_\alpha$ velocity field. Bottom right: Residual map H$_\alpha$ field

A.3   Presentation of the H_α monochromatic maps of the candidates of vertically perturbed disks
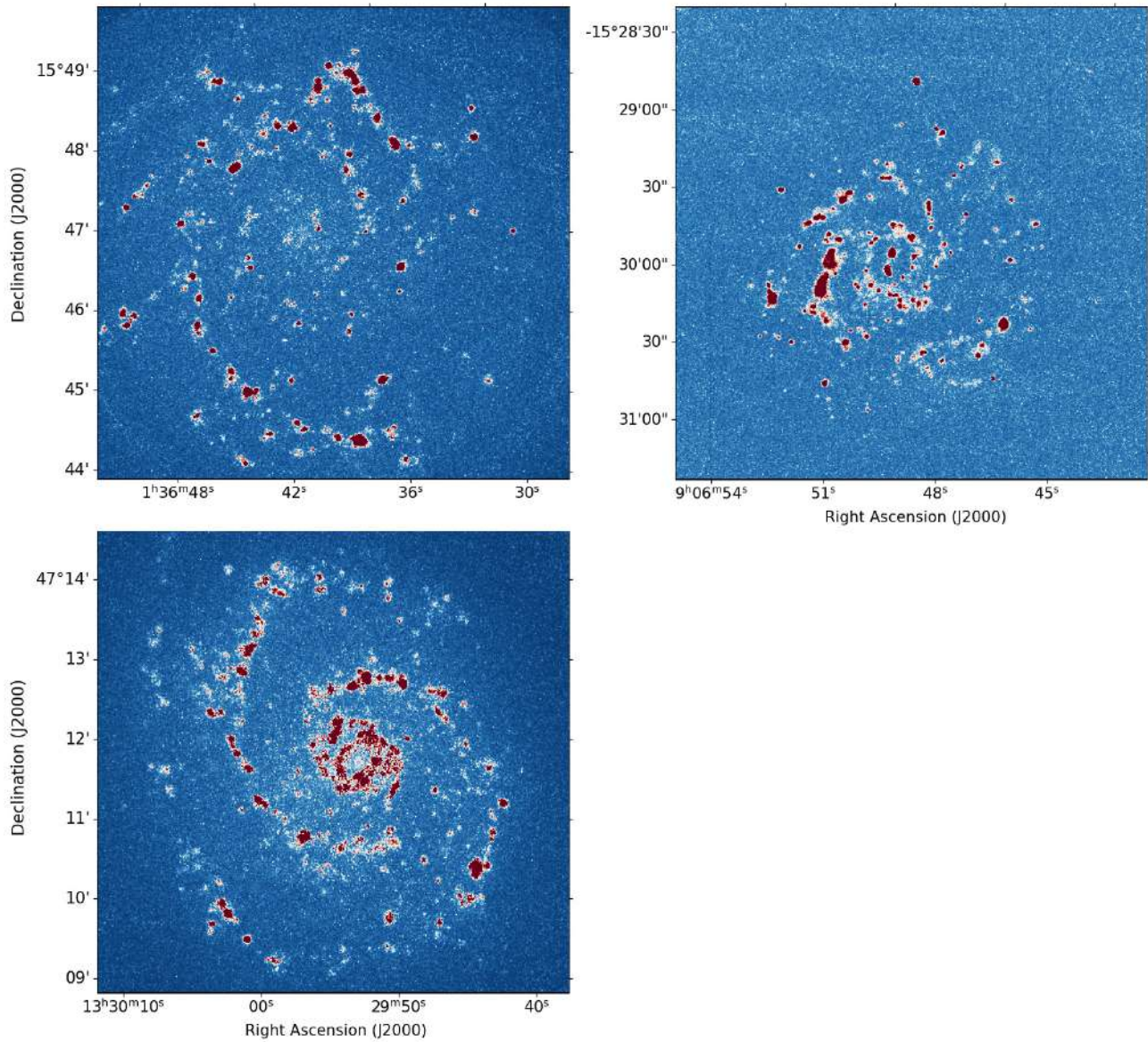
Figure A.3.1: H_α monochromatic maps. Top left: NGC 628. Top right: NGC 2763. Bottom left: NGC 5194.

Appendix B

Residual Maps of Additional Data

B.1 Residual maps without signs of vertical perturbations
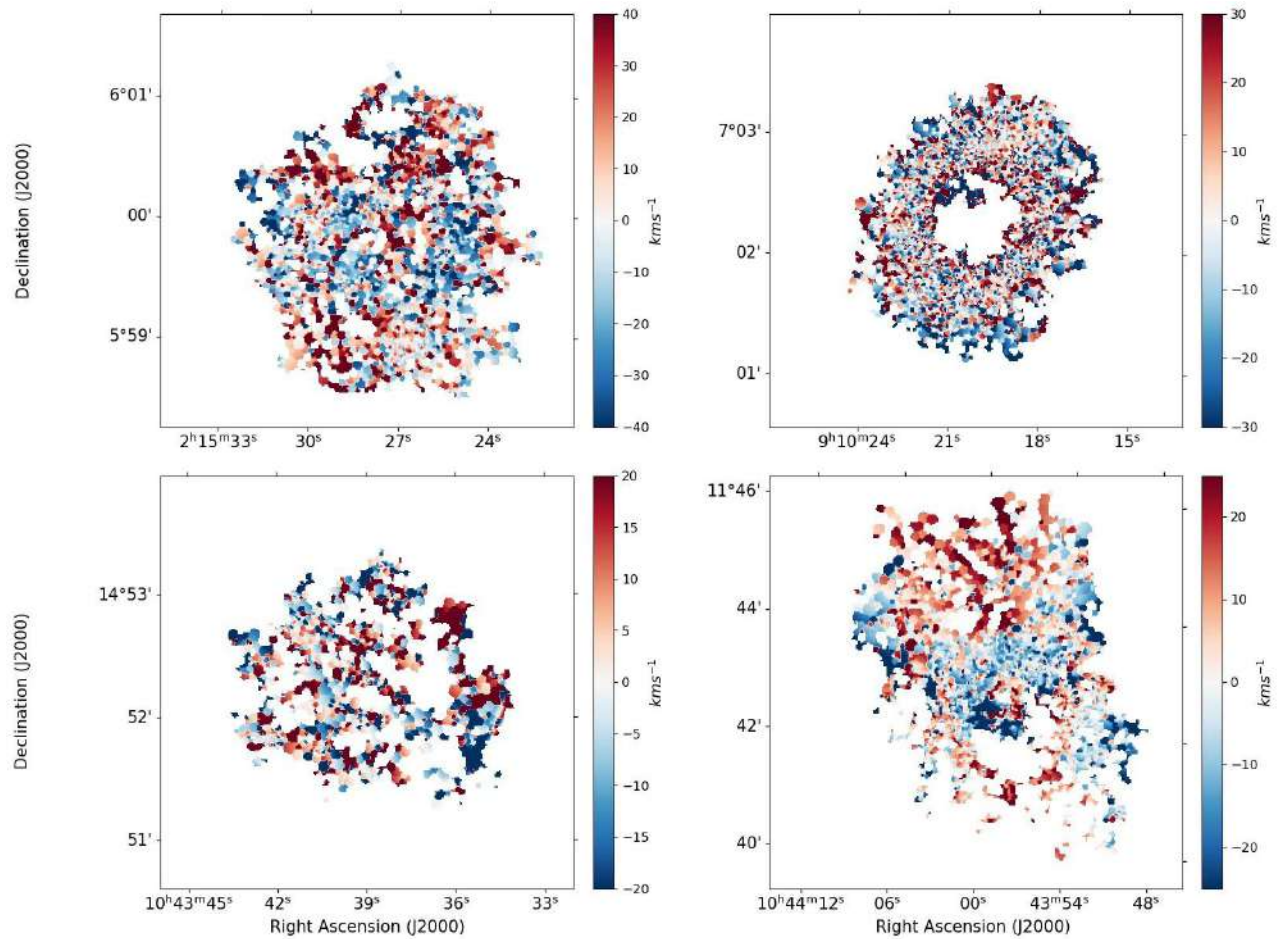
Figure B.1.1: H$_\alpha$ residual maps of WiNDS data cubes. Top left-hand panel NGC 864 (G). Top right-hand panel NGC 2775 (G). Bottom left-hand panel NGC 3346 (G). Bottom right-hand panel NGC 3351 (S).
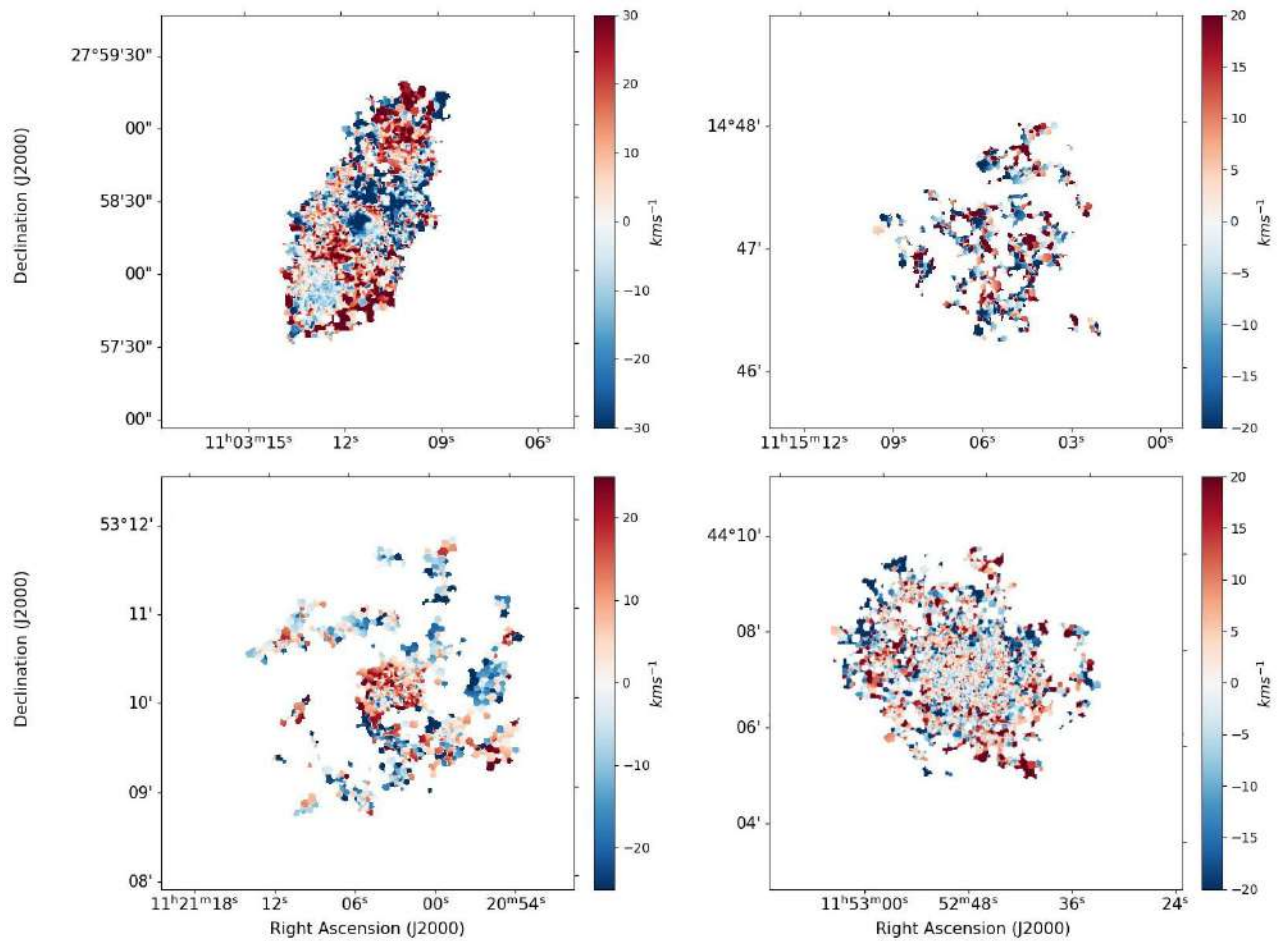
Figure B.1.2: H$_\alpha$ residual maps of WiNDS data cubes. Top left-hand panel NGC 3504 (G). Top right-hand panel NGC 3596 (G). Bottom left-hand panel NGC 3631 (H). Bottom right-hand panel NGC 3938 (S).
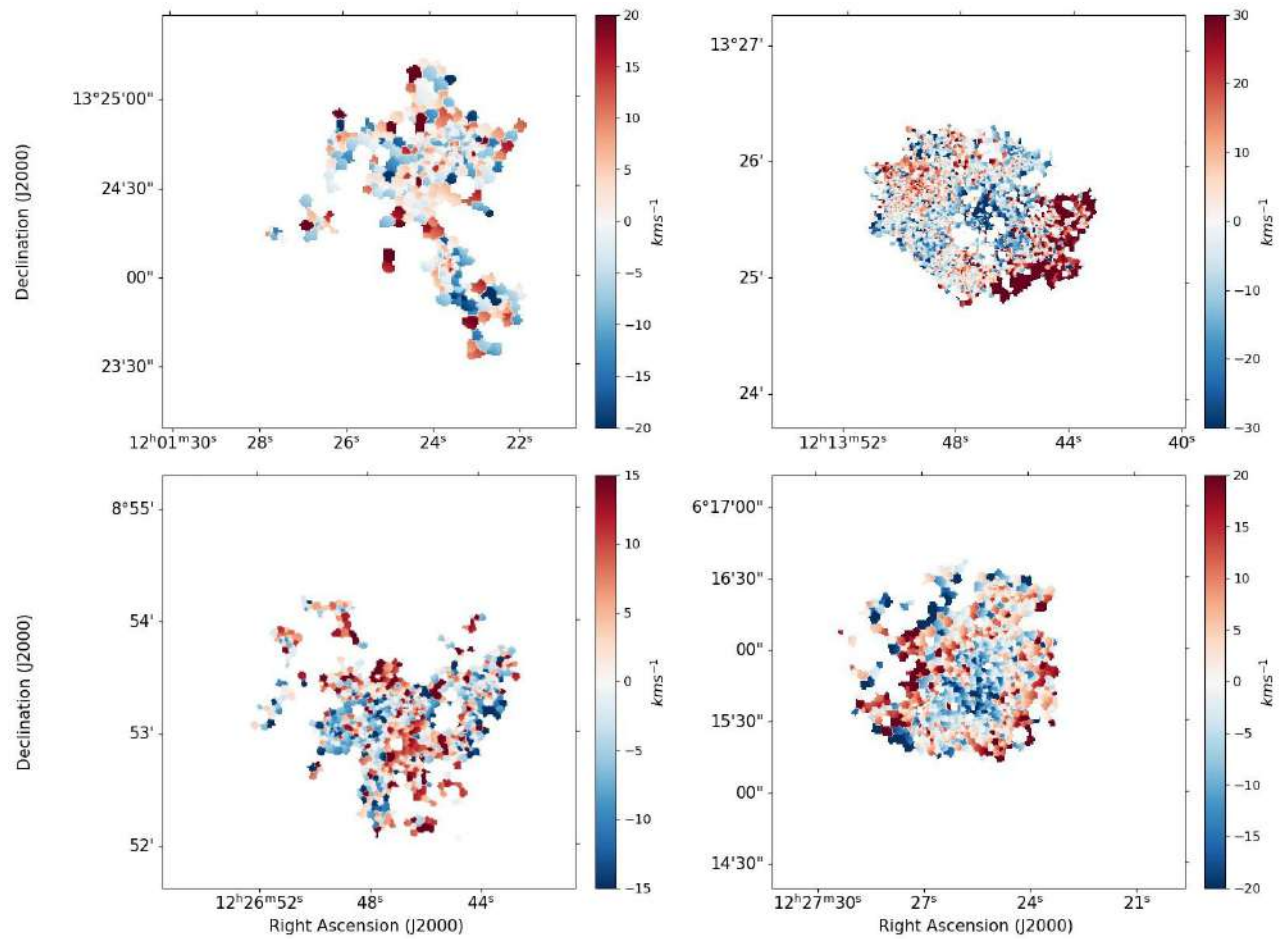
Figure B.1.3: H$_\alpha$ residual maps of WiNDS data cubes. Top left-hand panel NGC 4037 (H). Top right-hand panel NGC 4189 (V). Bottom left-hand panel NGC 4411B (G). Bottom right-hand panel NGC 4430 (H).
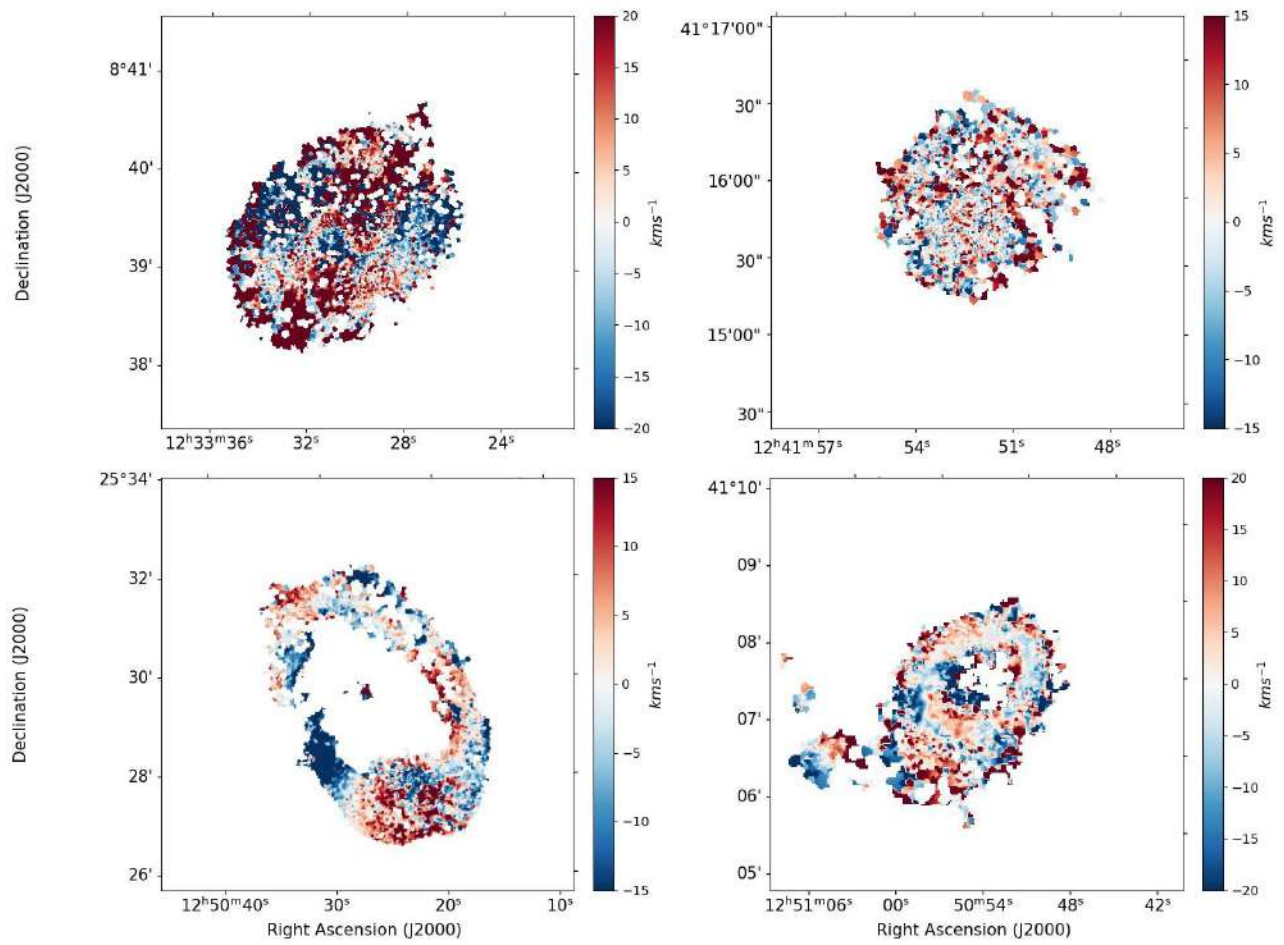
Figure B.1.4: H$_\alpha$ residual maps of WiNDS data cubes. Top left-hand panel NGC 4519 (V). Top right-hand panel NGC 4625 (S). Bottom left-hand panel NGC 4725 (S). Bottom right-hand panel NGC 4736 (S).
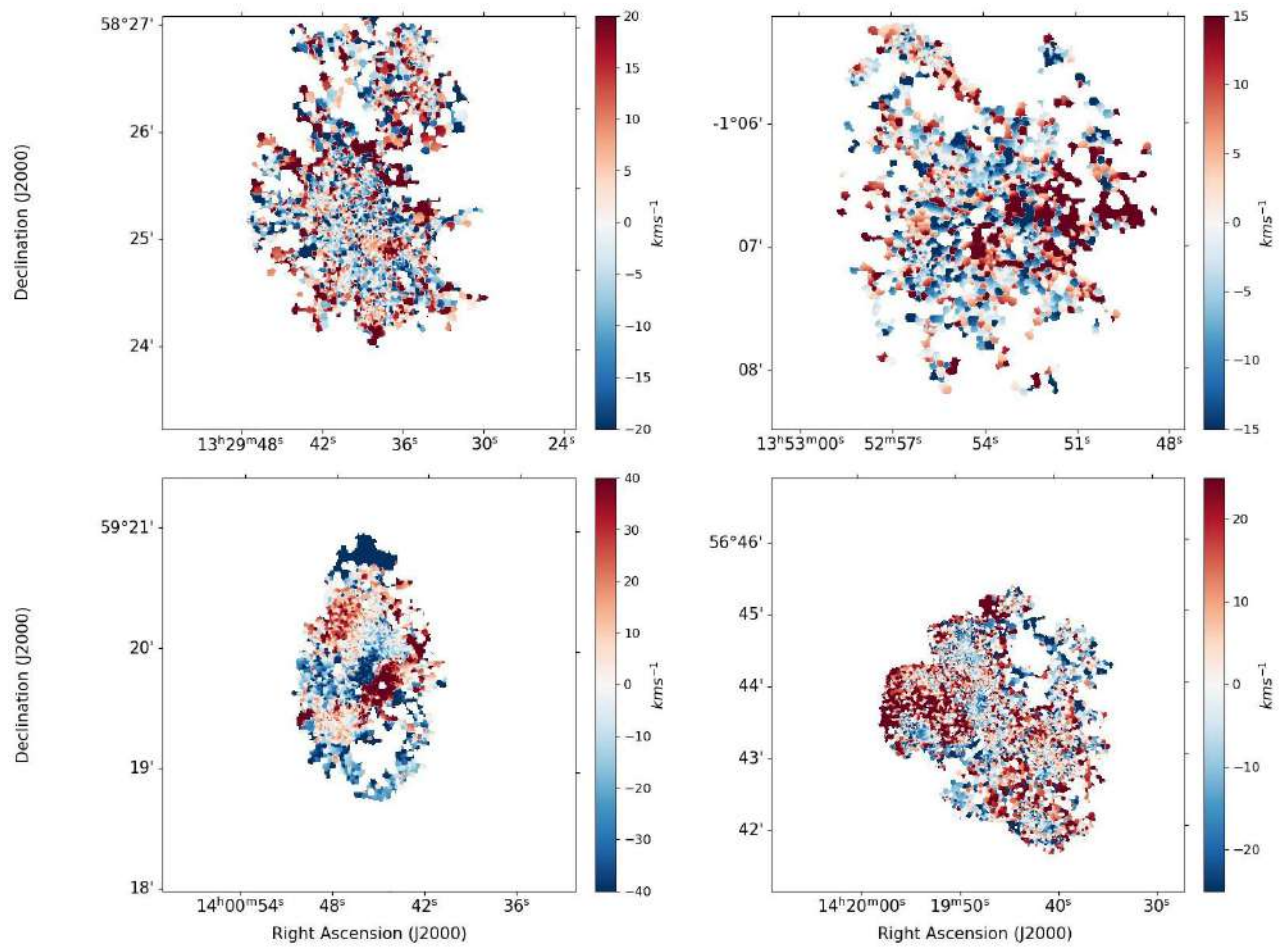
Figure B.1.5: H$_\alpha$ residual maps of WiNDS data cubes. Top left-hand panel NGC 5204 (G). Top right-hand panel NGC 5334 (H). Bottom left-hand panel NGC 5430 (G). Bottom right-hand panel NGC 5585 (G).
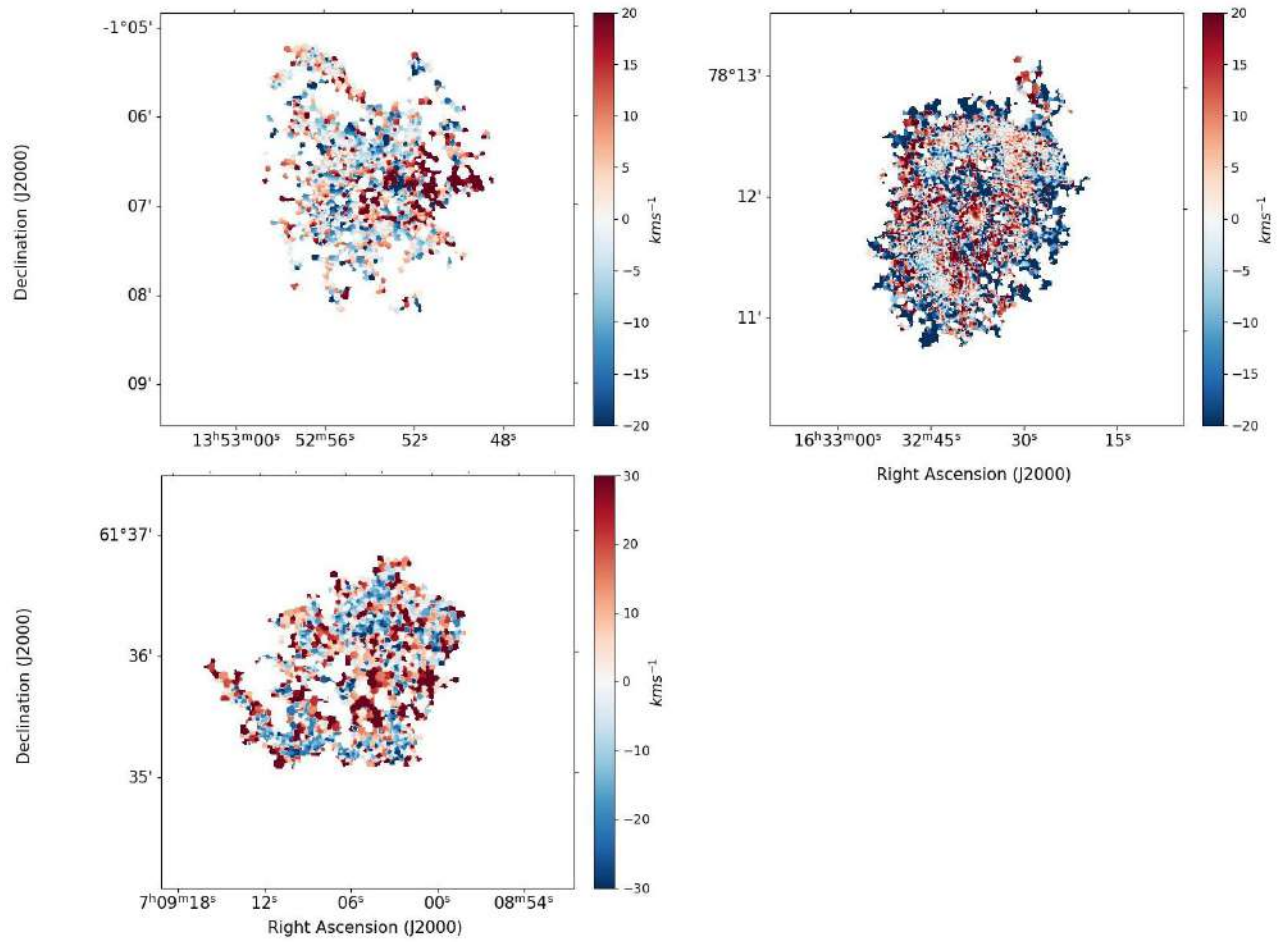
Figure B.1.6: H_α residual maps of WiNDS data cubes. Top left-hand panel NGC 5669 (H). Top right-hand panel NGC 6217 (G). Bottom left-hand panel UGC 3685 (G).

Appendix C

Rotation Curves of WiNDS

C.1   Presentation of the rotation curves of WiNDS
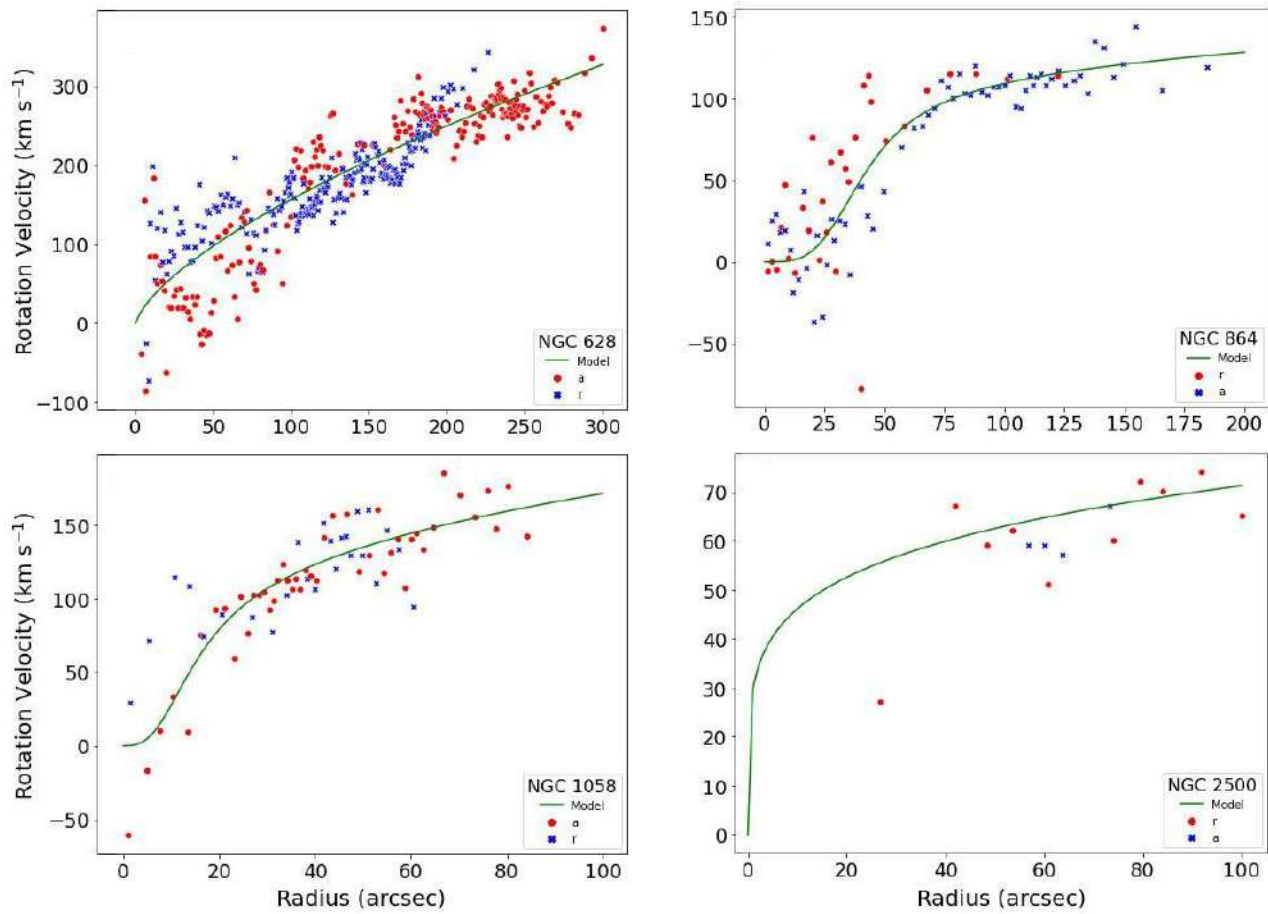
Figure C.1.1: Rotation curves of WiNDS. Top left-hand panel NGC 628. Top right-hand panel NGC 864. Bottom left-hand panel NGC 1058. Bottom right-hand panel NGC 2500. The symbols represent the receding (dots) and approaching (crosses) the side (with respect to the center).
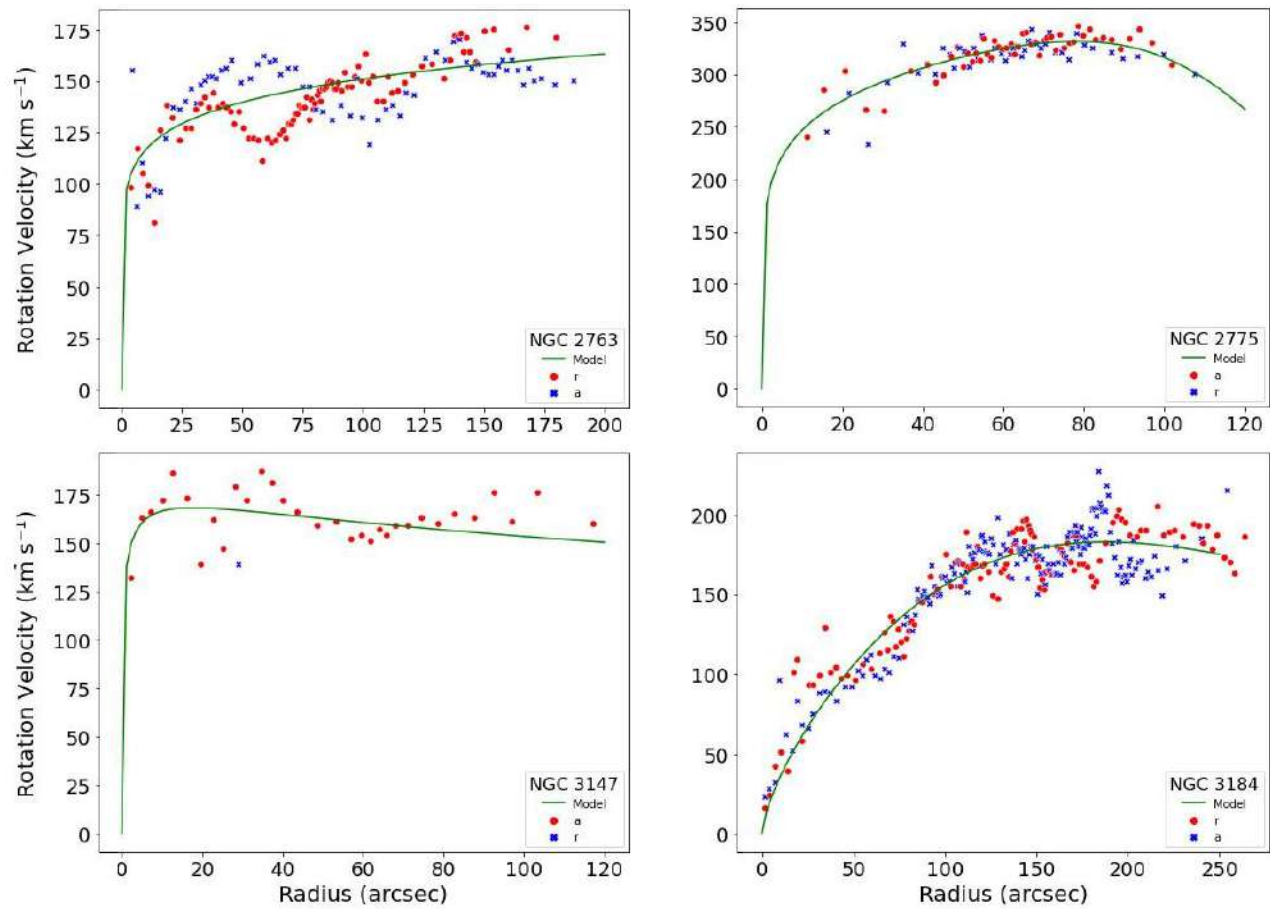
Figure C.1.2: Rotation curves of WiNDS. Top left-hand panel NGC 2763. Top right-hand panel NGC 2775. Bottom left-hand panel NGC 3147. Bottom right-hand panel NGC 3184. The symbols represent the receding (dots) and approaching (crosses) the side (with respect to the center).
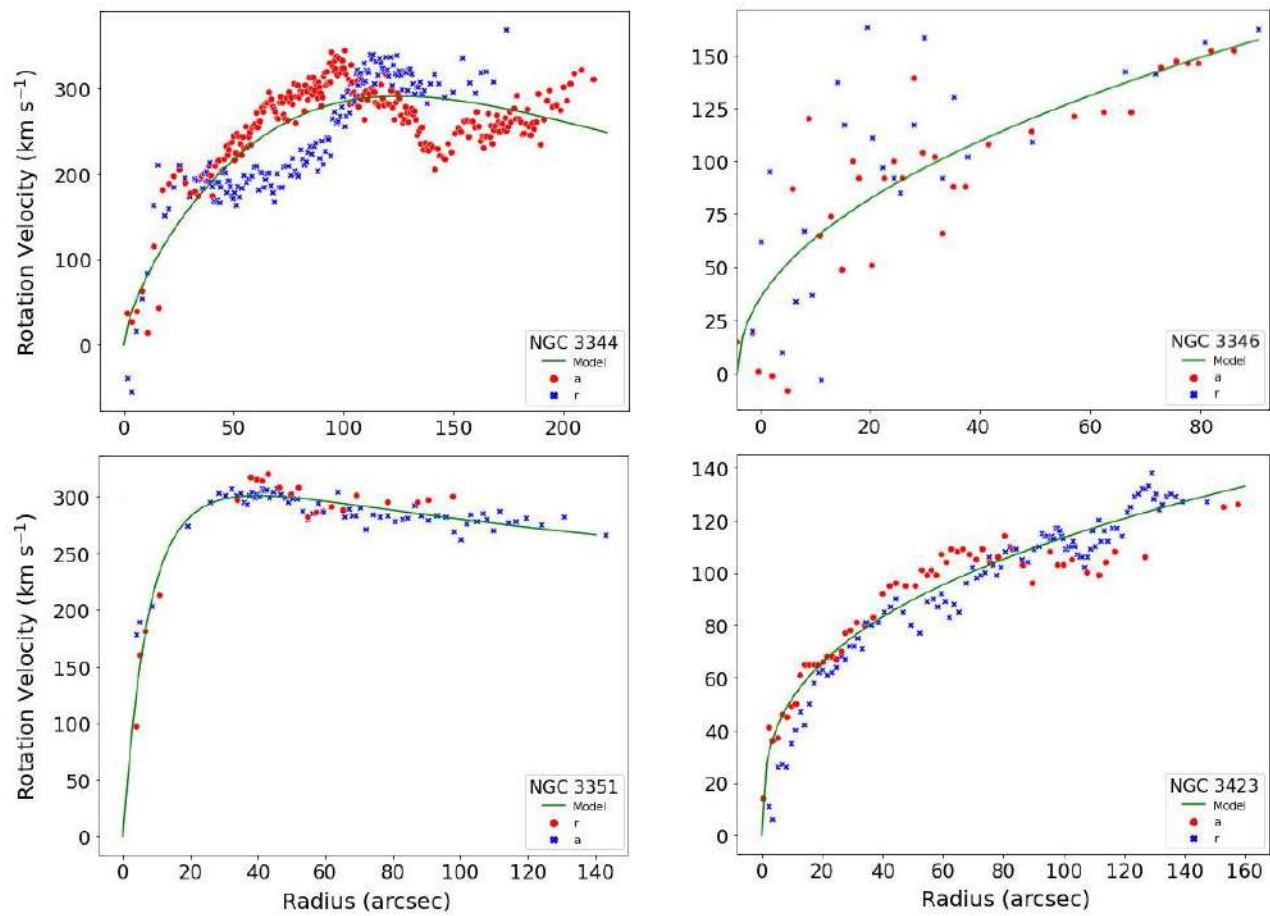
Figure C.1.3: Rotation curves of WiNDS. Top left-hand panel NGC 3344. Top right-hand panel NGC 3346. Bottom left-hand panel NGC 3351. Bottom right-hand panel NGC 3423. The symbols represent the receding (dots) and approaching (crosses) the side (with respect to the center).
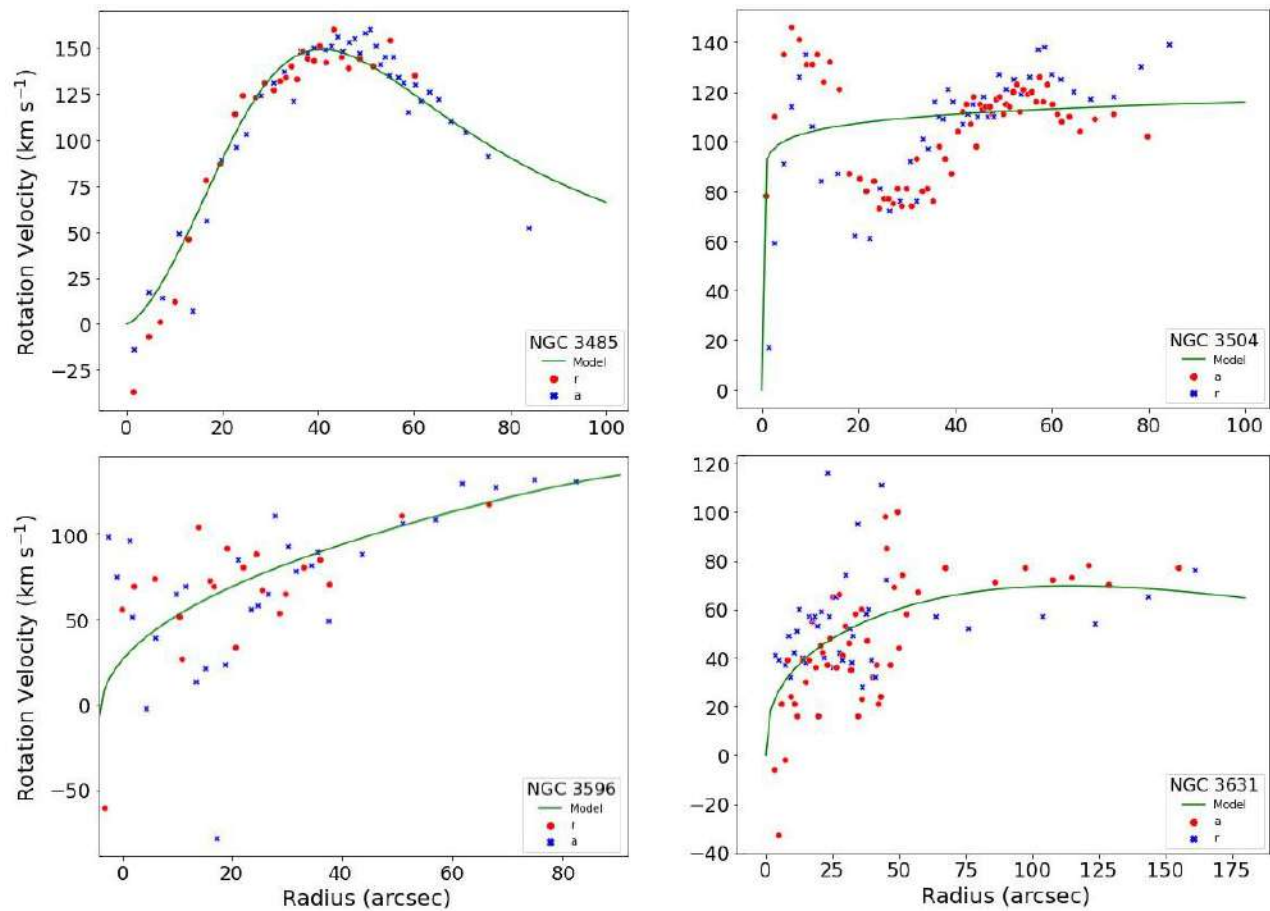
Figure C.1.4: Rotation curves of WiNDS. Top left-hand panel NGC 3485. Top right-hand panel NGC 3504. Bottom left-hand panel NGC 3596. Bottom right-hand panel NGC 3631. The symbols represent the receding (dots) and approaching (crosses) the side (with respect to the center).
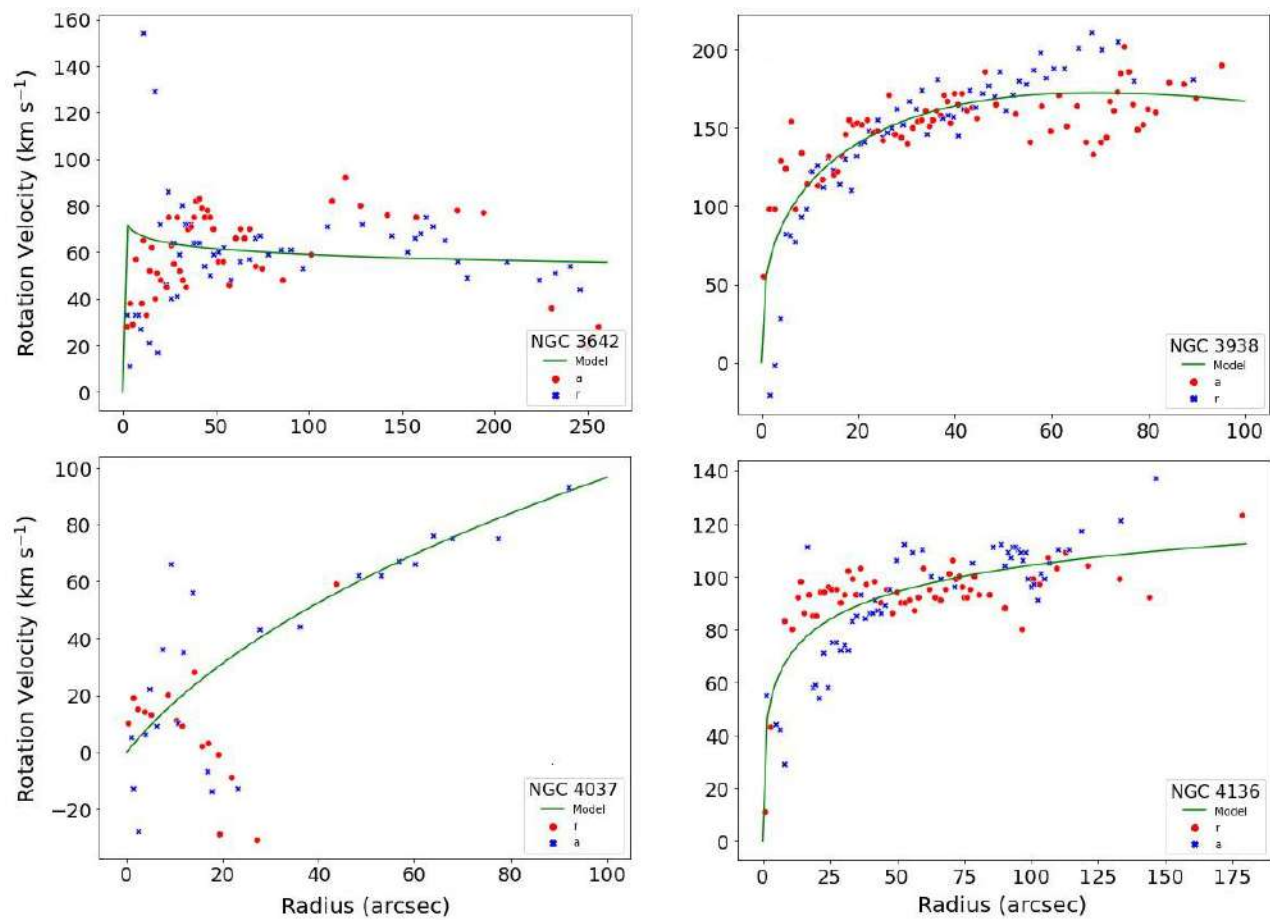
Figure C.1.5: Rotation curves of WiNDS. Top left-hand panel NGC 3642. Top right-hand panel NGC 3938. Bottom left-hand panel NGC 4037. Bottom right-hand panel NGC 4136. The symbols represent the receding (dots) and approaching (crosses) the side (with respect to the center).
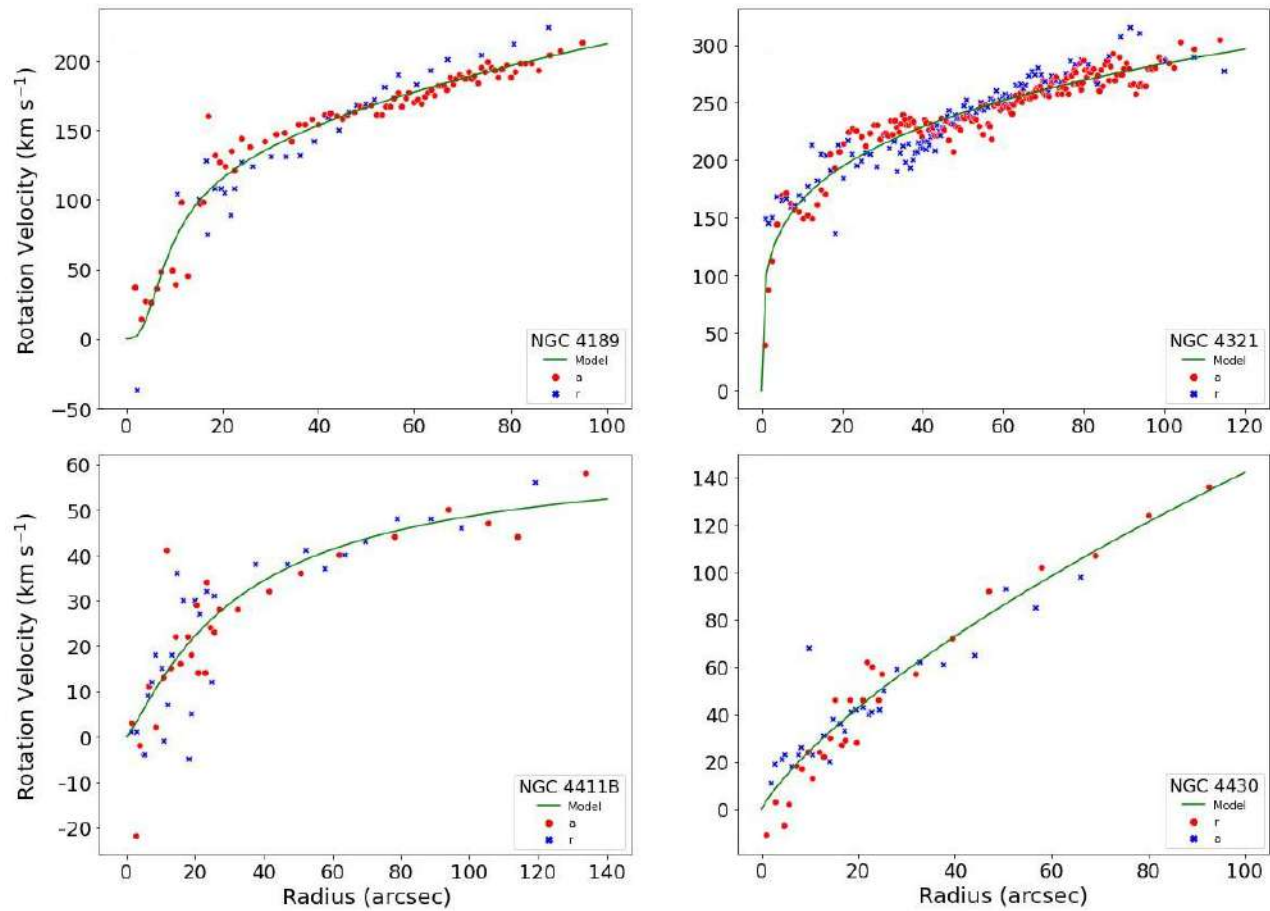
Figure C.1.6: Rotation curves of WiNDS. Top left-hand panel NGC 4189. Top right-hand panel NGC 4321. Bottom left-hand panel NGC 4411B. Bottom right-hand panel NGC 4430. The symbols represent the receding (dots) and approaching (crosses) the side (with respect to the center).
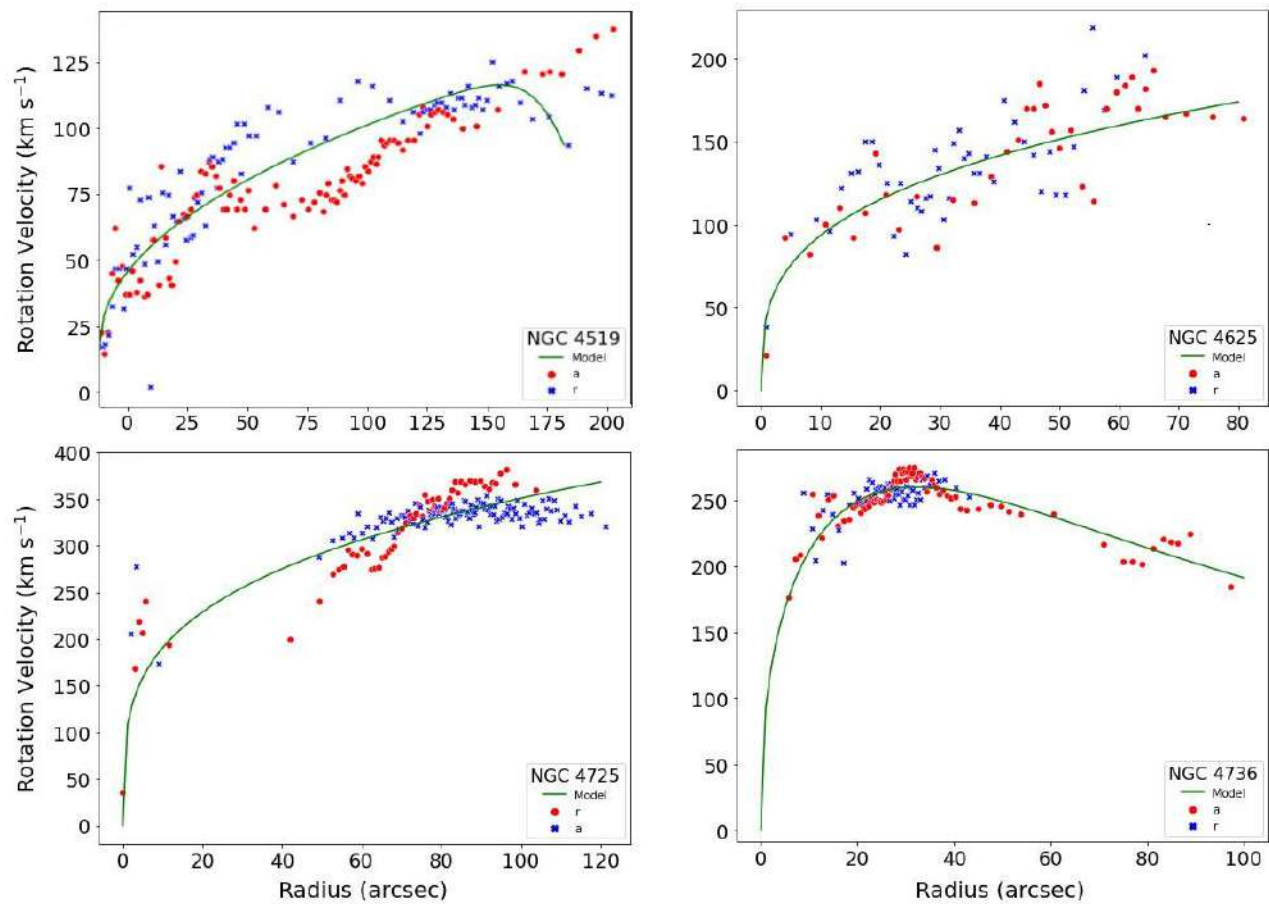
Figure C.1.7: Rotation curves of WiNDS. Top left-hand panel NGC 4519. Top right-hand panel NGC 4625. Bottom left-hand panel NGC 4725. Bottom right-hand panel NGC 4736. The symbols represent the receding (dots) and approaching (crosses) the side (with respect to the center).
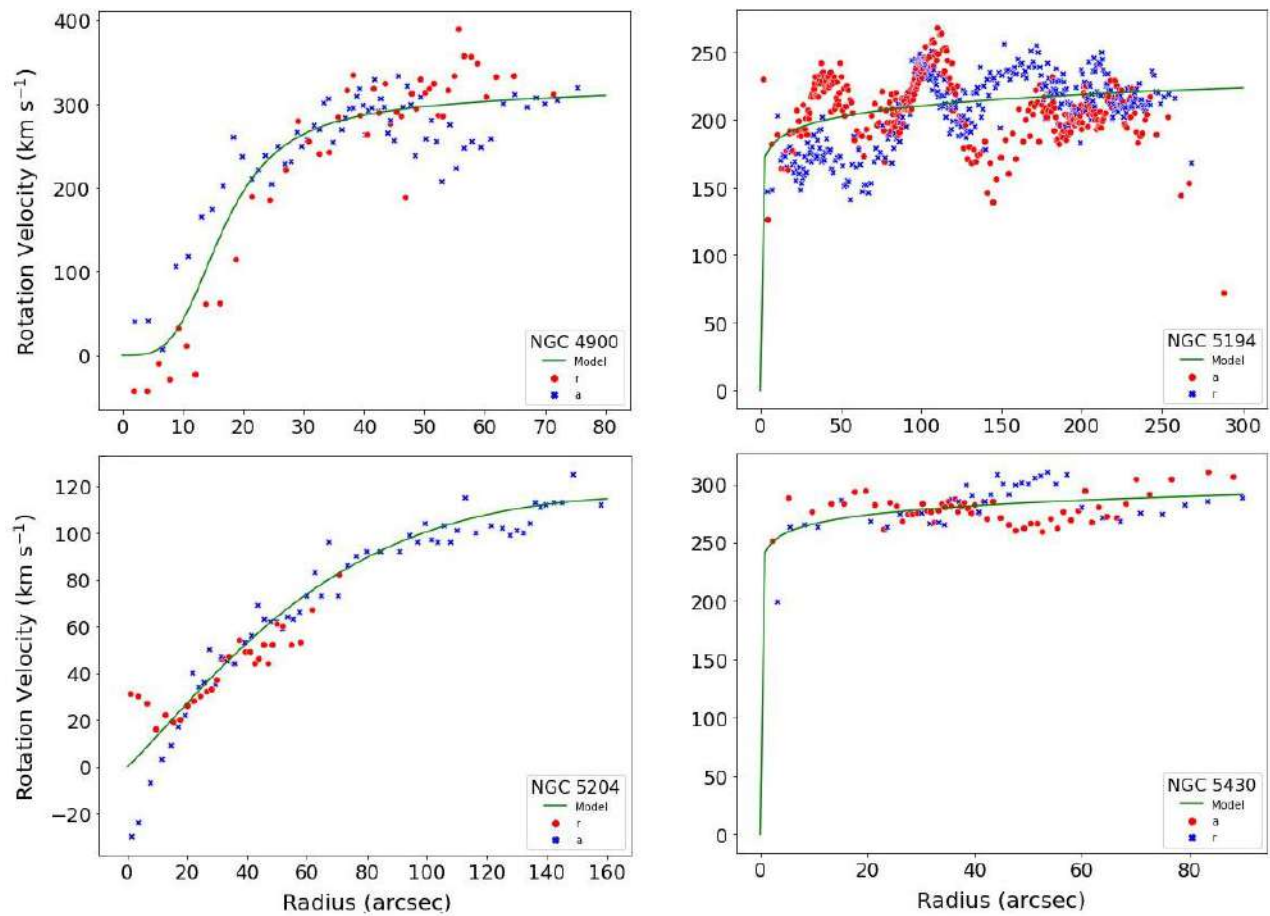
Figure C.1.8: Rotation curves of WiNDS. Top left-hand panel NGC 4900. Top right-hand panel NGC 5194. Bottom left-hand panel NGC 5204. Bottom right-hand panel NGC 5430. The symbols represent the receding (dots) and approaching (crosses) the side (with respect to the center).
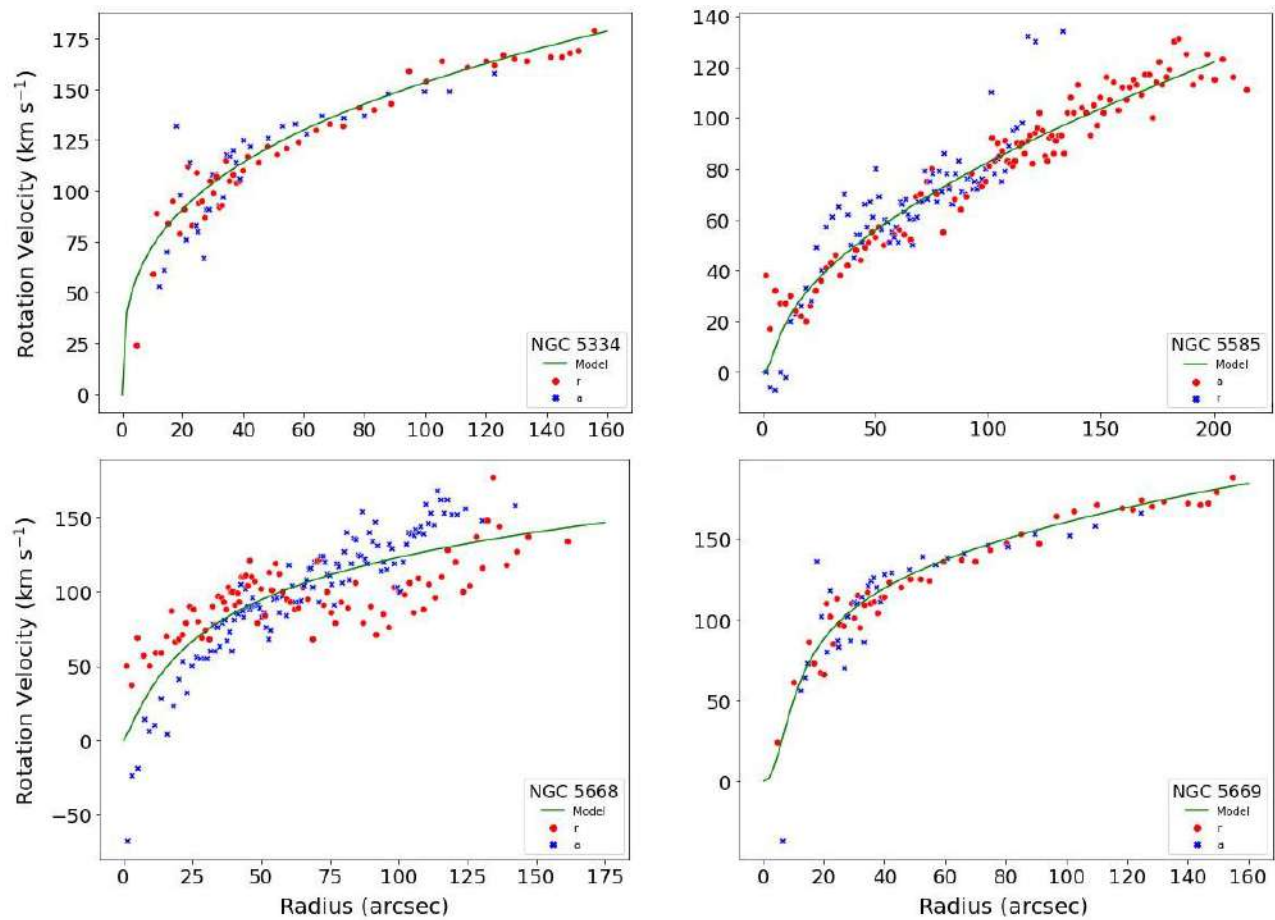
Figure C.1.9: Rotation curves of WiNDS. Top left-hand panel NGC 5334. Top right-hand panel NGC 5585. Bottom left-hand panel NGC 5668. Bottom right-hand panel NGC 5669. The symbols represent the receding (dots) and approaching (crosses) the side (with respect to the center).
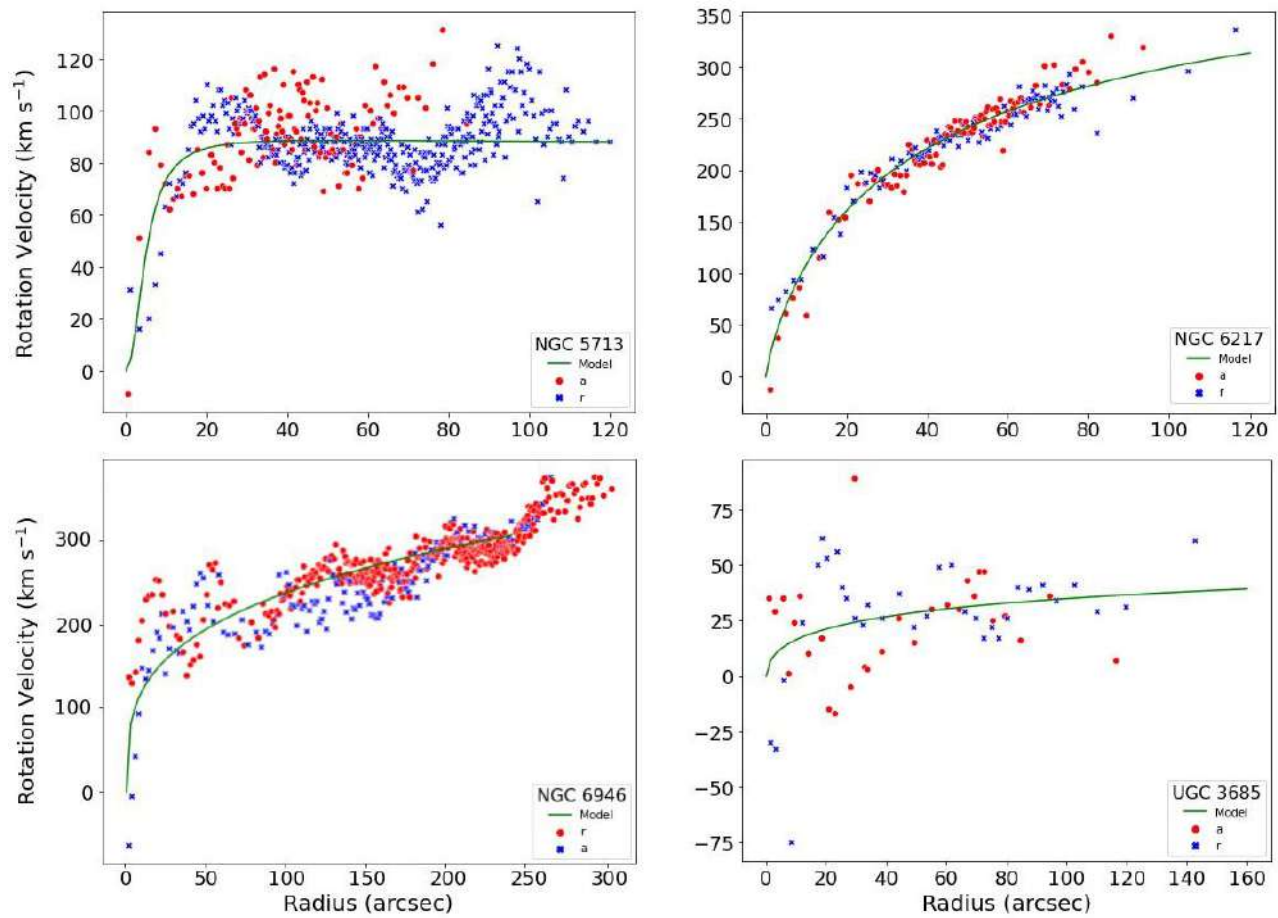
Figure C.1.10: Rotation curves of WiNDS. Top left-hand panel NGC 5713. Top right-hand panel NGC 6217. Bottom left-hand panel NGC 6946. Bottom right-hand panel UGC 3685. The symbols represent the receding (dots) and approaching (crosses) the side (with respect to the center).

Appendix D

TNG50 galaxy sample

D.1 Present-day face-on images of the B-band surface brightness
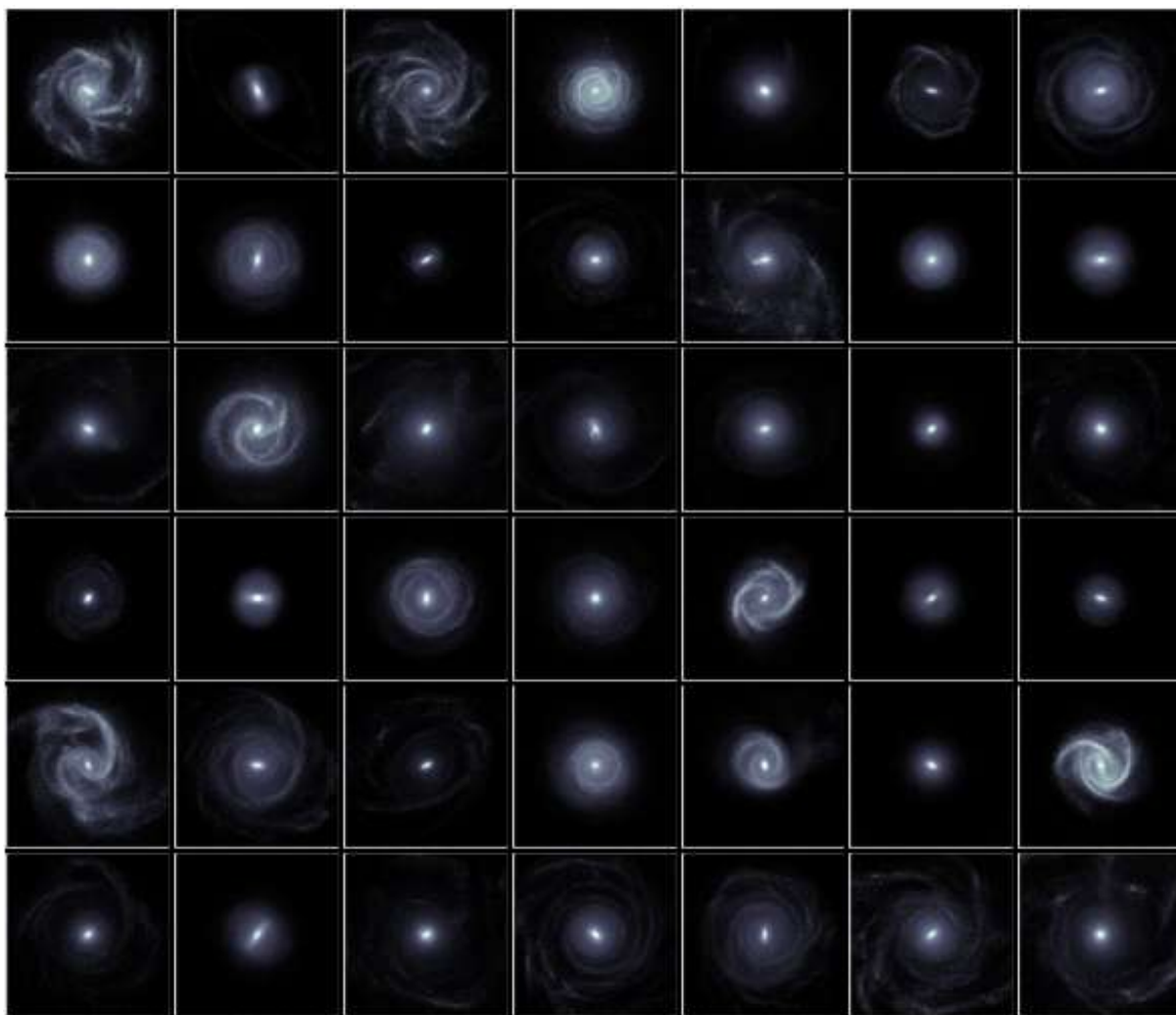
Figure D.1.1: Surface brightness profile in the B-band of TNG50 galaxy sample seen in face-on orientation.

Figure D.1.2: As in Fig. D.1.2.
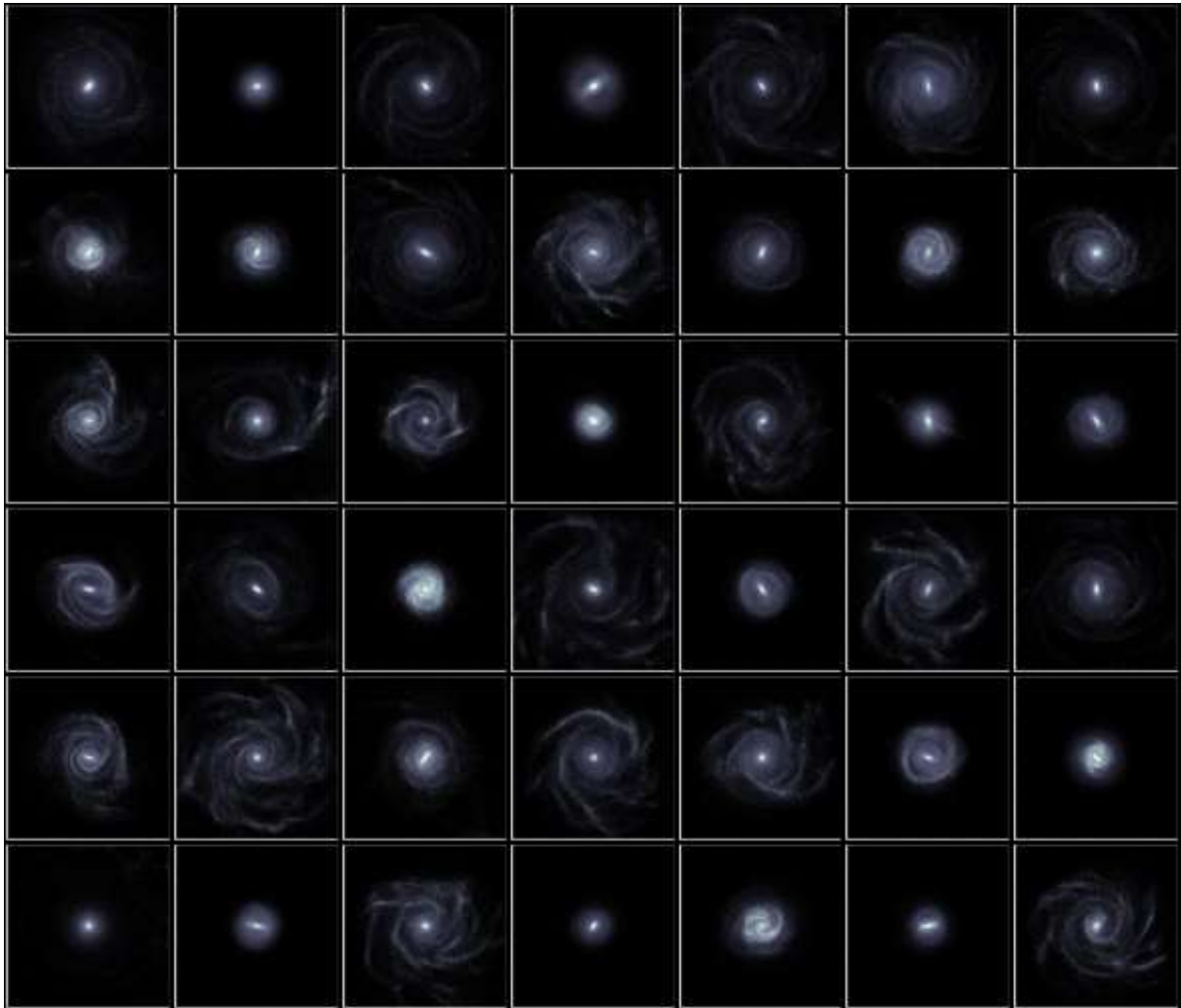
Figure D.1.3: As in Fig. D.1.3.
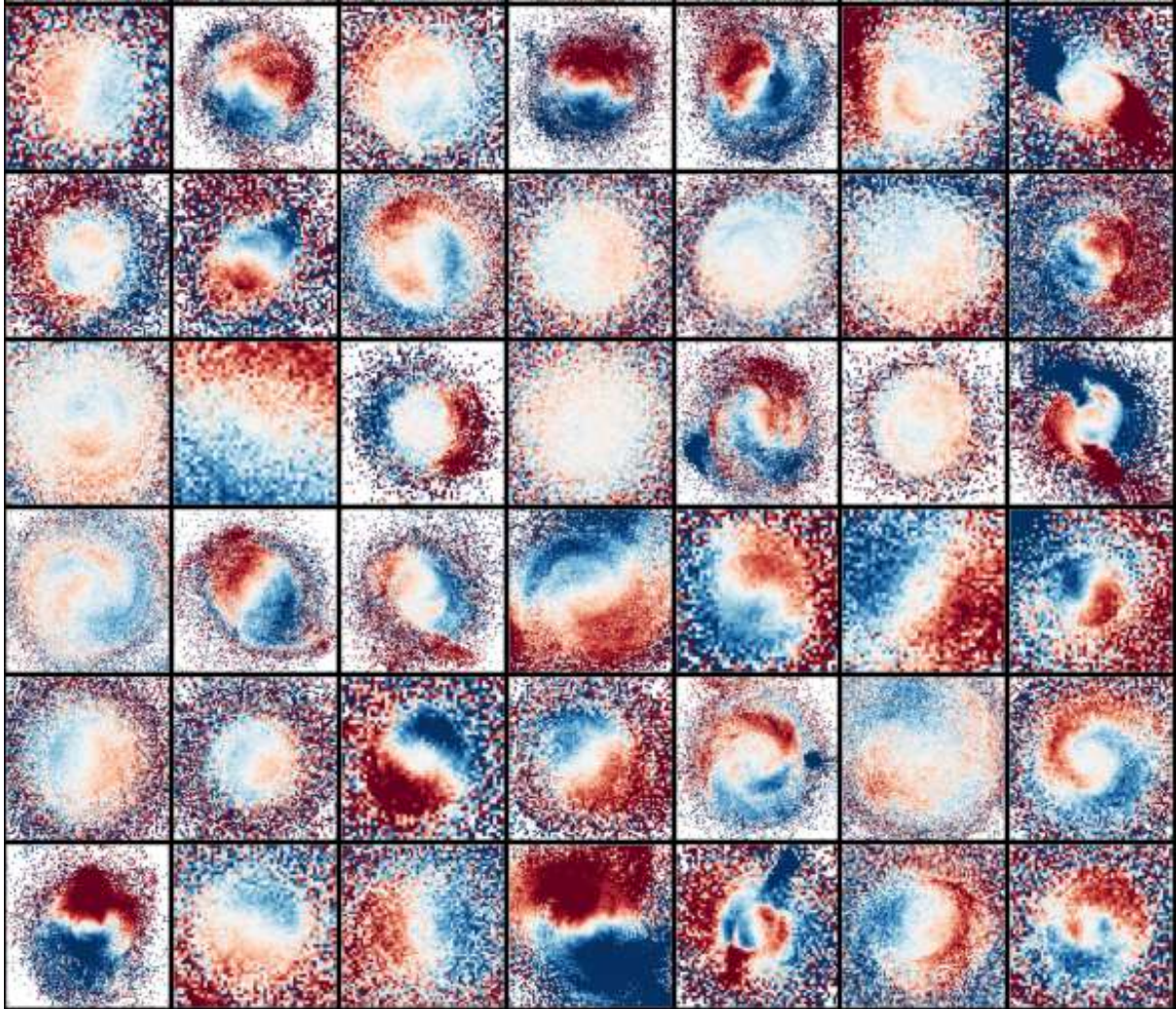
Figure D.1.4: As in Fig. D.1.4.

D.2 Mean height maps
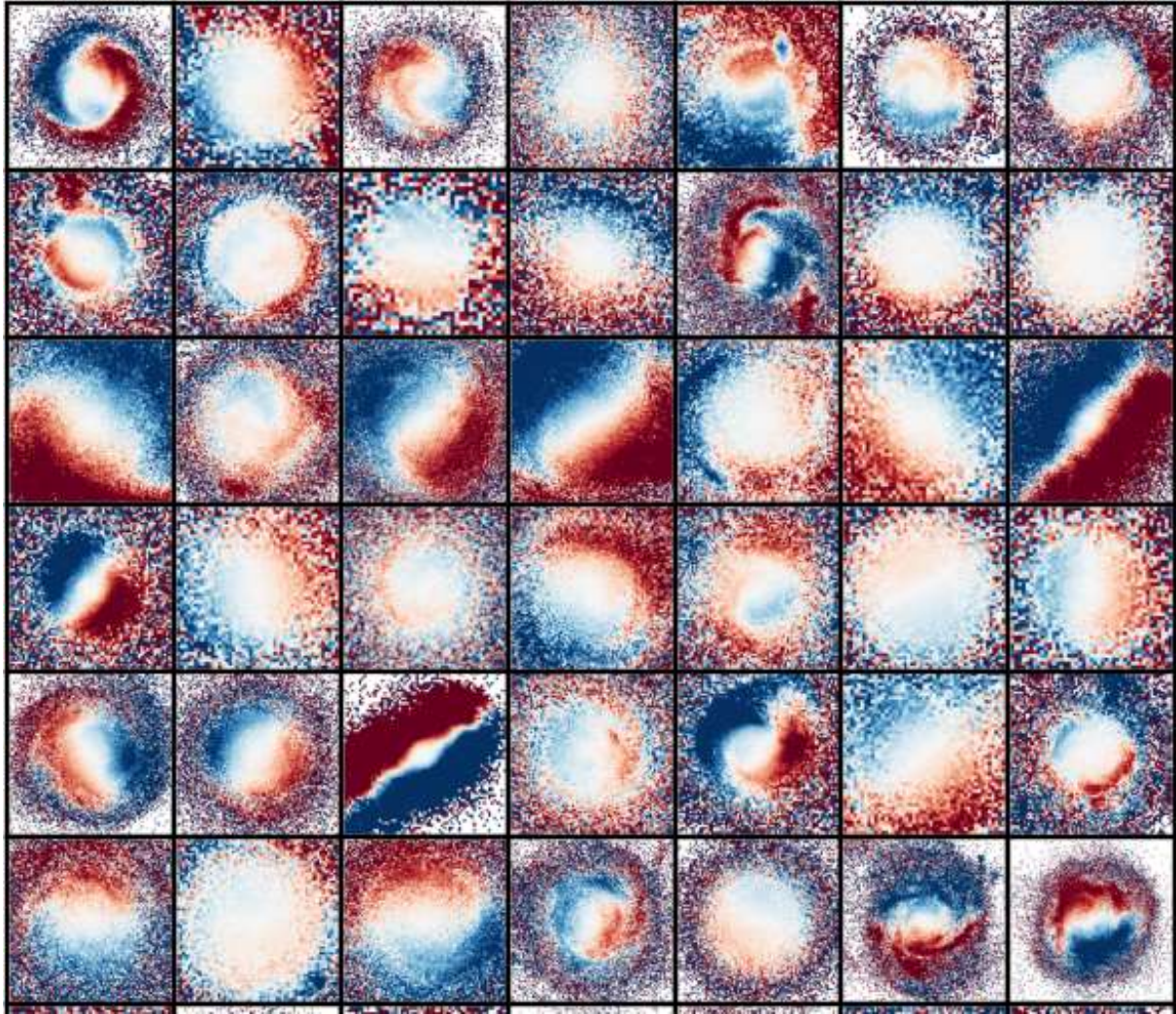
Figure D.2.1: Maps of the simulated stellar disk's mass-weighted mean height, $\langle Z \rangle$. The different map colors indicate different values of $\langle Z \rangle$ in kpc.
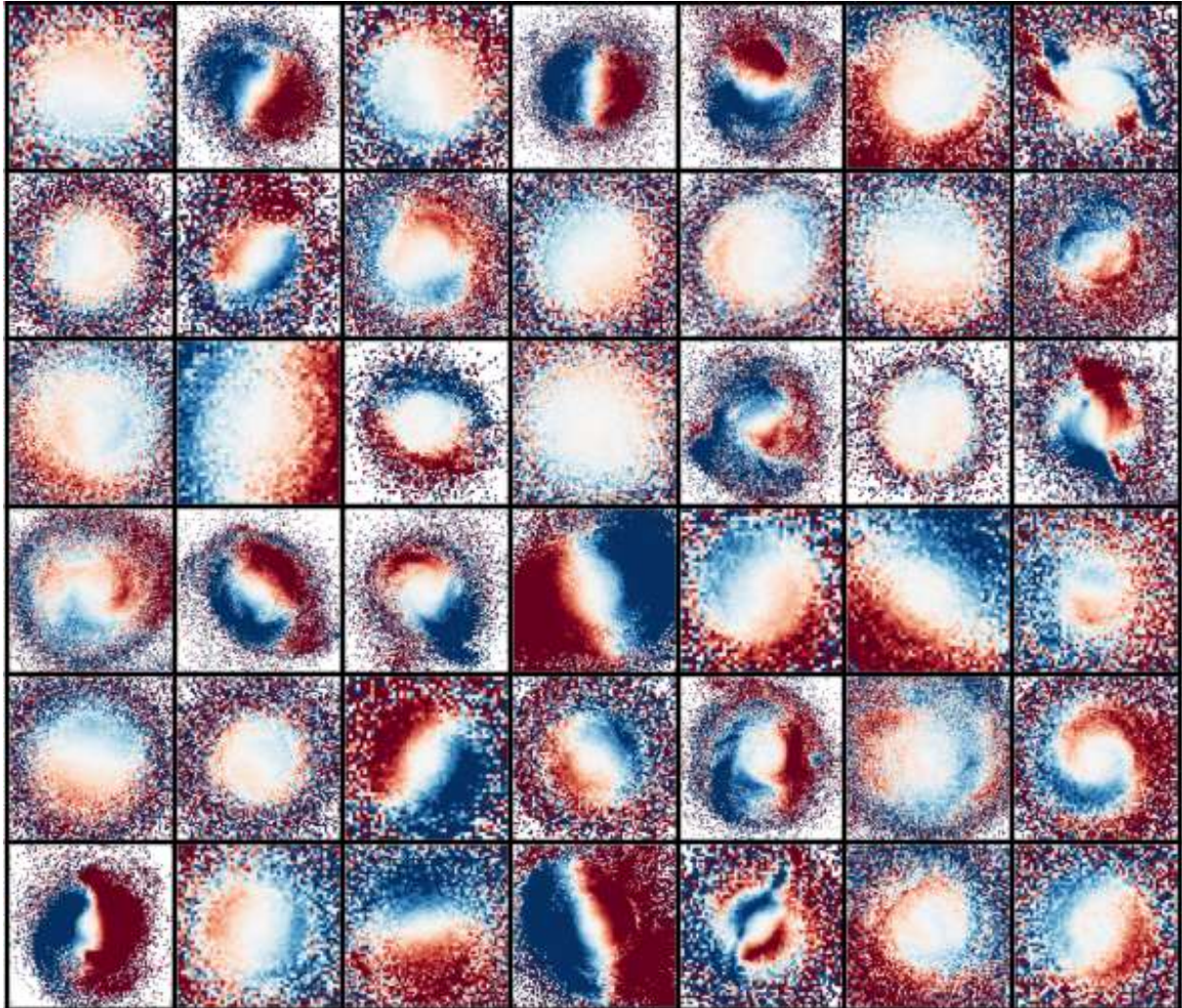
Figure D.2.2: Maps of the simulated stellar disk's mass-weighted mean height, $\langle Z \rangle$. The different map colors indicate different values of $\langle Z \rangle$ in kpc.
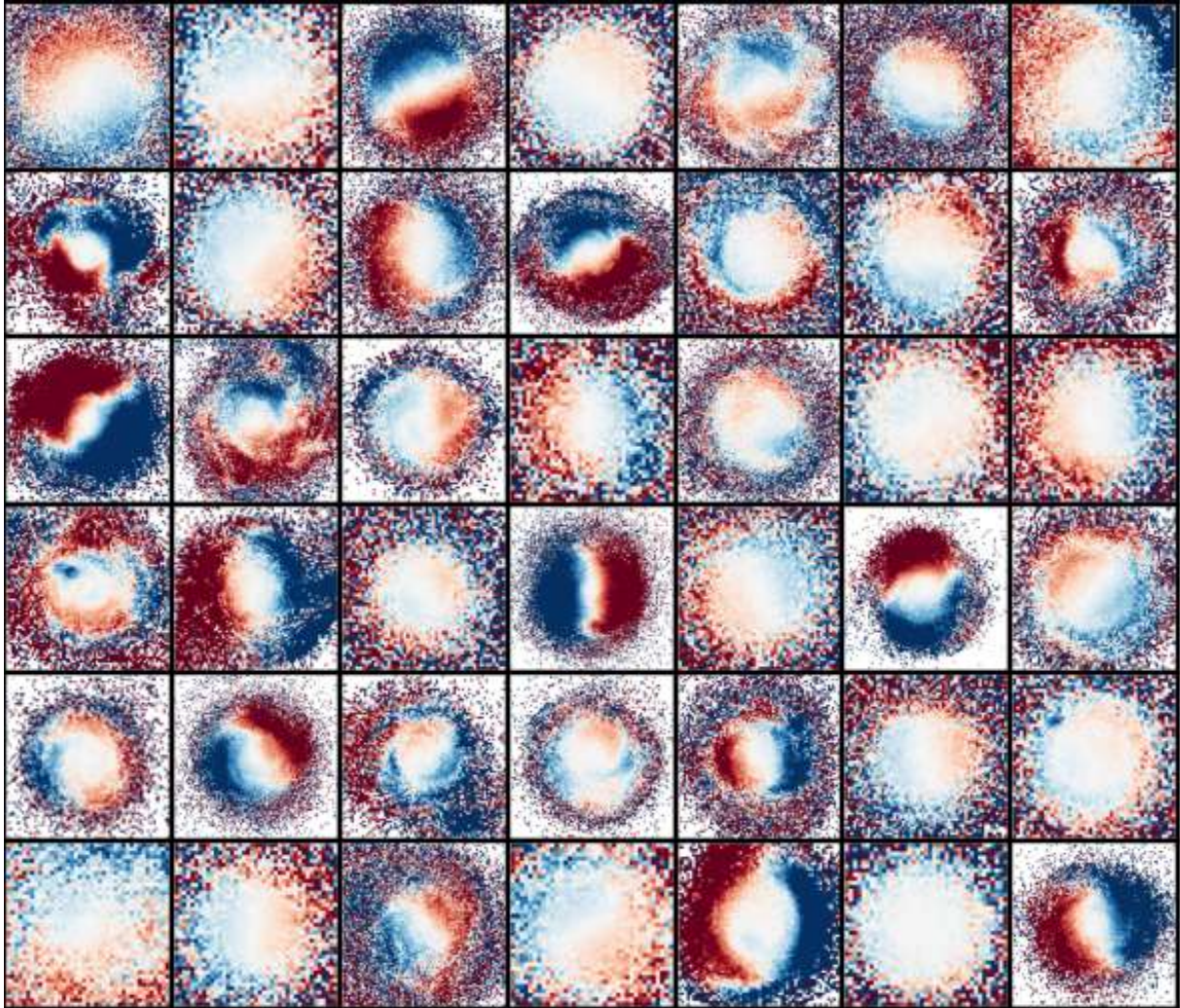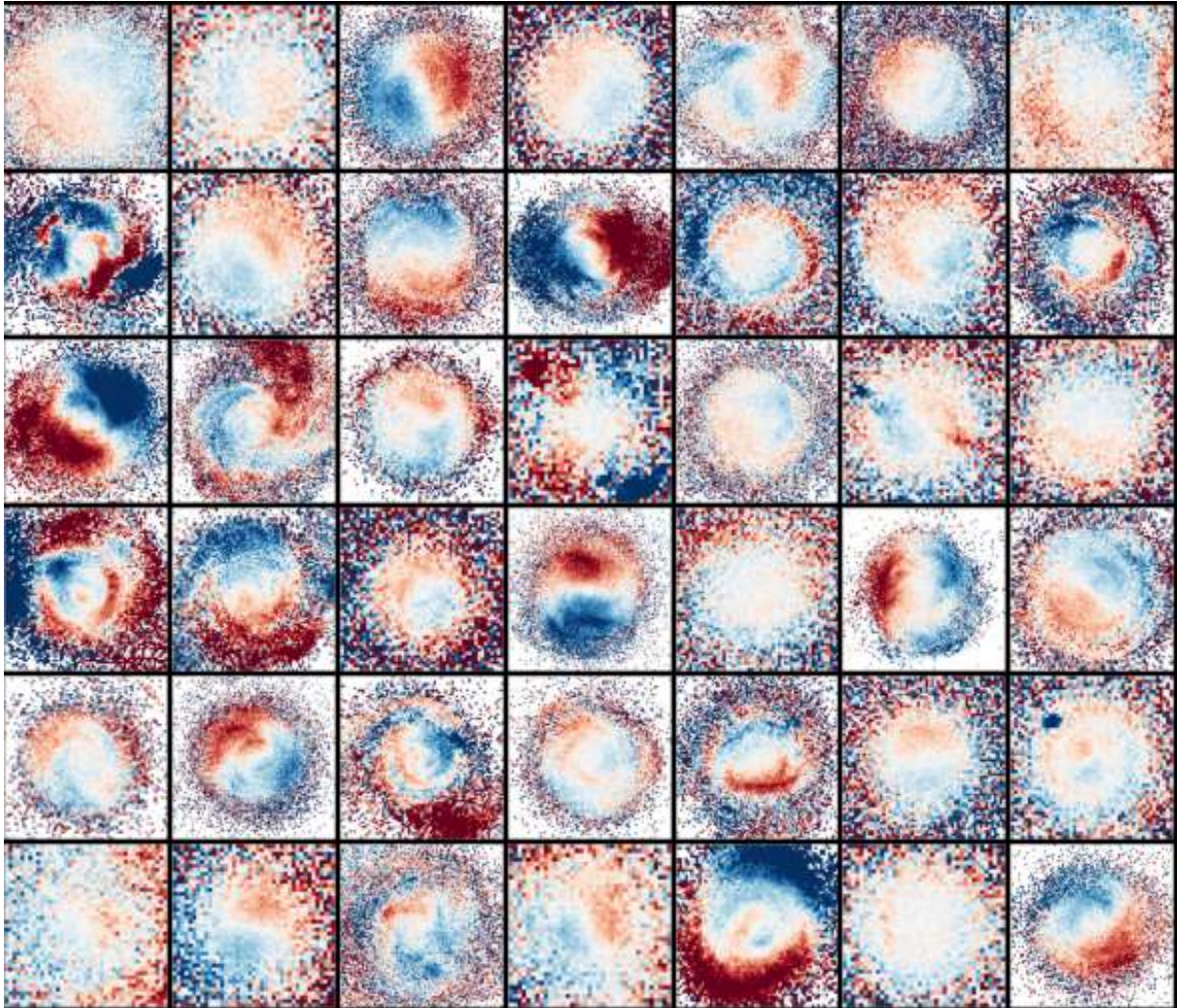
Figure D.2.3: Maps of the simulated stellar disk's mass-weighted mean height, $\langle Z \rangle$. The different map colors indicate different values of $\langle Z \rangle$ in kpc.
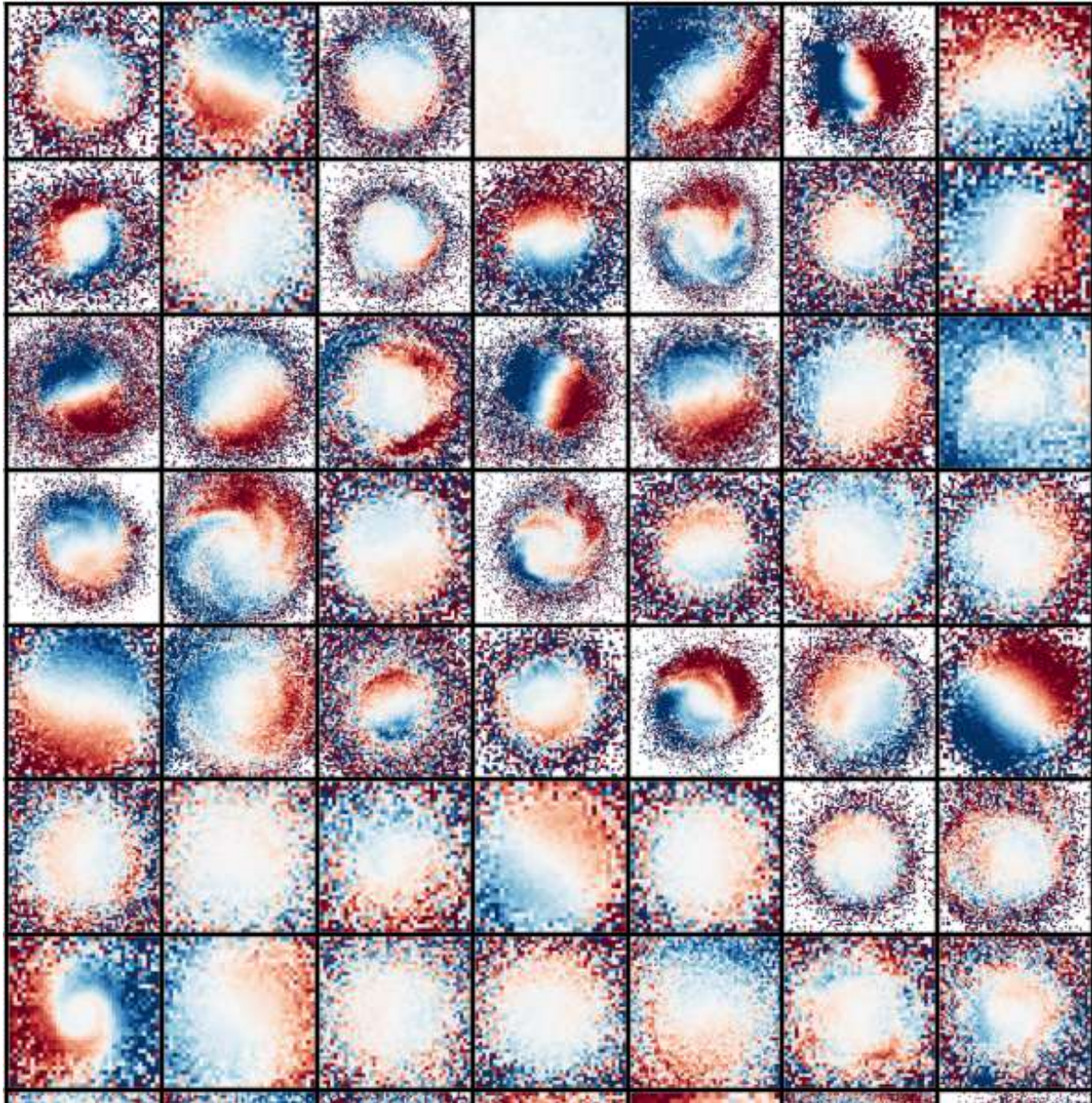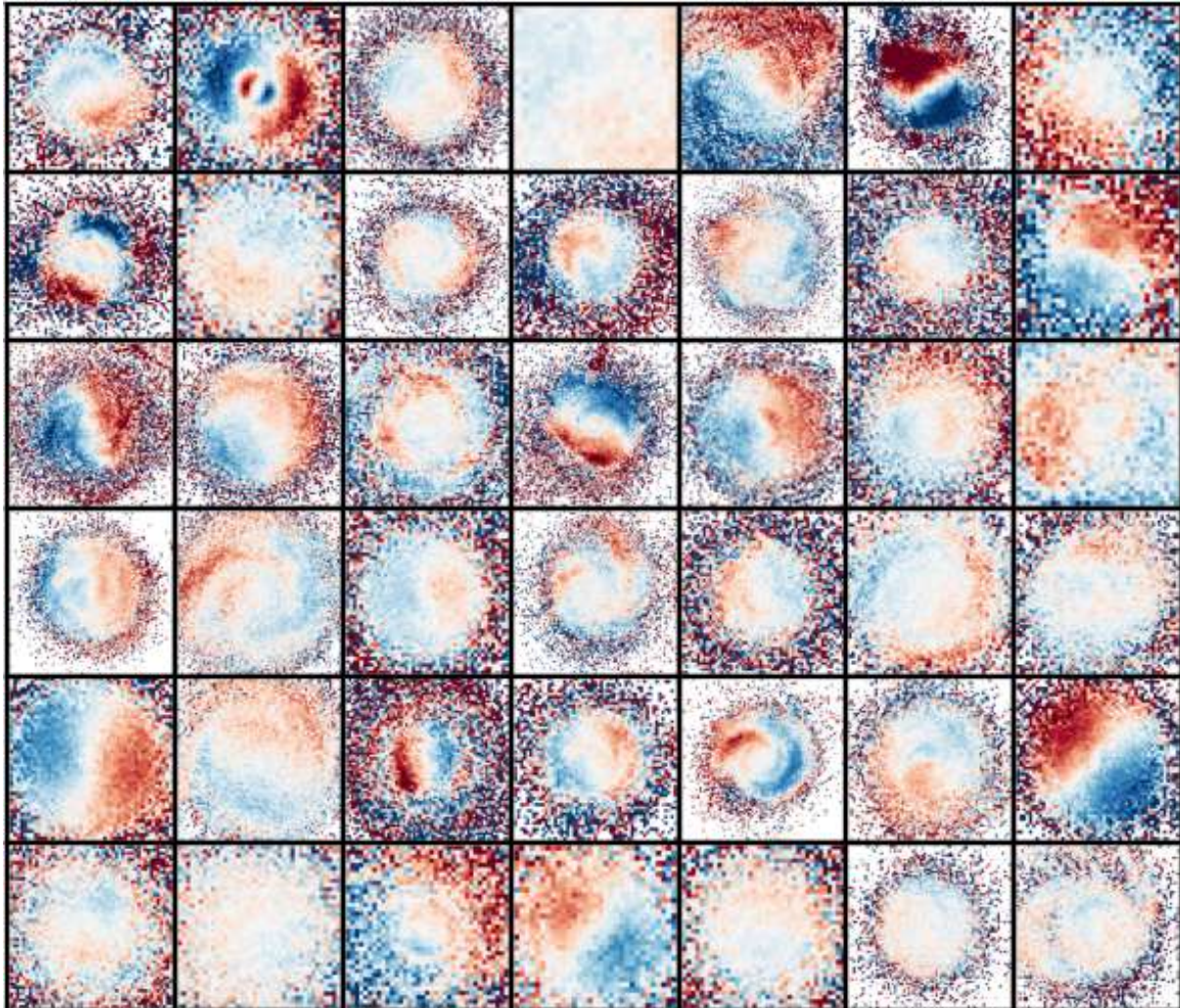
Figure D.2.4: Maps of the simulated stellar disk's mass-weighted mean height, $\langle Z \rangle$. The different map colors indicate different values of $\langle Z \rangle$ in kpc.
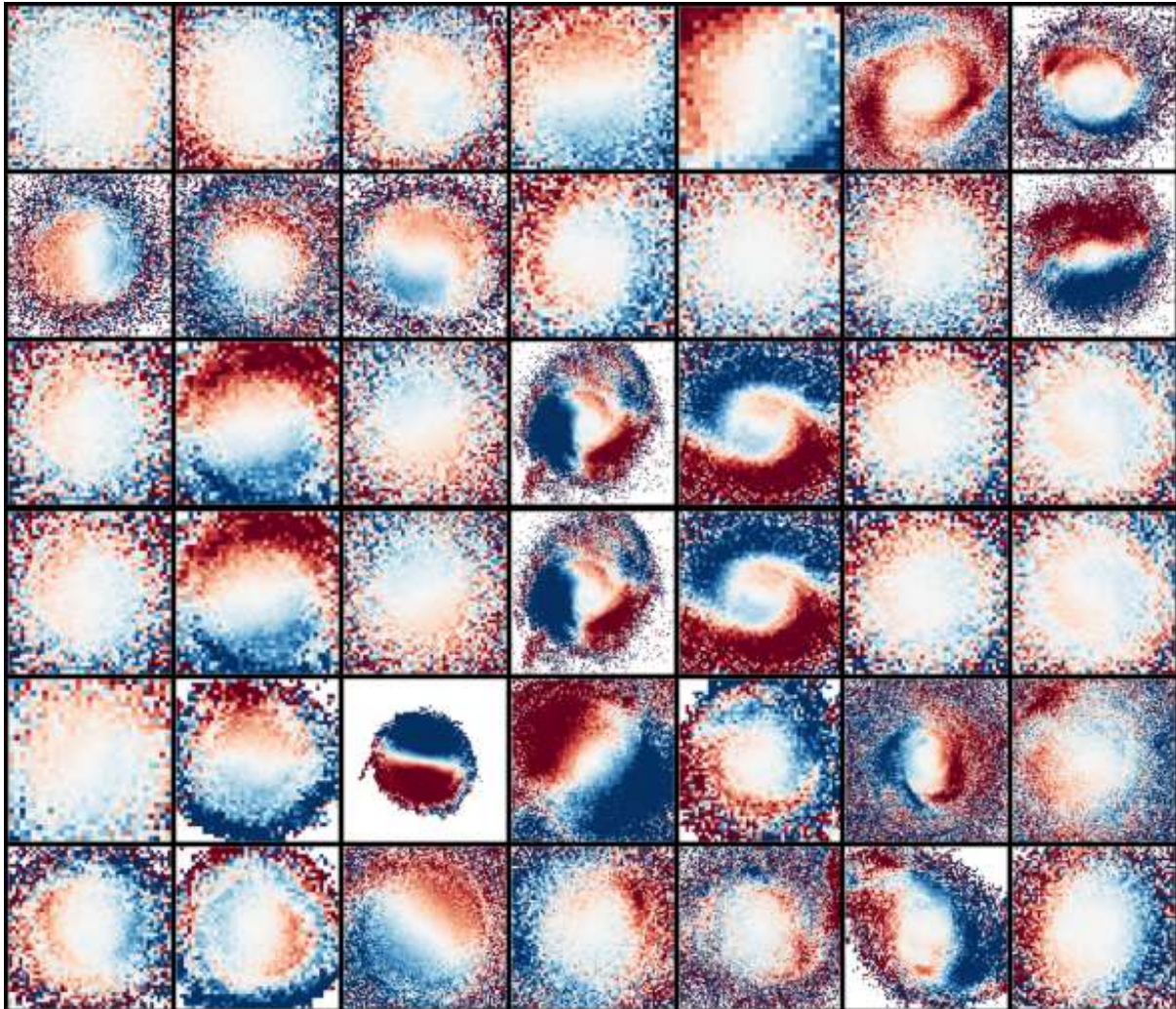
Figure D.2.5: Maps of the simulated stellar disk's mass-weighted mean height, $\langle Z \rangle$. The different map colors indicate different values of $\langle Z \rangle$ in kpc.
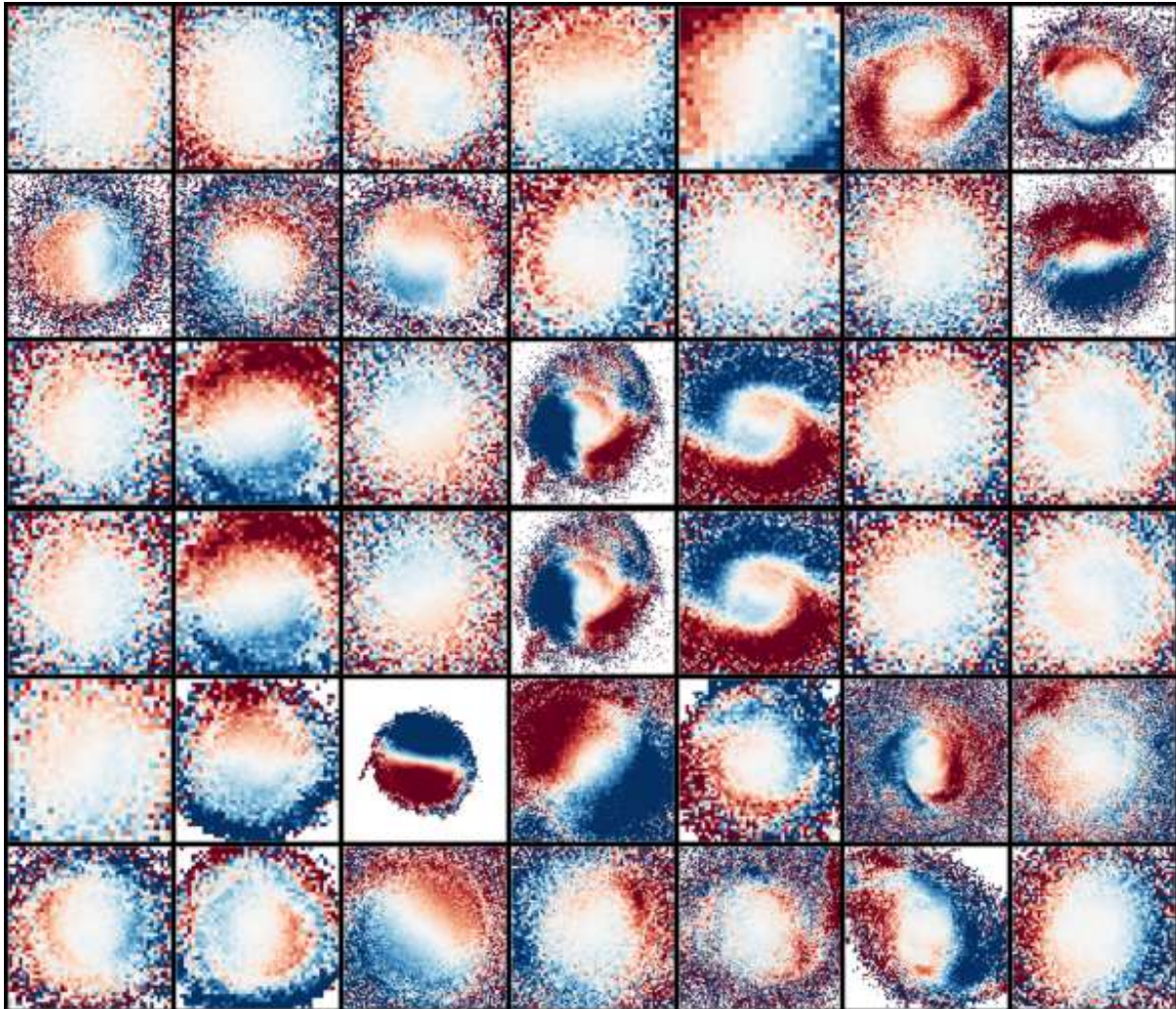
Figure D.2.6: Maps of the simulated stellar disk's mass-weighted mean height, $\langle Z \rangle$. The different map colors indicate different values of $\langle Z \rangle$ in kpc.
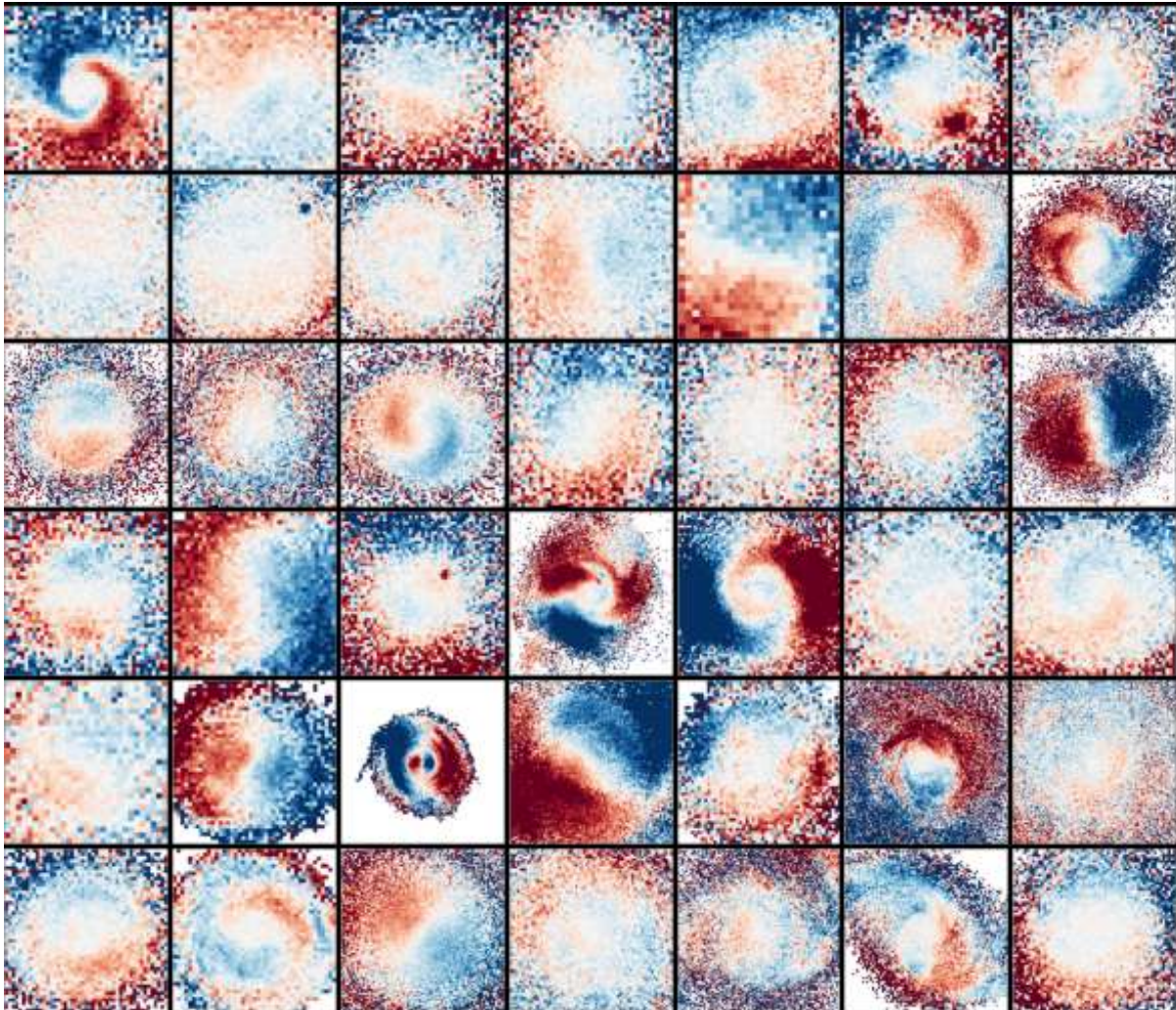
D.3 Mean vertical velocity maps
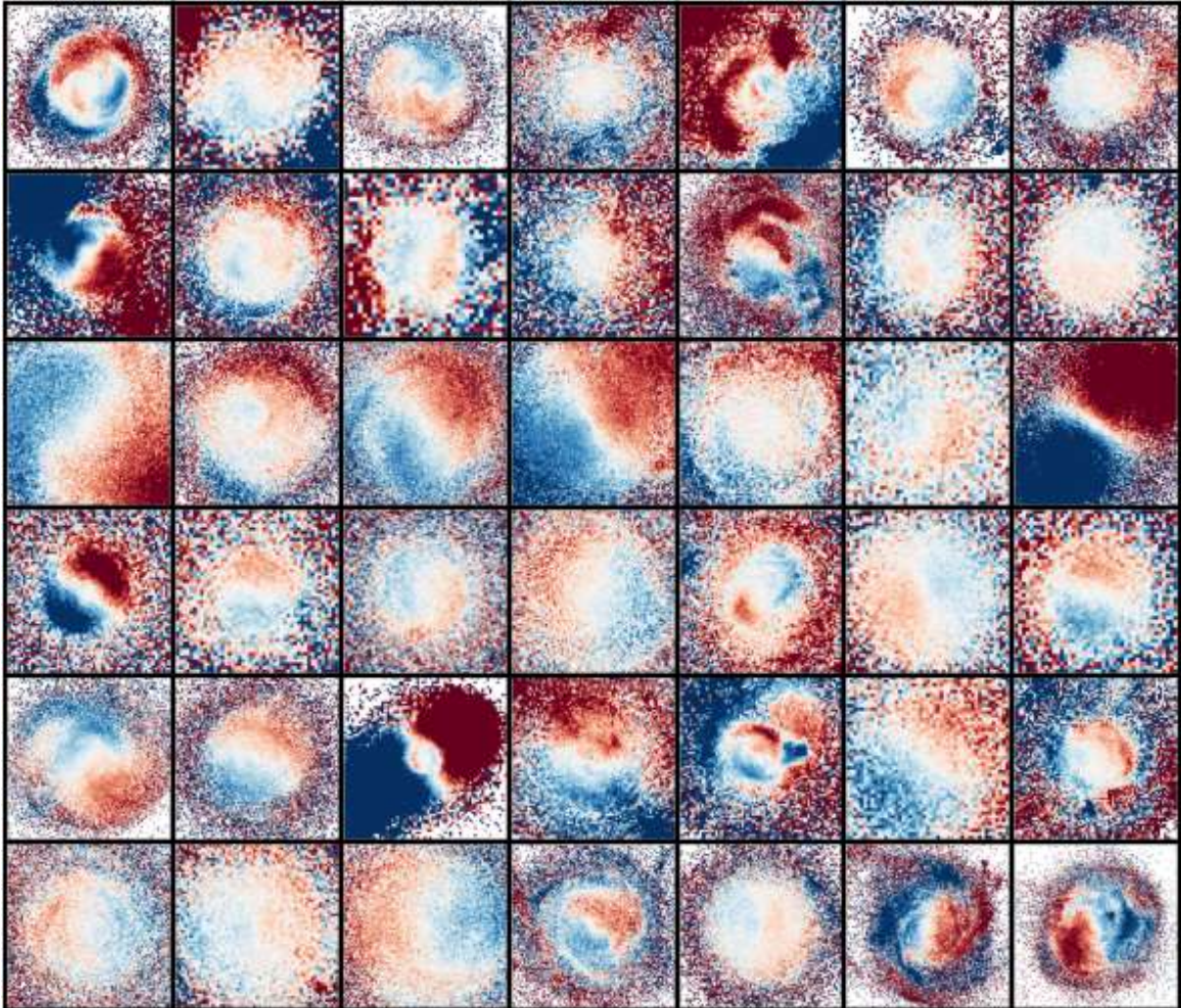
Figure D.3.1: Maps of the simulated stellar disk's mass-weighted vertical velocity, $\langle V_z \rangle$. The different map colors indicate different values of $\langle V_z \rangle$ in km s^{-1}.
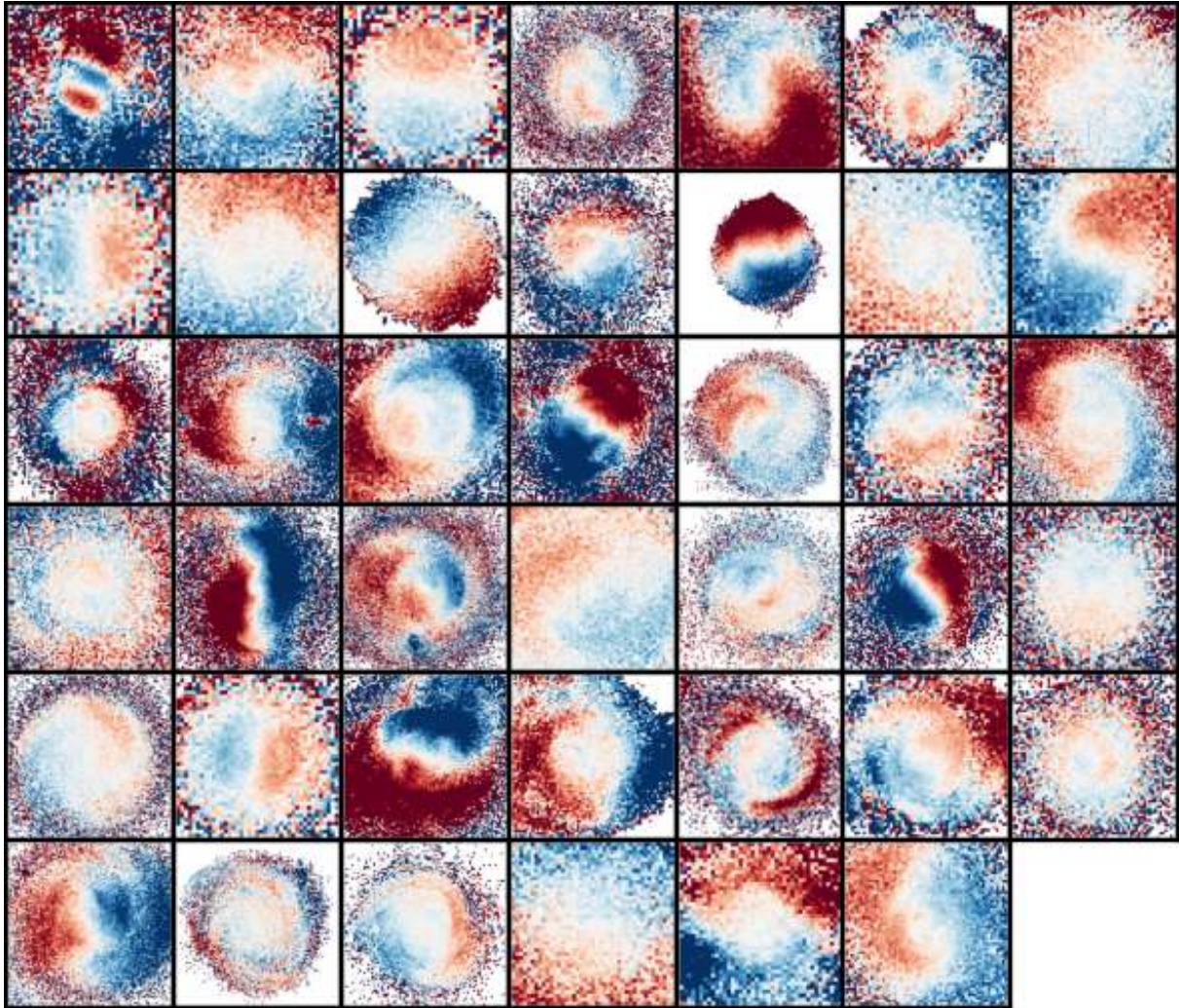
Figure D.3.2: Maps of the simulated stellar disk's mass-weighted vertical velocity, $\langle V_z \rangle$. The different map colors indicate different values of $\langle V_z \rangle$ in km s^{-1}.

Figure D.3.3: Maps of the simulated stellar disk's mass-weighted vertical velocity, $\langle V_z \rangle$. The different map colors indicate different values of $\langle V_z \rangle$ in km s^{-1}.

Figure D.3.4: Maps of the simulated stellar disk's mass-weighted vertical velocity, $\langle V_z \rangle$. The different map colors indicate different values of $\langle V_z \rangle$ in km s^{-1}.

Figure D.3.5: Maps of the simulated stellar disk's mass-weighted vertical velocity, $\langle V_z \rangle$. The different map colors indicate different values of $\langle V_z \rangle$ in km s^{-1}.

Figure D.3.6: Maps of the simulated stellar disk's mass-weighted vertical velocity, $\langle V_z \rangle$. The different map colors indicate different values of $\langle V_z \rangle$ in km s^{-1}.

Appendix E

The tidal field exerted on each central galaxy as a function of time

E.1 The tidal field exerted on each host by its ten most massive satellites as a function of time.
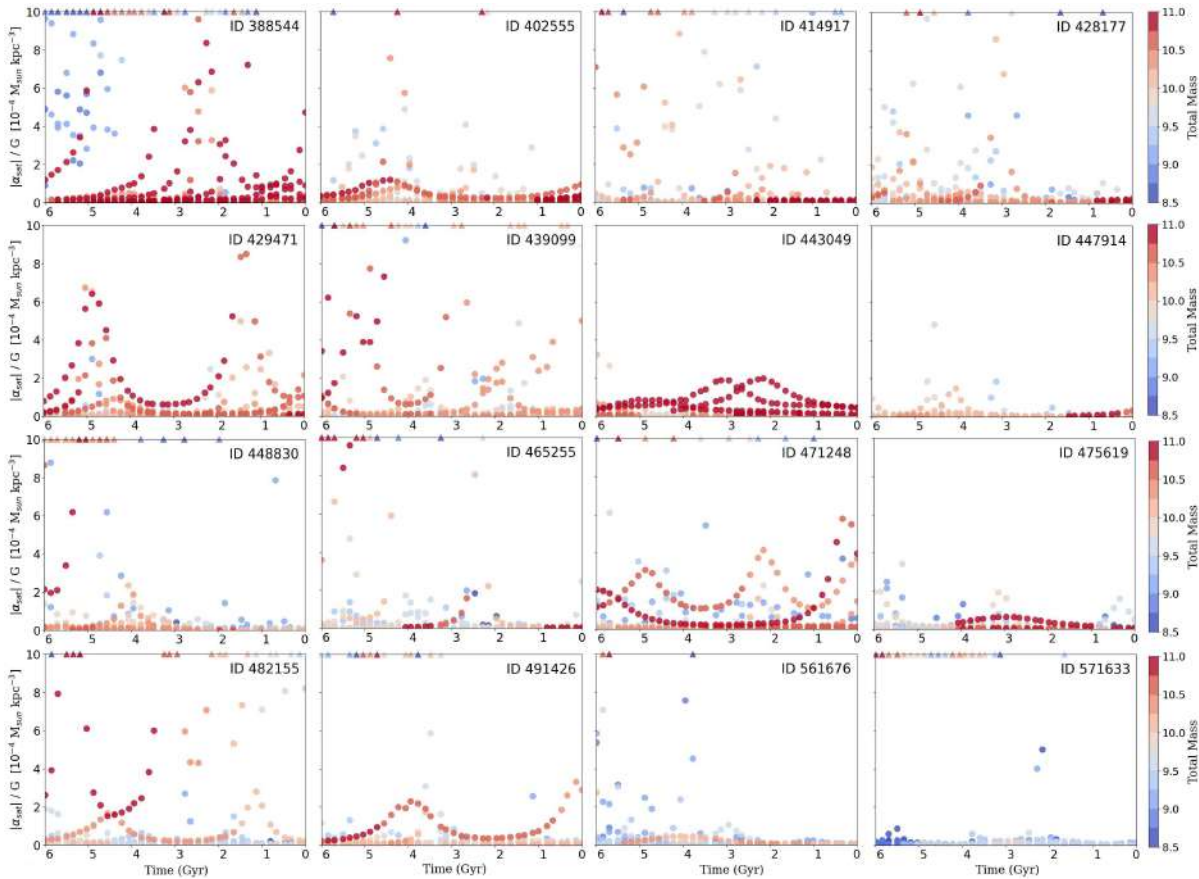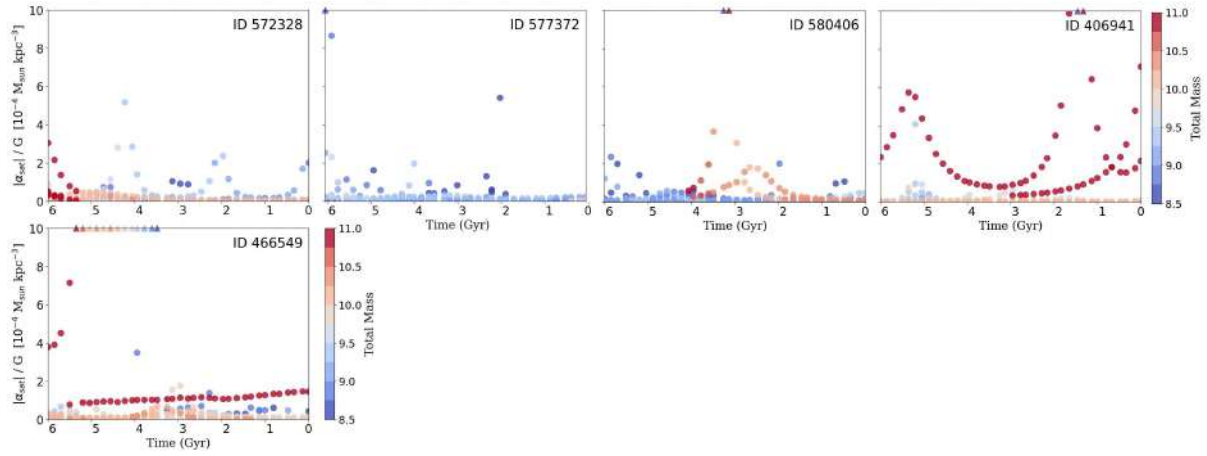

Figure E.1.1: The tidal field exerted on each host by its ten most massive satellites as a function of time for galaxies with flat disks.

Figure E.1.2: The tidal field exerted on each host by its ten most massive satellites as a function of time for galaxies with flat disks.
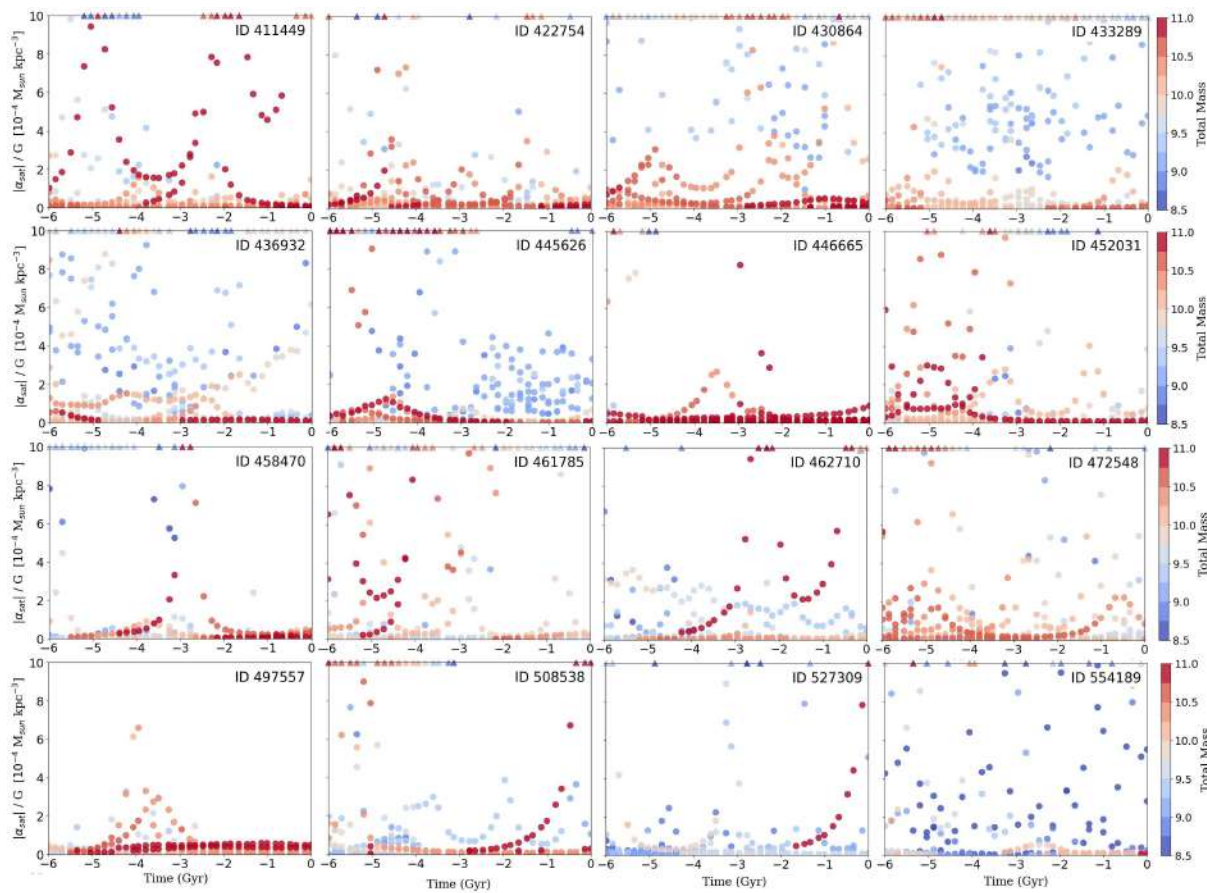

Figure E.1.3: The tidal field exerted on each host by its ten most massive satellites as a function of time for galaxies with simple warped disks.
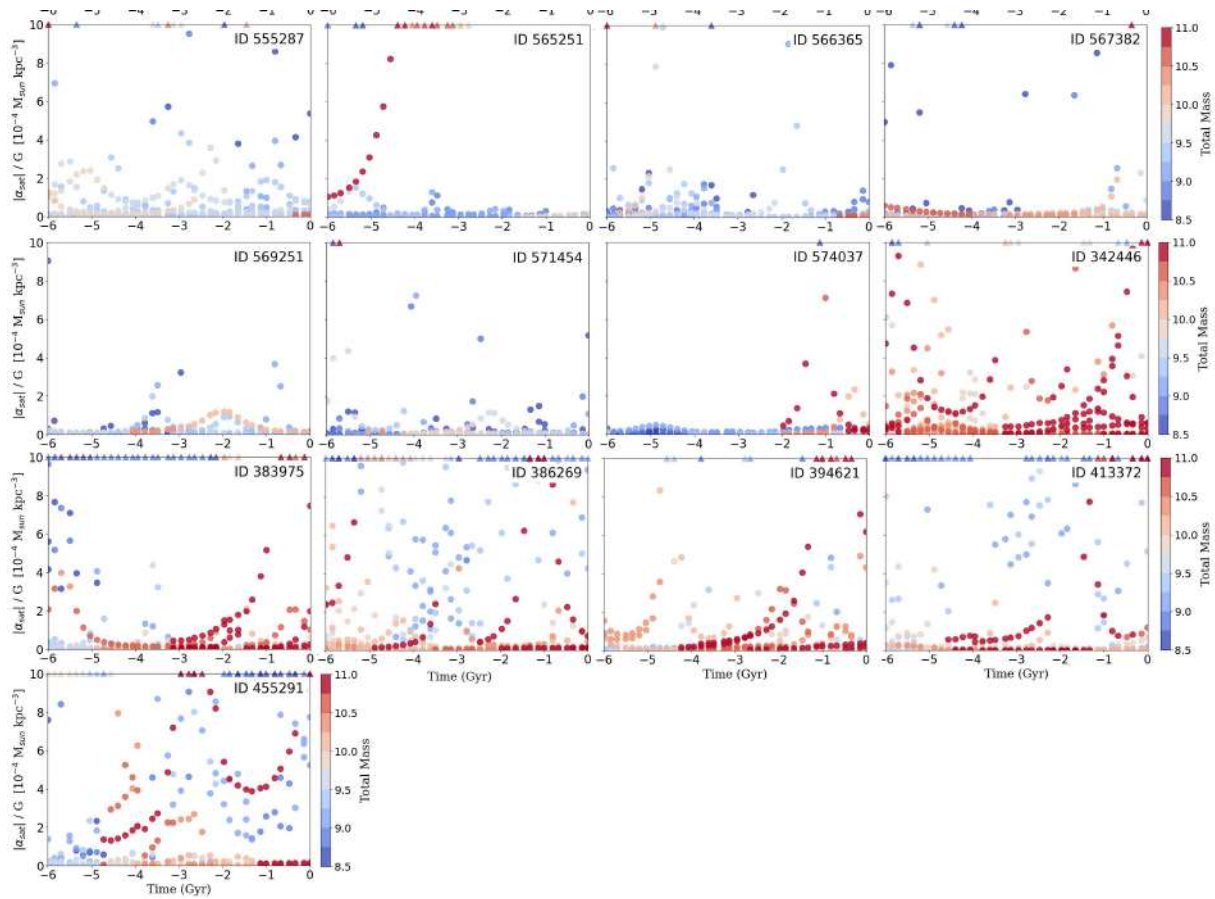
Figure E.1.4: The tidal field exerted on each host by its ten most massive satellites as a function of time for galaxies with simple warped disks.
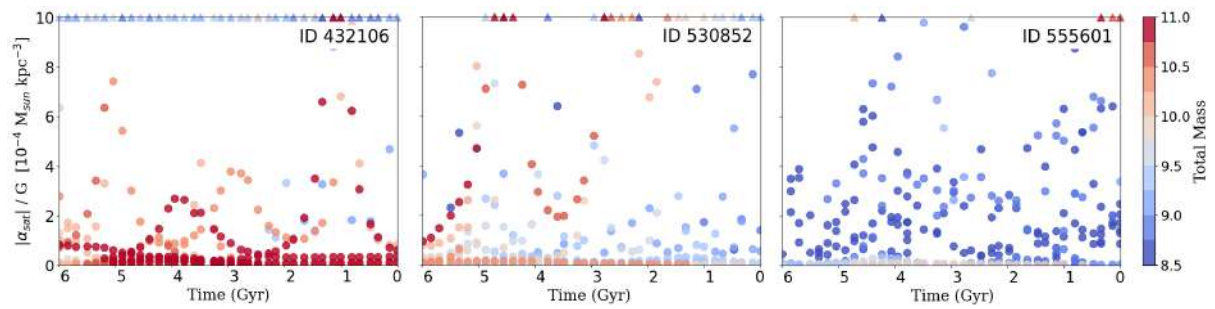

Figure E.1.5: The tidal field exerted on each host by its ten most massive satellites as a function of time for galaxies with corrugated pattern.